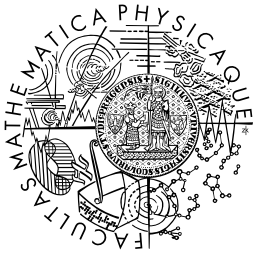

FACULTY
OF MATHEMATICS
AND PHYSICS
Charles University

DOCTORAL THESIS

Mgr. Vlastimil Vojáček

Properties of faint meteors studied by video observations

Astronomical Institute of the Czech Academy of Sciences

Supervisor of the doctoral thesis: RNDr. Jiří Borovička, CSc.
Study programme: Physics
Study branch: 4F1

Prague 2017

I declare that I carried out this doctoral thesis independently, and only with the cited sources, literature and other professional sources.

I understand that my work relates to the rights and obligations under the Act No. 121/2000 Sb., the Copyright Act, as amended, in particular the fact that the Charles University has the right to conclude a license agreement on the use of this work as a school work pursuant to Section 60 subsection 1 of the Copyright Act.

In ..... date ..... signature of the author

Title: Properties of faint meteors studied by video observations

Author: Mgr. Vlastimil Vojáček

Institute: Astronomical Institute of the Czech Academy of Sciences

Supervisor: RNDr. Jiří Borovička, CSc., Astronomical Institute of the Czech Academy of Sciences

Abstract: Parallel double–station video observations paired with spectroscopic video observations are a good way to study millimetre-sized meteoroids. Almost two decades of video observations of meteors at the Ondřejov observatory give us broad database to study large quantities of meteoroids and their properties.

In this work we combined spectral video observations and results of the modelling of the fragmentation of meteoroids. Along with complex information about meteoroid's trajectories and orbits, this can give us better understanding about origin, internal structure etc. of these millimetre-sized interplanetary bodies.

Meteoroids that contained small grains tend to release the sodium early. Since there is a smaller amount of sodium for Na depleted meteoroids, the sodium was released earlier than it was released for meteoroids with same grain sizes and without the sodium depletion. Overall, meteoroids with sodium depletion showed different composition: they were composed of stronger material without very small grains and they did not showed very bright wakes. Two iron meteoroids on Halley type orbits were observed. They are probably remnants of complicated early years of our solar system. The distribution of grain sizes of Jupiter–family members was in a good agreements with results from the COSIMA instrument from the ROSETTA mission.

Keywords: meteors meteoroids spectra fragmentation

I would like thank to my supervisor RNDr. Jiří Borovička, CSc. for many of his inspirational advises and for everything he learned me about the meteor science. I want to thank to my parents for their support throughout my years of study. My inspiration not only in everyday life is my girlfriend Pavlína. I want to thank to every observer. Without their sleepless nights this work would not be made. I also want to thank all my colleagues at the Ondřejov observatory for their warm welcome in their collective. I want to thank my two colleagues RNDr. David Čapek, Ph.D. and RNDr. Pavel Koten, Ph.D. for their advises that made this work better.

Contents

Foreword

The importance of meteor observations

The comets, asteroids and meteoroids are small bodies in our Solar system. Their rocky or icy material is believed to be remnant of earliest years of the formation of the Solar system. They may also represent primitive elements of planets. Thus study of comets, asteroids and meteoroids can reveal us important information about the history and the evolution of our planetary system.

Majority of meteoroids is debris of comets and asteroids. One of the main goals of meteor science is to resolve the composition of meteoroids. This knowledge can help us reveal more information about the composition of parent bodies of these meteoroids,

As some asteroids and comets, that are crossing the Earth orbit, can be potentially hazardous, the insight into their composition is crucial for possible and effective defence of our planet.

Our solar system was formed approximately 4.57×10^9 years ago [Bouvier and Wadhwa, 2010] from the gravitational accretion of interstellar molecular and dust cloud. It is generally believed that the original nebula had the same abundance as the Sun. Not only the Sun and planets were formed. Asteroids, comets and meteoroids were formed as well or they originated as leftovers from formation of larger bodies. Small bodies are also products of ongoing collisions in our Solar system. Some of the oldest known material can be found in primitive meteorites. They contain grains of compounds that formed in the cooling cloud of the forming Solar system. In comparison to Earth rocks, this material has not been reprocessed by geological activity. We can study material with the chemical composition of the very young Solar system.

In our Solar system, large number of comets are stored in Oort cloud, a sphere of diameter about $100,000$ AU. Orbits of these small icy bodies can be perturbed, which can send them into inner parts of Solar system. This flux of comets was much higher in history. Especially in the early ages of Solar system. As comets travel through interplanetary space, they can produce debris of particles - meteoroids. When these particles spread along comet's orbit and if this stream of meteoroids crosses Earth's orbit, we can observe annual meteor streams.

The main asteroid belt, located between orbits of Mars and Jupiter, is the main source of meteoroids. Because of relatively high population of asteroids in this area, collisions are frequent here. These collisions produce high amount of small rocky pieces and dust. Products of these collisions can be perturbed. If they collide with Earth, they can enter the atmosphere of our planet.

The motivation

The video observations are used more and more for the meteor observations by the professional astronomers. The availability of advanced equipment tempts amateur astronomers to use the video for meteor observation. Also the spectral observations of meteors are more common these days. The faint meteors research

is not focused only on the activity of major showers anymore. Astronomers are interested in differences between individual meteors, in the structure of meteoroids and in the abundances of individual elements in meteor spectra. New models of meteoroid erosion are developed. The long term video observations of faint meteors at Ondřejov observatory provides desired data and know–how for the meteor community.

We will try to combine the spectral observations with the study on the fragmentation of meteoroids. Meteor spectra can reveal information about individual meteoritic elements. Although only lines of sodium, magnesium and iron can be studied by our low resolution video spectra, relevant information about their abundances and the time resolved spectral lines can provide new knowledge about the behaviour of meteors. Models of meteoroid fragmentation can give us the estimation of physical parameters of small interplanetary bodies.

Although there were works that used both the spectral observations and the study of meteoroid fragmentation, they usually provided somewhat limited sample of meteoroids. This work tries to apply both the study of meteoroid fragmentation and the spectral analysis of broader sample of meteors. All known spectral types of meteors were used. Representative sample of members of major showers was selected. A large number of sporadic meteors has provided the necessary diversity of studied bodies.

1. Short introduction to meteor science

1.1 The definition

With the similarity of astronomy terms meteoroid, meteor or meteorite, people are often confused with their meanings. These terms are often used in this work, thus we will clarify them in a short summary.

Meteoroids are bodies in the interplanetary system that are too small to be called asteroids or comets. They are often fragments of comets or asteroids. They can also be formed as ejected debris from impact collisions of other Solar system bodies. Like other Solar System bodies, meteoroids are orbiting the Sun. Meteoroids of the same origin can form meteoroid streams. Members of the same meteoroid stream have similar orbital parameters. These stream are usually scattered during their existence by both gravitational and non–gravitational forces. A meteoroid can produce a light phenomenon called meteor when it collides with Earth atmosphere. This happens usually at heights of 80 to 120 kilometers above the Earth. The term meteor is from Greek *meteoron* that means *phenomenon in the sky*. Small part of the original mass of meteoroid that is massive enough can survive the collision with the Earth. The remnant then fall on the surface as meteorite. The graphical interpretation for this terminology is shown in Figure 1.1.

The definition of size limits for the meteoroids can be complicated. In the present state of knowledge the definition of meteoroid by International Astronomical Union (IAU) from 1961 is somewhat vague. The definition according to IAU is: "Meteoroid is a solid object moving in interplanetary space, of a size considerably smaller than an asteroid and considerably larger than an atom or molecule" [Millman, 1961]. The ability to produce meteor depends on the speed and size of the meteoroid. Rough limit for smallest size of meteoroid that can cause meteor is about 0.01 mm Ceplecha et al. [1998]. When we want to estimate the upper size limit for meteoroids, we have to determine the boundary between an asteroid and a meteoroid. The reasonable limit can be defined as the size of smallest asteroids that can be detected by instruments. The limit chosen by Ceplecha et al. [1998] and Beech and Steel [1995] was $\approx$ 10 m (at that time smallest asteroids detected were $\approx$ 10 m). But after the impact (and previous observation) of the object 2008 TC_3, with an estimated size of 4 m [Jenniskens et al., 2009], new comprehensive definition of the term meteor is offered by Rubin and Grossman [2010]: "A meteoroid is a 10 μm to 1 m size natural solid object moving in interplanetary space. A micrometeoroid is a meteoroid from 10 μm to 2 mm in size. Objects smaller than 10 μm are dust particles." Most recent and most credible definitions of terms in meteor astronomy was approved in 2017 by the International Astronomical Union (IAU) Commission F1. According to the Commision F1: "Meteoroid is a solid natural object of a size roughly between 30 micrometers and 1 meter moving in, or coming from, interplanetary space."[1]

As we can see, the difference in designation of meteoroids and asteroids is too

[1]Definition online at: `https://www.iau.org/static/science/scientific_bodies/commissions/f1/meteordefinitions_approved.pdf`

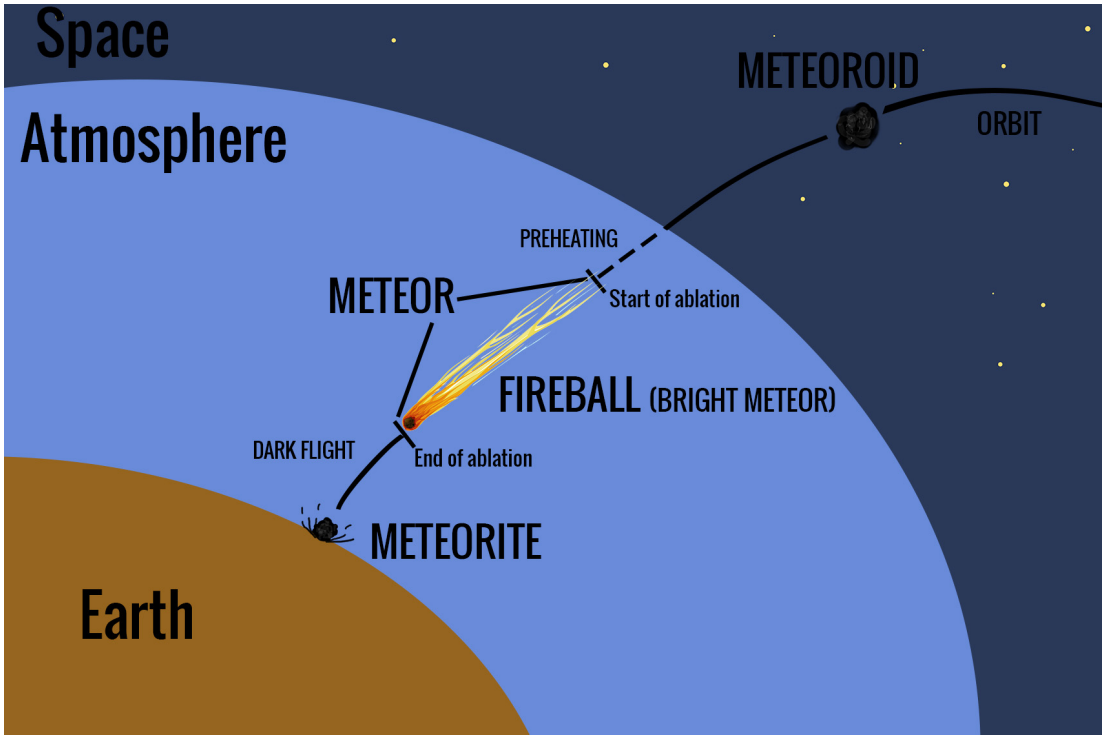

Figure 1.1: Graphical interpretation of the meteor terminology.

fuzzy. But it might change as we improve our observation achievements and our knowledge about small bodies in the interplanetary system. The urge of humans to sort and label natural objects is in contradiction in this case. We are sure there are all kinds of sizes of small bodies. The difference is only in the observation methods. Small meteoroids are observed during their flight in Earth atmosphere. Larger bodies are (fortunately) observed by telescopes on their interplanetary orbits. As the observation techniques develop, we will discover more objects in this fuzzy transition between asteroids and meteoroids.

1.2 How to study meteors and meteoroids

1.2.1 Spacecraft

We can study extraterrestrial material in the interplanetary environment using spacecraft.

First ever close observations of a comet were performed by Soviet Vega spacecrafts and European Giotto mission. Giotto passed the famous Halley comet in March 1986 and it took well known pictures of this comet before its camera was damaged by comet debris. The Giotto probe then visited the 26P/Grigg–Skjellerup comet with close 200 km approach in 1992, but the previously damaged instruments could not take pictures. Both Vega spacrafts, after successfully deployed descent modules onto the Venus surface, headed to the Halley comet. They passed it in March 1986. The PIA instruments on the Giotto probe and PUMA instruments on the Vega probes collected impacted material. The impact velocities were high (70 – 80 km/s for the μm sized particles) and caused complete vaporization of the collected dust and to a substantial degree of single ionization

[Hornung et al., 2016].

Sample return missions were used to collect material several times. These missions were able to return back to Earth with the collected material. This material was then studied in laboratories. Aerogel on Mir space station was collecting interplanetary dust for 18 months in the years 1997 – 1998. The orbital debris collector (ODC) was designed and built at the Johnson Space Center to capture and return analysable residues of the man–made and natural particulate environment in low-Earth orbit [Hoerz et al., 1999].

NASA STARDUST spacecraft passed by comet Wild 2 and returned with samples of material from cometary coma in 2006. These experiments studied the dust material of μm sizes and among other results they gave us a new look on the formation of comets [Brownlee et al., 2012]. As a target. they used an aerogel of thickness of several centimeters. Due the deceleration from $v \approx 6$ km/s to $v = 0$ within this target, the substantial shape change of the material often occurred during the STARDUST mission. Moreover, the vaporization and partial ionization of the material that collided with a compact silver target at the STARDUST/CIDA instrument occurred [Brownlee, 2014, Kissel et al., 2003].

The flight of ROSETTA mission near the nucleus of comet 67P/Churyumov-Gerasimenko in the years 2014 – 2016 made it possible, for the first time, to collect cometary dust at very low speeds [Hornung et al., 2016]. The COSIMA instrument onboard ROSETTA allowed to study cometary material that was fragmented upon the impact or remained unfragmented. First results from this instrument suggest that the fragments observed were not formed by the impact, but rather pre–existed in the parent dust agglomerate, and were simply broken apart during the impact [Hornung et al., 2016].

We can complete this list with non-meteoroid sample return missions. The US Apollo 11 Lunar mission in 1969 brought back to Earth the first sample of material from another Solar system body. Altogether, all further successful Apollo missions returned with hundreds of kilograms of Lunar material altogether. Soviet Luna 16, Luna 20 and Luna 24 returned with Moon material with fully automatic robotic missions between 1970 – 1976. In 2010, Japanese spacecraft Hayabusa returned with μm sized asteroid material after landing on asteroid 25143 Itokawa.

The sample return missions allow us to study the original extraterrestrial material in laboratories. But except for the Lunar material, we were able to study only the material of μm sizes. Although they are very important, these missions are very expensive and many complicatons can occur during their flight.

1.2.2 Meteorites

Another option to study the extraterrestrial material is to focus on meteorites, as they are products of collisions of meteoroids with the Earth. Laboratory research can provide detailed information about physical parameters and chemical composition. The instrumentally recorded falls of meteorites are the most valuable. In these cases we do not only have the meteorite itself, but we have also the information about its orbital trajectory and thus we can try to estimate its origin. On the other hand, this way we can study only somewhat limited population of meteoroids. Only meteoroids massive enough (or parts of them) with sufficient strength and with small entry velocities can survive the collision with Earth

and can be later found as meteorites. As of 2017, there are 30 instrumentally documented meteorite falls [Borovička et al., 2015].

On the other side of the size spectrum are the Interplanetry Dust Particles (IDPs). They are small enough to prevent significant heating during the entry into the Earth atmosphere. We can use high altitude flights to collect this material for futher study in laboratories.

1.2.3 Observations of meteors

Last option to study meteoroids is observation of meteors. The flux of extra-terrestrial material of sizes 10×10^{-21} – 10×10^{12} kg is about 50 tons per day [Drolshagen et al., 2015]. And about 7×10^6 meteoroids with masses between 10×10^{-6} and 10×10^{-4} kg hit the Earth atmosphere every day [Brown et al., 2002]. Compared to spacecraft missions, this is cheap alternative way to study meteoroids.

These observations still play the key role in the study of smallest bodies in our Solar system. In the long history of meteor observations, several different method of the observation were developed.

Even small grains can produce sufficiently bright events. We can observe meteors visually, with photographic or video technique or we can use radar technique. Our atmosphere is our laboratory. We can study individual meteoroids of millimetre to centimetre sizes. The trajectory, velocity and orbit can be determined using multi–station observations. The height of the ablation in the atmosphere correspond to the strength of the body. The composition of the body can be studied from the spectrum of the light produced by the vaporised material.

Visual observations

The easiest and oldest way to observe meteors is to just look at the night sky. For hundreds of years, naked–eye observations were the only way to study meteors and meteor showers. Ancient meteor observations had more folklore and mythological applications in Mesopotamia, in old Greece and in old Rome. But we have records of systematic observations in east Asia. Chinese, Japanese and Korean archives revealed ancient observations of meteors and meteor showers [Murad and Williams, 2002]. The historical observations are important and useful tool for search of long–term activities of meteor showers. Records of activities of Perseid showers and records of Leonid shower meteor storms are well known.

Data from amateur visual observers are still valuable today and statistical information about activities of meteor showers collected by IMO (International Meteor Organization) are often used by professional astronomers.

Photographic observations

The optical observations cover a wide range of meteoroid masses (from fireballs with observed masses of the order of 10×10^3 kg to faint video meteors with masses of the order down to 10×10^{-7} kg). Photography has always been more suited for brighter meteors. The limiting magnitude is typically ≈ 0 mag. Multistation observations allow precise orbital and trajectory computations. We can use photography to observe high resolution meteor spectra. To measure meteor motion,

photographic cameras have to be equipped with device that periodically disects the exposure. Rotating sectors, mechanical shutter etc. are used.

First known photograph of meteor was done in 1885 in Prague by Austro–Hungarian astronomer, director of the observatory of Prague, Ladislaus Weinek. He was observing Andromedids and managed to catch one meteor on the photographic plate. Since then, photography played the key role for the meteor science.

First systematic scientific photographic observations were performed since 1930s. The Harvard College Observatory used rotating shutters on patrol cameras and with double–stations observations this experiment run until 1951 [Whipple, 1939, 1954]. Between 1920s and 1960s, the important contribution to the knowledge about meteor complex was provided by Super-Shmidt cameras [McKinley, 1961]. Moreover, first fireball networks, like the Czechoslovak (and later European) fireball network, the Prairie Meteorite Network in United States and the Canadian Camera Network (MORP), were based on the photographic cameras. Their continuous observations allowed the very first scientifically documented meteorite falls [Ceplecha et al., 1998].

Video observations

Video cameras, sometimes equipped with image intensifiers, are used to study meteors too faint for photography. Without any additional equipment we can easily obtain meteor lightcurves with good time resolution. For their relatively low price, video cameras are now widely used by professional and amateur astronomers. Due to higher sensitivity, video cameras are able to capture more meteors than the photographic equipment.

The video technique was used for meteor observations since 1960s. Low light level television systems without image intensification were used at first. Since 1970s the advantage of image intensifiers allowed to record fainter meteors and fill the gap between photographic and radio technique. Early years of video–observations are described in detail by Hawkes and Jones [1986].

With widespread usage of all kinds of video cameras (security, car cameras, amateur videographers etc.) the accidental records of meteorite falls played the main role in the research of events like Peekskill, Morávka, Chelyabinsk and more [Brown et al., 1994, Borovicka et al., 2003, Borovička et al., 2016].

Video cameras can be equipped with spectral gratings. This way, the low resolution meteor spectra can be observed. Usually only a few spectral lines are visible in the video spectrum. This technique is not as precise as the photography technique. We often obtain lightcurves with low signal to noise ratio. Even with the digital image processing, the analysis procedures are still complex and time consuming.

Radar observations

The advances in radar technology in World War II in 1940s allowed scientists to study meteors using the radar technique. Thanks to existence of an ionized trail, the radar can be used for meteor observation in any weather conditions. The sensitivity of radar depends on the transmitted pulse power and parameters of the antenna. We can observe meteors fainter than it is possible with any optical

technique [Ceplecha et al., 1998]. Observations can be done during daylight and daytime meteor showers were discovered with radar. The discovery of head echo allowed to determine the meteoroid velocity [Hey et al., 1947]. Meteor head echoes are coming from irregularities of plasma around the meteoroids, which can backscatter the signal.

In general, two types of radars dedicated to meteor observation can be used. The VHF (Very High Frequency) radars are detecting meteor trails. The high-power and large aperture (HPLA) radars are used to detect meteor head echoes. We observe the ionized atmosphere instead of the actual meteor. We can observe large amount of very faint meteors, the radar observations suit the statistical analysis of large amount of meteors.

Another, still rather unorthodox, way to observe fireballs is the use of data from weather radars. The use of the imagery of the National Oceanic and Atmospheric Administration (NOAA) NEXRAD radar network. [Fries et al., 2016] summarised achievements and successful meteorite falls discovered thanks to weather radars.

Other methods (Acoustic, infrasonic, seismic, radiometers)

Not only traditional ways of meteor observations can be used. Some methods can complete the above-mentioned observation. This way we can obtain even more complex information about indivual meteors.

The Tunguska event in 1908 was detected by barometers in Great Britain and this was the impulse to study fireball events this way. The acoustic energy transferred to infrasonic sounds might be observed, though these observations are not very common. They are connected with very bright fireballs [Revelle, 1976]. The infrasound of fireballs can be used to study, detect and estimate a kinetic energy of bolides [Ceplecha et al., 1998].

Infrasound and seismic ways to study meteors has been used more and more in recent years. We can quote just a few examples as an illustration. Edwards et al. [2005] studied the Leonid and Perseid meteor showers using multiple camera systems (including the European Fireball Camera Network). They combined optical observations of a meteor with microbarometer detectors of infrasound array in Freyung, Germany. This is one station (I26DE) of the 60 stations of Comprehensive Nuclear-Test-Ban Treaty-International Monitoring System (CTBT–IMS). They delimited the altitudes at which these infrasound signals are generated and they found that meteor shower infrasound is much more common than previously thought. Revelle et al. [2004] analysed several types of data associated with the fall of the Neuschwanstein meteorites in 2002, including photographic and radiometer data along with the infrasound and seismic data. Pilger et al. [2015] used the 2013 Chelyabinsk event, the most energetic event recorded by the infrasound component of the CTBT–IMS, as the global reference to the IMS detection capability to explain infrasound detections. The US Air Force is monitoring infrasounds in the Earth atmosphere for the last few decades [Ceplecha et al., 1998].

In recent years, data from the US Government (USG) sensors are continuously published on the NASA JPL fireball and bolide reporting website [2]. They are

[2] http://neo.jpl.nasa.gov/fireballs/

able to estimate the place and the energy of the event. We have no detailed information about the USG sensors. Brown et al. [2016] used these data to compare them with scientifically observed meter-scale impactors. Borovička et al. [2017] also compared the USG sensors data with their observations of 2015 Romanian superbolide and found discrepancies. In other words, care must be taken when using these USG sensors data.

Spurný and Borovička [2002] equipped their autonomous cameras (the Czech part of the European fireball) with high time–resolution radiometers, that allowed to receive high time–resolution lightcurves of fireballs. They confirmed the existence of very short flares (spikes) in type I and II fireball lightcurves. The millisecond flares in meteor phenomena might be produced by triboelectricity[Spurný and Ceplecha, 2008], but it is still yet to be confirmed. Babadzhanov and Konovalova [2004] suggests autofluctuating mechanism for these flares.

1.3 History of meteor observations in Ondřejov

Meteor observations have a long tradition in the Czech region. As we mentioned before, the first known photograph of a meteor was taken in Prague in 1885 by Ladislaus Weinek.

Photographic observations of meteors were performed at Ondřejov observatory since 1947. Modern meteor astronomy was initiated by Zdeněk Ceplecha and his successful fireball observations. Double–station photographic observations started in 1951. Total number of 30 cameras with 180 mm focal length with panchromatic photographic plates and rotating shutters were used [Ceplecha et al., 1998]. Dr. Ceplecha managed to photograph the entry of the Příbram fireball and compute its orbital trajectory and to predict the location of meteorite finds. The Příbram meteorite fell on Earth on 7th April 1959. It was the first case of meteorite with orbital trajectory known in history [Ceplecha, 1960]. Ondřejov astronomers developed a number of reduction methods during that period. They used this procedures to compute geometric, dynamic, orbital and photometric data from their photographic records [Ceplecha, 1987]. The fireball network was founded in 1963 as the consequence of the Příbram meteorite fall and it continuously operates until today. After the addition of German stations and later station in other states, the network became the European Fireball Network with the center at the Ondřejov observatory. The Czech fireball network (as part of the European fireball network) now operates with fully automated analogue and digital cameras. Thanks to the scientific research at the Ondřejov observatory there are 5 cases of recorded and recovered meteorite falls in the area of Czech Republic. Moreover, of all of the 30 recorded known meteorite falls, more than a half of these cases (exactly 17) were analysed with the help of the scientific staff from the Ondřejov observatory ([Borovička et al., 2015] and [Spurný, 2016], situation in June 2017). With several thousands multi–station fireballs recorded during last 60 years, this network is the most successful fireball network.

Video observations of faint meteors and spectral video observations started in Ondřejov in 1990 ([Borovička and Boček, 1995] and [Štork et al., 1999]). Since then, the observations were conducted during the periods of activity of major meteor showers. Moreover, the equipment for continuous observations of meteors was recently developed [Koten et al., 2011a]. Observations in white light are

usually complemented by spectral observations. The analogue video technique is used since 1990s and new methods of digital video observations were developed and introduced [Koten et al., 2016]. One of the many results of long term video observations are databases and catalogues of meteor orbits, lightcurves and spectra (e. g. Koten et al. [2003a], Koten et al. [2004], Borovička et al. [2005], Vojáček et al. [2015]).

2. Fragmentation of small meteoroids

2.1 The ablation

The meteor phenomenon is consequence of meteoroid high speed (relative to Earth from 11 km/s to 72 km/s). At highest atmosphere altitudes, in the free molecule flow regime, direct collisions with molecules of air produce preheating of meteoritic material. With a higher surface temperature, the ablation process can start. Any process during the flight through the atmosphere that results in mass loss of meteoroid is called the ablation (see Figure 1.1). The ablation can be in the solid form as a fragmentation. It can also be in the fluid form as droplets or in the gas form as hot gas. Despite low density of the atmosphere in heights about 100 km, the heating and the evaporation of the material takes place here. Ionisation of meteoroid's and atmospheric atoms and molecules generates radiating region. Meteor light consists mostly of radiation of discrete emission lines of metals ([Ceplecha et al., 1998]).

During this phase some phenomena caused by ionisation and ablation can occur. A persistent train is created behind the meteoroid. It can last for a few seconds up to even a few hours. The train is caused by luminous matter and is less intense than the light around the ablating meteoroid. The radiation visible just behind the meteor is called the wake. Its formation and composition is still not well understood. We can observe meteor flares, as sudden increase of meteor brightness. They can be caused by sudden gross disruption or discrete fragmentation.

At lower altitudes, in the denser atmosphere, the diffuse shock wave forms in front of the body. This protective layer is formed and shields the meteoroid from direct impacts. The mass of small meteoroids is usually completely destroyed by ablation at heights around 80 km. Only larger meteoroids, that are slow enough, with enough mass and that are made of strong material have chance to survive the flight through atmosphere. As the meteoroid is more and more decelerated by the atmosphere, the ablation and radiation process stops and the so called dark flight begins. The dark flight is free fall and ends with the fall of the meteorite on the Earth's surface. In this thesis we will work only with small meteoroids, whose mass ablates completely.

Classical models of meteoroid ablation are dealing with single body meteoroids. They do not include any kind of fragmentation. The traditional theory assumes the ablation as evaporation with intense heating. This ablation is the primary process that converts the kinetic energy into light. The classical theory works only with macroscopic parameters such as the momentum conservation law and the kinetic energy conservation law. The compact homogeneous structure for spherical meteoroid is assumed. This theory is described in numerous works (among others: Opik [1958]; McKinley [1961]; Bronshten [1983]).

Some alternative processes are suggested to participate in ablation. The sputtering might explain high altitude meteors ([Brosch et al., 2001], [Rogers et al., 2005]). Spurný and Ceplecha [2008] suggested triboelectricity – catastrophic char-

ging as the main process that explains meteor phenomenon.

2.2 Fragmentation models of small meteoroids

The single body theory is in a good agreement only with a minority of meteors. But anomalies were found for faint meteors since early times of meteor observations. For example, trail lengths were observed to be shorter than the classical theory predicted [Hawkins and Southworth, 1958]. Lightcurves predicted by single body theory are increasing slowly up to maximum brightness with steep drop after that. In reality, faint meteors have wide variety of lightcurve shapes [Koten and Borovička, 2001, Koten et al., 2004]. In average, they tend to be symmetrical [Faloon et al., 2004].

The progressive fragmentation of a meteoroid during the flight in the atmosphere was suggested by Jacchia [1955]. This process can also explain other observed effects such as abrupt beginnings of meteors, flares, meteor wakes and terminal blending [Hawkes and Jones, 1975]. Jacchia [1955] proposed a meteoroid as a porous dustball conglomerate according to the cometary model by Whipple [1950, 1951]. Hawkes and Jones [1975] developed a quantitative model for the ablation of dustball meteors based on Jacchia's idea. They assumed two main components: high melting point metal grains that are held together by low melting point "glue". The nature of the glue was not known. Several substances such as organics or volatile light metals (sodium) were considered [Campbell-Brown and Koschny, 2004].This glue is not emitting any light and after it completely ablates at the first stage of the ablation, meteoroid starts to fragment. After that, individual fragments, that were released from the meteoroid, ablate according to the single body theory. Small meteoroids fragment completely before we can observe them and the more massive meteoroids continue to fragment during the visible flight. This predicts same beginning heights for all meteors with the same initial velocity independent on the mass of meteoroids. Small meteors have same end heights up to some critical mass. Meteoroids that are more massive than this critical mass decrease their end height with the increasing mass.

Koten et al. [2004] observed beginning heights for showers of different velocities and origin (Leonids, Perseids, Orionids, Taurids, Geminids) and found discrepancy for beginning heights of individual showers. For Perseids, Leonids, Taurids and Orionids they observed increasing beginning heights with increasing mass. This result is in a disagreement with the dustball theory. On the other hand, the Geminid shower showed no dependency of beginning height H_b on the mass. It seems that limiting magnitude of the observation system has the key role in this. For some showers, the observed beginning heights are not real beginnings of meteors. The ablation process started before they were observable. Then we have the obvious increase of beginning heights with the increasing mass for Leonids, Perseids, Orionds and Taurids. For Geminids, they were able to observe real beginning heights. Geminids with asteroidal origin are made of stronger material and thus they start to ablate at lower heights and more abruptly.

As we can see, the strength of the material can also change the beginning height of meteor. In some works, we can see different beginning heights for different populations of meteors (Borovička et al. [2005],Vojáček et al. [2015]). For given speed, the stronger the material is, the lower beginning heights meteoroids

tended to have. Iron meteors and meteors without sodium in their spectra had generally lower beginning heights for given speeds, compared to meteors that were poor in the iron or rich in the sodium in their spectrum.

Various dustball models have different approaches to the process of the fragmentation. For example, Jacchia [1955] suggested progressive fragmentation. The average meteor was visualized as very porous and fragile body as expected for the Whipple's icy–comet model [Whipple, 1950, 1951]. Fragments can be detached from the surface of larger meteoroids without destroying their unity. On the other hand, separation of fragments of similar size from small bodies may cause their complete disruption into a cluster of fragments. Larger meteors will disintegrate toward the end of their trajectories. Breakup of faint meteors may occur at early stage. Even at the very beginning of the visible trail.

The disintegration of a meteoroid before a significant evaporation starts is used in the quantitative dustball model developed by Hawkes and Jones [1975].

Campbell-Brown and Koschny [2004] used thermal disruption in their dustball model. The model is based on single body ablation and adds separation of fragments from the surface when certain surface layer reaches particular temperature. Usually all the fragments are released at the beginning of the luminosity for small meteors. This model was used to fit lightcurves of Leonids and Kikwaya et al. [2011] used it to estimate meteoroid densities.

Another approach is the use of quasi–continuous fragmentation used in the model developed by Borovička et al. [2007]. Gradual erosion is releasing grains continuously from the surface of the meteoroid. This model was used for their observations of Draconids in 2005 and explained the typical prolongation of Draconids by differential deceleration of grains of different masses.

Models developed by Campbell-Brown and Koschny [2004] and Borovička et al. [2007] were compared in Campbell-Brown et al. [2013]. They used their models to fit data from the Canadian Automated Meteor Observatory (CAMO) observatory mirror system (detail information on the system in Weryk et al. [2013]). Both models provided good agreement with the wide field measurements of lightcurves and decelerations, but predicted much longer wakes compared to observations by narrow field cameras. Comparison of different fragmentation models is needed, as models are often developed to fit designated members of meteor showers with different physical parameters.

Stokan and Campbell-Brown [2014] studied nine fragmenting faint meteors using the narrow field CAMO cameras. Fragments of eight of the nine meteors exhibited significant motion perpendicular to the meteor velocity. The authors discussed various models of fragmentation, like rotation and electrostatic charge accumulation, because standard models of aerodynamic loading did not produce perpendicular speeds of the orders what were observed.

Also, Stokan and Campbell-Brown [2015] developed a model for the ablation of small, non-fragmenting meteoroids. The goal of their model is to explain the ablation at free molecular flow regime at heights above 100 km. They modelled the wake formation and dimensions of wakes. Observations were made by the CAMO. They suggested that the width of the observed meteor wakes is related to the collision processes of evaporated meteoric particles, rather than lateral dispersion of fragments or other processes. On the other hand, the simulated meteor wakes tend to be shorter compared to observations. So they concluded

that the fragmentation in fact occured in the selected meteors.

One of the important goals for models of fragmentation might be the attempt to estimate the size of fragmented grains. As mentioned in Campbell-Brown et al. [2013], the size and distribution of fundamental grains is of particular interest for meteoroids in the millimetre size range. For comets, there are questions about their origin. The results of the sample return STARDUST mission to comet Wild 2 showed that there is an abundance of solid and refractory grains in the ten to hundred microns size range [Brownlee et al., 2012]. Before this mission, it was believed that comets are composed of presolar grains formed in interstellar space. It was supposed that these grains were silicates coated with a layer of ogranics and ice [Greenberg and Li, 1999]. But it was found that the solid and refractory grains were formed in high temperatures and that they contained chondrules and calcium–aluminium–rich inclusions (CAIs), similar to those in primitive meteorites of asteroidal origin [Brownlee, 2014]. Since no millimetre size examples were found among STARDUST mission and most of the comet loss is in the millimetre sized grains, the question about grain composition and structure is still of great interest.

2.3 The erosion model

In this work, we used the fragmentation model developed by Borovička et al. [2007] and applied originally to six faint Draconid meteors and one photographically observed bright Draconid meteor. We applied the model to 94 meteors, which showed sufficient deceleration to be used for the model. Lightcurves and deceleration of meteors can be a good source of information about processes of the fragmentation. We were able to deduce some physical parameters of meteoroids from the deceleration curves and lightcurves of meteors. Among these parameters are: the ablation coefficient, the erosion coefficient, the bulk density of meteoroid, the energy necessary to start the erosion. We were also able to deduce the sizes of grains and thus we could try to estimate the physical parameters of potential parent bodies and their material.

We will describe the model as it was described in the work of Borovička et al. [2007].

The standard drag, ablation and radiation equations are used to describe the single-body meteoroids before the erosion starts (Bronshten [1983])

$$m\frac{\mathrm{d}v}{\mathrm{d}t} = -\Gamma S\rho v^2 \tag{2.1}$$

$$\frac{\mathrm{d}m}{\mathrm{d}t} = -\Lambda\frac{S\rho v^3}{2Q} \tag{2.2}$$

$$I = -\tau\frac{v^2}{2}\frac{\mathrm{d}m}{\mathrm{d}t} \tag{2.3}$$

where Γ is the drag coefficient, S is the meteoroid cross-section, ρ is the density of the atmosphere, m is the meteoroid mass, v is the velocity of the meteoroid,

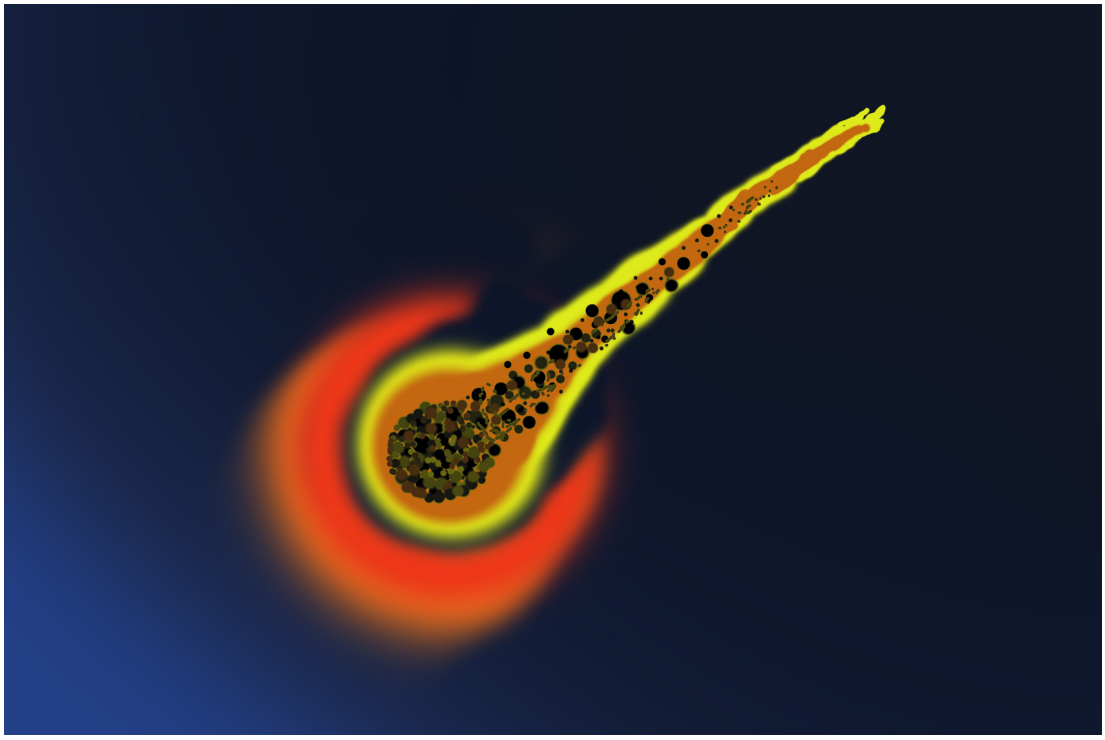

Figure 2.1: Illustration of the continuous fragmentation.

t is the time, Λ is the heat transfer coefficient, and Q is the energy necessary to ablate a unit of mass of the meteoroid. I is the meteor luminosity and τ is the luminous efficiency. The mass determined from the ablation is sometimes called *dynamical* mass to distinguish it from the *photometric* mass. The photometric mass is determined from the lightcurve.

We can define these quantities [Ceplecha et al. [1998]]:
the shape factor,

$$A = Sm^{-2/3}\delta^{2/3} \tag{2.4}$$

here δ is the meteoroid bulk density,
the shape density coefficient,

$$K = \Gamma A\delta^{-2/3} = \Gamma S m^{-2/3} \tag{2.5}$$

and the ablation coefficient,

$$\sigma = \frac{\Lambda}{2Q\Gamma} \tag{2.6}$$

The ablation coefficient describes the rate of the ablation of the whole meteoroid (and the ablation of grains in case of the fragmentation).

Equations (2.1) and (2.2) can be then rewritten:

$$\frac{\mathrm{d}v}{\mathrm{d}t} = -Km^{-1/3}\rho v^2 \tag{2.7}$$

$$\frac{\mathrm{d}m}{\mathrm{d}t} = -K\sigma m^{2/3}\rho v^3 \tag{2.8}$$

Analytical integrals of Equations (2.7) and (2.8) can be found in Ceplecha et al. [1998]. The solution assumes constant shape density coefficient K and constant ablation coefficient σ.

After the erosion starts, the model of Borovička et al. [2007] is using the concept of the dustball meteoroid. The grains are released gradually and then behave as individual meteoroids. We call this the quasi–continuous fragmentation. An illustration of this kind of fragmentation is given in the Figure 2.1.

The erosion starts at a given point along the trajectory after receiving the necessary energy. The mass loss is then

$$\frac{\mathrm{d}m}{\mathrm{d}t} = \left(\frac{\mathrm{d}m}{\mathrm{d}t}\right)_{ablation} + \left(\frac{\mathrm{d}m}{\mathrm{d}t}\right)_{erosion} \tag{2.9}$$

The mass loss due to the ablation is given by Equation (2.8).

Analogically, the erosion rate is

$$\left(\frac{\mathrm{d}m}{\mathrm{d}t}\right)_{erosion} = -K\eta m^{2/3}\rho v^3 \tag{2.10}$$

Where the erosion coefficient η describes the rate of erosion of the meteoroid, i. e. mass loss in the form of solid grains (ablation means evaporation here).

The eroded mass is distributed into individual grains of masses in the interval from m_l to m_u, where m_l is the lower mass limit and m_u is the upper mass limit for eroded grains. The masses of grains are assumed to have power–law distribution

$$n(m) = Cm^{-s}, m_l < m < m_u \tag{2.11}$$

Where $n(m)$ is the number of grains of given mass m, C is a constant, and s is the mass distribution index. After the release, the eroded grains ablate regularly and the erosion continues until all the mass of the meteoroid is exhausted.

The grains are released in different quantities at various heights. Because of their small mass, grains are significantly decelerated. Differential deceleration of grains of different masses, released at various heights, causes prolongation of the meteoroid. Thus the distribution of brightness in the meteor streak is more complicated than in case of single body. The model of meteoroid erosion provides the position of leading edge and the position of the brightest bin of grains along the meteor streak at each time.

Centimetre–sized meteoroids may contain some compact parts which are not subject to erosion. These parts ablate regularly and do not contribute much to luminosity of the meteor at greater heights. After exceeding their mechanical strength (5-20 kPa), the material breaks up into constituent grains. The ablation of these grains can be violent at smaller heights and can cause a short and bright meteor flare.

3. Observations and data reduction

Parts of this thesis are based on the work of Vojáček et al. [2015]. Some parts of chapters were already published in this work. Same source of data was used. This work uses extended database of observations and also uses data that were not selected for the Catalogue of representative meteor spectra, but were suficient for our analysis. As an addition, this work analysed, compared and connected the study of faint meteors spectra and the fragmentation process of meteoroids in the atmosphere.

If not specified, all velocities mentioned in this work are velocities at the top of the atmosphere (the entry velocity).

3.1 Observations and the equipment

The video-observations performed by the Department of Interplanetary matter of the Ondřejov observatory were the source of the data for this work. We used observations that took place between years 2004 and 2014, during the periods of activity of major meteor showers (Quadrantids, Lyrids, η-Aquarids, Perseids, Draconids, Orionids, Leonids, Geminids). These data were kindly provided for this work.

Stations used for observations and their coordinates are shown in Table 3.1. Most of the video observations were carried out in the Czech Republic on the base of Ondřejov - Kunžak observatories (see Figure 3.2). The distance between these stations is 92.5 km. The bases Ondřejov – Barrandov and Ondřejov – Třebíč with distances 32.2 km and 109.2 km, respectively, were used for observations only ocassionally (only until the year 2005). Data from the observation campaign of Leonids in Tajikistan in 2009 were also used. The distance between stations Kurgan Tube and Gissar was 126 km. Three Leonids, one Taurid and two sporadic meteors were used. Finally, data from the observation campaign of Draconids in Italy in 2011 were used. The distance between stations Barengo and Brenna was 56 km.

Some of the data in this work were already published by other authors. All seven Draconid meteors in this work observed from Italy were used for work of Borovička et al. [2014]. Data for three Leonids meteors from the Tajikistan expedition were published in the work of Koten et al. [2011b]. The meteor number 07406018, that was used for this work, was already published in the work of Borovička et al. [2008]. We would like to thank the authors for providing these data for us.

Each station was equipped with S–VHS camcorders with second generation image intensifiers (until 2005 it was Dedal–41, from 2005 Mullard XX1332). The size of the output window for the Dedal intensifier was 20 mm and for the Mullard intensifier the output window size was 40 mm. Lens Arsat 1.4/50 mm was used most of the time. With this lens and the Mullard intensifier the field of view was 54° [Borovička et al., 2008]. With the Dedal intensifier the field of view was 25° [Borovička and Jenniskens, 2000]. Lenses Jupiter 2/85 mm and Flektogon

Figure 3.1: Pictures of used equipment. Direct camera with Mullard image intensifier on the left, spectral camera setup on the right.

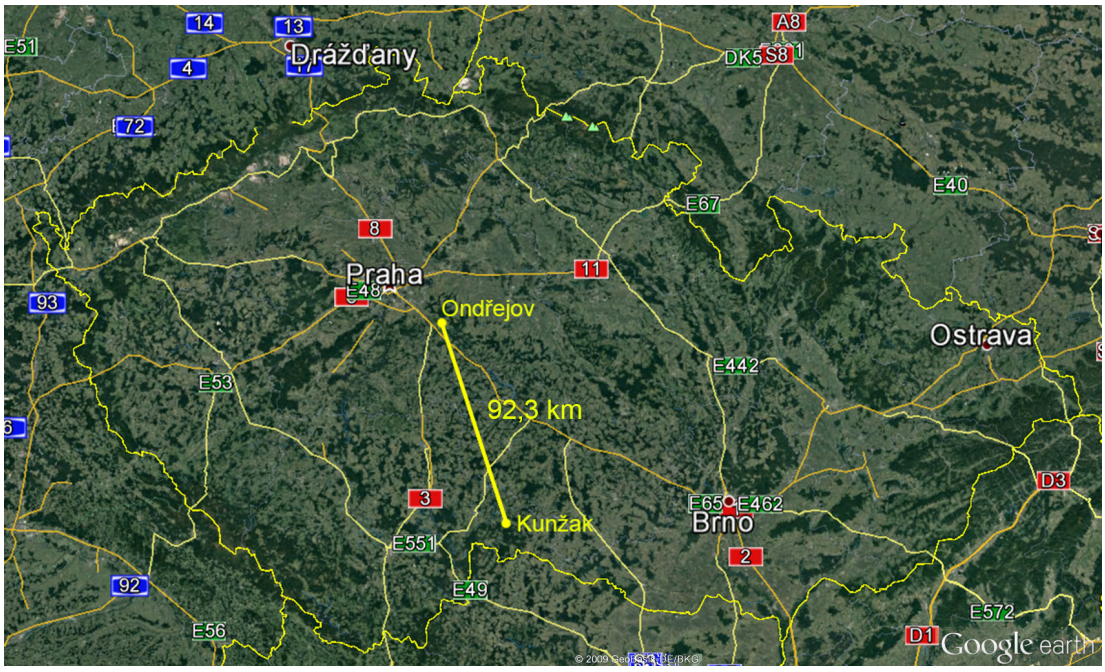

Figure 3.2: The most used observation base: Ondřejov - Kunžak on the map of the Czech Republic. Map printed from Google Earth ©.

Table 3.1: The coordinates of used stations.

Station	Latitude	Longitude	Altitude (m)
First, spectral Ondřejov	N49°54′36.8”	E14°46′48.8”	524
Second Kunžak	N49°06′27.2”	E15°12′2.8”	652
Second Třebíč	N49°13′6.0”	E15°51′13.0”	418
Second Barrandov	N50°01′55.0”	E14°22′18.0”	200
First, spectral Kurgan Tube	N37°21′12.5”	E68°46′18.3”	425
Second Gissar	N38°29′23.3”	E68°40′53.0”	722
First, spectral Brenna	N45°44′01.3”	E09°11′16.5”	333
Second Barengo	N45°33′57.8”	E08°30′18.2”	238

Table 3.2: The observation technique used for this work: lenses.

Lens		Focal length	f-stop	FOV	Dispersion
Arsat	*with Mullard*	50mm	1.4	54°	2.7nm/pix
	with Dedal			25°	1.15nm/pix
Jupiter	*with Mullard*	85mm	2	32°	1.5nm/pix
Flektogon	*with Dedal*	35mm	2.4	35°	*not used for spectra*

2.4/35 mm were used too. In Figure 3.1 we can see example pictures of used camera setup. One direct camera and one spectral camera was operated from the first station and one direct camera was operated from the second station. Details on lenses can be seen in the Table 3.2 and details on cameras are in the Table 3.3. Video recordings were stored on S–VHS video tapes until 2008. From 2009 direct recordings on hard drive were used. Direct recording to the DV cassette was used during expeditions. For meteor spectroscopy observations, spectral grating Milton Roy with 600 grooves/mm blazed to 470 nm was used. The spectral sensitivity extends from 380 nm to 900 nm. The sensitivity curve for the equipment (the camera, the image intensifier Mullard XX1332 and the lens) is given in Figure 3.3. The calibration curve was obtained by measuring stellar spectra. The sensitivity is affected by the image intensifier by far the most. The individual differences between different lenses and two similar cameras (NV–S88, NV–SX50) can be neglected. The resulting dispersion for the 1.4/50 mm lens and the Dedal intensifier was 1.15 nm/pix in the first order [Borovicka et al., 1999]. We measures the resulting dispersion for the 1.4/50 mm lens and the Mullard intensifier to be 2.7 nm/pix in the first order.

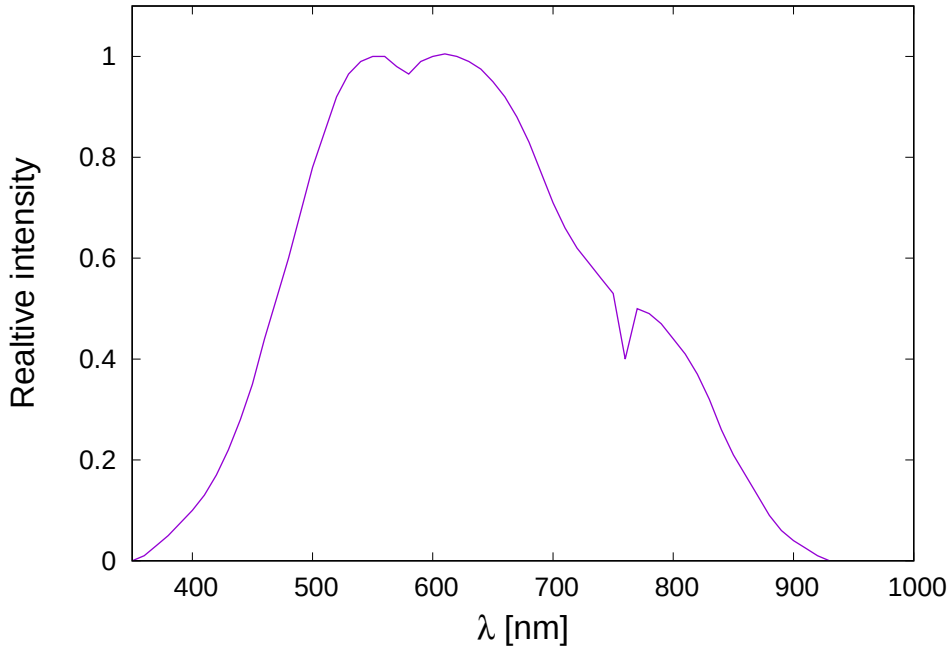

Figure 3.3: The spectral sensitivity of the equipment. The relative spectral intensity has been normalized to unity at 550 nm. The dip at 760 nm is due to O_2 atmospheric absorption.

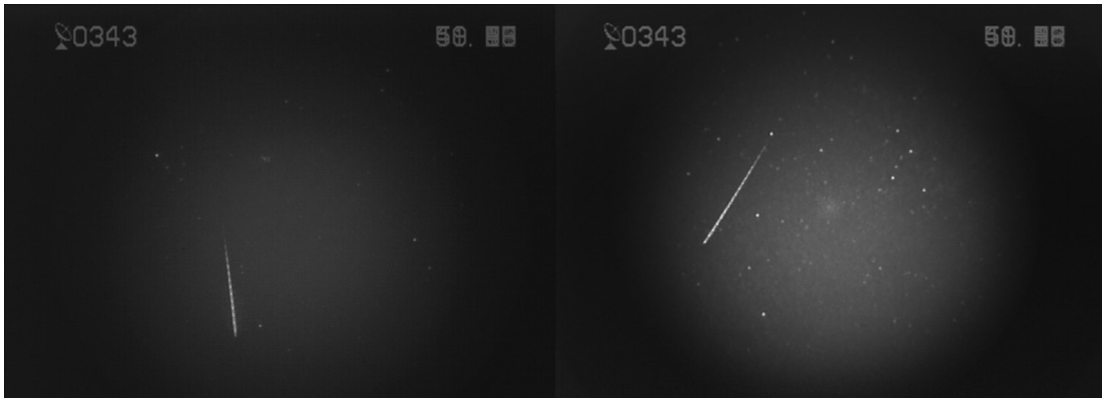

Figure 3.4: Example of direct camera video file. Meteor 08927195 from stations Ondřejov (left) and Kunžak (right). The final pictures are composition of all frames where the meteor was visible.

Table 3.3: The observation technique used for this work - cameras and image intensifiers.

Camera	Panasonic NV-S88 Panasonic NV-SX50
Image intensifier	Mullard XX 1332 Dedal 41
Resolution	768×576
Framerate	25 frames/s
Exposure	0.04 s

3.2 Data reduction

3.2.1 Meteor search

Meteors were searched on recordings that spanned more than 60 observing nights in the years 2004 – 2014.

Meteors were searched automatically on the recordings from the direct observations and from the spectral observations (the recordings were usually one video file per night per camera). Screen shot examples of the video files from direct and spectral cameras are in Figures 3.4 and 3.5.

To automatically search for the meteors the meteor detection software MetRec [Molau, 1999] was used. The meteor spectra were searched semi–automatically. In first step we performed the automatic search with MetRec software. The results from both meteor and spectral searches were assigned to each other according to the time. Because the automatic search by the MetRec was not able to find all spectra (especially the fainter ones) we tried to do it manually. The manual search for spectra of selected meteors was done. We used the time stamp of selected meteors received from the automatic MetRec search of direct video recordings. Then we search the corresponding time interval in the spectral recordings. The final meteor records (both direct and spectral) were then cut from these recordings as an uncompressed AVI files with resolution 768 x 576 pixels x 8 bit and 25 images per second. These AVI files were then used for all measurements and data analysis presented in this work.

3.2.2 Numbering of files

The number of each meteor is given in the form YYMDDXXX. The date of the observation of the meteor is encoded in this number. Where YY represent the last two digits of the year. M is the month of the year in this form: numbers 1 to 9 represent January to September and letters represent remaining months (A – October, B – November and C – December). The digits DD are the evening date when the observation started. It means that the actual day of the observation is equal to DD if time $T > 12$ UT and DD+1 if $T < 12$ UT. Last three digits XXX are the serial number of the meteor, the counting starts at the beginning of each observation. As an example, meteor 12B13179 was the 179th metor observed

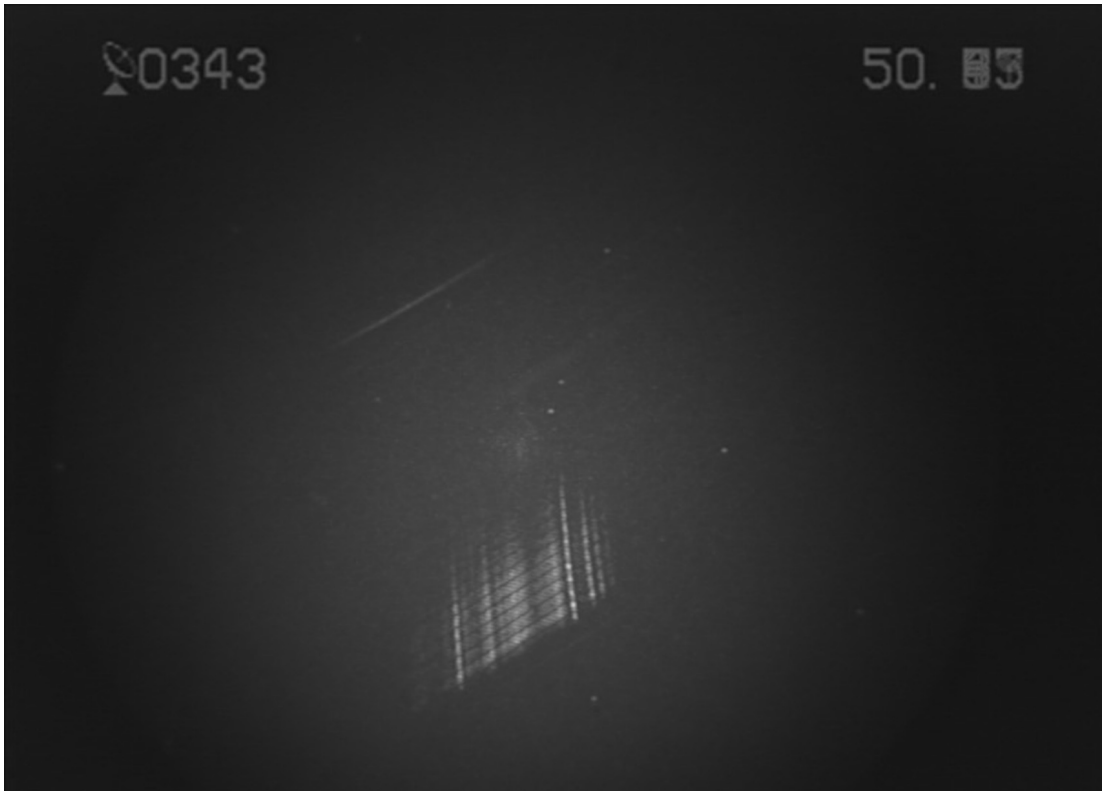

Figure 3.5: Example of spectral camera video file. Spectrum SX793 of meteor 08927195 from station Ondřejov. The final picture is composition of all frames where the spectrum was visible.

on the 13th November of 2012. The only exception in the numbering are the Draconid meteors. These meteor were observed during the Draconid observation campaign in Northern Italy on the 8th October of 2011 and they are numbered according to the work of Borovička et al. [2014].

The meteor spectra contains prefix SZ or SX followed by the number of the spectrum. The numbering is carried out continuously in chronological order. The prefix SZ is for spectra observed by camera equipped with Dedal 41 image intensifier. The prefix SX stands for spectra observed by camera equipped with Mullad XX1332 image intensifier.

3.2.3 Reduction of individual meteors

Meteors that were suitable for this work were selected from the digitalized records. We included only meteors observed from both stations with most of their path inside the field of view of the direct cameras. Only then we could compute meteor trajectories and orbits with good accuracy. Meteors with spectrum bright enough, so at least some spectral lines were visible, were selected. We excluded bright meteors if their spectrum was oversaturated. We included only meteors that had at least the most important part of the spectrum (500–800 nm) inside the filed of view of the spectral camera.

We focused on sporadic meteors and members of minor meteor showers. The association to minor showers is not always clear and hence we counted them as sporadic. In addition, selection of meteors from major showers meteors was

made. Not all sufficient spectra were included. Instead only a few representative ones were chosen for each major shower. The Southworth-Hawkins D-criterion [Hawkes and Jones, 1975] was used for the determination of the meteor shower membership. The D-criterion was chosen to be 0.2.

The total number of meteors used for further processing was 152, 121 of these were sporadic meteors and the rest, 31 meteors, were members of major showers.

Photometry and positions of each meteor were measured manually in each video frame with the Respec software [Borovička et al., 2005]. Dark–frame and flat–filed were applied to all frames. The zero–order images of catalogue stars in the field of view were used for photometric and positional calibration. Plotting the magnitudes of catalogue stars against their signal intensity logarithm provided calibration curve used to compute the meteor apparent magnitude. Aperture photometry was used, the aperture was automatically set by the software and adjusted by the operator when necessary. The signal was then computed as a sum of pixel intensities in the aperture.

Using the combined data from both stations, we were able to determine atmospheric trajectories and heliocentric orbits of meteoroids by the least–square method [Borovička, 1990]. By knowing these trajectories we could estimate their absolute magnitudes and photometric masses. The photometric mass is highly affected by the selected luminous efficiency. We used the luminous efficiency of Pecina and Ceplecha [1983]. The geocentric radiant, the zenith distance of the apparent radiant, the beginning height, the terminal height and the maximum brightness were also computed.

3.2.4 Spectral reduction

Every frame in the spectral video was scanned. The calibration of spectral wavelengths was done using the wavelengths of well known atomic lines of the meteor emission. The wavelength calibrated spectra were then manually fitted in the software FITSP developed at the Ondřejov observatory. We estimated intensities of spectral lines, but this procedure is not trivial. Several components such as continuous emission, nitrogen bands and other lines can contribute to the intensity of the peak at the line position. We had to set all of these components to fit each spectrum as well as possible. Parameters of the fit (e. g. intensities of spectral components, the temperature of the Planck emission and the vibrational and rotational temperature of nitrogen bands) were changed manually by the operator of the software. The fitting was done on each frame separately. One temperature was sufficient for all frames for the Planck continuum and for the nitrogen bands. All spectra were calibrated for spectral sensitivity of the system (Figure 3.3). Figure 3.6 is shown as an example of difference between uncalibrated and calibrated spectrum. Notice the increase of intensity of signal (in arbitrary units) in parts with low sensitivity of the system and related increase of the uncertainty in these peripheral parts of the spectrum. For this reason we have to be very cautious in examining line intensities and their identification within these parts.

Results from video technique allowed us to study spectra on each individual frame of the recording. On the other hand, we were able to sum every spectrum along the trajectory. This way we obtained not only the estimation of total

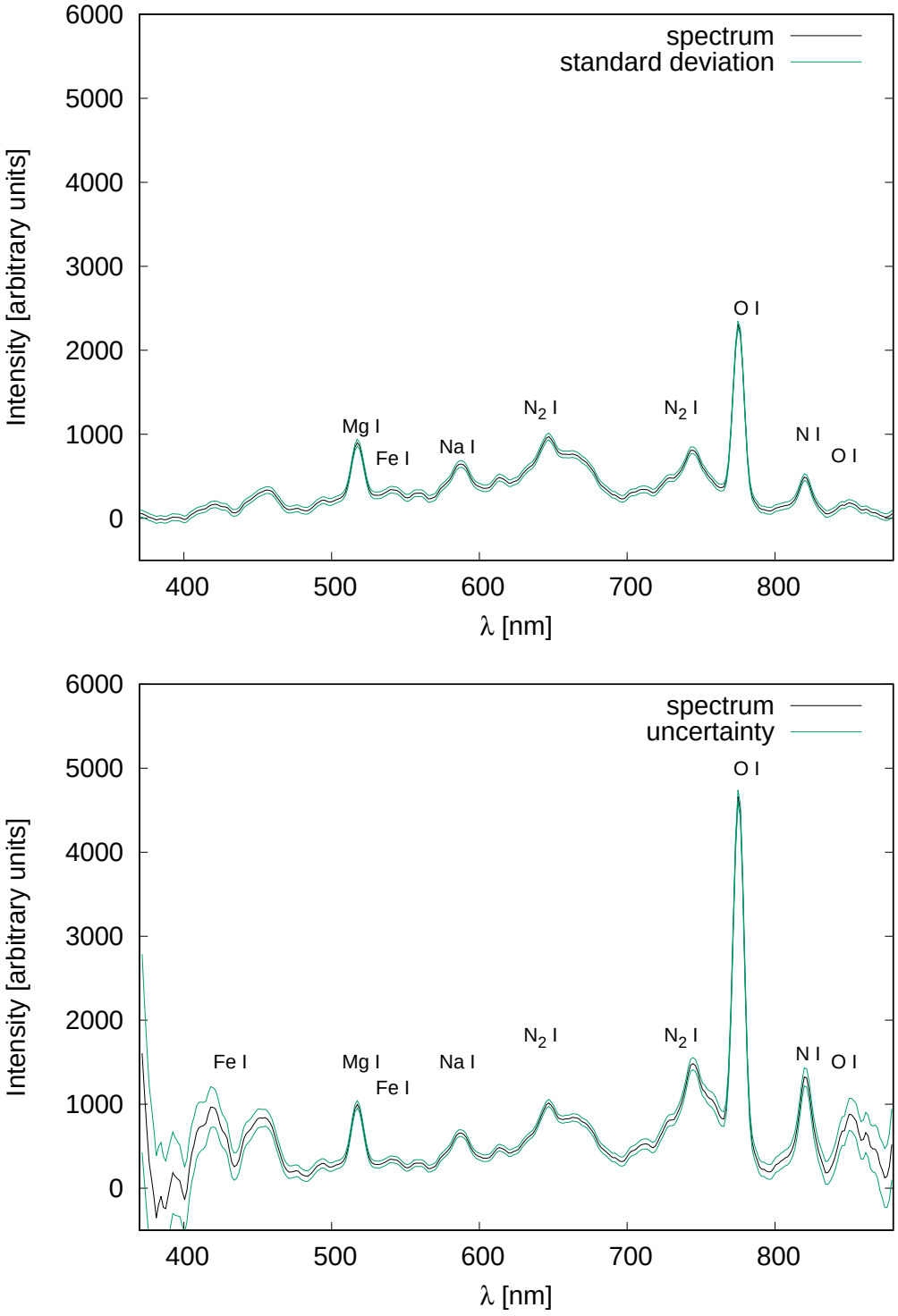

Figure 3.6: Example of uncalibrated spectrum (upper image) and calibrated spectrum (lower image). The spectrum SX784 of the meteor 08927015 was used. Some typical meteoric and atmospheric lines and molecule bands were marked.

intensities for corresponding mutliplets (from summed spectra), but we still had time resolved meteor spectra from the fitting of each video frame (we call these time resolved line intensities monochromatic lightcurves).

3.2.5 Noise analysis

Simple analysis of the image noise was done for selected recordings. Since the level of noise depends highly on the image intensifier, we made analysis for the Dedal and Mullard intensifiers separately. Parts of the image without signal (no spectrum, no stars) were scanned on selected video recordings. Brightness of each pixel in the scanned area was measured and the Gaussian fit of the pixel brightness histogram was done for each selected video. The average value of standard deviation of all Gaussian fits was obtained (separately for each image intensifier). For the Dedal intensifier the average standard deviation of the Gaussian noise was $\sigma = 33$ (in device arbitrary units). For the Mullard intensifier the average standard deviation of the Gaussian noise was $\sigma = 14$ (in device arbitrary units). Obtained average Gaussian fits and examples of pixel brightness for two spectral recordings are shown in the Figure 3.7.

These values were used to compute uncertainties for all spectra. Since spectra presented in this work are sums of spectra from individual frames, we determined spectral uncertainties as the multiplication of the standard deviation and the square root of number of frames used for the given spectrum. Relative uncertainties for calibrated spectra were obtained by dividing by the spectral sensitivity curve.

The fitting was individual for every spectrum. The parameters of spectral components were manually estimated. Because of that, we are not able to determine uncertainties for line strengths and for their ratios respectively.

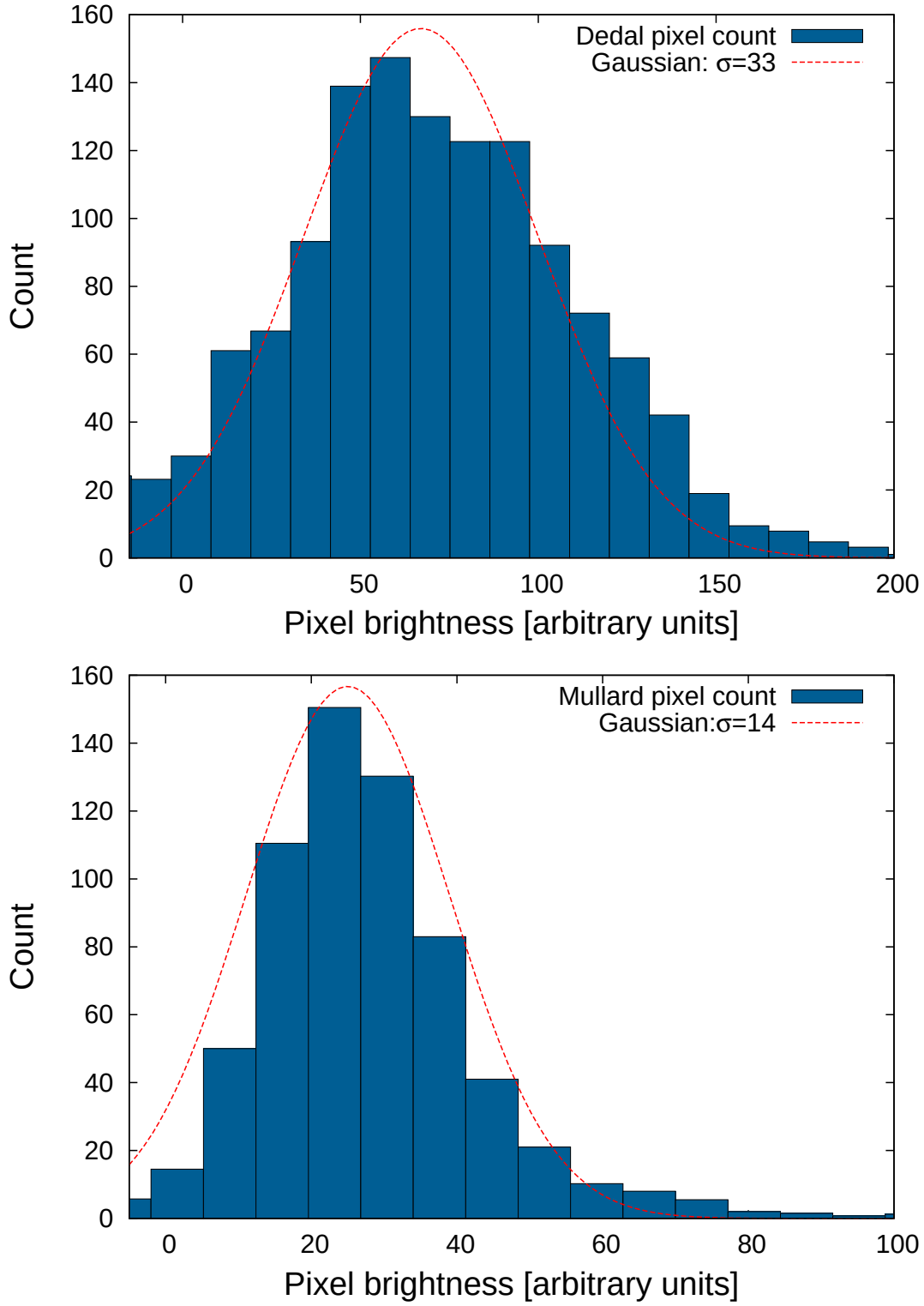

Figure 3.7: Example of noise analysis. Top figure shows the brightness of pixels for the videos acquired using the Dedal image intensifier. The Dedal image intensifier was used. The bottom figure shows the brightness of pixels for the videos acquired using the Mullard image intensifier. Gaussian distributions with computed average values of σ are shown.

4. Faint meteor spectra

4.1 Description of spectrum

Several components contribute to overall appearance of the faint meteors spectrum. We can divide these components into three main groups. Most of the visible light originates in the emission of evaporated meteoroid material. The emission from the heated atmosphere (mostly the oxygen and nitrogen lines and nitrogen molecular bands) prevails in infrared and ultraviolet emission for fast meteors. Last main component is the Planck continuum emission. These three components are shown in Figure 4.1.

List of lines that can significantly contribute to meteor spectra is shown in Table 4.1. The lines are sorted in several groups according to their origin. In the first group there are lines of low–temperature ($\approx$ 4500 K) spectral component. The second group consists of the high–temperature ($\approx$ 10 000 K) spectral component [Borovička, 1994]. The high–temperature component is of low importance for faint meteors (within the magnitude range presented in this work). Since these lines are usually visible in bright and fast meteors. The lines emitted just behind the meteor in the meteor wake are in the third group. They last only a fraction of a second. Their origin is of the low–energy excitation intercombination and they cannot be fitted by a thermal model [Borovička and Jenniskens, 2000]. Although typically present in the meteor wake, they can occur in the meteor heads, if the collisional deexcitation rate is low [Borovička et al., 2005]. Another group consists of lines and molecular bands of the atmospheric origin (mostly formed by the oxygen and the nitrogen at $\approx$ 10 000 K). These lines can be very bright for fast meteors. There is only one line in the last group. The forbidden oxygen line at 557.7 nm. This line is visible mostly in fast meteors as well. It can persist up to a few seconds after the meteor disappears and thus creates a short–duration trail.

In this work will focus on the meteor lines from the first, low-temperature, group. These lines are best observable meteoric lines in faint meteors. For video meteor spectra in the range of sensitivity of our equipment (the range of visible light and highest frequencies of near–infrared radiation), there are four meteoric lines that can be clearly recognized. These lines are: the magnesium line (Mg I), the sodium line (Na I), lines of iron (Fe I) and the calcium line (Ca I). Because our technique has already small sensitivity in the blue part of the spectrum, the calcium line Ca I is sufficiently visible only for bright meteors. The Cr I lines are blended with the Fe I lines and therefore cannot be resolved.

Although the meteoric spectral lines have their origin mostly in the evaporated ionised material around the meteoroid and not in the body itself, we can try to conclude the chemical composition of the meteoroid from the spectrum. On the other hand, the shape of the meteor spectrum is affected by other conditions such as the brightness, the speed and the temperature. For bright and fast meteors temperatures can be higher compared to faint (and slow) meteors. The lines of the high-temperature component (Ca II, Mg II, Si II) can be visible. The Figure 4.2 shows difference between faint and bright meteor spectrum. Two Perseid meteors ($v \approx 60$ km.s^{-1}) are compared. As a bright meteor, the Perseid

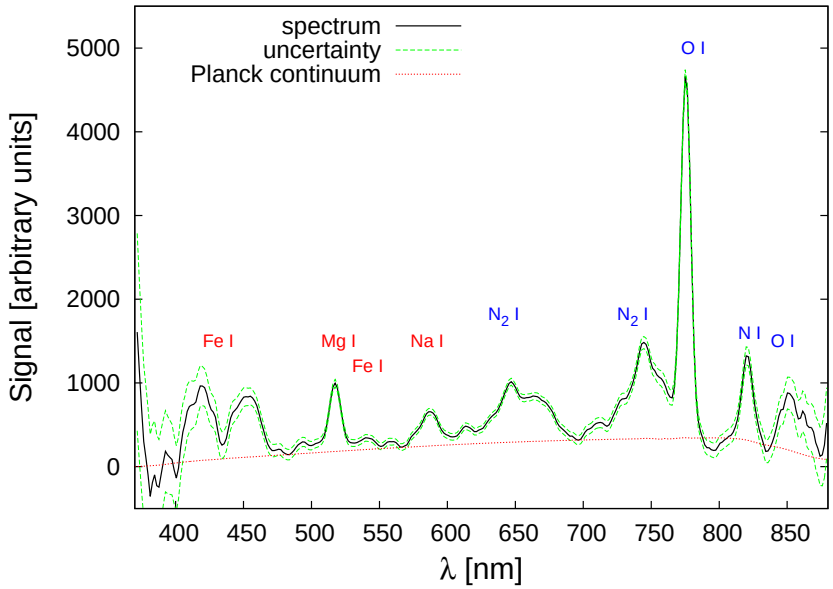

Figure 4.1: Example of video spectrum. Spectrum SX784. Three main components of faint meteor spectrum are shown: Planck continuum as red line, meteoric lines are marked with red labels and atmospheric lines and bands are marked with blue labels.

spectrum SX1837 was chosen. This meteor was too bright and overexposed on the video and for this reason it is not included in this work. Another reason why we did not work with bright meteors was the spectral classification. The spectrum classification, that we will use later, was developed for small meteors of 1 – 10 mm size range. The Perseid SX1837 was about 2 cm in diameter. Due the saturation we show only one frame from the video sequence. We selected frame where the spectrum was not yet saturated. The maximum brightness of this meteor was -9.2 mag. In the spectrum we can see low–temperature meteoric lines (Na I, Mg I), but there are also high–temperature lines in the spectrum (Mg II, Ca II). This meteor was captured and studied by multiple cameras, for more information about this meteor with exceptional beginning height see Spurný et al. [2014]. On the other hand, the faint Perseid spectrum SX1798 contains only low–temperature meteoric components Mg I, Na I and Fe I. The maximum brightness of this meteor was -2 mag. This was within the sensitivity range of our system.

We can observe differences between meteors with similar brightness but with different speeds. In general, the faster the meteor is, the brighter the atmospheric lines and bands are, compared to relative intensity of meteoric lines. As an example of a spectrum of a fast (50.7 km.s^{-1}) meteor, the spectrum SX457 is shown in Figure 4.3. The spectrum SX1206 of slow meteor (24.5 km.s^{-1}) is shown in the same Figure. For fast meteor, the red and near infrared parts of the spectrum are brighter compared to the spectrum of slow meteor. The atmospheric lines of O I, N I, the nitrogen bands N_2, and the forbidden green oxygen line [O I] are brighter for fast meteors. The only one atmospheric line that we can observe in the spectrum SX1206 is the brightest oxygen line O I at 777 nm.

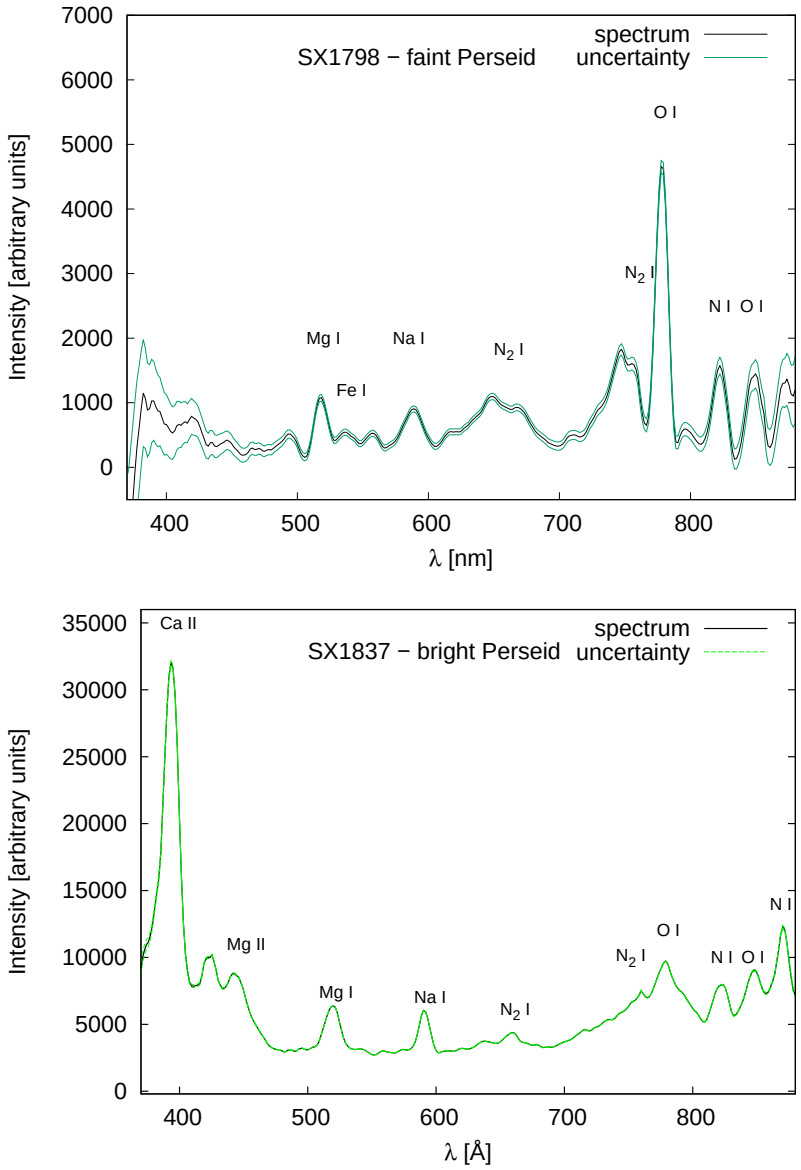

Figure 4.2: Example of difference between faint and bright meteor spectrum.

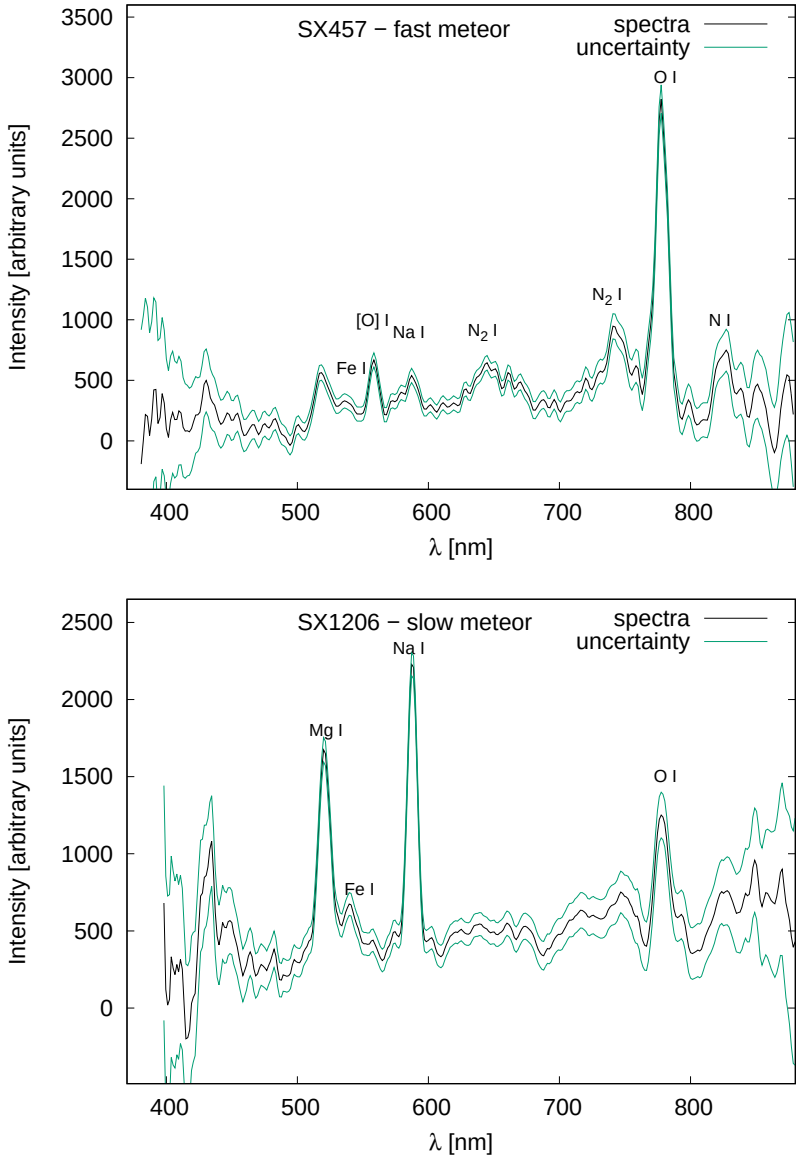

Figure 4.3: Example of difference between spectrum of fast and slow meteors with similar brightness.

Table 4.1: The list of lines contributing to the meteor spectrum in the range of 380 nm – 870 nm. Only if lines are separated enough to be resolved in the video spectra, they are given individually within the multiplet. The multiplet numbers are given according to Moore [1945]. Table taken from Vojáček et al. [2015].

λ (nm)	**Chemical species**	Multiplet
Low temperature lines		
383.1	Mg I	3
385.9, 388.5, 392.6	Fe I	4
404.5, 406.6, 414.3	Fe I	43
420.1, 427.3, 430.8, 432.6	Fe I	42
422.6	Ca I	2
425.5	Cr I	1
438.4, 440.5	Fe I	41
470.3	Mg I	11
487.2, 489.1, 492.0, 495.7, 500.8	Fe I	318
518.2	Mg I	2
526.9, 532.8, 537.1, 540.4, 543.1, 544.9	Fe I	15
589.2	Na I	1
High temperature lines		
393.4, 396.9	Ca II	1
448.1	Mg II	4
634.7, 637.1	Si II	2
Wake lines		
437.6, 442.7, 446.2, 448.2	Fe I	2
457.1	Mg I	1
516.9, 520.5	Fe I	1
Atmospheric lines and bands		
533.0	O I	12
570.0 – 600.0	N_2 1st. positive	$\Delta\nu = 4$
620.0 – 680.0	N_2 1st. positive	$\Delta\nu = 3$
700.0 – 750.0	N_2 1st. positive	$\Delta\nu = 2$
615.7	O I	10
645.5	O I	9
648.4	N I	21
742.4, 744.2, 746.8	N I	3
777.4	O I	1
818.6, 821.8, 814.3	N I	2
844.6	O I	4
868.2	N I	1
Train lines		
557.7	[O I]	3F

4.2 Spectral classification

As we mentioned above, only three meteoric lines are clearly visible in video spectra that are typical for our equipment – lines of Na I, Mg I and Fe I. In case of iron lines, we used the multiplet 15 at 527 – 545 nm to measure the Fe intensity and we summed contributions of all lines of the multiplet. Again, the reason was good sensitivity in this spectral region (compared to the Fe lines at 440 nm). For lines of Na and Mg the bright lines of multiplet 1 and multiplet 2, respectively, were used. The differences in the relative intensities of these lines can tell us about different composition of individual meteoroids.

To simplify the differences between each meteor spectra we can use spectral classification for faint meteors developed by Borovička et al. [2005]. As real examples of each spectral class, we show non–mainstream spectral classes observed by video technique in Figure 4.8. Examples of mainstream spectral classes can be seen in Figure 4.9. Meteoroids were divided as follows:

- *Iron meteoroids*

  No sharp lines are present. Two bands are formed by unresolved Fe multiplets (at 420 – 450 nm and 510 – 550 nm). The Mg line at 518 nm can contribute to the intensity of the second band, but is much fainter than in normal spectra. The Na line is missing.

- *Na–free meteoroids*

  No Na line, but not classified as iron meteoroids. The Fe/Mg ratio varies widely.

- *Na–rich meteoroids*

  The spectrum is dominated by the Na line. The lines of Mg and Fe are present, but they are faint.

- *Mainstream meteoroids*

  Mainstream meteoroids form the majority of meteoroids. Their spectra are closer to the expected chondritic spectra. There are strong variations in the Na line intensity. Almost the whole range between the Na–free and the Na–rich meteoroids is covered. The mainstream meteoroids are divided into four subclasses:

  - *Normal meteoroids*

    Normal meteoroids are defined as those lying near the expected position for chondritic bodies in the ternary diagram. Sometimes they can have lower Fe intensity.

  - *Na–poor meteoroids*

    The Na line is weaker than expected for given speed, but still reliably visible in contrast to Na–free meteoroids.

  - *Na–enhanced meteoroids*

    The Na lines are significantly brighter than expected for the given speed, but not as dominant as for Na–rich meteoroids.

– *Fe–poor meteoroids*

Meteoroids with the expected Na/Mg ratio, but with the Fe lines too faint to be classified as normal.

In our work we found two meteors, for which we could not resolve meteoric lines. Only atmospheric lines and molecular bands were visible for spectra SX1101 and SX2175. We excluded them from the spectral classification and marked these cases as *spectra with atmospheric lines*.

The contributions of individual multiplets were summed along the visible path. For the classification, we did not take the differential ablation into account and we worked only with total intensities.

To better visualize the spectral classification we can use the Mg–Na–Fe ternary graph (Figures 4.4 and 4.5). The ternary graphs are often used in physical chemistry, petrology, mineralogy and other physical sciences to show the composition of three species systems. The meteor position in the ternary graph represents the computed relative intensities of three spectra lines (Mg I – 2, Na I – 1, Fe I – 15). In Figure 4.4 we can see the black curve that represents the expected theoretical positions for meteoroids of chondritic composition. Meteors with chondritic composition are expected near this curve. The curve was taken from the work of Borovička et al. [2005]. The relative Mg–Na–Fe intensities depend not only on the elemental abundances but also on the physical properties in the ionized environment. The temperatures in the ionized gas can be in the range from 3500 K to 5000 K and they correspond to the speed of the meteoroid. According to Borovička et al. [2005] the Na/Mg ratio for high speeds (above $\approx$ 40 km.s^{-1}) corresponds to temperatures of $\approx$ 5000 K. For velocities around 15 km.s^{-1} the temperature is $\approx$ 4000 K. The Na line is of low excitation (2.1 eV) compared to the Mg line (5.1 eV). Thus the dependence of the Na/Mg ratio on the temperature. For lower temperatures, the intensity of Na line should be highest, on the other hand the intensity of Mg line should be highest for higher temperatures. Since the temperature changes along the chondritic curve can be viewed as velocity dependent we show the curve as a function of the velocity of the meteoroid (velocities in km.s^{-1} are marked above the curve).

Spectra with only atmospheric lines and molecular bands (SX1101, SX2175) were not included in the ternary graph. They did not showed any meteoritic lines and thus could not be placed in the Na–Mg–Fe figure.

The decision to classify between Na-poor and Na-free meteoroids from the ternary graph was not always obvious. The velocity dependence of the brightness for the Mg and Na lines can help us to better distinguish between different spectral classes. For this purpose, the dependence of the Na/Mg ratio on the velocity of the meteoroid can be used. We show this in Figure 4.6. Iron and Na–free meteors were excluded due to very inaccurate or even impossible determination of the Na and Mg line intensities for their spectral classes. According to Figure 4.6, the Na/Mg ratio increases for velocities below 35 km.s^{-1}. For speeds higher than 35 km.s^{-1}, the ratio is speed independent. Keeping in mind the dependence of the Na and Mg line intensities on the velocity, we can decide in which spectral class we should include the given meteor. This way, spectral classes represent the elemental abundances and the dependence of the Na/Mg ratio on the physical conditions (the temperature i. e. the velocity) can be omitted. We made the fit

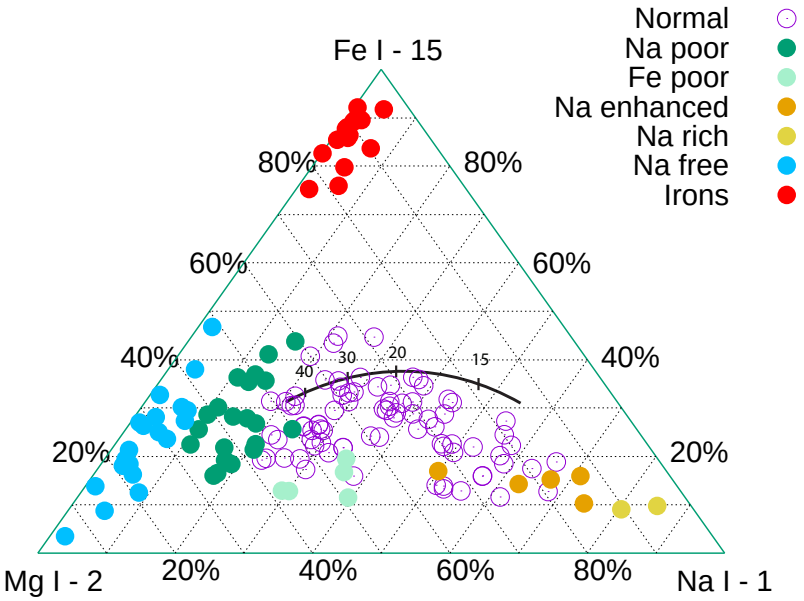

Figure 4.4: Classification of meteor spectra in ternary graph. Every spectral group is represented with different symbol. The black line shows theoretical position of meteors with normal chondritic composition and was taken from the work of Borovička et al. [2005]. The position depends on the speed of the meteor. The speed in km.s^{-1} is marked with numbers above the line.

of meteors classified as Normal. The fit was divided in three segments according the low/high velocity dependence/independence. For given speed, if the meteor is below the Normal class, we can classify it as Na–poor and when the meteor is above this dependence it could be, accordingly, Na–enhanced or even Na–rich.

In Figure 4.7 we show the ratio of O/Mg line intensities as a function of velocity. The O/Mg ratio increases with the velocity. Bright atmospheric lines are typical for fast meteors. For speeds below 30 km.s^{-1} the scatter is large, mainly due to the faintness of the O line. Meteors classified as Iron meteoroids were excluded.

As we can see in Figure 4.4, the majority of normal meteors are below the chondritic curve, because they have lower intensity of Fe lines than expected for chondritic compositions. There are also $\approx 24\%$ of all meteors that are members of non–mainstream classes: Irons, Na–free and Na–rich meteors. These classes were observed among brighter meteors as well, but the amount of non–chondritic meteoroids was only about 1% [Harvey, 1973]. Recent works of Kikwaya et al. [2009], Campbell-Brown [2015] predict variations in the characteristics of the meteor population with limiting magnitude. The smaller the sizes of meteoroids are, the more iron meteors are present. As suggested by Borovička et al. [2005], the diversity of millimetre size material might be partly due to the environmental factors (solar wind, solar radiation and cosmic rays can change the bulk compositions) and partly due to the real inhomogeneity inside the parental bodies.

The scatter of shower meteors in the Mg–Na–Fe ternary graph is shown in

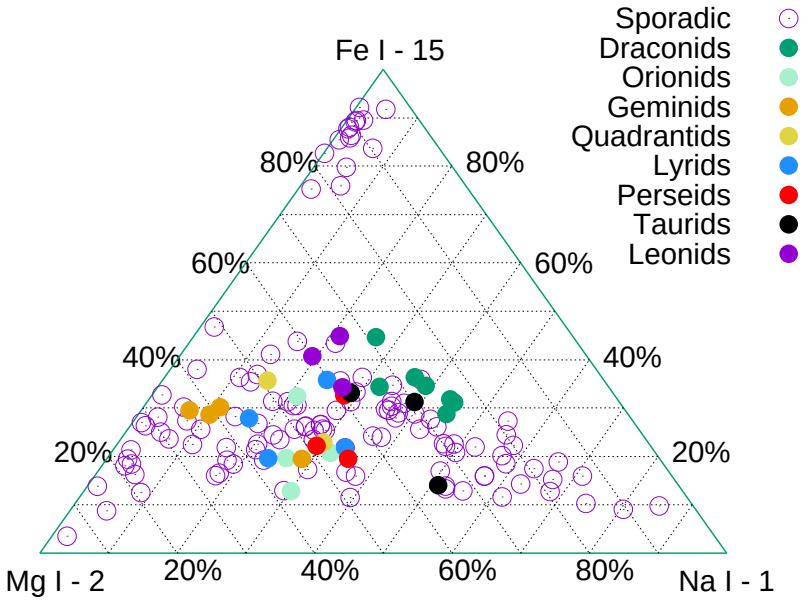

Figure 4.5: Meteor spectra in ternary graph. Every color represents different meteor shower.

Figure 4.5. Except for one Na–free Geminid meteor, all of the shower meteors were classified as mainstream meteors. Inside the mainstream group, most of the shower meteors were classified as Normal. Two Geminids were Na–poor and one Geminid meteor was classified as normal. The reason for the wide variety of amount of the sodium in Geminids might be in different sizes, structure and porosity of individual meteoroids [Borovička, 2010]. Of the two Quadrantids meteors, one was classified as Normal the other one as Na–poor. Of the four Lyrids meteors, one was also Na–poor, the other three were Normal. One Perseid and one Orionid meteor were classified as Fe–poor. Other members of orionids and Perseids were Normal. Rest of showers (Taurids, Leonids, Draconids) have only members classified as Normal.

This work confirmed previous results: minority of millimetre sized meteoroids show chondritic composition. The millimetre sized meteoroids show wide variety of Na depletion, Fe depletion or Na enrichment. The mainstream spectral class (particularly the Normal class) is typical for shower meteors.

The classification of faint meteor spectra can be useful. On the other hand, the differences between individual meteor spectra might be very minor and the classification can be somewhat arbitrary. The ratio of Na/Mg lines fills almost the entire possible range and there are no sharp boundaries for faint meteors in Figure 4.4. We can see only one exception. The only isolated group are members of the Iron class. Their spectra are very different, compared to the rest of the population of meteors. Other classes form a complex group in the ternary graph. The classification tries to reflect the inner structure of individual meteoroids. But the more meteors we observe, the more ambiguous and transition cases we will find. We can see that the population of faint meteor is very heterogeneous,

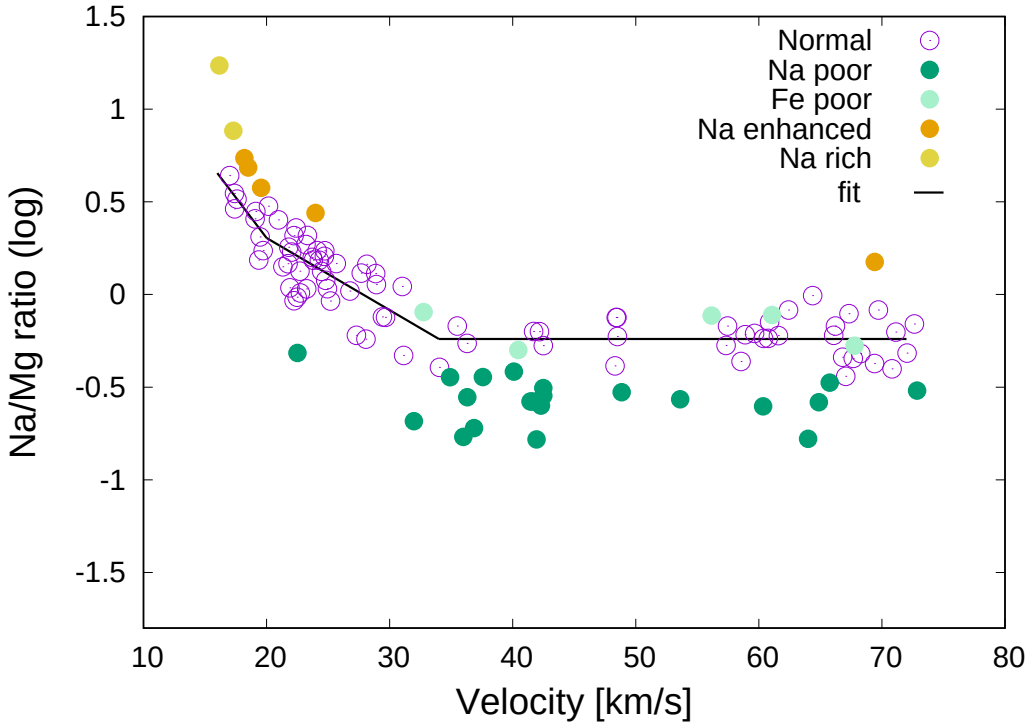

Figure 4.6: Na/Mg lines intensity ratio as a function of the meteor speed. Iron and Na–free meteors were excluded due to the high uncertainty in the determination of the Na and Mg line intensities for their spectral classes.

diverse and we can observe wide variety of spectra. From that point of view, the classification might seem sometimes artificial and strained, yet is very useful tool for further work. For all these reasons, the classification have to be sometimes very complex. We have to use parameters like the velocity and beginning height to classify each meteor and still keep in mind that the smooth transition in Na/Mg spectral ratios reflects the wide variety of elemental abundances for millimetre sized meteoroids.

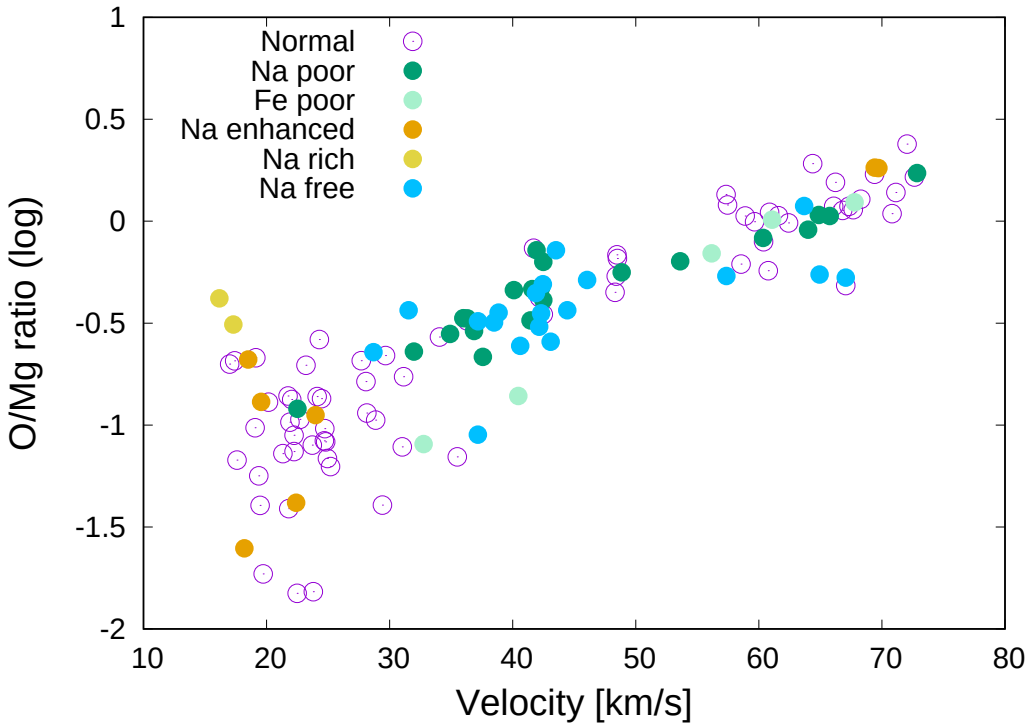

Figure 4.7: O/Mg lines intensity ratio as a function of the meteor speed.

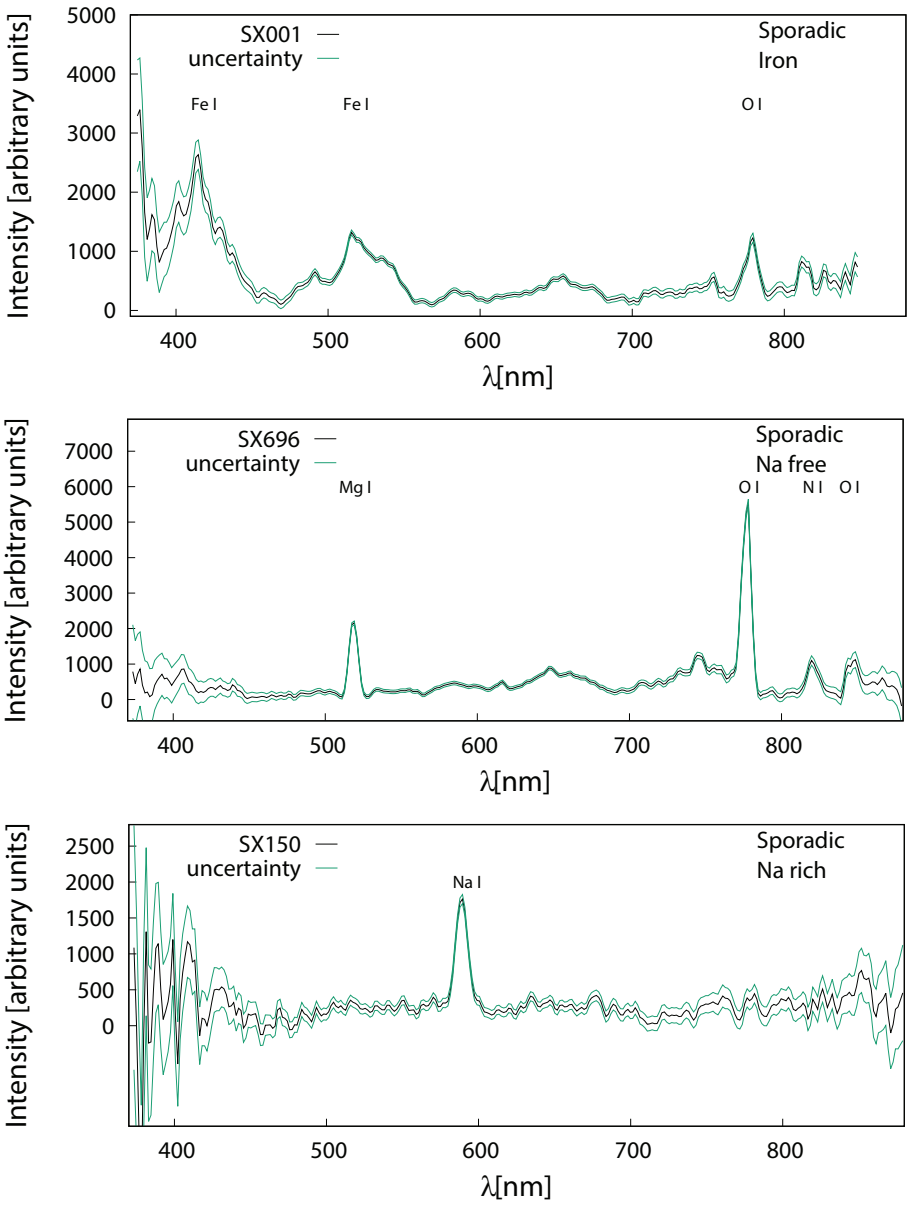

Figure 4.8: Spectra of non–mainstream spectral class members.

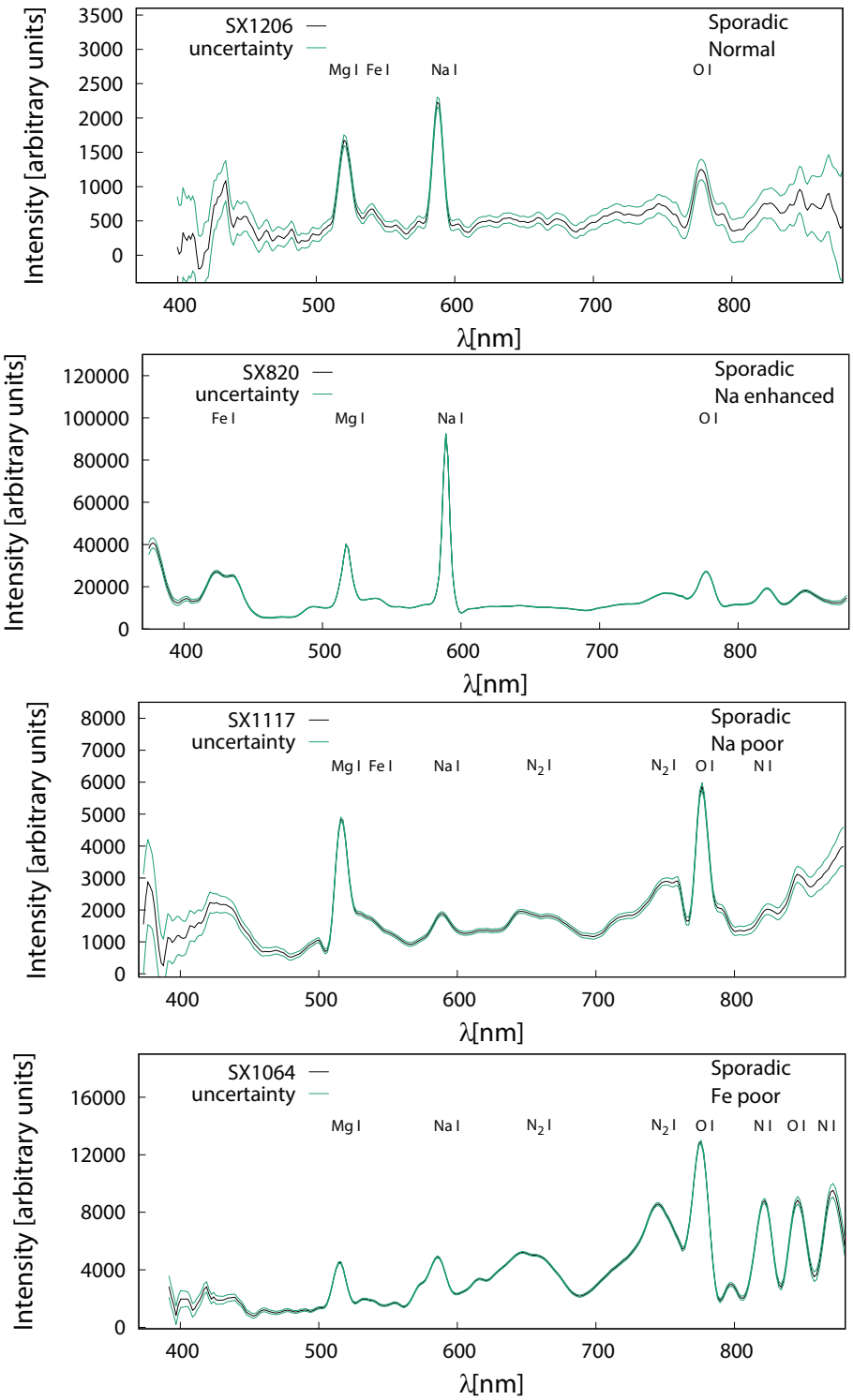

Figure 4.9: Spectra of mainstream spectral class members.

5. Atmospheric trajectories and orbits of meteoroids

5.1 Atmospheric trajectories

With double–station observations, we can precisely determine meteoroids atmospheric trajectories. Parameters like the beginning height and the terminal height can tell us more about the meteoroid composition and strength. Moreover, the combination of atmospheric and spectral data can be used as an important verification of the correct spectral classification.

It is well known that different strength categories of meteoroids in the millimetre size range have different beginnings of the meteor luminous path [Ceplecha, 1988]. For the given speed, the meteoroid composed of stronger material has lower beginning height than the meteoroid formed by weaker material. As we can see in Figure 5.1, the Irons and the Na–free meteoroids started to ablate at lower heights for given speed, compared to the majority of meteoroids. The Fe–poor and Na–rich meteoroids seem to have lower strength of the material. The members of these two spectral classes had higher beginning heights for given speed. One exception is the meteor 05A31001. The spectrum SZ2466 of the meteor 05A31001 was classified as Fe–poor, but for given velocity and spectral class the beginning height seems to be lower than expected. In fact, the real beginning height of this meteors was higher. On both stations we did not observe the beginning part of this meteors and thus we cannot determine the real beginning height. This meteor was omitted from futhers analyses where the beginning height plays a role.

In both figures the solid line shows mean beginning heights of meteoroids with average strength. The dashed lines mark their limits (±5 km). The equation of the empirical line is $H_s = 54v^{0.195}$.

Koten et al. [2003b, 2004] found that for given velocity, the beginning height of members of cometary meteor showers depends on the meteoroid mass. Nevertheless, the mass range in our sample is limited. So we are considering that the dependence of the beginning height on the speed is sufficient for our purpose. This way we can distinguish the variance of material strength of different spectral classes of meteoroids. On the other hand, we can look at the Figure 5.2. This Figure shows the same velocity dependence of the beginning heights, but different meteor showers and sporadic meteors are marked. According to Koten et al. [2004], the meteor showers of cometary origin (like Leonids, Orionds, Perseids and Taurids) show the increase of beginning heights with the increase of photometric mass. For Geminid shower, with asteroid Phaeton as parent body, they found very negligible or none dependence of beginning heights on the speed. In our sample, we have only few meteors for each shower, so these are not statistically representative and therefore we do not show the dependence of beginning height on the velocity for each shower. But regardless of that, we can see that showers like Draconids, Lyrids, Orionids, Taurids, Leonids and Perseids show noticeable range in their beginning heights. On the other hand, beginning heights for Geminid meteoroids are similar. And although we have only two members

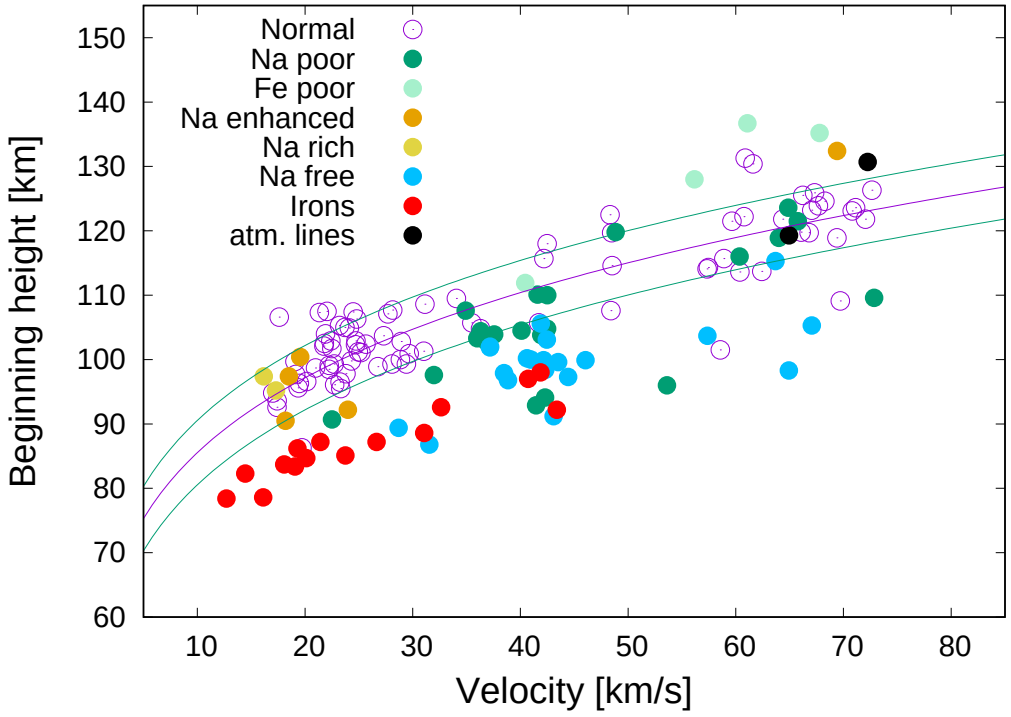

Figure 5.1: Beginning height as dependence of the velocity. Different classes are marked with different symbols. Uncertainties for beginning heights and velocities were negligible for display in the graph.

of Quandratid shower (the parent body is asteroid or extinct comet 2003 EH_1 [Jenniskens, 2004]), they both have very similar beginning heights (103.8 km and 103.1 km).

5.2 Meteoroid orbits

Observed meteors presented in this work have orbits with wide variety of orbital elements. The orbital elements, like the inclination i, the perihelion distance q, the argument of periapsis ω and the ascending node Ω, are presented in large range of values.

The measurement precision is good for all elements with one exception. The accuracy for semimajor axis can be sometimes low due its sensitivity to the determination of velocity. Even the uncertainty within a few tenths of km.s^{-1} for the velocity cannot be sufficient for precise determination of the semimajor axis. Especially semimajor axes near the parabolic limit are hard to determine. Moreover, few orbits are formally hyperbolic, but we believe it is due to measurement error. This uncertainties are the effect of low resolution of video technique compared to the photographic observations.

Using orbital elements for each meteoroid, we can try to estimate its origin or the type of the parent body. For this, the inclination and the Tisserand parameter relative to Jupiter $T_J = (a_J/a) + 2\sqrt{(a/a_J)(1-e^2)}cos(i)$, where $a_J = 5.2$ AU is the semimajor axis of Jupiter, can be used. The perihelion distance q and the aphelion distance Q can be used as well. All these parameters are used

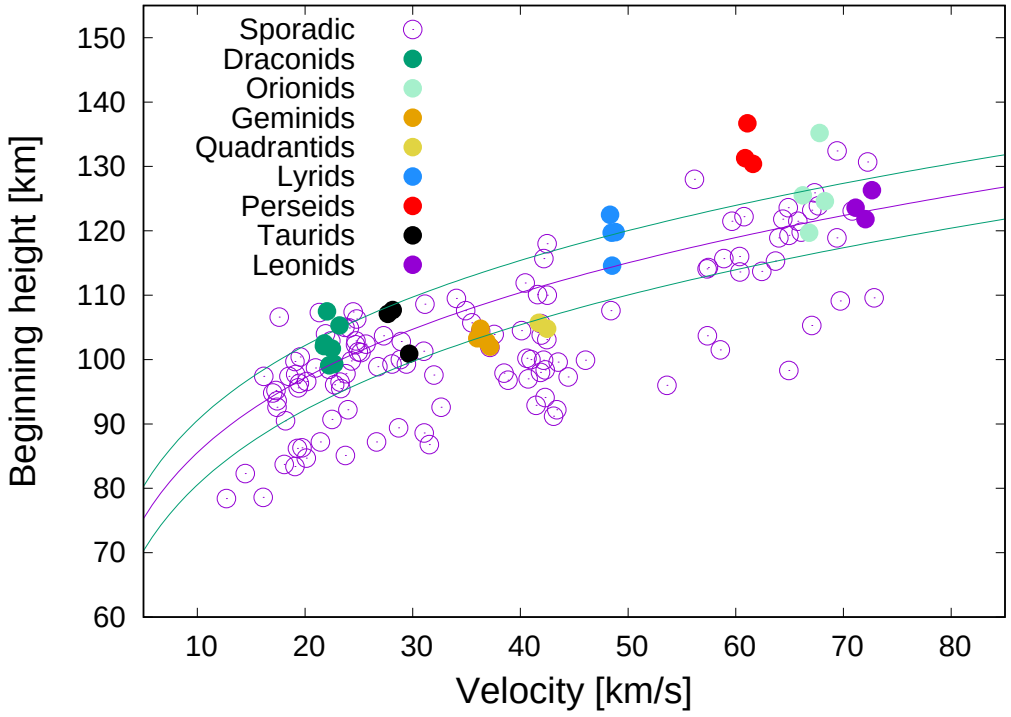

Figure 5.2: Beginning height as dependence of the velocity. Different meteor showers are marked with different symbols.

to determine typical orbits of asteroids, Jupiter family comets and Halley type comets. Five classes of meteoroid orbits were defined by Borovička et al. [2005]:

- (SA) *Sun-approaching orbits:* $q < 0.2$ AU.

  Orbits with small perihelion distances are defined as a separate class.

- (ES) *Ecliptic shower orbits:*

  Members of ecliptical meteor showers. For example the Taurid meteors derived from the comet 2P/Encke and other showers with orbits close to the boundary between asteroids and Jupiter family comets.

- (HT) *Halley type orbits:* $T_J < 2$ or $2 < T_J < 3$ and $i > 45°$.

- (JF) *Jupiter family orbits:* $2 < T_J < 3$ and $i < 45°$ and $Q > 4.5$ AU.

- (A-C) *Asteroidal-chondritic orbits:* $T_J > 3$ or $Q < 4.5$ AU.

5.3 Combining spectral and orbital classification

Now we can combine the spectral and orbital classification and material strength. The positions of meteoroids within the orbital classification schemes can be seen in Figures 5.3 and 5.4. Figure 5.3 shows the Tisserand parameter and the inclination. Figure 5.4 shows perihelion and aphelion.

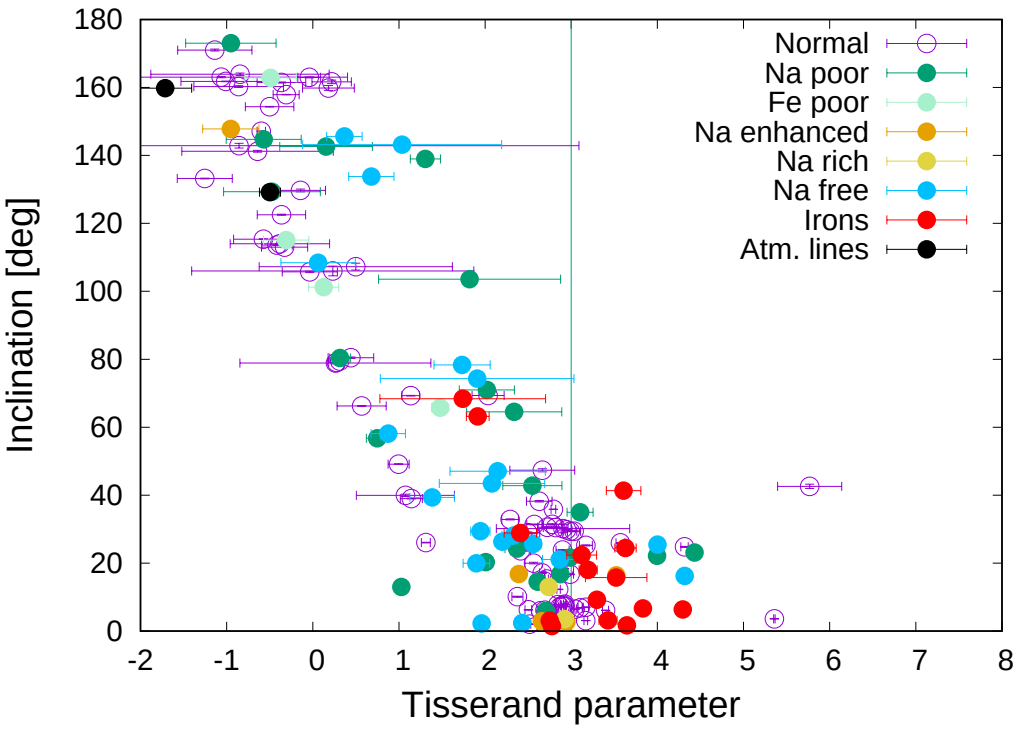

Figure 5.3: Tisserand parameter versus inclination with given uncertainties. Uncertainties for the inclination were too small to be visible for the resolution of the figure. Every meteor is represented with given spactral class. The green vertical line marks Tisserand parameter $T_J = 3$.

Moreover, every meteoroid is represented with given spectral class. The percentage of each spectral class for given orbital class and vice versa is shown in Figure 5.5. We can see orbital classes in the ternary graph in the Figure 5.6 and the velocity versus beginning height graph for different orbital classes in the Figure 5.7. In general, meteoroids with Jupiter – family, asteroidal and ecliptical orbits tend to have more sodium in their spectra. Meteoroids with Halley type and Sun approaching orbits have less sodium in their spectra (or none in the case of Na – free spectra. But the correction of the Na/Mg ratio on the velocty must be taken into consideration for velocities lower than $\approx$ 35 $km.s^{-1}$ (see Figure 4.6). Since spectral classification is corrected on the velocity we can compare spectral classification with orbital classification. Using the Figure 5.5 we can see that Normal chondritic class prevails among the Jupiter–family members and among members of the ecliptical orbits. The asteroidal class contains 53 % of Iron meteors and 37 % of Normal meteors. More than half (56 %) meteoroids on the Halley type orbits are of Normal spectral type. Na–poor and Na–free classes were also among the Halley type orbits (16 %, respectively 14 %). The Sun–approaching orbital class shows lack of the sodium. Members of the Na–free (57 %) and Na–poor (37 %) prevailed in this orbital group.

We will now discuss individual spectral classes separately.

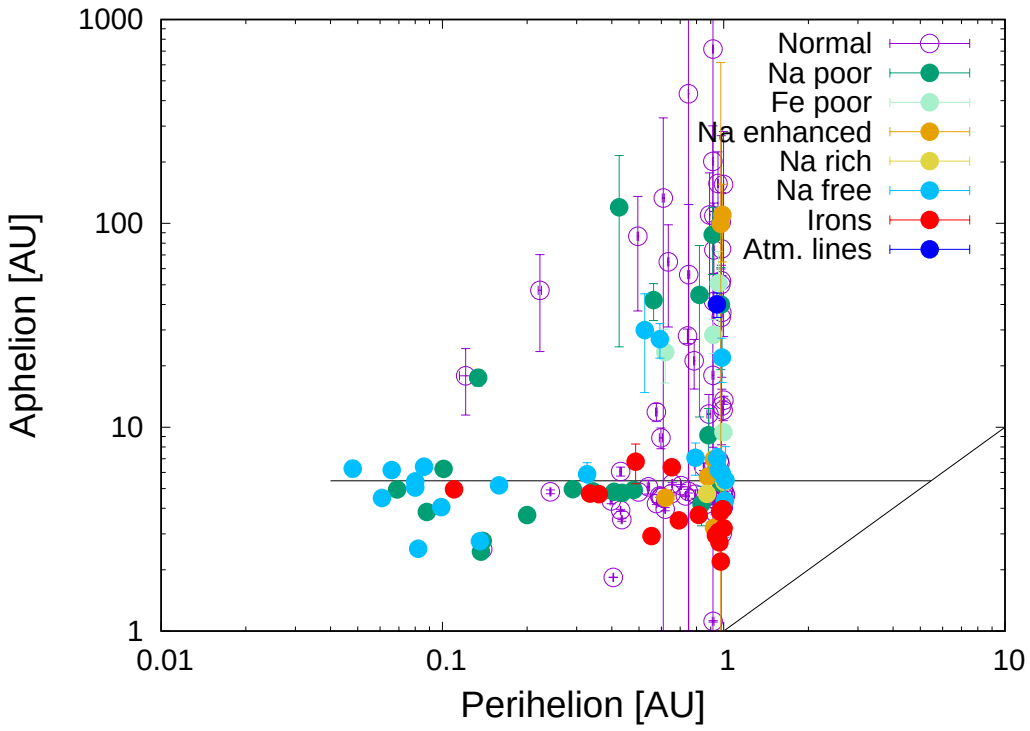

Figure 5.4: Perihelion versus apahelion with given uncertainties. Every meteor is represented with given spactral class. The solid horizontal black line marks the Jupiter's aphelion $Q_J = 5.5$ AU.

5.3.1 Iron meteoroids

Fifteen meteors were classified as Irons. All of them were sporadic meteors. We can see some orbital parameters in the Table 5.1. Most of them had typical asteroidal–chondritic orbit. Their aphelion distances Q are below 4.5 AU and their Tisserand parameters T_J are greater than 3. On the other hand, five Iron meteors have different orbits. The meteoroid SX001 have perihelion of only 0.11 AU and thus can be classified as the Sun–approaching meteoroid. The orbits of meteoroids SX661 and SX1194 can be classified as Jupiter family orbits, but asteroidal origin cannot be excluded for both of them, since the inclination is only 1.5° and 3° and the aphelion of 4.7 AU for both of them is not particularly high. Moreover, according to the low inclination these can be classify as members of ecliptical meteor shower.

The most surprising was the discovery of two meteors among Halley type orbits. Although both of these orbits are somewhat transitional between Halley type orbits and Jupiter family orbits they showed inclinations more than 60°. The measurement of orbit for the meteoroid with spectrum SX1938 is not particularly precise. The uncertainty for Tisserand parameter is high ($T_J = 1.7 \pm 1.0$). Another Iron class meteor with Halley type orbit was the meteor with spectrum SZ2410. High inclination ($i = 63.2 \pm 0.2°$) and overall accurate orbit measurement assigns clearly Halley type orbit.

5.3.2 Na–free meteoroids

Two different sources for members of Na-free class can be observed: the Sun–approaching population with small perihelion and the Halley type population with high inclinations. Actually, there are three populations, if we add Iron meteors.

Sun–approaching meteoroids

Almost all meteoroids with perihelion distance $q < 0.2$ AU are Na–free or Na–poor. This is in agreement with the conlcusion of Borovička et al. [2005]. The frequent approaches within ≈ 0.2 AU to the Sun lead to the loss of Na from meteoroids in the millimeter-size range, irrespective to their origin (see also Čapek and Borovička [2009]). Two exceptions from the Na–free, Na–poor dominance in the Sun–approaching orbital class were found. One is the Iron meteoroid SX001, which, nevertheless, also does not contain sodium. The second exception is the Geminid meteor SX336 with normal type of spectrum. This is not surprise, because Geminid shower meteors (with small perihelion distance $q = 0.14$ AU) are well known for their variability of the sodium intensity in their spectra. We can find Na–free, Na–poor and also Normal types of spectra within this meteor stream. Analysis of Borovička et al. [2010] suggests that differences in porosity may be the main reason of different Na content in Geminids.

According to the Figure 5.7, the material of Sun–approaching meteoroids tends to have larger strength. For given velocity, their beginning heights are lower. This corresponds with the lack of sodium in their spectra.

Cometary Na–free meteoroids

We found 10 Na–free meteors that do not approach Sun as close as the Sun–approaching meteors. Nine of them have Halley type orbit (SZ2227, SZ2443. SZ2454, SX350,SX696, SX786, SX1044, SX1104, SX2365). The orbit of meteor SX1073 was classified as Jupiter family type. So the close approach to the Sun is not the only process that causes the depletion of Na in meteoroids.

According to Borovička et al. [2005] the reason of Na depletion at these types of orbits might be the long exposure to cosmic rays of the surface of comets during their residence in the Oort cloud. This process can lead to the formation of Na–free refractory crust. The gradual or sudden disintegration of the crust during the cometary passage through the inner Solar system then produces millimetre–sized compact Na–free meteoroids.

5.3.3 Na–rich meteoroids

Only two spectra were classified as Na–rich (SX150, SX2395). Both meteoroids had Jupiter family type orbits. Velocities for these meteors SX150 and SX2395 were small, v = 13.4 km.s^{-1} and v = 12.0 km.s^{-1} respectively. Their beginning heights were normal for given velocity (see Figure 5.1).

5.3.4 Normal meteoroids

Among meteoroids classified as Normal we can find the cometary and asteroidal orbits. But only part of these meteoroids have typical chondritic composition. Many of them show somewhat fainter Fe lines. Borovička et al. [2005] assumed that the meteoroids classified as Normal are mixture of normal chondritic material and cometary material similar to Leonids. They used the computation of the chondritic composition and the Halley dust composition (confirmed by the data of Leonid observations). Except for one Na–enhanced meteor with ecliptical shower type orbit (SX820), all of the remaining meteoroids with ecliptical orbits were classified as Normal.

5.3.5 Fe–poor meteoroids

Five of the meteoroids in this work (SZ2428, SZ2466, SX211, SX1064, SX1802) were classified as Fe–poor. The iron lines were too faint to classify these meteoroids as Normal. As mentioned before, the establishing of the boundary between Normal and Fe–poor meteors is not trivial and can be somewhat arbitrary. Four of the Fe–poor meteoroids have cometary Halley type orbits.

Beginnig heights suggest that these meteoroids should have lower material strength, their beginnings of ablation are usually high (see Figure 5.1).

Transitional orbit between Asteroidal–chondritic and Ecliptical was computed for the meteoroid with spectrum SZ2466 with Tisserand parameter T_j =3.0 . The Asteroidal–chondritic orbit is not expected for fragile Fe–poor bodies. Unfortunately, recordings from both stations does not contain beginning and end of this meteor. Thus we cannot reliably compute the atmospheric trajectory and the orbit. We decided to omit this meteor from further study of orbits and atmospheric trajectories. Since the meteor was long (through the whole field of view) we think that the orbital parameters would not change much, if the whole meteor was observed. Theoretically, if the whole meteor was observed and similar orbital data were obtained, the transition between Asteroidal–chondritic and Ecliptical would explain why Fe–poor body was observed on such an orbit. Compared to other Fe–poor meteoroids, this was the only iron depleted body with low inclination ($i = 5.7°$). It also showed smallest semimajor axis ($a = 2.2$ AU). There are well known comets (like the 2P/Encke) inside the asteroid belt and we think that one of these comets can be source of this meteor. Moreover we recorded brightest part of the spectrum. Thus we think that at least the computation of relative intensities of spectral lines are trustworthy, since most of the total intensity of lines comes from the brightest parts.

5.3.6 Na–poor meteoroids

Na–poor meteoroids are the transition between Normal and Na–free meteoroids.As well as Na-free meteoroids, some of them have low perihelia, others have cometary orbits. Thus they have probably the same two origins as the Na–free meteoroids.

5.3.7 Enhanced–Na meteoroids

Five meteor spectra (SX498, SX500, SX820, SX1057, SX1197) were classified as Na–enhanced. Meteoroid with spectrum SX500 had typical Asteroidal-chondritic orbit. Orbits for SX498 and SX1197 were classified as Jupiter family types. Meteoroid with spectrum SX820 had ecliptical shower type orbit and meteor SX1057 was classified with Halley type orbit. We can see that there is wide variety of orbital types among Na–enhanced meteoroids. Even though we have only five spectra within Na–enhanced class.

Na–enhanced meteors have usually smaller velocities with one exception. The SX1057 meteor with high velocity (v = 69.4 km.s^{-1}), and clearly Halley type orbit, showed increased intensity of sodium for given speed (see Figure 4.6).

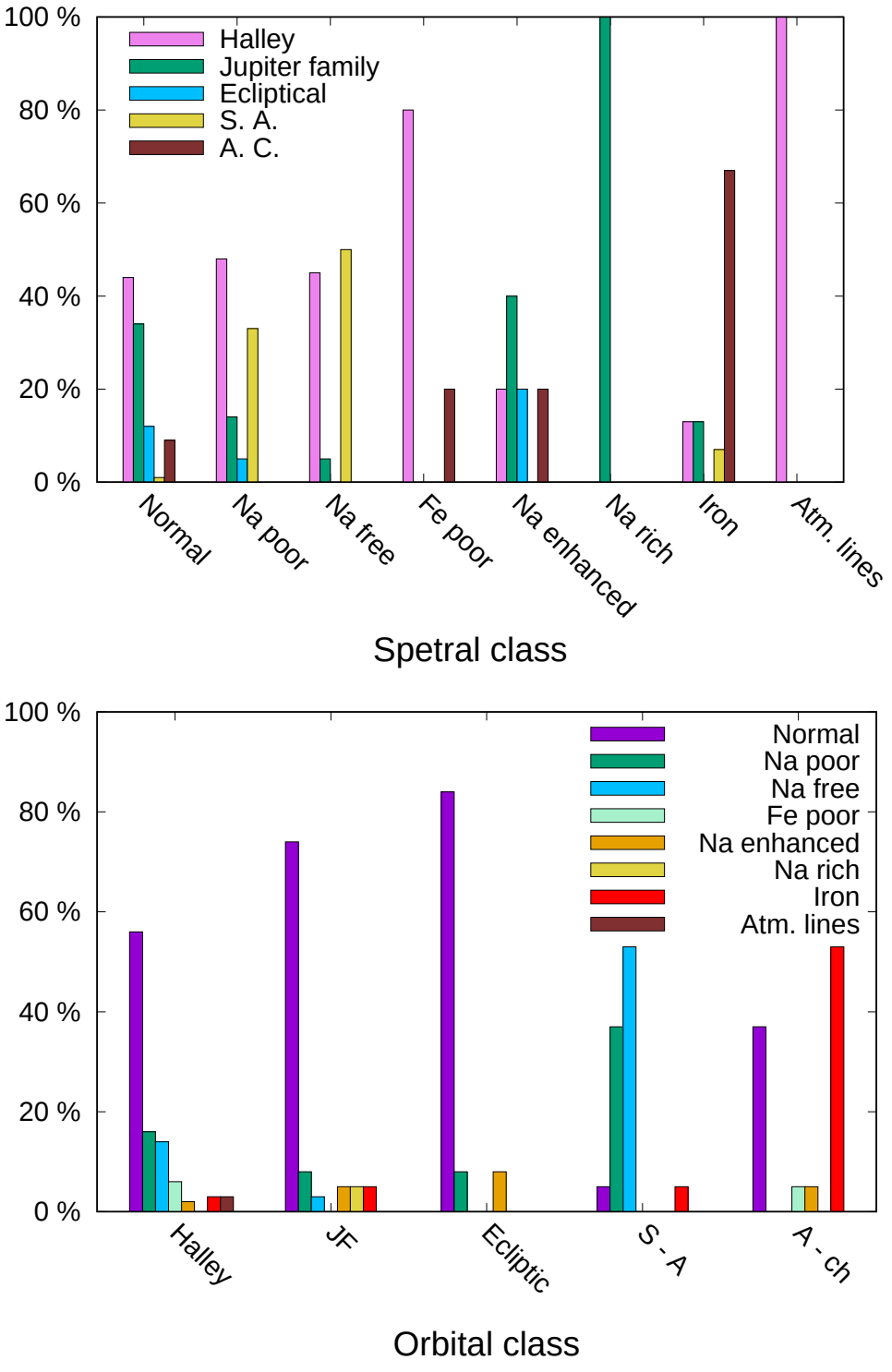

Figure 5.5: Percentage of orbital classes for given spectral classes and vice versa. Abbreviation S. A. stands for Sun approaching class, A. C. stands for asteroidal chondritic class and JF stands for Jupiter family orbits. Meteor SZ2466 is included in this statistic.

Table 5.1: Orbital elements of meteoroids classified as Irons. Second row for each meteor contains corresponding errors. A–C stands for the Asteroidal–chonditic orbit, SUN is the Sun–approaching orbit, JF is the Jupiter–family orbit, Hall is the Halley orbit.

spectrum	a (AU)	q (AU)	Q (AU)	i (°)	ω (°)	Ω (°)	v (km/s)	T_J	orbit
SZ2410	3.50	0.654	6.4	63.2	103.2	14.32	40.7	1.9	Hall
	0.09	0.001	0.2	0.2	0.3	-	0.1	0.1	
SZ2417	2.1	0.69	3.5	3.2	257	125.79	21.4	3.4	A-C
	0.1	0.01	0.2	0.3	2	-	0.2	0.1	
SX001	2.5	0.110	5.0	28.9	325.1	16.95	41.9	2.4	SUN
	0.1	0.004	0.2	0.9	0.7	-	0.2	0.3	
SX058	1.94	0.938	2.95	24.5	219.0	122.67	20.1	3.6	A-C
	0.04	0.002	0.09	0.3	0.6	-	0.2	0.1	
SX393	1.59	0.976	2.19	6.4	194.1	262.71	12.70	4.3	A-C
	0.02	0.001	0.05	0.2	0.3	-	0.08	0.2	
SX661	2.53	0.360	4.67	1.5	292.7	195.10	31.06	2.78	JF
	0.05	0.002	0.09	0.2	0.3	-	0.09	0.03	
SX689	1.84	0.966	2.72	41.3	150	45.77	24.1	3.6	A-C
	0.04	0.002	0.02	0.3	1	-	0.2	0.2	
SX692	2.1	0.999	3.2	16	194	45.80	26.6	3.5	A-C
	0.2	0.004	0.4	1	3	-	0.2	0.6	
SX701	2.26	0.815	3.7	9.2	119.7	126.01	19.3	3.30	A-C
	0.05	0.001	0.1	0.2	0.2	-	0.1	0.06	
SX984	2.41	0.972	3.9	18.0	204.1	31.75	18.0	3.2	A-C
	0.09	0.001	0.2	0.3	0.4	-	0.2	0.1	
SX1088	2.5	0.993	4.0	22.4	162.0	147.81	19.1	3.1	A-C
	0.1	0.001	0.2	0.4	0.6	-	0.2	0.2	
SX1114	1.74	0.554	2.92	6.7	94.9	55.43	23.8	3.8	A-C
	0.05	0.006	0.09	0.2	0.09	-	0.2	0.08	
SX1187	2.01	0.959	3.1	1.7	28.5	196.74	14.4	3.65	A-C
	0.06	0.001	0.1	0.1	0.5	-	0.1	0.06	
SX1194	2.53	0.335	4.7	3.1	295.6	19.91	32.6	2.75	JF
	0.07	0.003	0.1	0.2	0.4	-	0.1	0.05	
SX1938	3.6	0.486	7	63	277	143.30	43.4	1.7	Hall
	0.8	0.008	2	1	2	-	0.8	1.0	

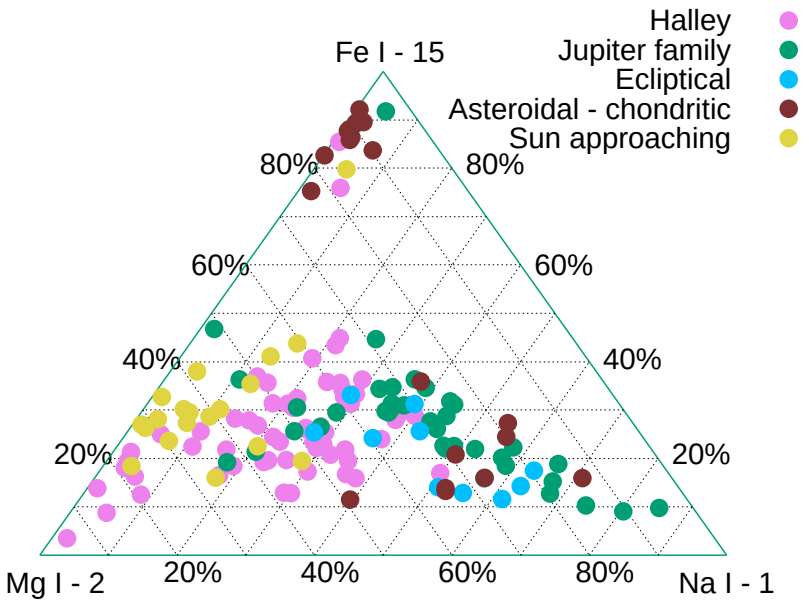

Figure 5.6: Position of every meteor in this ternary graph is given by computed relative intensity of Mg I – 2, Na I – 1 and Fe I – 15 lines. The color of each point represents orbital classification. Meteor SZ2466 is included in this figure.

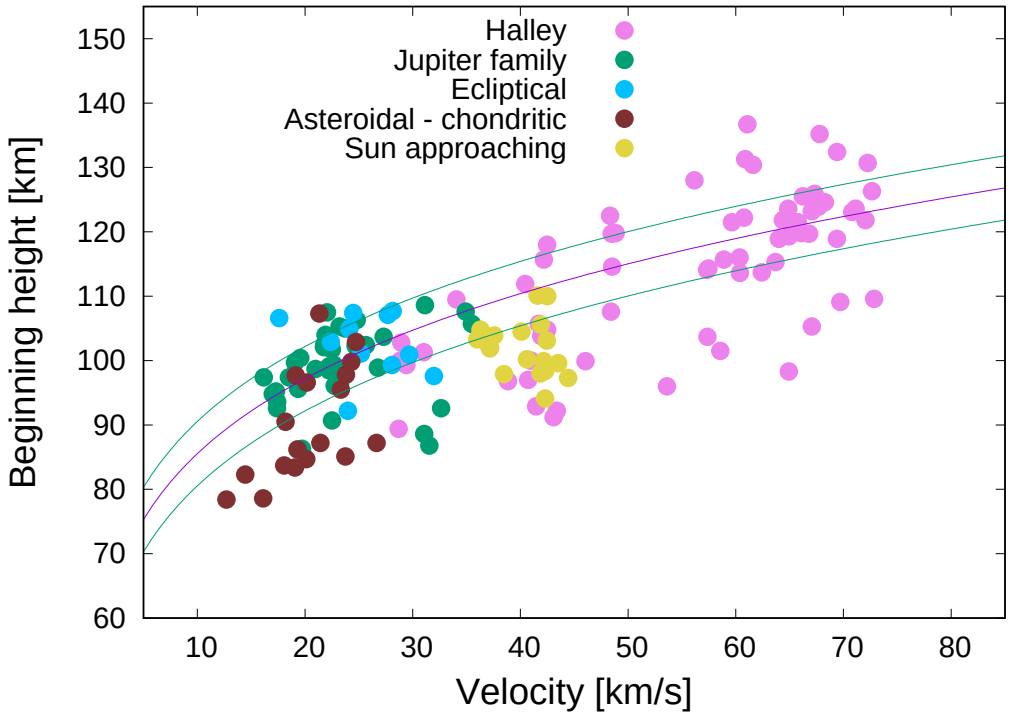

Figure 5.7: Beginning height as dependence of the velocity. Meteors are marked with different symbols representing different orbital classes. The solid line shows mean beginning heights of meteoroids with average strengths as in Figures 5.1 and 5.2.

6. Results of fragmentation model

6.1 Fitting lightcurves and deceleration curves

Of the total number of 152 meteoroids in this work, 94 meteoroids showed sufficient deceleration and thus we were able to use the model of fragmentation. As mentioned earlier, the fragmentation model developed by Borovička et al. [2007] is using the dustball concept with quasi–continuous fragmentation.

This model uses lightcurves and curves of deceleration. The goal is to find best fit for these curves with the least square method. Free parameters of functions used for fitting are physical parameters of individual meteoroids. Among the free parameters are: initial mass and initial velocity, the ablation coefficient, the energy per unit cross–section necessary to start the erosion, the bulk density, erosion coefficient, the number of fragmented grains and distribution of these grains etc.

If possible, data from all observation stations were used. If the data from any station had low quality, they were excluded from the model and the data only from one station were used.

In Figure 6.1 we can see example of four meteors, their lighcurves and deceleration curves. Measurements from each station are represented by points. The fitting curve is the result of the fragmentation model. We chose four different types of lightcurve shapes as examples. Lightcurves show the dependence of meteor brightness on the time. The lightcurve of meteor 08506016 (spectrum SX696) have its maximum in the middle. The meteor 12811384 (spectrum SX1802) has the maximum at the end of the lightcurve. The meteor 08928141 (spectrum SX799) has the maximum at the beginning of the lightcurve. Some meteors showed signs of at least two phases of the fragmentation. We can sometimes see the sudden brightening of the lightcurve. This is the case of the meteor 08927101 (spectrum SX788). We tried to fit these lightcurves and deceleration curves with two phase modelling. Then we could estimate physical differences between these two parts.

The deceleration curve shows the dependence of the length difference on the meteoroid's atmospheric height. The length difference is the difference between measured real position of the meteor and the computed position for no deceleration (if the meteor had constant velocity along the trajectory). Position with no deceleration is marked by the green horizontal line in Figure 6.1. If the meteoroid is decelerated, we can see typical deviation of observed meteor positions as seen in examples in Figure 6.1. The violet line is the result of the fitting by the fragmentation model and represents the computed length difference of the brightest point of the meteor.

Table 6.1 shows some of the results of the model of meteors shown in Figure 6.1. Parameters like the initial mass and the initial velocity, bulk density of meteoroid δ, ablation σ and erosion coefficient η, sizes (their limits) of grains and number of grains released and energy received before the start of the erosion (per unit cross section) E_s are shown.

Figures from A.17 to A.35 in the Appendix of the electronic version show all of the modelled meteoroids.

6.1.1 Parameters of the erosion model

The process of modelling was not always straightforward and we have to keep in mind some of the limitations of this fragmentation model. First of all, since the model uses trial–error method, we are not able to provide standard deviations of the parameters. One of the problems is: from our data, we are not able to determine the density of individual grains. Therefore we assumed grain density $\delta_g = 3000$ kg .m^{-3} and we assumed spherical shape for all grains. If this density is different, the grain mass and the number of grains need to be changed accordingly. If the meteor was identified as Iron, we assumed the grain density to be $\delta_g = 6000$ kg .m^{-3}. In reality, meteoroids do not contain only spherical grains. Some of them can be made of seemingly monolithic material, but this material contains cracks. The cracked material then behaves like it was composed from small grains. For Irons, the separating grains may be liquid droplets in reality [Čapek and Borovička, 2017].

Other external parameters were fixed. The drag coefficient Γ and also the heat transfer coefficient Λ were assumed to equal unity, because the ablation energy cannot exceed the total kinetic energy of the oncoming stream molecules [Bronshten, 1983]. We used spherical grains and the shape factor $A = 1.21$. As the luminous efficiency τ, we used the Pecina and Ceplecha [1983] function. As a model of the atmosphere, the empirical model NRLMSISE-00 [Picone et al., 2002] was used to compute the density of the atmosphere ρ.

We used the same ablation coefficient σ for the meteoroid and for the fragmented grains.

As mentioned before, some meteors showed more phases of the erosion (like the meteor 08927101). Usually there were two phases of the erosion. The initial erosion was modelled up to some amount of mass was lost. The rest of the mass was modelled in the second phase. Different sets of free parameters were used to fit the the lightcurve and the deceleration in each phase.

Sometimes we can observe the meteor before the start of the fragmentation. This allows us to derive the meteor bulk density δ. According to equations 2.3 and 2.9 for the luminosity and mass loss, when there is ablation without erosion, the luminance I is proportional to the shape density coefficient K, the luminous efficiency τ and the ablation coefficient σ ($I \sim \tau K \sigma$). We know the mass and velocity of the meteoroid and we can compute the shape density coefficient at the beginning height K_∞. To compute the meteoroid beginning cross–section S_∞ and the bulk density δ, we have to know the shape of the meteoroid. Since the shape is unknown, we assumed the shape to be spherical (the shape factor $A = 1.21$). Using the Equation 2.5 for the shape density coefficient K we can finally compute the meteoroid cross–section and the bulk density of the meteoroid. But for most cases, we didn't observe the meteor before the fragmentation. For these cases, it is hard to estimate the bulk density since every change in bulk density can be corrected by the change of the erosion coefficient to obtain the same fit of lightcurve and deceleration curve.

Bulk density can be used to compute the porosity of meteoroids. The porosity

p can be defined as proportion of the meteoroid bulk density δ to the density of grains δ_g:

$$p = 1 - \delta/\delta_g \tag{6.1}$$

The porosity shows how much of the meteoroid volume was filled with the actual meteoritic material and how much of the volume consisted of the "space" between grains.

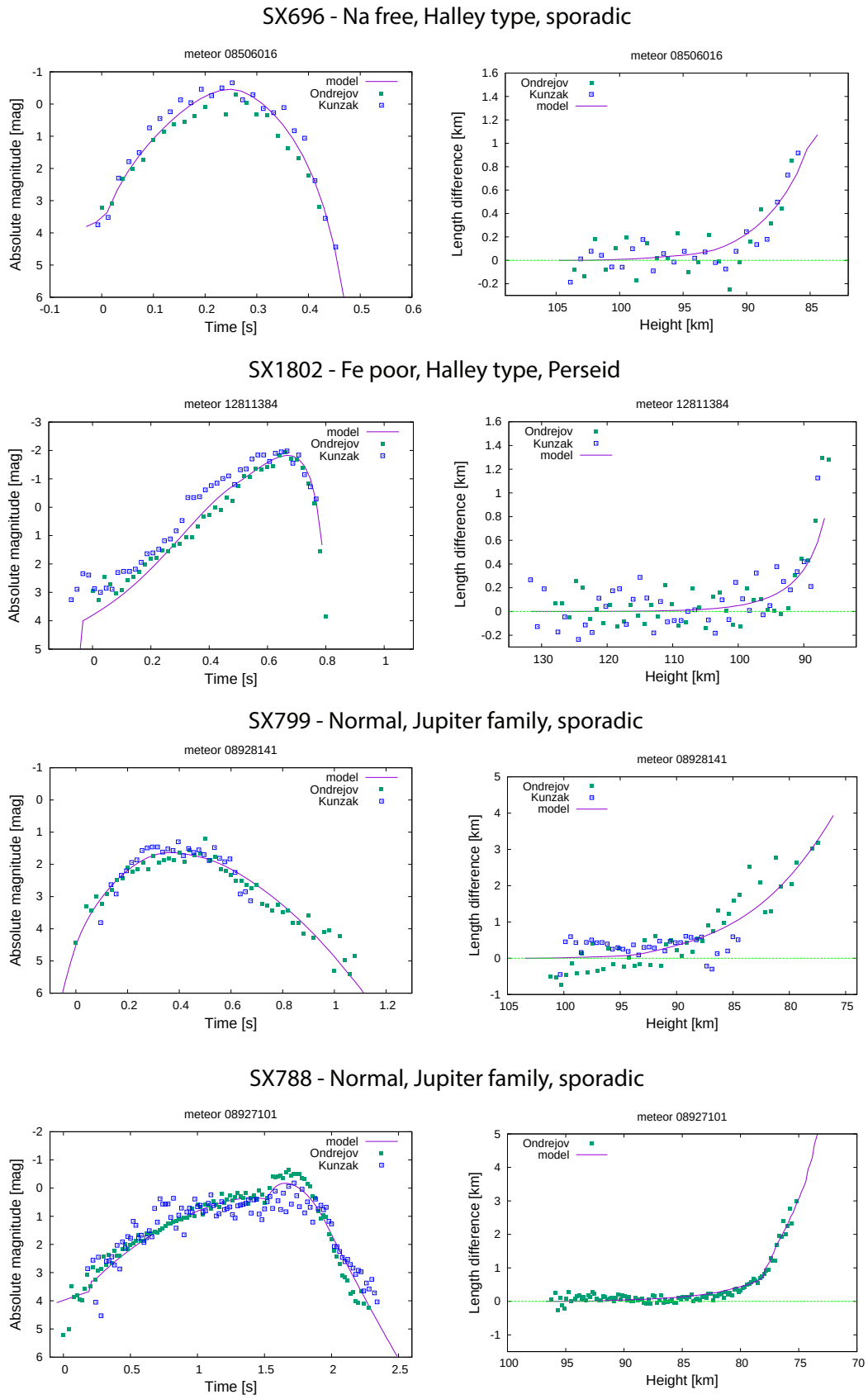

Figure 6.1: Examples of different shapes of lightcurves and their corresponding deceleration curves for four meteors. Lightcurves on the left, deceleration curves on the right. Only data used for model are shown.

Table 6.1: An example of results of the modelling. Two stages of erosion were modelled for meteor 08927101, both parameters are shown: FE stands for first erosion, SE stands for second erosion. GUML is Grain upper mass limit, GLML is Grain lower mass limit. E_s is the energy needed for the start of erosion. δ is the bulk density of meteoroid. σ is the ablation coefficient, η is the erosion coefficient.

meteor	spectrum	init. mass	init. velocity	δ	σ	η	GUML	GLML
		g	km . s^{-1}	kg . m^{-3}	s^2 . km^{-2}	s^2 . km^{-2}	g	g
00850616	SX696	1.60×10^{-2}	58.1	2500	0.009	0.20	3.16×10^{-5}	5.01×10^{-7}
08927101 FE	SX788	1.54×10^{-1}	19.7	700	0.014	0.23	1.00×10^{-4}	7.94×10^{-6}
08927101 SE					0.014	0.27	6.31×10^{-5}	3.98×10^{-7}
08928141	SX799	6.58×10^{-2}	27.8	800	0.007	0.91	5.01×10^{-6}	3.16×10^{-8}
12811384	SX1802	5.71×10^{-2}	62.2	150	0.010	0.27	9.33×10^{-6}	9.33×10^{-6}
meteor	spectrum	erosion start	erosion end	grain sizes	number of grains	E_s	spec. class	orbital class
		km	km	mm		J . m^{-2}		
00850616	SX696	103.2	92.6	0.27–0.07	5.9×10^3	4.5×10^6	Na–free	Halley
08927101 FE	SX788 FE	94.3	79.1	0.40–0.16	4.8×10^4	3.9×10^6	Normal	J–F
08927101 SE		82.2	78.2	0.34–0.06	3.1×10^5			
08928141	SX799	103.0	93.3	0.15–0.03	4.3×10^5	1.0×10^6	Normal	Halley
12811384	SX1802	130.	102.5	0.18–0.17	5.9×10^3	1.5×10^5	Fe–poor	J–F

6.2 Morphology

The meteor morphology studies the appearance of individual meteors. There are some phenomena connected with meteors.

According to Ceplecha et al. [1998] meteor wake is a region of radiation just behind the meteor. Typical dimensions of wake are several hundred meters to several kilometers. Meteors wake can last up to several tenths of seconds. Spectral observations of wakes show lines of the same elements as in the meteor head radiation, although the excitation energy is lower. The meteor train is a radiation emitted behind the meteor for seconds or more [Ceplecha et al., 1998]. The substantial part of train is formed by forbidden line of oxygen at 557.7 nm. The train that radiates in a forbidden line of oxygen for a few seconds is then called the short duration green train. The work of Borovička [2006] summarized the terminology and distinguished between different phenomena connected with the passage of a meteor. Wakes and short duration green trains might occur with faint meteors. According to their paper, the green trains are typical for high–velocity meteors of medium or low brightness.

The internal structure of meteoroid and related process of fragmentation can affect the behaviour of a meteor during the atmospheric flight. Therefore we investigated morphology of individual meteors. We went through all meteor videos and we tried to analyse meteor shapes, lengths and visibility of meteor wakes and trains.

We observed variety of scenarios for the meteor wake and the meteor train. From meteors with no visible train and wake, meteors with only train or meteors with only wake, through meteors with faint trains and wakes and to meteors with bright wakes or trains. But we were interested not only in brightness and visibility of these features. We observed different behaviour of wakes and trains. Some wakes were visible through the whole meteor flight. Other wakes formed in the second half of the flight. Moreover, some trains disappeared right after the meteor ended, other trains lasted up to another few seconds. Also endings of meteors were different. Most of the meteors ended quickly, but we observed cases when meteors were blurred at the end of its trajectory with equal brightness of the meteor streak.

In Figures 6.2 and 6.3 we can see some examples of different shapes for meteors included in this work.

6.2.1 Morphology and spectral classification

We did not measure features like wakes and trains quantitatively. We described these features qualitatively and organized our meteors in different groups based on these descriptions. For wakes, we created three groups of meteors. We marked meteors with *no wake*, meteors with *short or faint wakes* and meteors with *bright or long wakes*. For trains we also created three groups of meteors. We marked meteors with *no trains*, meteors with *faint trains* and finally meteors with *bright trains*. In the group of *bright trains* there are meteors with short duration green trains. These trains lasted up to several seconds after the meteor ended. The brightness of the wake or train was determined by the operator as the relative brightness to the meteor head. For simplicity we did not take the time evolution

of wakes or trains into consideration. In other words, we did not take into account if the wake was visible during the whole flight or if the wake visible during the second half of the meteor flight.

Then we compared these groups with spectral classification of given meteors. Results can be seen in Figure 6.4 for wakes and in Figure 6.5 for trains.

For Normal spectral class, meteors with no wake (38% of all Normal meteors) and short wake prevail (46%), but meteors with long and bright wakes are not negligible (16%). There is similar amount of meteors with bright (36%), faint (36%) or no trains (28%) among Normal spectral class. We can see similar rates of wake types for Na–poor and Na–free meteors. There is only one case with bright wake for Na–poor class and no bright wake for Na–free case. Meteors with no wake or short wake are present in similar amount (48% : 48% for Na–poor and 45% : 55% for Na–free). Also there is similar number of meteors with no train and with faint train for both Na–poor and Na–free class (33% : 38% for Na–poor and 45% : 55% for Na–free). The only difference is higher amount of meteors with bright train for Na–poor class (29%) compared to only 5% of these for Na–free class. Unsurprisingly, the Iron meteors with no wake and no train prevail among this spectral class (67% meteors with no wake and 67% with no train).

Other spectral classes contain only small number of meteors. Simple statistics like the one in previous paragraph might be misleading for very small numbers. With this in mind, we will try short recapitulation. We did not observe any wake for two of the meteors with only atmospheric lines in their spectra (09820190/SX1101 and 13811452/SX2175). On the other hand, their trains were bright and the short duration green train was visible after the actual meteors ended. This is not surprising for meteors with only atmospheric lines in spectra, since these types of trains are formed by forbidden line of oxygen at 557.7 nm. The Fe–poor and Na–enhanced class showed similar number of meteors with no wakes, faint wakes or bright wakes. We did not observe any Fe–poor meteor without a train. Both of the two meteors classified as Na–rich showed no train and they have no or only faint wake.

Is there any connection between spectral classes and the appearance of the wake or train? In Figures 6.6 and 6.7 there is again the dependence of the beginning height on the velocity of meteoroid. This time each color of individual symbols represents different wakes or train types.

Meteors with no wake occur in the whole range of velocities and beginning heights. On the other hand, meteors with wakes (both short and long) tend to have lower velocities. Although there are fast ($v > 50$ km . s^{-1}) meteors with wakes, there are just few of them. We also noticed that slow meteors with wakes have higher beginning heights for given velocity, compared with meteors without wakes. Moreover, fast meteors with wakes tend to have lower beginning heights for given velocity. One of the reasons why we observe much less wakes for fast meteors might be the observer effect. Slower meteors are seen on video frames as points and we can see actual shape of the meteor and its wake. Fast meteors are seen as line on individual frames, because they are fast enough to move on single frame during the short (0.04 s) exposure. The wake, if there is any, might be covered by meteor head because in the video the meteor head is prolonged by the fast movement during the exposition. This can explain the lack of short

wakes for fast meteors. We think that we would be still able to see bright and long wakes. But we do not see anything like that in the Figure 6.6. There are more meteors with short wakes than meteors with long bright wakes. This can be further investigated in the future and with more sophisticated methods and by a technique with better resolution.

Lets look at the meteor trains in Figure 6.7. We can see that almost all meteors without train have low velocities. Meteors with trains (both faint and bright) are present almost in the whole range of velocities. Slow meteors with trains tend to have only faint trains. The faster the meteor is, the brighter train it has. In the region of fast meteors ($v > 50$ km . s^{-1}) and high beginning heights ($H_B > 115$ km) there are only meteors with bright short duration green trains. This result is not surprising when we, again, take the origin of short duration green trains and the dependence of brightness of atmospheric lines on velocity into account.

6.2.2 Morphology and fragmentation model

The next step was the comparison of results from the fragmentation model to results of the morphology investigation.

We did not try to compare results of analysis of meteor trains and results of meteoroid fragmentation model. We consider meteor trains of faint meteors mainly as the result of ionisation of atmospheric atoms (green trains). We tried to look at different types of meteor wakes and tried to compare them with the results of the fragmentation model.

Unfortunately, there was no clear dependence between our wake types and the parameters obtained from the fragmentation model. So we then looked at the dependence of the velocity and beginning height of meteors in Figure 6.8. In this case, the initial velocity was estimated by the fragmentation model and instead of the beginning height we used the height when the erosion started – the erosion start height. The difference between the beginning height and the moment the erosion starts (according to fragmentation model) was negligible for most of the time, since we observed most of the meteors just after the fragmentation started. But sometimes the difference was up to several kilometres of height (in cases when we observed the meteor prior the start of the fragmentation). We also used the end height of the fragmentation in Figure 6.8.

We can see that there are only two meteors with velocity above 50 km . s^{-1} classified with short or faint wake. Meteors with wakes (both short and long) tend to have lower velocities and thus lower starts of the erosion and also lower ends of their erosion. Meteors with wakes tend to end their erosion at lower heights for given velocity. This is visible on the second graph of Figure 6.8. There is a clear cut–off for the length of erosion (see Figure 6.9). There are only two meteors with lengths of erosion shorter than 10 km and with wakes at the same time. These meteors are the two Draconid meteors. Draconids are known to be composed from one of the most fragile materials among meteoroids. Other meteors with short length of erosion have no wakes and we think that in these cases the wake have not time to form. Probably only very fragile meteoroids can form the wake despite the short length of the fragmentation. Another explanation can be that for very short meteors this might be an observer effect – very short meteors are

visible only on few frames and thus it is very hard to see any wake.

It is believed that wakes are formed by fragmented grains from the meteoroid body. Smaller grains are decelerated more than grains of larger sizes. The larger the difference between largest and smallest grains, the longer the wake should be. Our model gives us sizes and numbers of grains for all size bins of these fragmented grains. Thanks to this, we can look at sizes of largest and smallest grains and see if longer wakes are caused by drag difference for different sizes of grains. As seen in Figure 6.10, we did not clearly observe such phenomenon. This figure shows the ratio of largest to smallest grain size as a function of the number of all grains for given meteoroid. Different colours of symbols represent different type of wake appearance. According to the model most of the meteoroids had between 1×10^3 and 1×10^7 grains. For meteors with less than 1×10^3 grains, the less grains they had, the smaller ratio of largest and smallest grains they tend to have. The only exception is one meteoroid with bright wake. In this case the ratio between largest and smallest grains was ≈ 10 and still the fragmentation model estimated only $\approx 1 \times 10^3$ grains for this meteoroid. We could not observe any dependence of wake appereance on the ratio between largest and smallest grains. Meteors with no wake or with wakes are present rather equally in this range of size difference.

Same fragmentation model, as we used for our data, was used in the study of Campbell-Brown et al. [2013]. They studied meteor wakes recorded by narrow–field cameras. The model failed to fit the observed brightness profiles of meteors. For most cases the modelled wakes were longer than the observed ones. Thanks to this result we are not able to confirm or disprove if larger size differences of grains can cause longer meteor wakes. The work of Stokan and Campbell-Brown [2015] also focused on the formation of meteor wakes. Their newly developed particle-based model for faint meteor ablation was able to reproduce the widths of nine selected meteors. They assumed that light is emitted from collisions between atmospheric and evaporated meteoric particles. They were not able to satisfactorily simulate the length of wakes. One of their approach used the assumption that the probability that the collisions will produce light is proportional to the collision energy. Using this assumption they received better result compared to the simple assumption that all collisions above a certain energy threshold produce light with equal efficiency. Many of their simulated wakes resulting from their single–body model were shorter than observations. They suggested that fragmentation makes a significant contribution to the wake length.

We did not prove the dependence of the wake length on the size range of fragmented grains for millimetre sized meteoroids. The low resolution of our recordings did not allowe us to study the meteor morphology in detail. Other fragmentation models have problems with simulation of the wake formation. Future work will be needed.

6.2.3 Meteors with "fade out" ending

Most of the meteors ended as more or less point like objects. Only few meteors showed endings with elongated ends and with similar brightness along the whole strike. This is typical for Draconids [Borovička et al., 2007], as they are among the most fragile meteoroids we know. We observed this phenomenon for three

sporadic meteors and for five (out of six) Draconid meteors (for the seventh Draconid meteor in our work, DRA05, we did not have the original video, we were able to get only processed data). The only Draconid meteor without the elongated ending was the meteor DRA06.

We compared parameters of these three meteors obtained from the fragmentation model with the parameters of all Draconid meteors that were included in our work. Some of these parameters are listed in Table 6.2. We can notice that parameters of the three sporadic meteors (06730083, 08728076, 08728233) are quite similar. They have similar low velocities, initial masses, ablation coefficients, lower and upper mass limits, beginning and end heights of erosion, sizes of grains and total number of grains and also the energy needed for the start of erosion E_s. On the other hand, both the bulk density and the erosion coefficient were different. We get high densities for meteors 06730083 (1700 kg . m^{-3}) and 08728233 (1100 kg . m^{-3}). The bulk density of 450 kg . m^{-3} for meteoroid 08728233 is lower and more similar to Draconid meteoroids densities. But as mentioned before, we have to be aware of the uncertainty for bulk density (at least by a factor of two), in cases when we do not observe the meteor before the fragmentation starts. We are aware that the different sets of bulk densities and erosion coefficients can lead to same fits in the fragmentation model. Unfortunately we did not observe the three sporadic meteors before the fragmentation started. The parameters of the three sporadic meteors were similar to Draconid meteoroids, even though the parameters of individual Draconid meteoroids varied a little bit.

It is clear that these objects are very similar to Draconid meteoroids, for which this behaviour is typical. These meteors had low velocities, their grain size range is the order from 1×10^{-2} mm to 1×10^{-1} mm, meteoroids have quite a lot of grains compared to other bodies in our work (1×10^{5} – 1×10^{7}). Their masses were among the higher ones in our work. The energy necessary to start the erosion was average (of the order of 1×10^{6} J . m^{-2}).

10406060

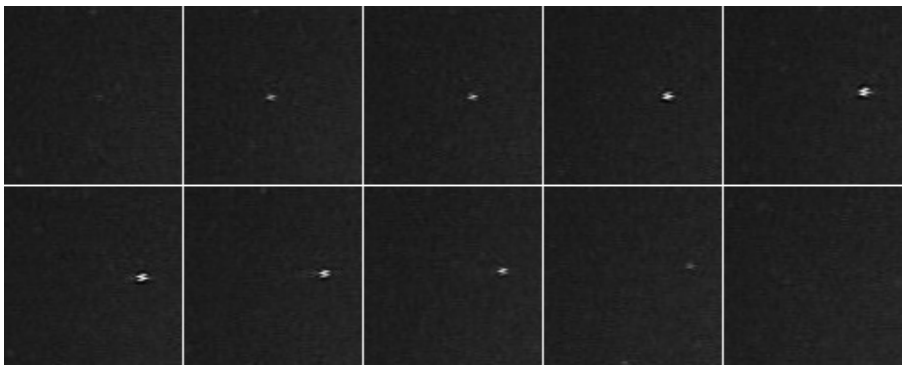

06B18075

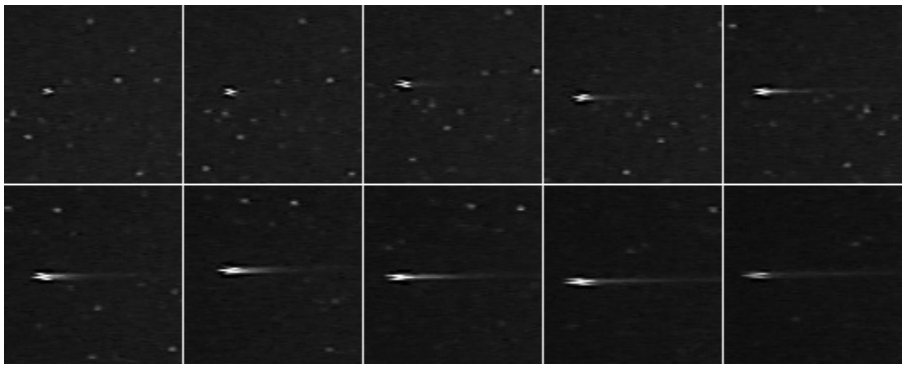

06A20013

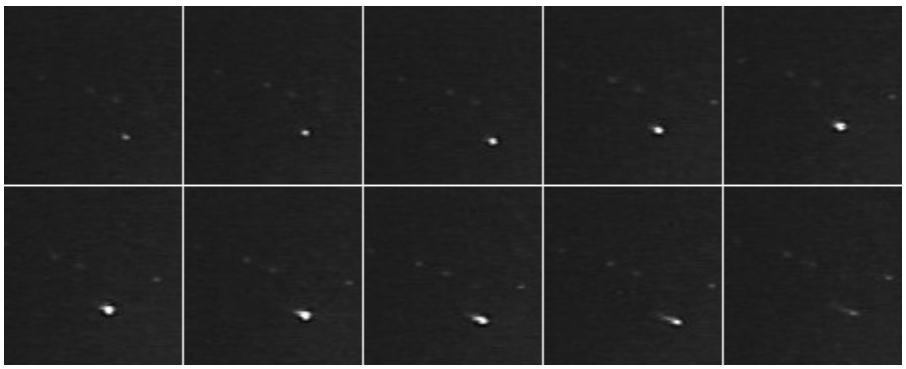

Figure 6.2: Examples of different meteor features. The 10406060 meteor contains no or very faint train and wake. Meteor 06B18075 show wake almost on entire path. Meteor 06A20013 shows wake only at the end of its path.

14814147

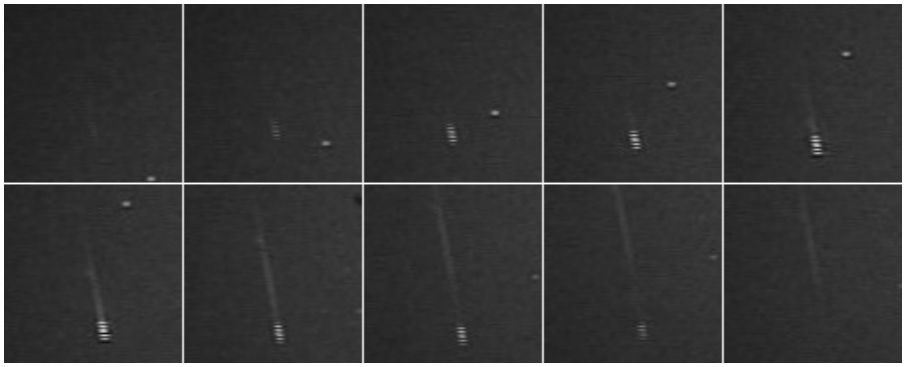

08728076

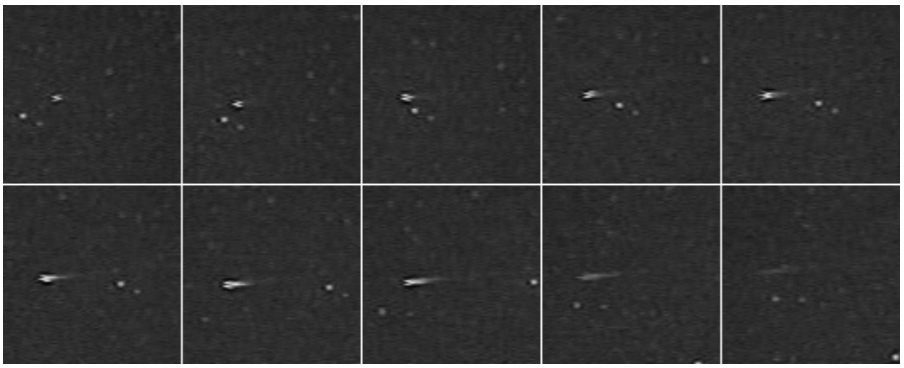

Figure 6.3: Examples of different meteor features. The train of meteor 14814147 developed during the first half of the path and at the end separates from the head and persists after the meteor disappears. The meteor 08728076 ends as blurred object with head and wake of similar brightness.

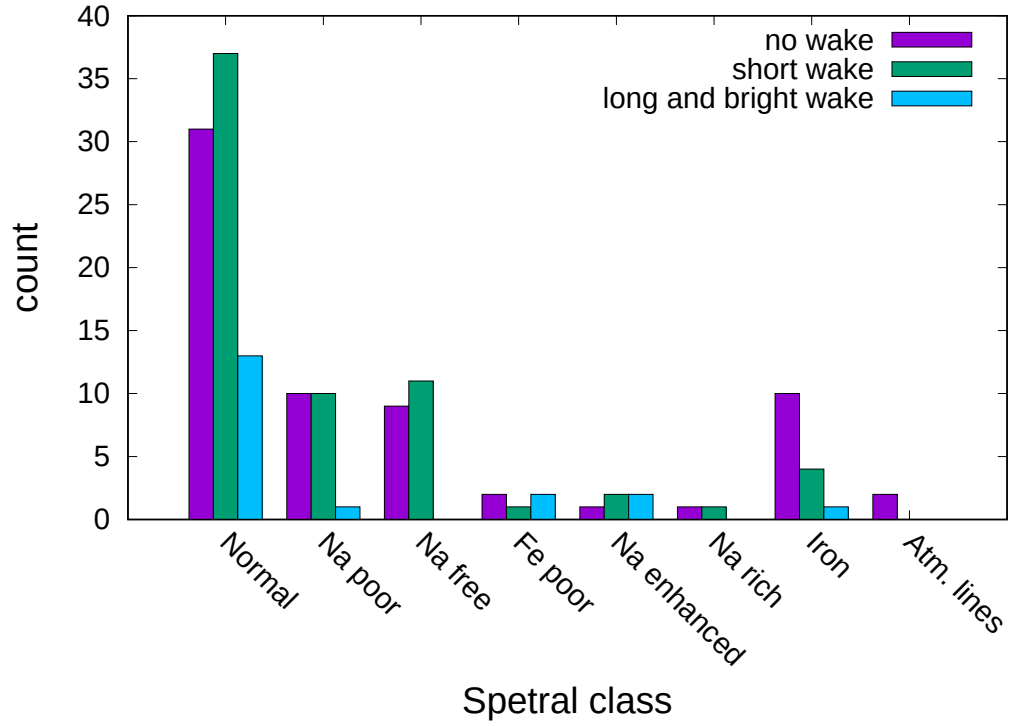

Figure 6.4: The amount of three different wake types for different spectral classes.

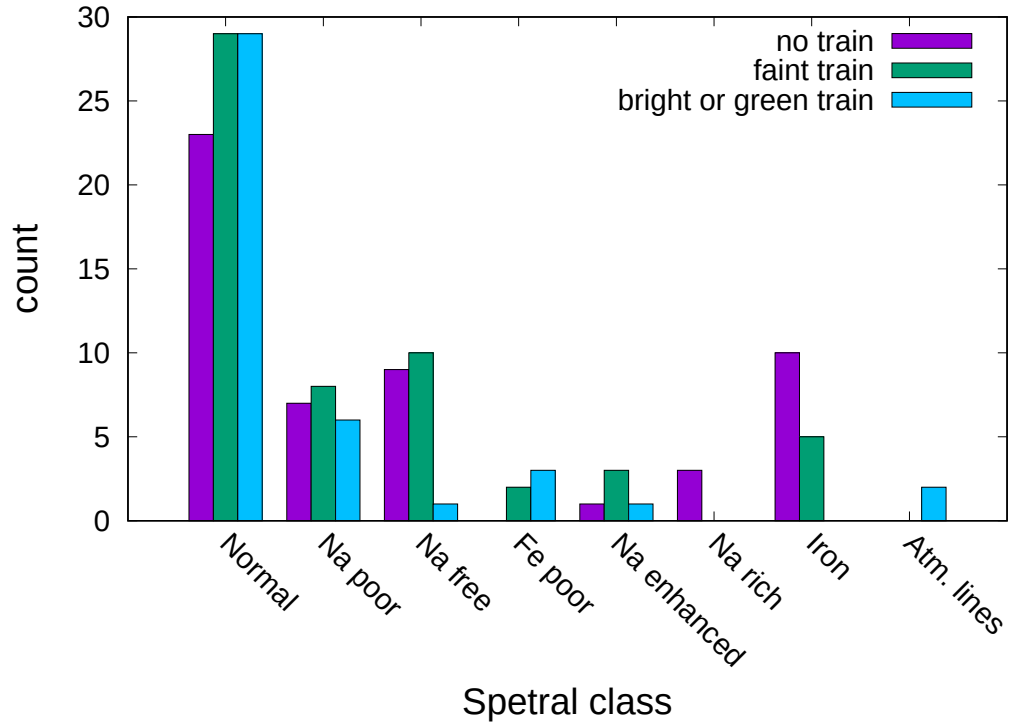

Figure 6.5: The amount of three different train types for different spectral classes.

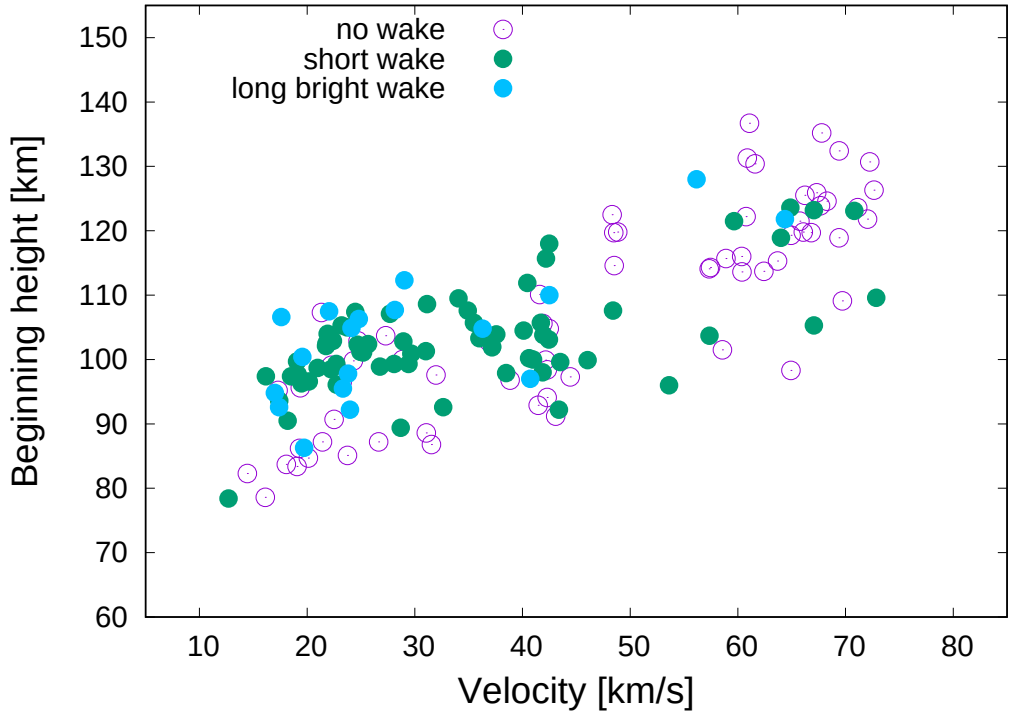

Figure 6.6: Beginning height as a function of velocity. Different colours of symbols represent different type of wake appearance.

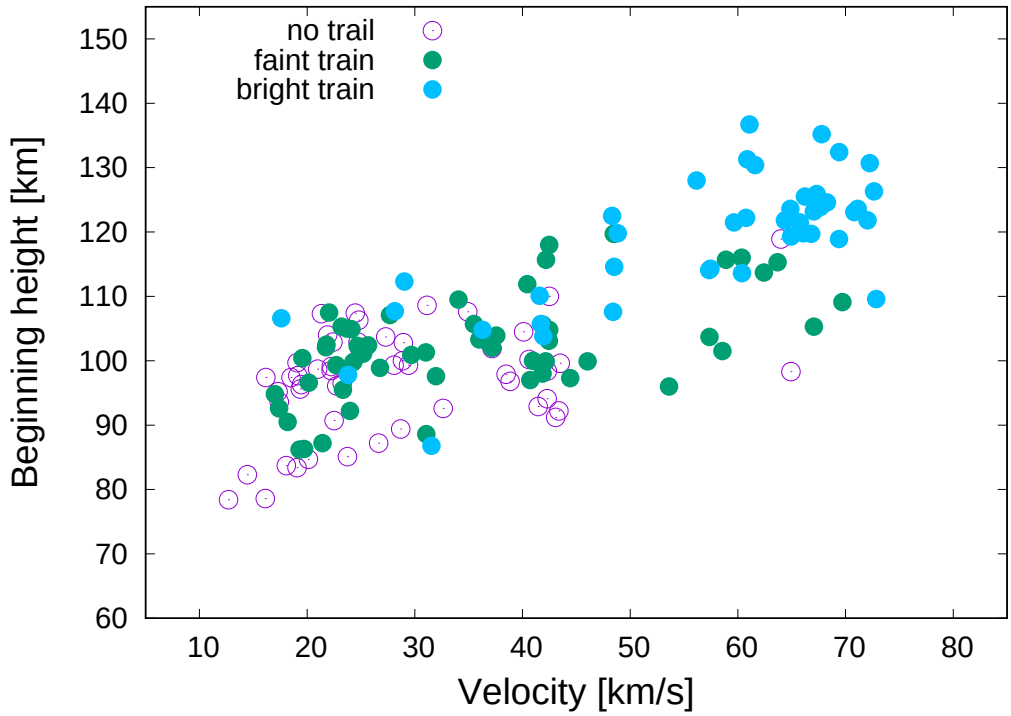

Figure 6.7: Beginning height as a function of velocity. Different colours of symbols represent different type of train appearance.

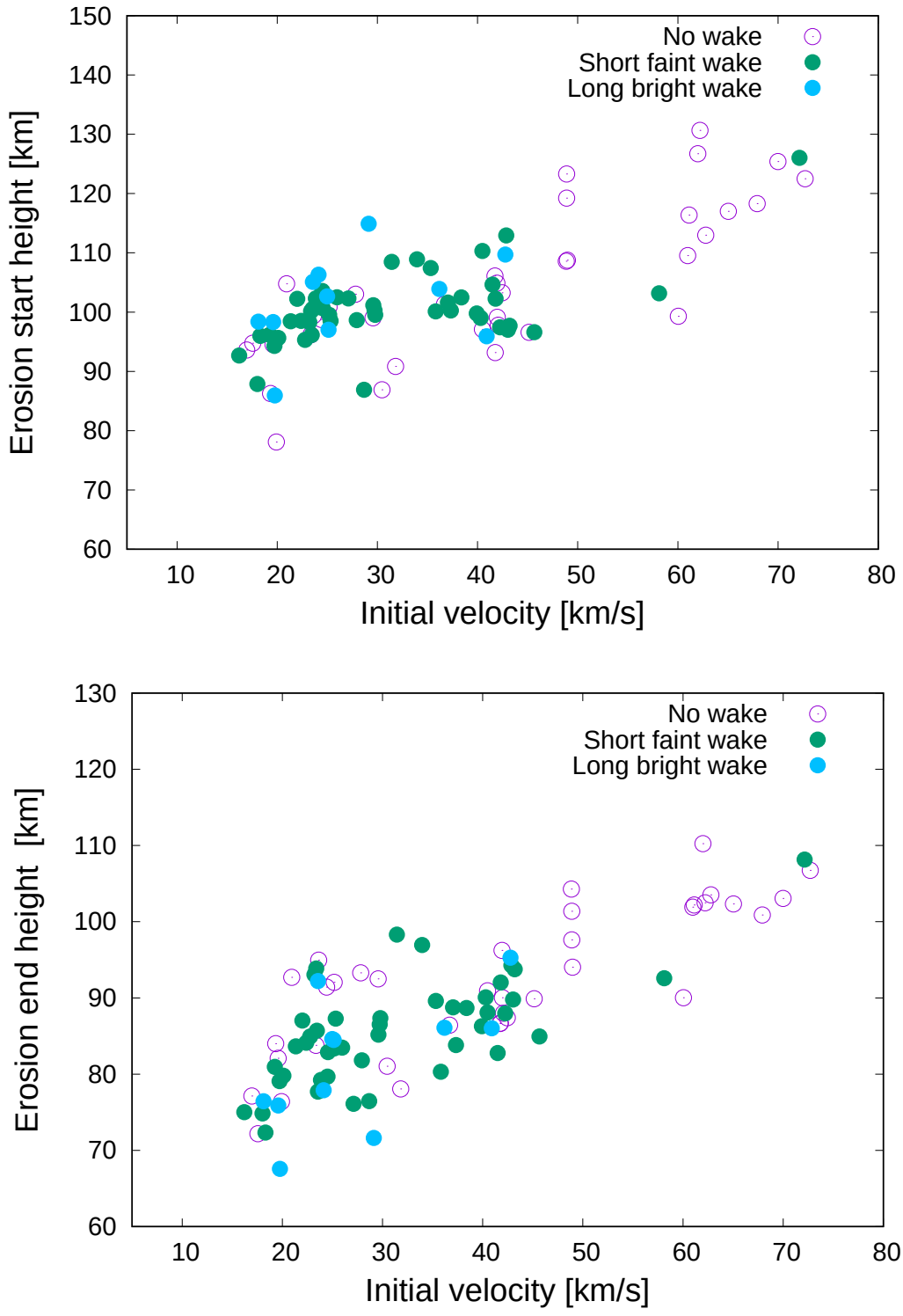

Figure 6.8: Erosion start height as a function of velocity in upper figure. Erosion end height as function of velocity in upper figure.

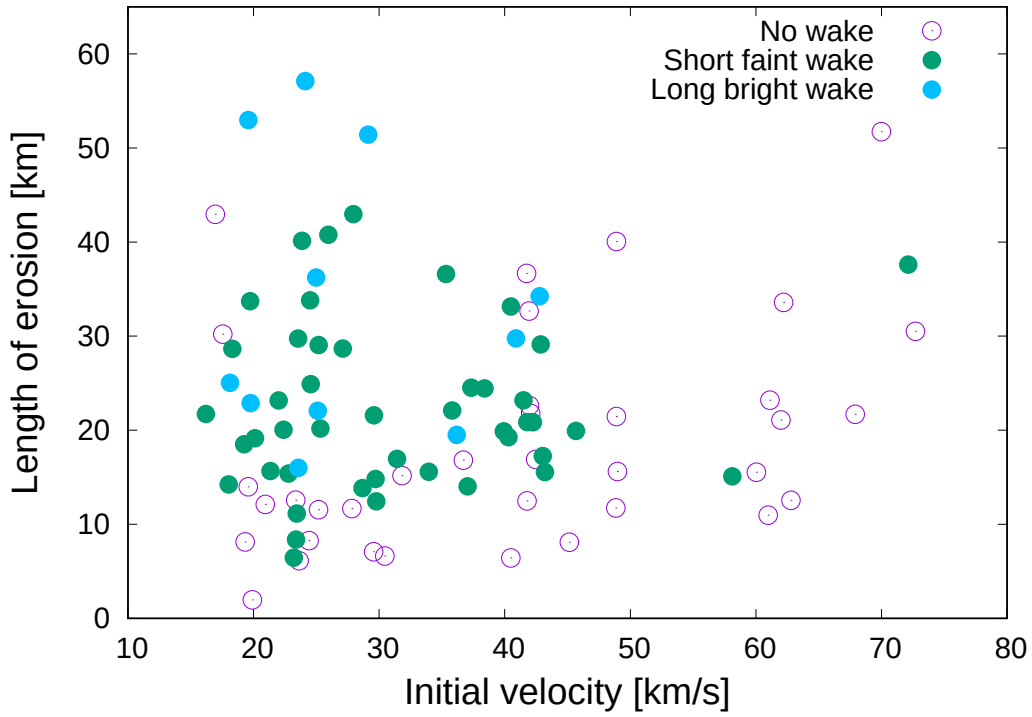

Figure 6.9: Erosion length as a function of velocity. Different colours of symbols represent different type of wake appearance.

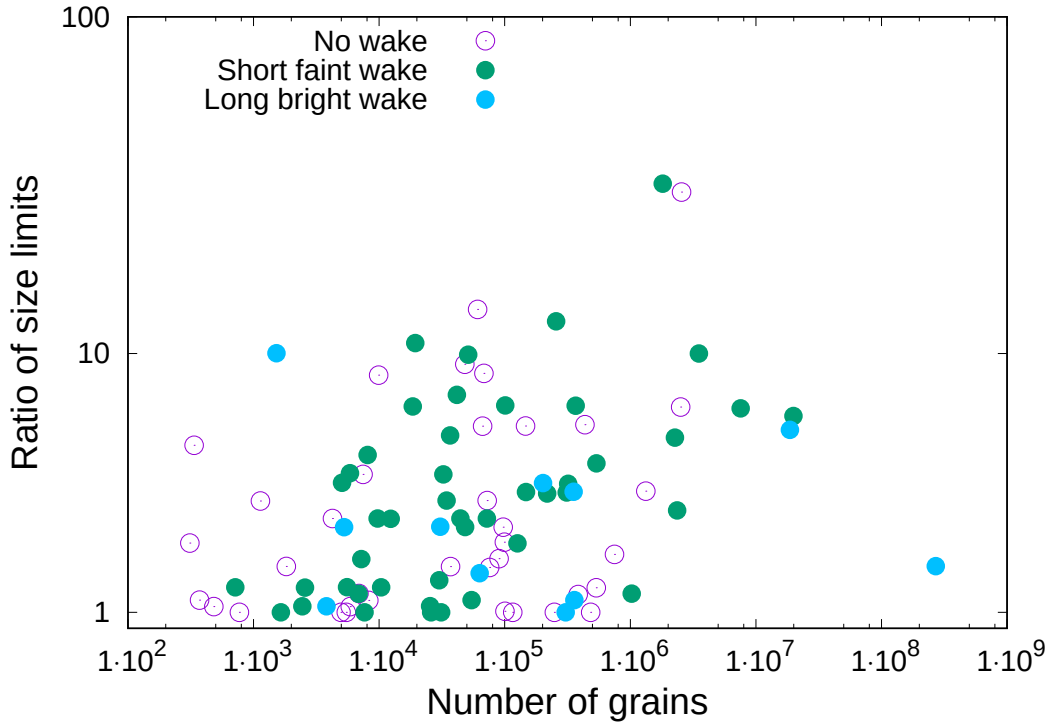

Figure 6.10: The ratio of largest to smallest grain size as a function of the number of all grains for given meteoroids. Different colours of symbols represent different type of wake appearance.

Table 6.2: Ffragmentation model parameters for meteors with elongated ending. Compared to results of Draconid meteors. GUML is Grain upper mass limit, GLML is Grain lower mass limit. E_s is the energy needed for the start of erosion. δ is the bulk density of meteoroid. σ is the ablation coefficient, η is the erosion coefficient.

meteor	spectrum	init. mass	init. velocity	δ	σ	η	GUML	GLML
		g	km . s^{-1}	kg . m^{-3}	s^2 . km^{-2}	s^2 . km^{-2}	g	g
06730083	SX116	1.87×10^{-3}	25.12	1700	0.019	0.86	7.94×10^{-8}	2.51×10^{-9}
08728076	SX708	5.05×10^{-4}	25.18	1100	0.012	0.31	3.98×10^{-8}	1.00×10^{-9}
08728233	SX726	9.52×10^{-4}	24.98	450	0.012	0.24	5.01×10^{-8}	1.09×10^{-9}
Draconids								
DRA01	SXDRA01	1.54×10^{-4}	23.44	440	0.022	0.30	2.14×10^{-9}	2.04×10^{-9}
DRA03	SXDRA03	4.26×10^{-4}	23.20	99	0.027	0.63	7.70×10^{-9}	7.70×10^{-9}
DRA04	SXDRA04	3.73×10^{-3}	23.57	375	0.015	2.31	5.01×10^{-9}	3.89×10^{-11}
DRA05	SXDRA05	3.56×10^{-4}	23.48	370	0.032	0.73	1.38×10^{-8}	1.00×10^{-10}
DRA06	SXDRA06	2.68×10^{-3}	23.55	390	0.015	0.15	3.63×10^{-9}	2.24×10^{-11}
DRA07	SXDRA07	2.98×10^{-4}	23.38	161	0.014	0.96	1.56×10^{-9}	5.02×10^{-12}
DRA08	SXDRA08	1.02×10^{-4}	23.63	180	0.019	0.98	1.60×10^{-9}	7.96×10^{-12}

meteor	spectrum	erosion start	erosion end	grain sizes	number of grains	E_s	spec. class	orbital class
		km	km	mm		J . m^{-2}		
06730083	SX116	97.0	84.5	0.37–0.11	3.5×10^5	2.3×10^6	Normal	A–C
08728076	SX708	99.5	83.4	0.30–0.09	1.5×10^5	1.5×10^6	Normal	Ecl/J–F
08728233	SX726	102.7	84.6	0.32–0.09	2.0×10^5	1.1×10^6	Normal	J–F
Draconids								
DRA01	SXDRA01	96.1	85.7	0.11–0.10	5.5×10^4	1.9×10^6	Normal	J–F
DRA03	SXDRA03	98.3	93.1	0.17–0.16	2.5×10^4	1.5×10^6	Normal	J–F
DRA04	SXDRA04	105.1	92.2	0.15–0.03	1.9×10^7	5.2×10^5	Normal	J–F
DRA05	SXDRA05	102.0	90.6	0.06–0.05	5.3×10^5	8.7×10^5	Normal	J–F
DRA06	SXDRA06	100.6	77.7	0.13–0.02	2.0×10^7	1.1×10^6	Normal	J–F
DRA07	SXDRA07	100.2	93.9	0.10–0.02	7.6×10^6	1.2×10^6	Normal	J–F
DRA08	SXDRA08	99.4	95.0	0.10–0.02	2.5×10^6	1.5×10^6	Normal	J–F

6.2.4 Summary of the morphology study

The work about meteor morphology presented in this chapter might be considered as the first step in the investigation of faint meteors wakes and trains. We are aware of the limitations of our method. First of all, the division of wakes and trains into three groups is very rough. The more meteors we observe, the more nuances between individual meteors we find. The classification into three groups was done manually. Because of this approach, this analysis is somewhat subjective. Measurements independent on the manual selection and classification would be needed for more detailed results. For example, we could obtain accurate brightness profiles or even the time evolution of discussed meteor features. We encountered limitations of our technique in terms of the image resolution and frame rate for wakes. Fast tracking system with longer focal length such as CAMO is more suitable for detailed study of physics of formation of meteor wakes.

Nevertheless, we obtained some interesting results. According to our study, Na–poor meteors showed mostly faint or no wakes and Na–free type meteors showed only faint or no wakes. Most of the Iron meteors had no wakes or only faint wakes. Considerable amount of meteors with bright wakes were observed only for Normal meteors. Other spectral classes had only small number of members for reliable statistics. Meteors with higher velocities ($v > 50$ km . s^{-1}) tend to have no wakes.

We also observed a few cases of meteors that were elongated at the end with similar brightness along the whole strike. Their meteoroids had similar parameters as the Draconids. Draconids are known to consist of one of the most fragile material known for meteoroids.

6.3 Parameters of the erosion model – results

The outputs of the fragmentation model will now be analysed. Individual parameters will be compared to each other. Some dependencies can be seen in Figure 6.11.

Values of the erosion and the ablation coefficients show increasing dispersion with the increasing meteoroid mass. The meteoroids with smaller masses had only low values of the ablation coefficient and the erosion coefficient. Since small meteoroids showed higher velocities, the situation is similar for dependence of the erosion and the ablation coefficients on the velocity. Fast and small meteoroids showed small dispersion. The slow and large meteoroids showed higher dispersion of both the erosion and the ablation coefficients. According to Equation 2.6 the ablation coefficient σ depends on the heat transfer coefficient Γ, the drag coefficient Λ and the energy necessary to ablate a unit of mass Q. We assumed the heat transfer coefficient Γ, the drag coefficient Λ to equal unity. So the ablation coefficient in our modelling is inversely proportional only to the energy Q. The analogous coefficient of erosion η depends on the energy necessary to erode a unit of mass. In other words, small and fast meteoroids need high energy per unit mass to ablate and erode, but large and slow meteoroids could obtain both higher or lower energy for ablation and erosion of unit mass. Thus we think that small meteoroids (mass lower than ≈ 0.1 g and size smaller than ≈ 8 mm) are

harder to ablate with grains that are strongly held together. On the other hand, larger meteoroids show wide range of inner composition: from strong material to material with grains that are held together more loosely. We can imagine, that meteoroids of centimetre size can be composed of millimetre sized material. This material is further composed of individual grains. In this millimetre sized material larger or smaller cracks are present. The larger the meteoroid, the higher probability of cracks. This might cause different overall strength of meteoroids.

The higher the meteoroid bulk density was, the lower was the start height of the erosion. Assuming same grain density of all non–iron meteoroids, this is in agreement with the assumption that for given velocity there is a dependence of meteor beginnig height on the meteoroid material strength. More massive meteoroids tend to have larger grains and thus larger the upper and lower mass limits for grains. The total number of grains and the number of grains n_0 in the bin of largest grains were independent on the initial mass of meteoroids. As for the energy necessary for the start of the erosion E_s (expressed per unit cross-section), the higher the bulk density of the meteoroid, the higher the energy E_s. For a given energy E_s the higher the velocity, the higher is the start height of erosion. This behavior can be seen for spectral classes. Class with only atmospheric lines in the spectrum, Na–free and Na–poor had generally higher velocities and thus for given energy E_s they tend to start the erosion at higher altitudes.

The height of start of modeling was increasing with increasing velocity and we observed well known dependencies between meteoroid masses, beginning heights and velocities [Koten et al., 2004]. The end height of the erosion depends on the meteoroid mass.

Since the drag coefficient Γ and the shape–density coefficients K are same for the erosion and the ablation, the comparison between the ablation coefficient σ and the erosion coefficient η can give us direct comparison between the ablation energy and the fragmentation energy (see the equations in the Chapter 2.3). The dependence of the ratio of these two coefficients (η/σ) on the Grain upper mass limit in Figure 6.12 shows us, that the energy for the ablation is higher (in the range of two orders from 3× to 300× higher). The larger the upper limit for masses of grains, the smaller the difference is. Meteoroids with smaller upper limits for grain mass tend to have higher ablation energy compared to the erosion energy. This is not surprising. In general, the ablation energy is expected to be higher than the erosion energy. Because the erosion energy is used only for the release of grains and the ablation energy is used for the complete vaporistaion of the meteoroid. The dependence of the η/σ ratio is caused mainly by the tendency of the ablation coefficient σ to be smaller (the ablation energy is higher) for meteoroids with smaller Grain upper mass limit. The erosion coefficient η is more or less independent on the Grain upper mass limit.

We can also notice that for given Grain mass upper limit, both the erosion coefficient and the ablation coefficient tend to be lower for Na–poor and Na–free meteors (compared to the Normal class). In other words, the ablation and the erosion energy is higher for given Upper grain mass limit for Na–poor and Na–free meteors. There were just a few members of other spectral classes (Na–enhanced, Na–rich) to determine any kind of dependence of erosion or ablation coefficients on the grain masses.

6.3.1 Porosity and density

As mentioned before the porosity p of meteoroids is computed from the bulk density of the meteoroid δ and from the density of grains δ_g. Both values are either estimated with high uncertainty from the fragmentation model or the values are assumed. But despite that, we received quite reasonable results.

Figure 6.13 shows dependence of the porosity on the energy necessary to start the fragmentation E_s. Upper figure shows assigned spectral classes. The lower figure shows assigned orbital classes. As a generall trend, the less porous the material was, the more energy was needed to start the fragmentation. We can notice in the upper figure that Na–free, Na–poor and the Iron meteoroids were usually less porous (compared to the Normal class) and they needed more energy to start the fragmentation. All but three Na–poor and Na–free members had their porosity lower than 0.7. The Na–poor and Na–free meteoroids with low porosity were mostly of Sun–approaching origin. The Na–poor and Na–free members with higher porosity were of cometary origin. Most members of the Normal class showed high porosity. We can clearly see a cluster of Normal meteoroids with porosity higher than 0.7 with E_s around 1 MJ .s^{-2}. As expected, the Iron members had low porosity $p < 0.5$. On the other hand, members of Na–enhanced and Na–rich were porous with $p > 0.5$. The Sun – approaching members were less porous, the cometary (both Halley and Jupiter family) members had porosities in the whole spectrum, but very porous material prevailed among them. Surprisingly, members of the Asteroidal – chondritic class showed two groups, one with very porous material and second one with significantly less porous material.

Kikwaya et al. [2011] studied densities of millimetre sized meteoroids. They obtained densities for different orbital classes. Perhaps the most significant results is surprisingly high density for meteoroids on Jupiter–family orbits. Their average density for Jupiter–family orbits was $\delta = 3190^{+490}_{-480}$ kg . m^{-3}, suggesting ordinary chondritic composition with low porosity. Their average density for meteoroids on Halley type orbits was much lower $\delta = 360^{+400}_{-100}$ kg . m^{-3}. Our results were different. One of the reason might be that we assumed the grain density to be same for all non–Iron meteors $\delta = 3000$ kg . m^{-3} and thus our highest possible density for non–Irons was still lower than the average density for meteoroids on Jupiter–family observed by Kikwaya et al. [2011]. On the other hand, their lack of low density fragile cometary material amog Jupiter–family orbits is very unusual.

In our sample we were able to use the fragmentation model to 30 meteoroids on Jupiter–family orbits. The average value for density for meteoroids on Jupiter–family orbits was $\delta = 850 \pm 110$ kg . m^{-3}, with the median $\delta_M = 695$ kg . m^{-3}. The range of values was from 99 kg . m^{-3} to 2100 kg . m^{-3}. We obtained similar average value for Halley type orbits $\delta = 960 \pm 220$ kg . m^{-3} and the median was $\delta_M = 400$ kg . m^{-3}. The higher average density for Halley type (compared to Jupiter family) is affected by presence of iron meteors on Halley orbits, otherwise it would be lower and within uncertainty of results of Kikwaya et al. [2011]. But our results for Jupiter–family orbits do not correspond even within the uncertainty. Moreover, our lower value is more in agreement with the concept of low density cometary material. But as we said, the densities derived by our modelling are questionable (uncertainty at least by factor of two) for cases when the ablation was not observed before erosion. We observed ablation before erosion only for twelve meteoroids, three of them were on Jupiter–family orbits (one sporadic, two

Draconid meteors) and we can be more sure about their density. The sporadic meteor 14505037 showed density $\delta = 800$ kg . m^{-3}, the Draconids had very low densites: DRA03 $\delta = 99$ kg . m^{-3}, DRA06 $\delta = 390$ kg . m^{-3}. These low densities are expected for Draconids and the density of 14505037 meteor is close to average density for Jupiter–family members. Thus we think that only high (chondritic) density for Jupiter–family orbits is not likely. As an example of low density material on Jupiter–family orbits can be used the Draconids. They are known to be one of the most fragile materials among meteoroids with very low densities. On the other hand, the Stardust mission found surprisingly high amount of μm sized CAI's and other high–temperature materials similar to meteoritic components in debris from Jupiter–family comet 81P/Wild. We think that higher variety of densities for millimetre sized cometary materials is common. We can expect the cometary material to be formed of very fragile components with low density and high porosity, but we can also expect stony chondritc materials with high density and low porosity.

6.3.2 Irons and the fragmentation model

Only four Iron meteoroids of the total number of 15 were modelled by the fragmentation model. Two of them were on Asteroidal–chondritic orbits (SX692–08505025, SX701–08728012), one was Sun–approaching (SX001–06406048) and one was on Halley type orbit (SZ2410–05403028). Meteors belonging to Iron class are usually faint and very short, so it is really hard to observe any deceleration. The results of the modelling for Irons are a matter of debate. Recent studies suggest that the processes of mass cannot be explained by the classical single body ablation theory or by the fragmentation models [Campbell-Brown, 2015, Čapek and Borovička, 2017]. The disintegration of the body into constituent grains is probably not the main process of the mass loss for Irons. More reliable approach to modelling of the ablation of iron meteoroids can be seen in the work of Čapek and Borovička [2017]. They suggest ablation in form of droplets released as liquid layer from the surface of the body. Also the oxidation of iron material plays key role for the ablation.

On the other hand, the grains in our model can be considered to be iron droplets in reality. The grain density for Irons were set up to be higher than for other spectral classes $\delta_g = 6000$ kg . m^{-3}. The range of bulk densities was from 5000 kg . m^{-3} to 5700 kg.m^{-3} and porosity was low, as expected, from 0.16 to 0.05. The energy necessary to start the fragmentation was among the highest for Iron meteors. But other parameters were not so uniform for the Irons. Most of them had very small number of grains in first bin (from 12 to 153), but the SX692 meteor had 2×10^5 grains in first bin. The total number of grains, from 5×10^3 for SZ2410 to 5×10^5 for SX692, was rather average. The SX692 meteor contained smallest grains with Grain upper mass limit to be only 3×10^{-7} kg (one of the lowest one). Other Iron members showed high to average values for Grain upper and Grain lower mass limits. The overall highest ablation coefficient was for the Iron meteor SX701 ($\sigma = 0.08$ s^2 . km^2). In contrast, other Iron meteors had very low value of ablation coefficient ($\sigma < 0.013$ s^2 . km^2). The erosion coefficient was among the highest for SX692 and SX701 and low for SX001 and SZ2410. Despite only four modelled meteoroids, we can clearly

see different physical parameters for Asteroidal–chondritic Iron meteors and for Irons on other orbits (Sun–approcahing and Halley). These differences suggest different evolution of these meteoroids.

6.3.3 Grains

Information about grains released during the fragmentation can give us important knowledge about inner structure of the meteoroid. The fragmentation model estimates the initial mass and number of grains in the meteoroid. Released grains can have different sizes. These sizes are grouped in size bins. The power–law mass distribution was assumed. Important parameters are the upper and lower limits for grain masses (GUML, GLML). In Figure 6.14 we can see number of grains for each mass bin for all modelled meteoroids. Different colors represent different spectral classes. The slope of the point line is determined by the mass distribution index S with values from 1.3 to 2.9, most of the meteoroids have mass distribution index S of $\approx$ 2.0. Meteoroids with only one mass bin are marked with abbreviation *OM* (One Mass). Some meteors were modelled with two stages of fragmentation. Since usually most of the mass was released in first fragmentation stage, we show results from this stage. These meteoroids are marked with abbreviation *FE* (First Erosion).

Values were computed assuming the density 3000 kg . m^{-3}. Only for the Iron meteoroids the grain density of 6000 kg . m^{-3} was assumed. Grain masses were approximately from 1×10^{-10} g to 3×10^{-2} g. Numbers of grains in bins were approximately from 1 to 1×10^{7}. Total number of grains released during the fragmentation for individual meteoroid was approximately from 1×10^{2} up to 1×10^{8}. As we can see, there were noticeable differences between individual meteoroids. These differences (of several orders) show us very high diversity in composition of millimeter sized bodies and very high diversity for individual grains of which millimeter sized meteoroids consist of. We observed some differences for individual spectral classes. The normal spectral group showed high diversity of grain masses and grain numbers and also the mass distribution index S. The Na–free group members tend to contain less and more massive grains. The Na–poor members were somehow transition between Normal and Na–free classes in terms of grain masses and grain numbers. It was also kind of surprising that members of Na–enhanced class also contained rather large grains. Only the number of grains was higher compared to the Na–free class.

The COSIMA instrument on the ROSETTA spacecraft collected a number of cometary particles when orbiting the 67/P Churyumov–Gerasimenko comet. Hornung et al. [2016] analysed these particles. They measured sizes of captured grains. The particle sizes were from 15 μm up to $\approx$ 300 μm and total number of particles was 7524. The histogram of grain sizes was fitted by power law function with index -3.3. Since the 67/P Churyumov–Gerasimenko comet is a member of Jupiter–family comets we tried to compare results of the COSIMA instrument with our sample of meteoroids on Jupiter–family orbits. The grain sizes derived from the modelling were from 5 μm (mass 1×10^{-10} g) up to $\approx$ 2.5 mm (mass 3×10^{-2} g), Assuming density 3000 kg . m^{-3} and sphere shape grains. The total number of grains for all meteoroids summed together was 1.6×10^{10}. The larger range of grain sizes was probably given by larger sample of our meteoroids. The

distribution of grain sizes up to $\approx 300\mu$m was similar. The power law fit of our data was with index -3.4 and it was in a good agreement with the power law function of grain sizes from the 67/P Churyumov–Gerasimenko comet. The histogram of grain sizes up to 450μm is given in Figure 6.15. The power law fit is showed as well as the power law fit with index taken from Hornung et al. [2016].

6.4 Meteoroids without deceleration

The fragmentation model was succesffully applied to 94 of the total number of 152 meteors. The remaining 38% of all meteors could not be modelled. This is not negligible amount and thus we wanted to investigate the difference between meteoroids that we were able to model and meteoroids we could not model. Are there any actual differences in their composition? Are meteoroids, that were not modelled, single bodies? Can all of this this cause any kind of observation effect and thus affect our results?

We actually tried to model all selected meteoroids. However, the model failed to work for cases when there was no or very little deceleration. The model also failed if the meteor was too short and thus there were only few points for the fit.

The not–modelled meteors were divided into a few groups. One group were meteors that were too short for accurate fit. The boundary between short and long enough was selected to be 15 km in length. The second group were meteors without (or with very small) deceleration. The third group were meteors that showed deceleration, but we were still not able to find the right combination of parameters to fit their deceleration curve and their lightcurve. The last group were meteoroids with low precission. The data were good enough for the trajectory determination, but they were not sufficient for the fragmentation model. This group contained both meteors with or without deceleration.

6.4.1 Short meteors

In cases of very short meters the results, that are given by the model, can be very inaccurate. The uncertainty of free parameters of the model can be very high. Different combination of free parameters of the fitting curves can give us very similar residuals of the fit and thus we are not able to decide which of the combination of free parameters are more correct. The reason can be that the short meteors show usually very low or no deceleration and moreover small number of points of the measueremnts causes inaccuarcy of the fit.There were meteors shorter than 15 km and still we were able to apply the model. But not modelled cases prevail for short meteors according to the Figure 6.16. There are only 3 modelled meteors shortet than 15 km, the rest 15 meteors shorter than 15 km were not modelled. Nine of the short meteors were of Iron class. Of the total number of 15 Irons, only 4 of them were modelled. Irons are naturally short and faint and thus it is really hard to apply the fragmentation model.

6.4.2 Long meteors

There were meteors with all possible lengths among the not modelled cases. The main reason, why some meteors were not modelled, was the lack of the deceleration. If the meteor did not show deceleration or showed only small deceleration, the fragmentation model could not be successfully applied. The model often gave us very inaccurate results, if any. Again, different combination of free parameters of the fitting curves could give us similar minimal residuals of the fit.

On the other hand, 10 meteoroids showed sufficient deceleration. The measurements were precise, but we were not able to successfully fit both the deceleration curve and the light. We could not find proper combination of meteoroid parameters applied by the fragmentation model to fit these curves.

Meteoroids with inaccurate measurements that not allowed modelling were omitted from further analysis.

Beside the length of the meteor, the Figure 6.16 shows the F parameter as well. The F parameter is determined as the position of the maximum brightness on the lightcurve of the meteor. The F parameter takes values in the interval from 0 to 1. The lower the number is, the earlier was the maximum on the lightcurve. If the value is 0.5, the maximum was in the middle of the lightcurve. The classical theory of the single body ablation predicts that the value of the F parameter should be ≈ 0.7 [Hawkes and Jones, 1975]. On the other hand, the dustball theory predicts that meteors can have different values of the F parameter. So the F parameter can help answer the question: was the reason that meteoroids that cannot be modelled due to the fact they were single bodies? If most of the not modelled meteoroids showed F values around the 0.7, we could have at least suspicion that they can be single bodies and thus the fragmentation model did not work. As seen in the Figure 6.16, regardless if the meteors were modelled or not, they have all kinds of values of the F parameter. All three groups of not modelled meteors (short, with deceleration, without deceleration) showed different values of F parameter. The group, that was not modelled, because there was no deceleration, can be suspected to be single body. But as we can see, members of this group had the F parameter from 0.4 to 0.9, contrary to the single body theory prediction. So the reason that the meteoroid could not be modelled was not the difference in terms of composition between modelled and not modelled cases. Both groups showed lightcurve shapes according to the prediction of the dustball theory.

As it can be seen in Figure 6.17, the not modelled meteoroids span the full range of beginning heights, velocities and magnitudes (in maximum). Even the division of long meteors between those with and those without deceleration cannot reveal between these two groups. They both span the full range of beginning heights, velocities and magnitudes. As expected, short meteors start at lower heights and have lower velocities. The bottom graph in Figure 6.17 marked different spectral classes for long (> 15 km in length) and not modelled meteoroids. Most of them were of Normal class (16 cases, i. e. 20% of all Normal meteors). In this group there were 7 Na–poor meteors (30% of all Na–poor meteors). Other classes contained only small number of meteors (3 Na free, 2 Irons, 1 Na–enhanced and 1 Fe–poor). There were no members of Na–rich class in this selection and no meteors with only atmospheric lines in their spectrum. But each of these two spectral classes contained only two members overall.

This analysis did not found any apparent differences in properties for meteoroids that were modelled using the fragmentation model and meteoroids that were not modelled. The reason, why some meteors with deceleration were not modelled, was probably just coincidence.

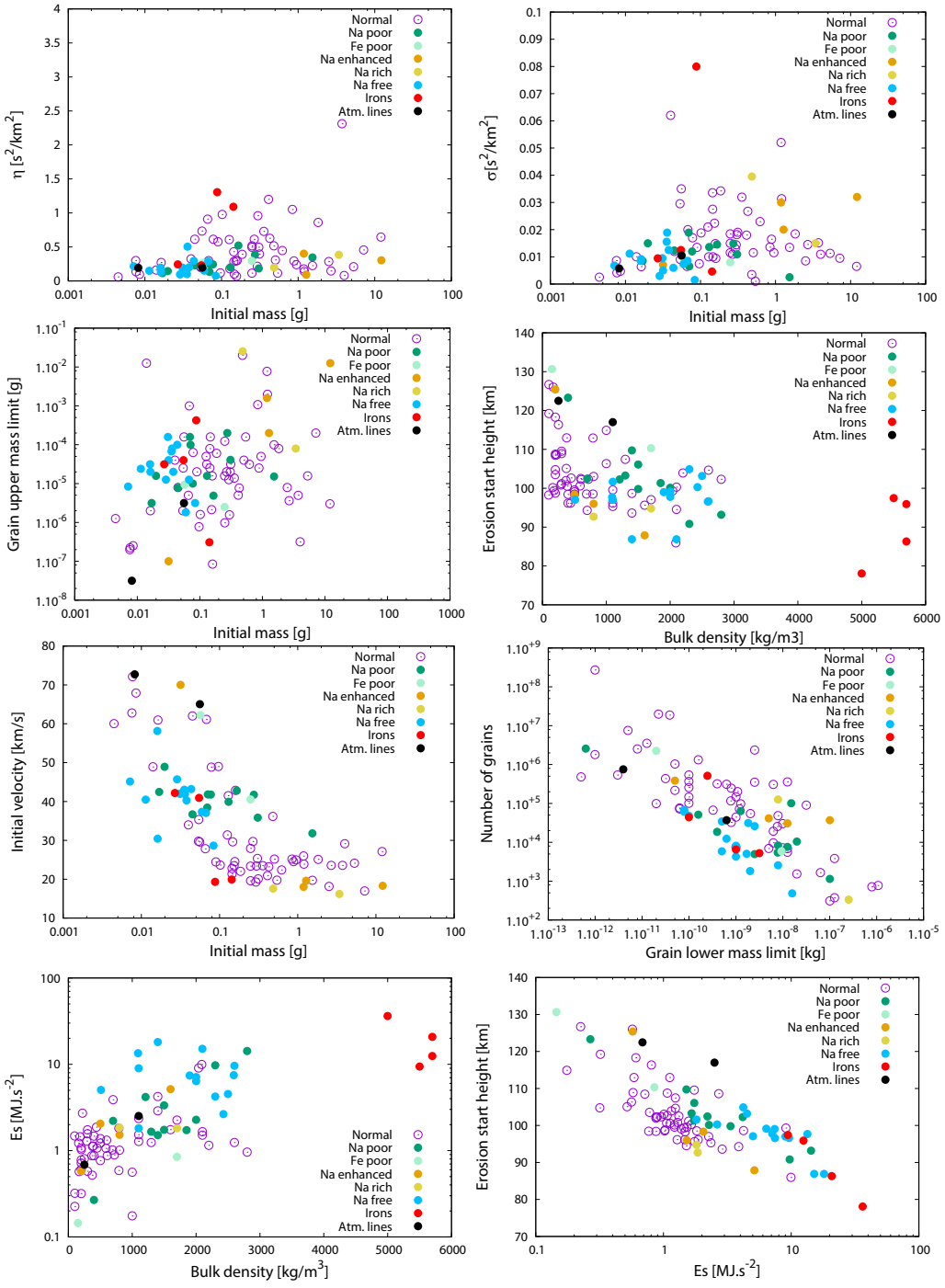

Figure 6.11: Parameters of meteoroids as results of the fragmentation model. η is the erosion coeffcient, σ is the ablation coeffcient. E_s is the energy necessary for the start of the erosion.

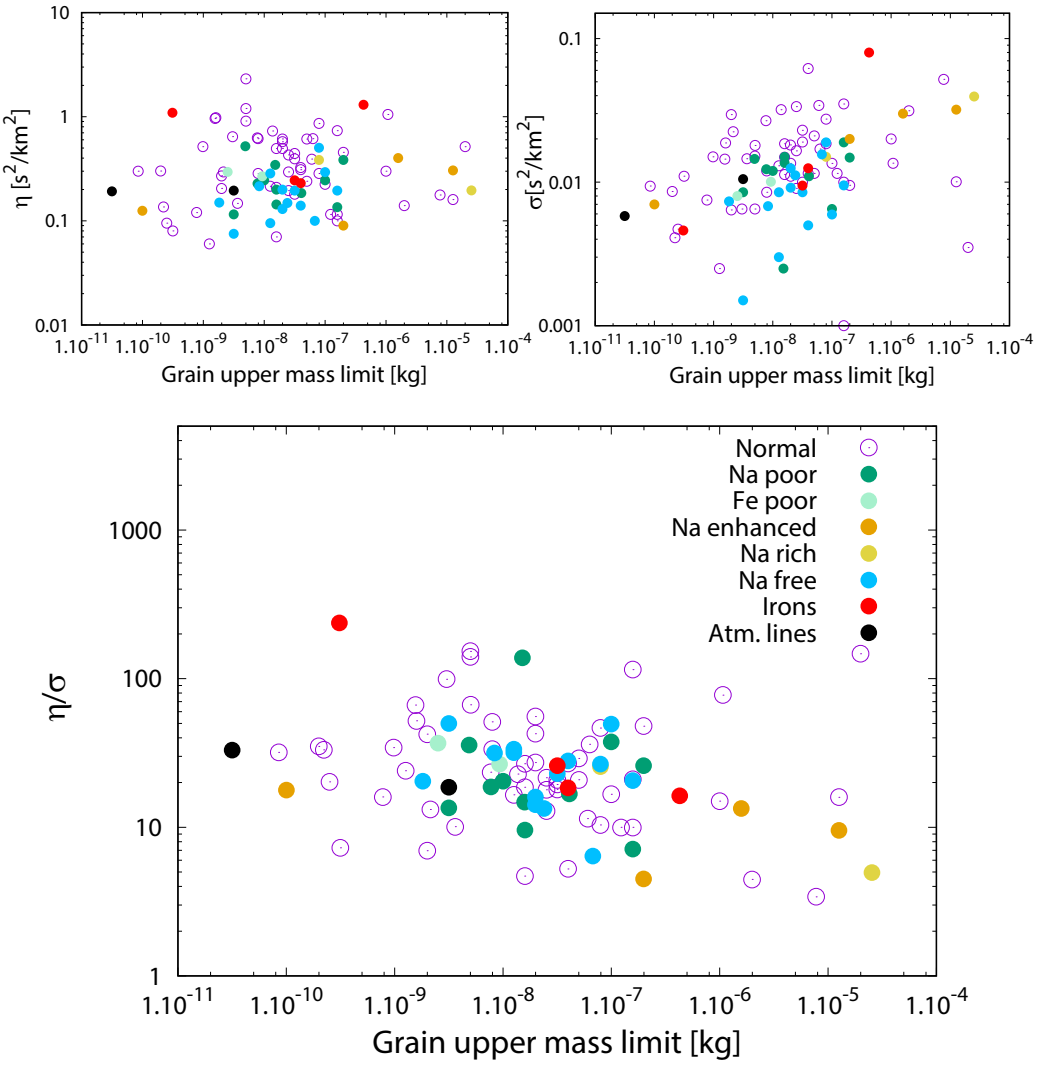

Figure 6.12: Top left: The erosion coefficient as function of the Grain upper mass limit. Top right: The ablation coefficient as function of the Grain upper mass limit. Bottom: The ratio of the ablation coefficient σ to the erosion coefficient η as function of upper mass limit for grains.

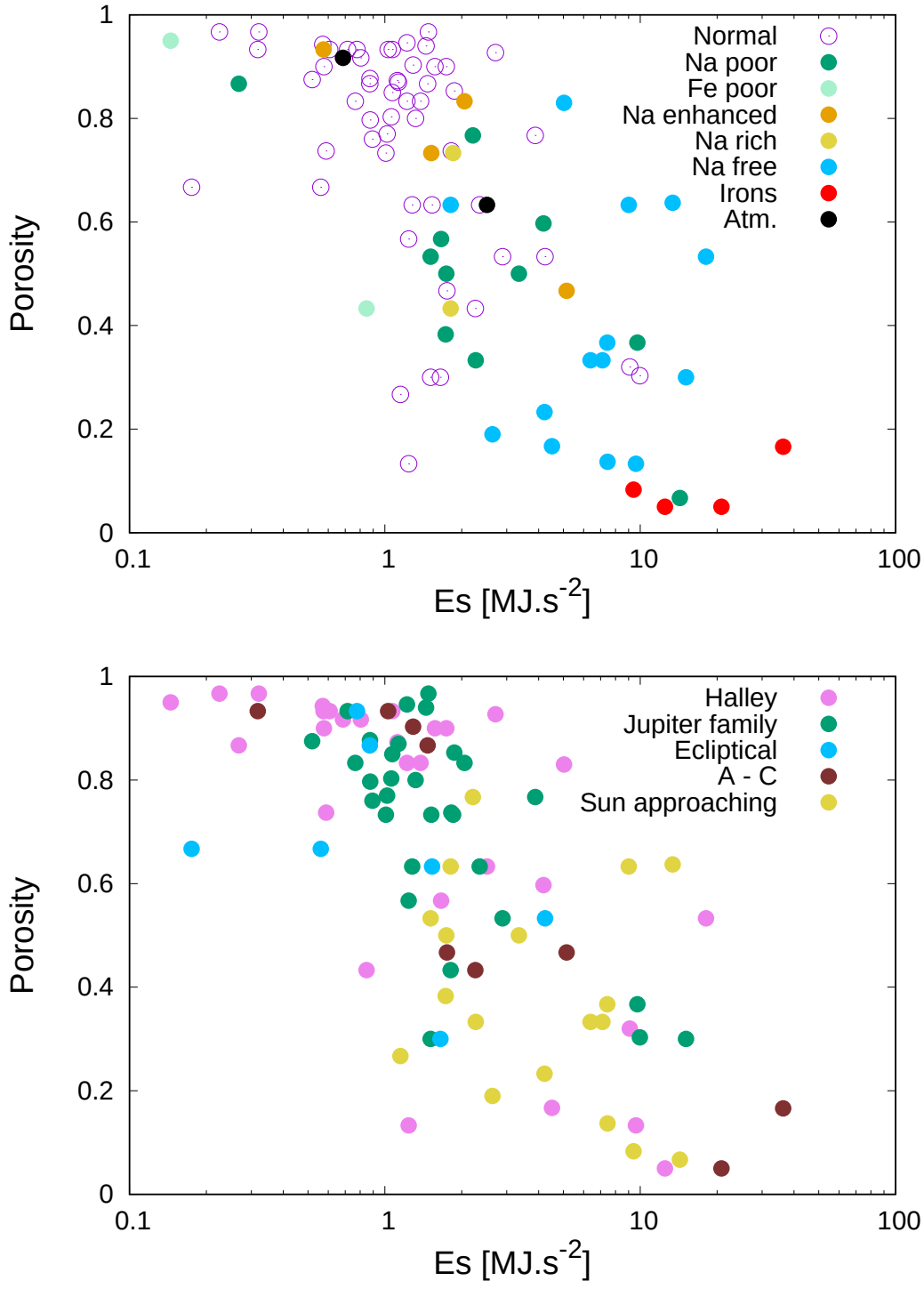

Figure 6.13: The porosity p as a function of the energy necessary to start the fragmentation. First figure: different spectral classes are marked with different colors. Second figure: different orbital classes are marked with different colors. A – C stands for the Asteroidal – chondritic class.

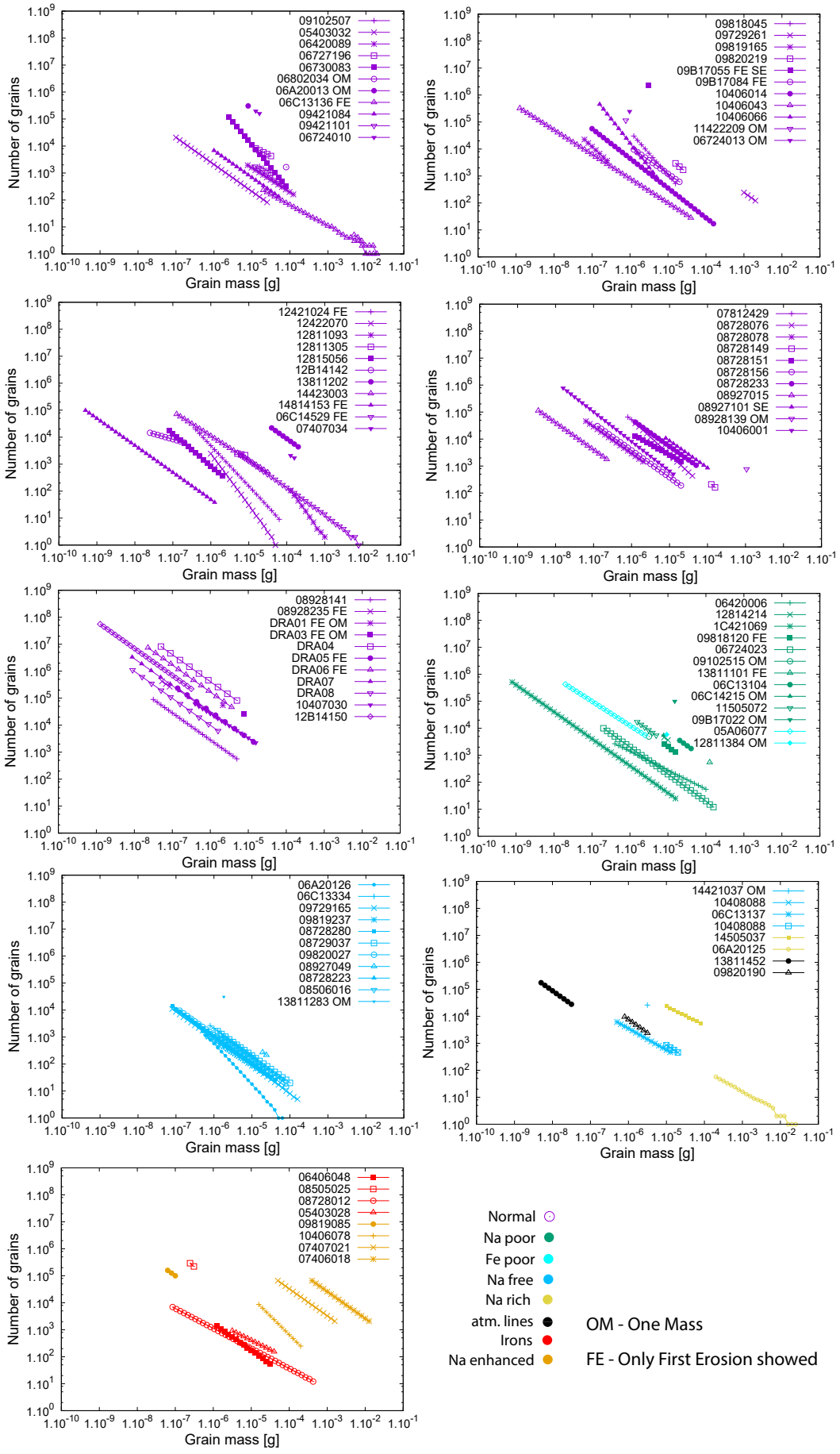

Figure 6.14: Grain masses and number of grains in each mass bin for each meteor.

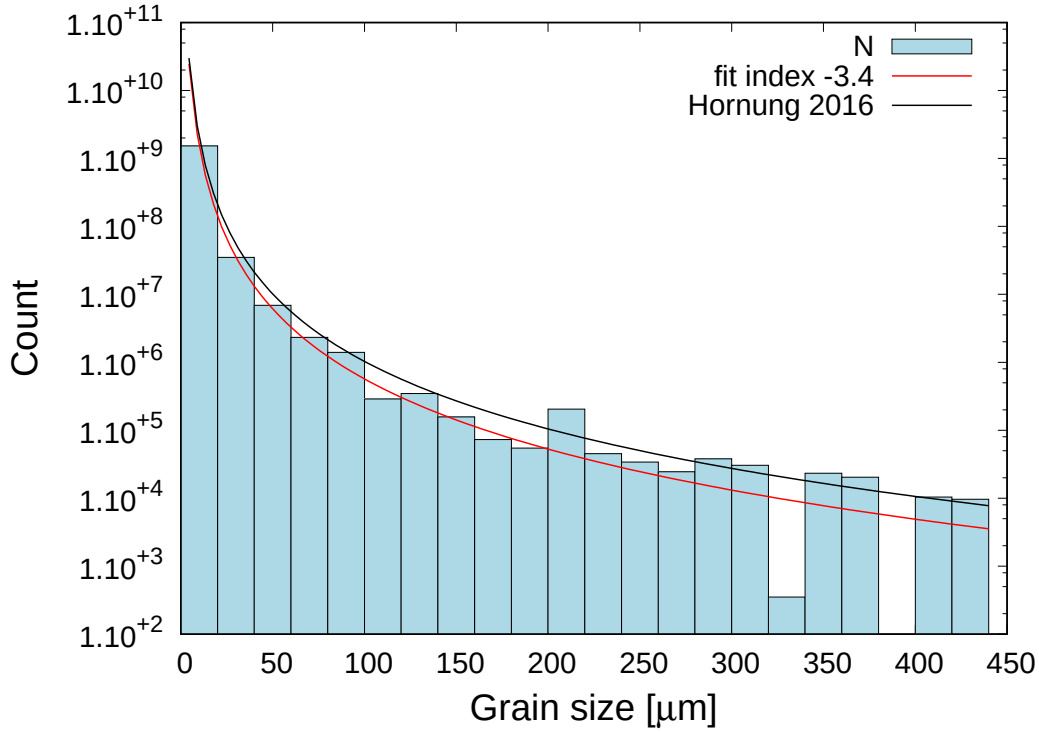

Figure 6.15: Histogram of grain sizes of Jupiter–family meteoroids up to 450 μm. The power law fit with index -3.4 is showed. The power law fit of grain sizes captured by ROSETTA with index -3.3 taken from Hornung et al. [2016] is also showed.

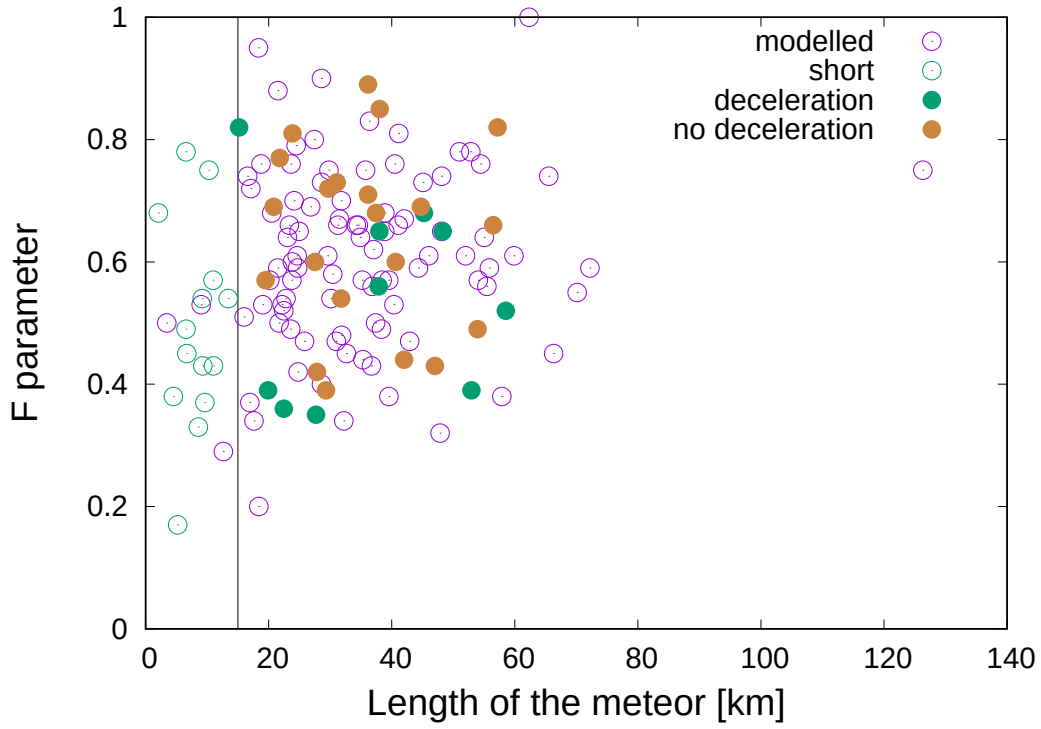

Figure 6.16: The length of meteor as a function of the F parameter. Meteors that were modelled using the fragmentation model and meteors that were not modelled are marked by different colours. The vertical line indicates the 15 km in length of the meteor. Of the not modelled meteors, only those that were measured with good accuracy were used.

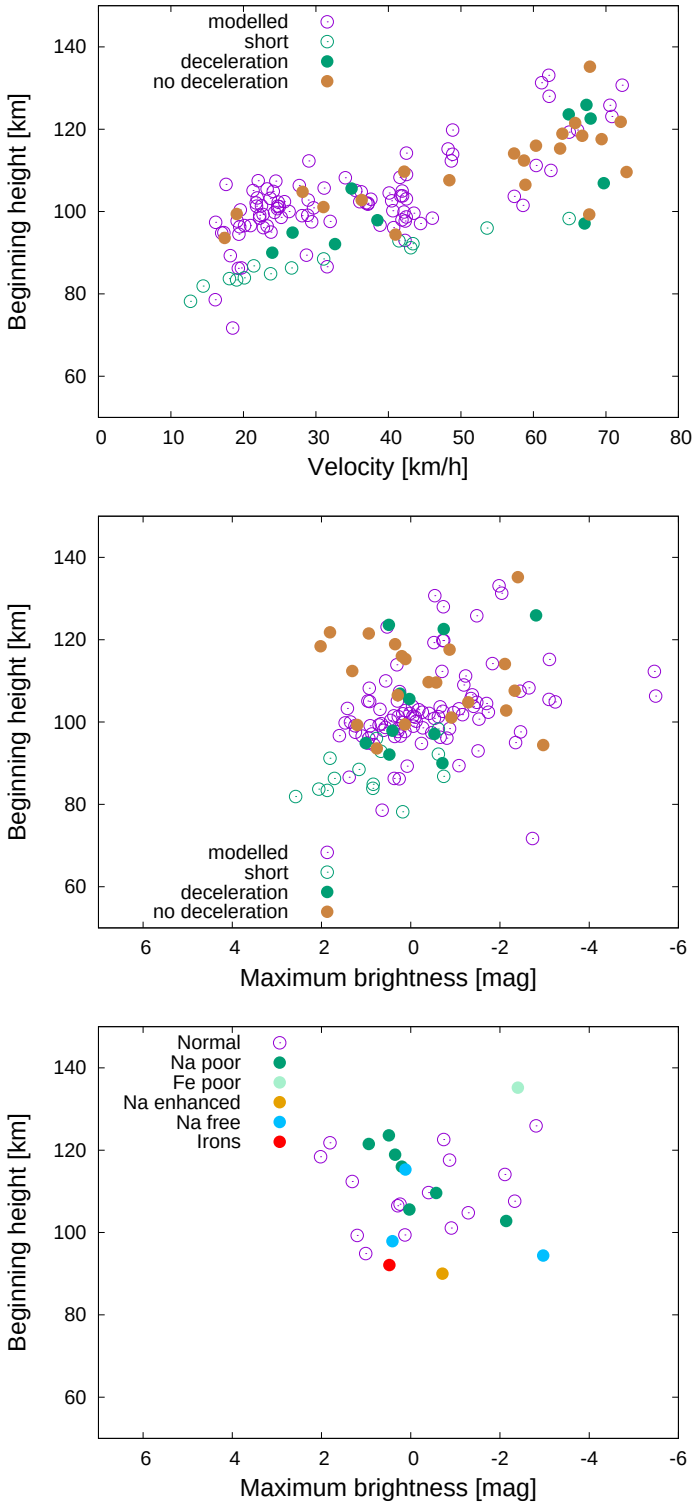

Figure 6.17: Properties of not modelled meteoroids compared to modelled bodies. Top figure shows the beginning height and the velocity. Modelled, short (< 15 km in length) and not modelled, long and not modelled were marked with different symbols and colours. The middle figure shows the beginning height and the maximum brightness of same sample. Not modelled meteoroids were divided in three groups: short, with deceleration, without deceleration. The bottom figure shows only long and not modelled meteoroids with accurate measurements. Different spectral classes are marked.

7. Combining spectral analysis and results of fragmentation modelling

In this chapter we will combine results of spectral analysis with results from the fragmentation modelling. Combination of results from the fragmentation model (the meteoroid parameters) with results from the spectral analysis can give us new insight into the inner structure of the millimetre sized bodies. This approach was already used by Borovička et al. [2014], but only for Draconids. This work uses larger and diverse sample of shower and sporadic meteoroids. Thanks to this, we can reveal some new information about the composition of different millimetre sized meteoroids.

7.1 Monochromatic lightcurves and the differential ablation

The video observations allow us not only to study the overall intensity of spectral lines, but we can easily obtain the time evolution of intensities of individual spectral lines. For simplicity, we call these time evolutions of lines monochromatic lightcurves. The time evolution of individual lines can help us to better understand the processes of the ablation of individual elements.

The monochromatic lightcurves of three low temperature meteoric lines of Mg I, Na I and Fe I were studied.

Few examples of these monochromatic lightcurves are shown in the Figure 7.1. We can clearly see the differences between individual meteors. There is obvious difference in intensities of individual lines for different spectral lines. The lines of sodium, magnesium and iron can have various relative intensities for Normal class, but all three lines are clearly visible. In contrast, the iron line dominates for the SX001 meteor, classified as Iron. Similarly, the sodium line dominates for the Na–enhanced SX498 meteor. On the contrary, we could barely observe the sodium line for the SX151 Na–free meteor. But what we can notice in all these examples above, despite different overall intensities, for given meteor, these three lines have similar shapes with approximately same maximum position. When we focus on meteors SX1135 and SX043 in the Figure 7.1, we can see that their sodium lines somewhat differ from other two lines. In case of the meteor SX1135, the sodium line has the same beginning as other two lines, but its maximum is earlier and the line fades away whereas the magnesium and iron line still radiate. For the SX043 meteor we can observe that the maxima of these three lines are different. This differential ablation of some millimetre sized meteoroids is well known and processes, that are causing this, are a subject of the study. Vondrak et al. [2008] developed chemical ablation model. In this model the Na and K elements are released $\approx 10 - 15$ km higher than other (less volatile) major elements: Si, Fe and Mg. Janches et al. [2009]observed as first the micrometeoroid differential ablation using the radar observations.

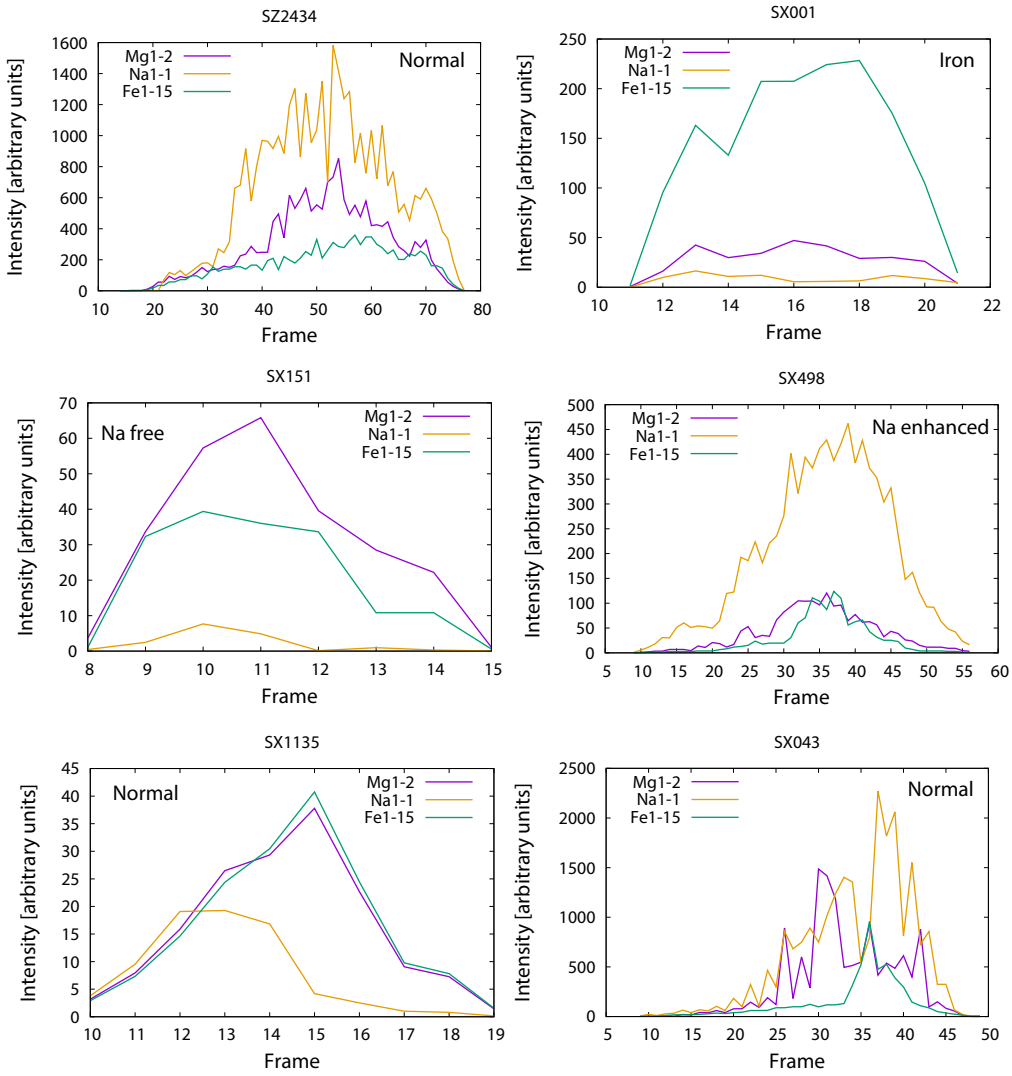

Figure 7.1: Examples of monochromatic lightcurves. The intensity of three meteoric lines in arbitrary units as it changes on individual frames of the video. Different lines are marked with different colours. Determined spectral classes of individual meteors are showed.

One technical note: for monochromatic lightcurves we work with half of the time resolution in the video compared to the lightcurves in white light. The reason is in our choice to use the half frame of the video for measurements from the direct cameras (lightcurves in white light). For the spectral measurements we use whole frames of the video. Thus we have actual time resolution of 50 fps for direct observations and 25 fps for spectral observation. When we add the lower sensitivity of the spectral system, we obtain usually four times less points for the monochromatic lightcurves compared to the number of measurements for the integral lightcurves.

In our desire to study this differential ablation we tried to describe the shape of individual lightcurves using simple analysis. Despite the sometimes complicated shape of monochromatic lightcurves we used one quantity to describe the monochromatic lightcurve shape. We studied the height, where half of the individual element was radiated out, instead of using the position of the maximum of

the lightcurve (because of the complicated shape). This quantity was computed by integrating the monochromatic lightcurve along the trajectory. The height, where the integral reaches half of its total value, is the height where half of the element was radiated out. The shapes of the iron curve and the magnesium curve were always very similar and only the sodium curve sometimes showed significant differences. Thus, for further analysis, we focused on heights where half of the mass of the sodium or the magnesium was radiated. Comparison of these heights can help us to better see if the sodium was released earlier or later than the magnesium.

The difference between heights where half of the sodium and magnesium was radiated are shown in Figures 7.2 and 7.3. This difference is in kilometres. If the value was 0, half of the magnesium and sodium were radiated at the same height. When the sodium was released earlier, the value of the difference was positive and when the sodium was released later than magnesium, the value of the difference was negative. The Na–free and Iron meteoroids and meteors with only atmospheric lines in their spectrum were excluded from the figure, since the determination of the Na – Mg half mass height difference is very inaccurate for them.

The dependence of the difference between these heights for Na and Mg on the grain sizes of the meteoroid was discovered. As it can be seen in Figures 7.2 and 7.3, the larger is the upper mass limit and the larger is the lower mass limit for grains, the later is the release of the sodium. As mentioned in previous chapter, assuming same shape and density of grains, the mass and the size of grains are proportionate. We can also see, that meteoroids with smaller mass tend to release the sodium early. The total mass of meteoroid is connected to limits of grain masses (meteoroids with smaller grains have smaller total mass).

Including the spectral classes we can see, that for given grain size, the Na–poor members tend to release their sodium earlier. Knowing just one quantity (and not the whole shape of monochromatic lightcurves) one can assume that the lack of sodium for the Na–poor meteors is the cause of the early release of the sodium. In other words, the sodium runs out faster. To confirm this presumption, we have to look at monochomatic lightcurves of Na–poor meteors. From a total number of 21 meteors classified as Na–poor, 11 of them were successfully modelled. We show monochromatic lightcurves of these 11 modelled Na–poor meteors in Figure 7.4. They are sorted according to the value of the lower grain mass limit from lowest (SX1738) to highest (SX2133) mass limit. Sodium lightcurve for Na–poor meteors usually does not start earlier than magnesium line. But the sodium can end earlier than the magnesium. The beginning brightening of Na and Mg suggests, that the release rate for sodium and magnesium is more or less same, but since there is less of the sodium in the meteoroid, this element simply "runs out". Thus the different behaviour is probably caused by the smaller amount of sodium in Na–poor meteoroids.

The bottom graph of the Figure 7.3 shows orbital classes for individual meteoroids. The meteoroids on cometary orbits can have any lower mass limit for grains. The Halley type members have rather smaller lower mass limits and thus they released the sodium usually earlier. The Jupiter family members showed wide range of lower mass limits for grains, but generally they did not have the smallest grains. There were not many members of the Asteroidal – chondritic

orbital class, but the modelled meteoroids had quite wide range of meteor sizes. There were bodies on the Asteroidal – chondritic orbits with both early and later release of Na. The Sun approaching orbital class usually do not have extremely low or large values of mass limit, but their grain lower mass limit is usually somewhere in the middle range of masses (from $\approx 1 \times 10^{-7}$ g to $\approx 1 \times 10^{-5}$ g).

We did not find strong connection between the strength of the material (derived from the beginning height for given velocity) and differential ablation of sodium and magnesium. But the fragile material showed wider spread of the height difference, where half of the sodium and magnesium element was radiated out. The stronger the material was, the smaller the difference between sodium and magnesium was. But the strongest material in the form of Iron and Na–free meteoroids was not included, since these classes contain none or only very faint lines of sodium. We can conclude that the fragile material contains conglomerates of different composition, hence we can expect very different behaviour for sodium and magnesium for individual meteoroids. The stronger material is expected to be more homogeneous and thus we did not observe differential ablation for these meteoroids.

7.2 Second stage of the fragmentation

Millimeter sized meteoroids usually disintegrated by one continuous fragmentation. But some lightcurves showed more (typically two) stages of the fragmentation. In that cases the first stage of the erosion was applied only to some amount of the initial mass. The rest of the body was unaffected (it only ablated) and at some point it started fragment as the second stage of the fragmentation. The parameters of the first and the second stages of the fragmentation were usually different. This suggests that even millimetre sized meteoroids inner structure can be quite complex nuances. There can be materials with different strengths within one meteoroid or every meteoritic component might have different chronology of fragmentation.

Meteors with more than one stage of fragmentation can give us good opportunity to study differences in physical parameters within one body. In addition to the modelling the fragmentation, we can also use the monochromatic lightcurves to complete the information about different parts of the meteoroid.

7.2.1 Meteoroids with two stages of the fragmentation

How the lightcurves for two stages of the fragmentation look can be seen in Figures 7.5 and 7.6. The sudden brightening or the change in the shape of the lightcurve suggests the start of the different stage of the fragmentation. Total number of 15 meteors were chosen for the analysis of two different stages of the fragmentation. We can compare lightcurves in white light with monochromatic lightcurves for each individual meteor in Figures 7.5 and 7.6. Parameters for first and second fragmentation stage, as a result of the modelling, are shown in Table 7.1.

We can notice immediately that nine meteors were classified as shower meteors and that four of these shower meteors were Draconids. Since there is a total number of seven Draconids in this work, it seems that second stage of the

fragmentation might be typical for this shower. Moreover, all of the three Taurid meteors included in this work showed a second stage of the fragmentation. Among shower meteors with second fragmentation, there was one Lyrid meteor and one Geminid meteor.

Most of the meteors with two stages of the fragmentation were classified as Normal. There were two (SX1041, SX2133) meteors classified as Na–poor, both of them were sporadic. Other spectral classes did not show more than one stage of the erosion.

The sources of second stage fragmentation meteoroids were of cometary and of Sun–approaching. There were three members of Halley type class, six members of Jupiter family class and three members of Ecliptic class. All meteoroids with second stage fragmentation on ecliptic orbit were Taurids. Of the six members of the Jupiter family four of them were Draconids. The only one Lyrid meteoroid was on the Halley type orbit. The Geminid was on the Sun – approaching orbit.

The comparison of monochromatic lightcurves with the results from the fragmentation modelling showed a special nature of the SX336 Geminid meteor. We will analyse different stages of fragmentation of the SX336 meteoroid in a separate section.

From all 121 sporadic meteors, only six were used for the modelling of the second stage of erosion. The selection between one or two stages of fragmentation modelling was done by the operator according to the shape of the lightcurve. This process might cause omission of some meteors with actual second fragmentation, but the discrepancy between sporadic and shower meteors is quite distinct. Only a few representative members of each major showers were selected selected for this work. This might cause a selective effect in the rate of meteoroids with second stage of the fragmentation among shower members. Nevertheless, the shower meteors were in the whole range of magnitudes and masses of our sample of meteors. One would expect the two stages of the fragmentation to occur more often for bright and large meteoroids. And the two brightest and largest meteoroids (both Taurids: SX1122, SX1999) showed second fragmentation. But the least massive modelled meteoroid (SX2414) also showed two stages of fragmentation. The other meteoroids with two stages of the fragmentation were in wide range of brightness from $+1$ mag to -3 and they were in the larger half of masses for modelled meteoroids.

We can compare properties of both stages of the fragmentation. As it can be seen in Table 7.1, the ablation coefficient σ is the same for both stages of fragmentation in all meteors except for the Geminid meteor 06C13136 (SX336). On the other hand, the erosion coefficient η is usually different. The differences were sometimes small, sometimes the erosion coefficient in the second stage was up to one order smaller (06C13136) and sometimes it was one order larger (DRA06). This means, that the rate of the ablation was usually same for both stages, but the difference in the rate of erosion varied.

The mass that was subject to the second fragmentation varied among individual meteoroids. This varied from only 10 % of the initial mass up to 70 % of the initial mass.

The limit masses for grains and the limit sizes of these grains also varied. The upper mass limit for second stage of the erosion was up to six orders larger or of four orders smaller (compared to the grain upper mass limit of the first

erosion). But for most meteoroids, the difference was within two orders (both ways – smaller or larger). Very similar results were found for the Grain lower mass limit. Again, there was no simple trend. In the second stage we could observe larger grains or smaller grains, or the dispersion of limits of masses was greater in the first stage compared to the second stage or vice versa.

When we look at numbers of eroded grains in the first stage and the second stage, we can observe (not surprisingly) that in cases with more grains in the second stage of the erosion, these grains were smaller, the part of the meteoroid that eroded later was more fine grained. But most of the second stages of the erosion contained less grains compared to the first stage, and these grains were then larger. The part of the meteoroid that eroded later was more coarse grained. Except of the case of meteor DRA05, all the rest of the Draconid meteoroids contained (up to two orders) more grains in the second stage of the erosion. Even so fragile and fine grained meteoroids as Draconids showed smaller grains during the later stage of the erosion.

We can try to compare monochromatic lightcurves of meteors with two stages of erosion with their lightcurves in white light in the Figures 7.5 and 7.6. We can see, that the brightening during the second stage was sometimes caused by the brightening of only one lines (e. g. Mg line SX2133) and sometimes by multiple lines at once (e. g. SX804, SXDRA06). For some cases the shapes of monochromatic lightcurves were more complicated and we could not assign the brightening in white light lightcurve to the brightening of individual monochromatic lightcurves (e. g. SX461, SX1041). Some cases showed differential ablation for sodium (e. g. SX2414, SXDRA03).

Comparing the monochromatic lightcurves to the results of the modelling, we could not see much dependence of the difference of grain sizes between individual fragmentation stages and the shape of the monochromatic lightcurves. There was not such a rule between (for example) more ablation of magnesium or sodium in the second stage and the cases with larger or smaller grains in the same stage of erosion.

We can see that if the brightening in the second stage was caused by magnesium, the erosion coefficient η was smaller (second stage compared to the first stage). Moreover, if the brightening in the second stage was caused by the sodium, the erosion coefficient η was usually similar or smaller (second stage compared to the first stage). And not surprisingly, if the monochromatic lightcurve was more complicated, the erosion coefficient η stayed usually similar during the first and the second stage of the erosion.

One of the results of this analysis is simple result, that the structure of millimetre sized meteoroids can be sometimes more complex than we would expect from such small bodies. They can be composed of different materials (in terms of strength, grains, grain sizes). These differences can be found even within one body. There are some similarities between the members of one shower.

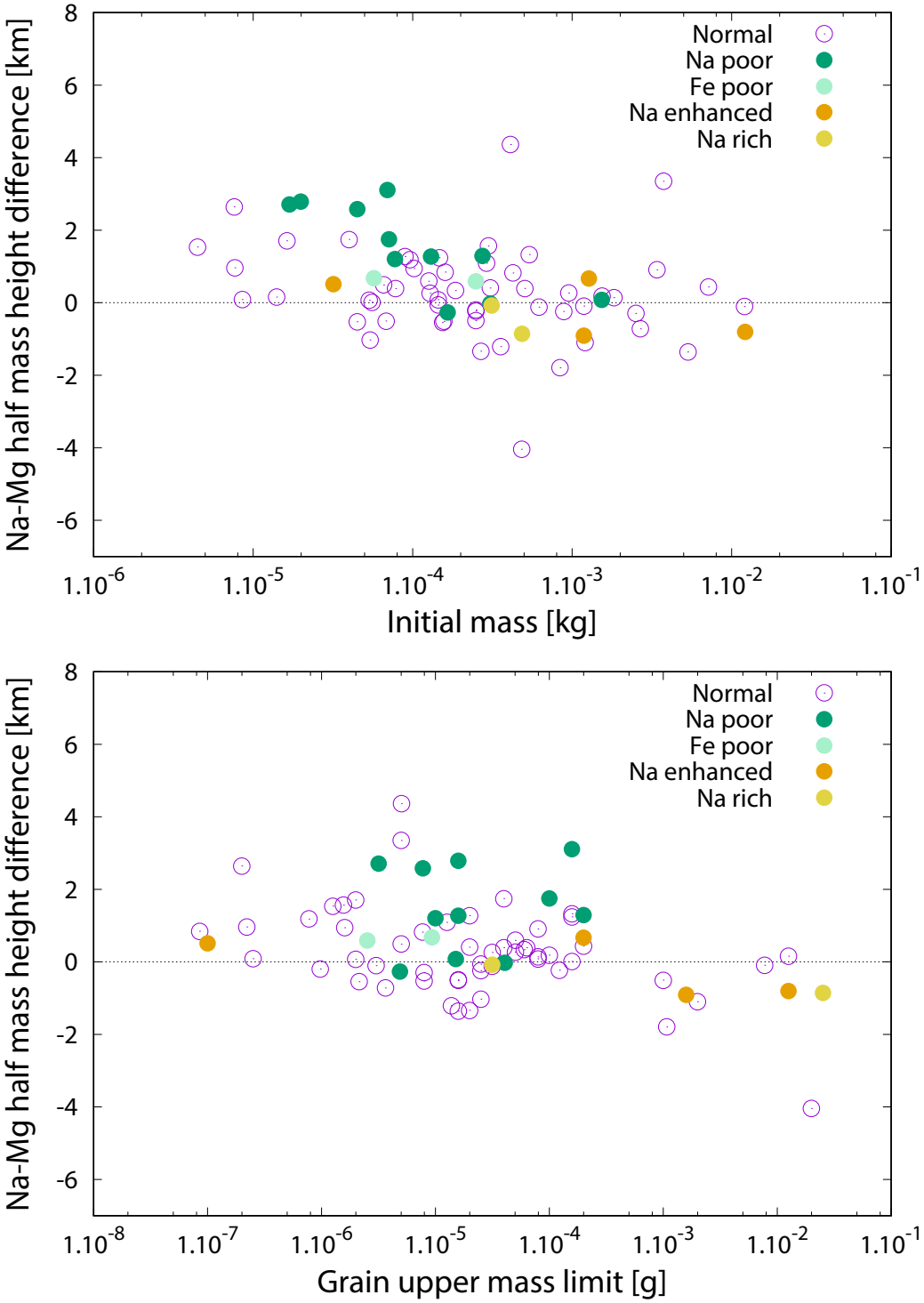

Figure 7.2: The difference of heights where half of the mass of the sodium and the magnesium was radiated out as a function of photometric mass and the upper mass limit of grains. A positive number stands for early release of Na and vice versa.

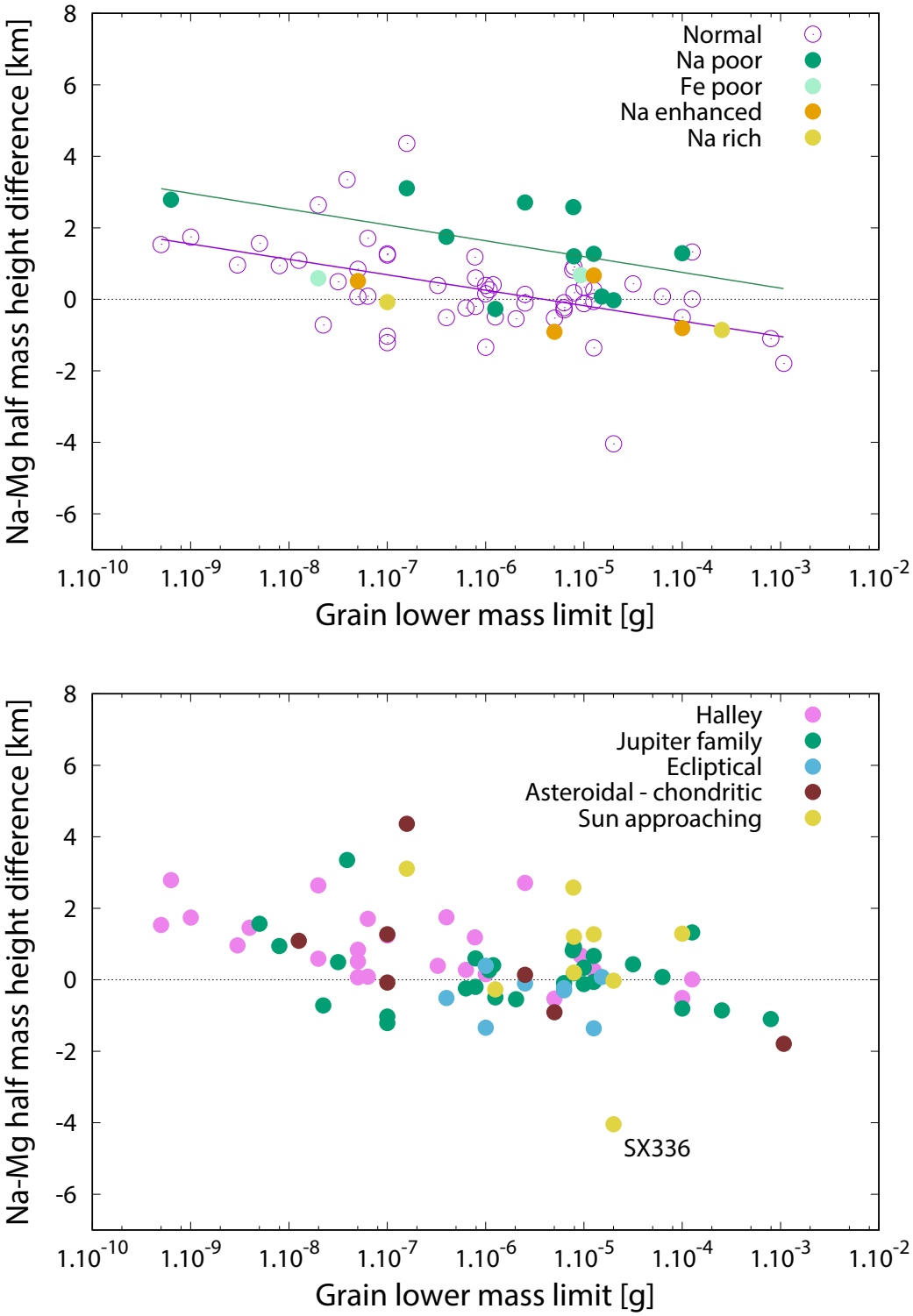

Figure 7.3: The difference of heights where half of the mass of the sodium and the magnesium was radiated out as a function of lower mass limit of grains. The upper figure shows the fit for the Normal class (purple line) and the for the Na–poor class (green line). The lower figure shows different orbital classes of meteoroids. A positive number stands for early release of Na and vice versa.

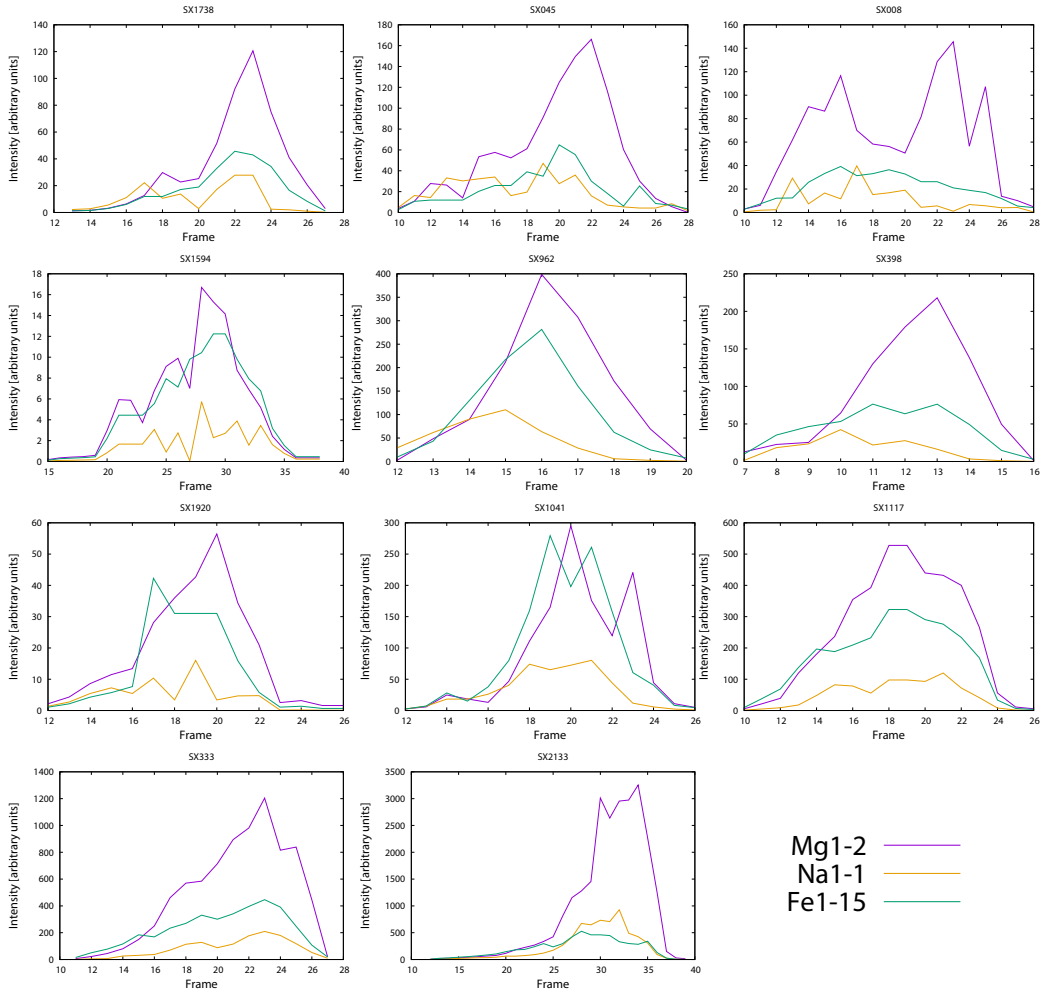

Figure 7.4: Monochromatic lightcurves of Na–poor modelled meteors. Figures are sorted according to the lower grain mass limit, from the lowest (SX1738) to the highest (SX2133) value.

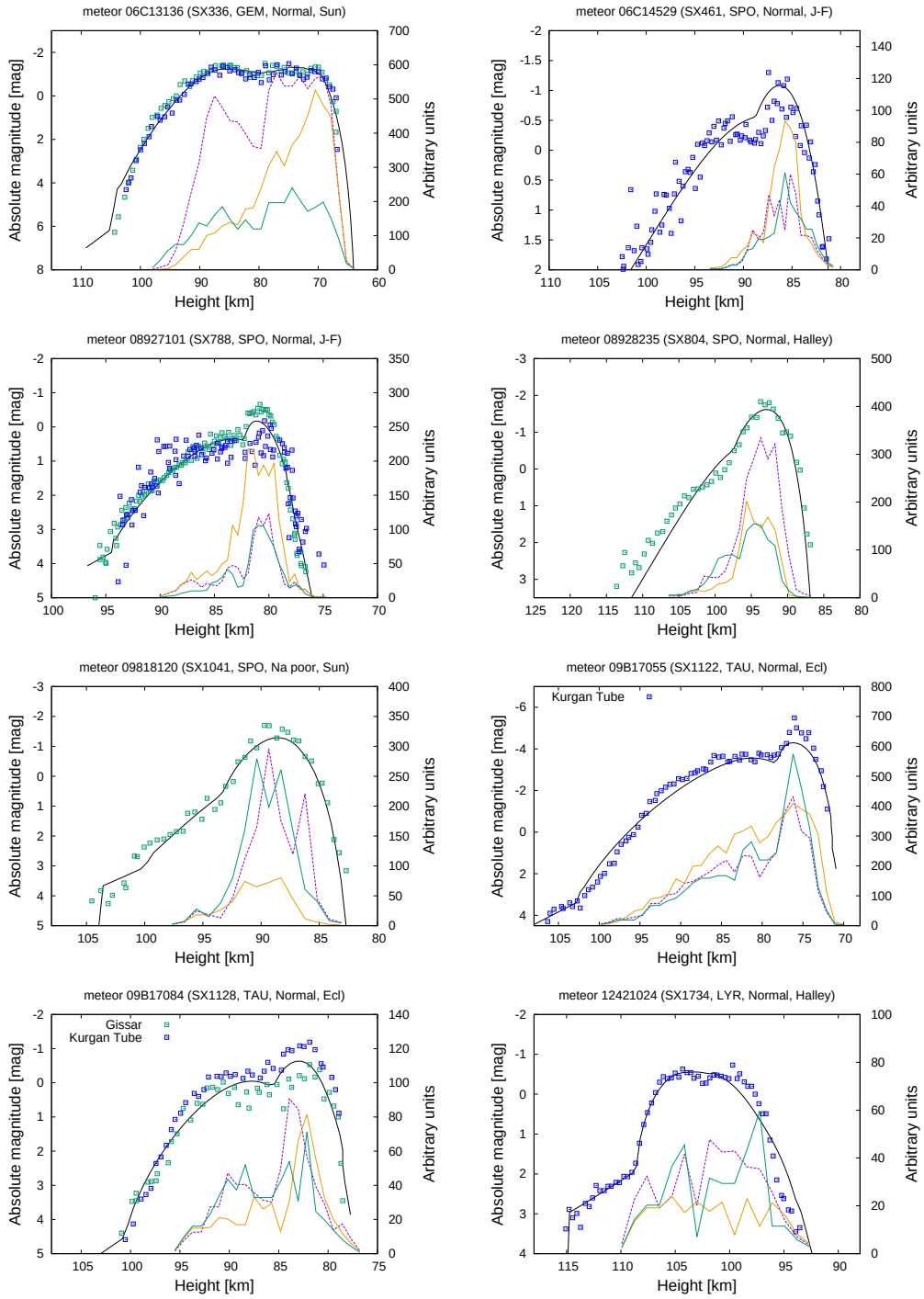

Figure 7.5: Meteors with two stages of erosion. Lightcurves in white light and monochromatic lightcurves of Na, Mg and Fe are shown. The scale for intensity for white light is in absolute magnitudes. For monochromatic lightcurves the intensity is in arbitrary units (linear scale). Both types of lightcurves were adjusted manually for illustrative purpose. The key and the rest of lightcurves of meteoroids with two stages of erosion are shown in Figure 7.6.

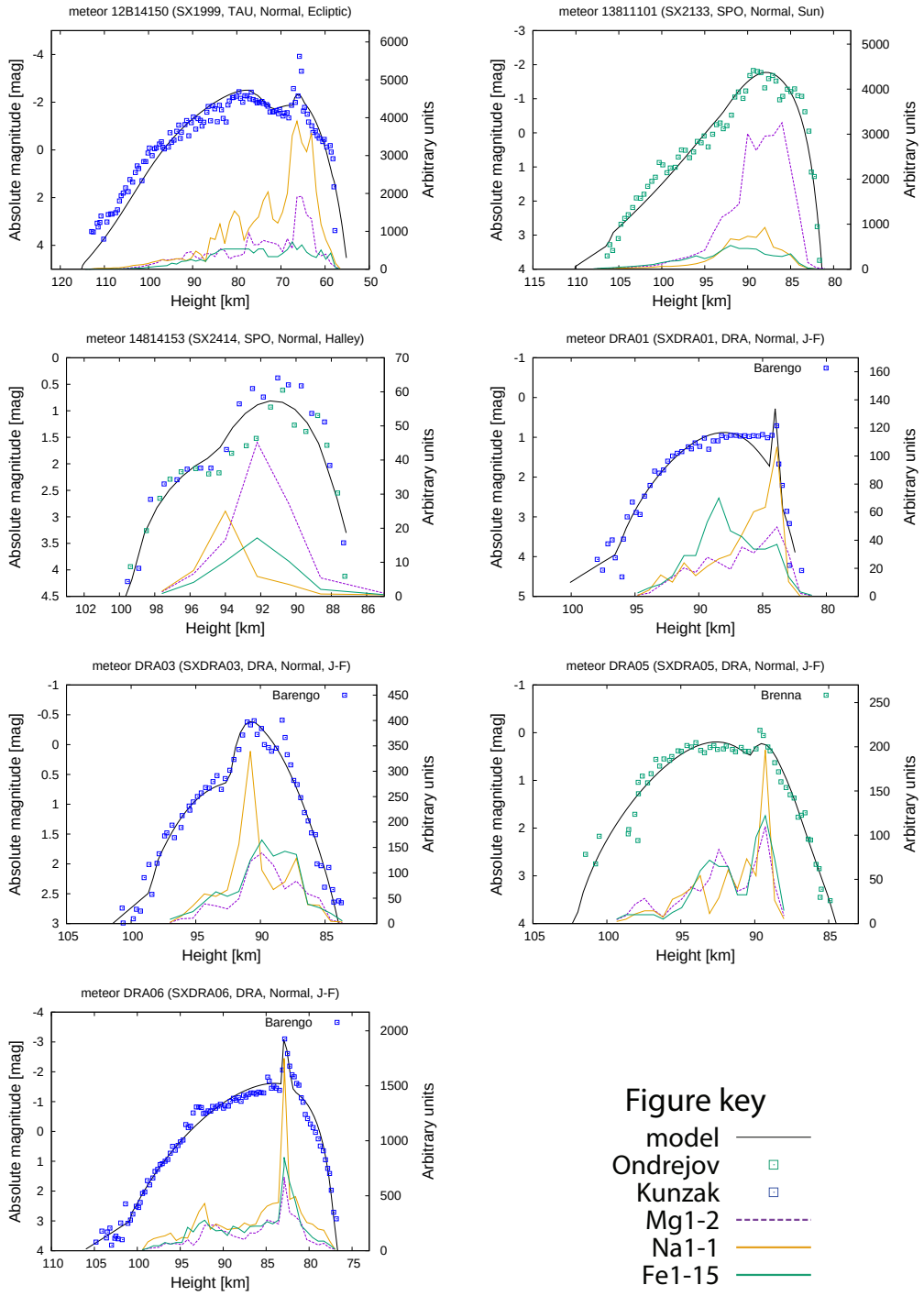

Figure 7.6: Meteors with two stages of erosion. Lightcurves in white light and monochromatic lightcurves of Na, Mg and Fe are shown. The scale for intensity for white light is in absolute magnitudes. For monochromatic lightcurves the intensity is in arbitrary units (linear scale). Both types of lightcurves were adjusted manually for illustrative purpose. If not specifically listed in the individual lightcurve figure, the key is shown in the right bottom corner.

Table 7.1: Results of the fragmentation model for the cases with two stages of erosion. Two lines for every meteor. Parameters for first erosion are in the first line. Parameters for second erosion are in the the second line. The initial mass of meteoroid is shown, the percentage of the initial mass mass that was subject of the second erosion is also shown.

meteor	spectrum	σ	η	GUML	GLML	sizes	N	mass	δ	
		s^2 . km^{-2}	s^2 . km^{-2}	g	g	mm		g	kg . m^{-3}	
06C13136	SX336	0.004	0.52	2.00×10^{-2}	2.00×10^{-5}	0.23–2.33	1.5×10^{3}	5.00×10^{-1}	2200	GEM
SE	Normal	0.019	0.03	3.89×10^{-2}	5.01×10^{-3}	1.46–2.32	1.9×10^{1}	30%		
06C14529	SX461	0.052	0.18	7.76×10^{-3}	6.31×10^{-6}	0.16–1.70	1.9×10^{4}	1.19	600	SPO
SE	Normal	0.052	0.23	2.51×10^{-4}	2.00×10^{-4}	0.47–0.54	1.7×10^{3}	55%		
08927101	SX788	0.014	0.23	1.00×10^{-4}	7.94×10^{-6}	0.16–0.40	4.9×10^{4}	1.54	700	SPO
SE	Normal	0.014	0.27	6.31×10^{-5}	3.98×10^{-7}	0.06–0.34	3.1×10^{5}	30%		
08928235	SX804	0.009	0.30	8.51×10^{-8}	5.01×10^{-8}	0.02–0.02	1.0×10^{6}	1.60×10^{-1}	790	SPO
SE	Normal	0.009	0.17	1.00×10^{-5}	7.94×10^{-6}	0.32	8.1×10^{3}	56%		
09818120	SX1041	0.014	0.20	1.58×10^{-5}	1.26×10^{-5}	0.22	2.3×10^{3}	1.30×10^{-1}	1500	SPO
SE	Na–poor	0.014	0.26	1.58×10^{-5}	6.30×10^{-6}	0.16–0.22	7.6×10^{3}	70%		
09B17055	SX1122	0.007	0.64	3.02×10^{-6}	2.51×10^{-6}	0.12	2.4×10^{6}	1.20×10^{1}	2800	TAU
SE	Normal	0.007	0.62	2.00×10^{-5}	7.94×10^{-7}	0.08–0.23	1.5×10^{6}	40%		
09B17084	SX1128	0.011	0.61	2.00×10^{-5}	1.00×10^{-6}	0.09–0.23	4.4×10^{4}	2.67×10^{-1}	2100	TAU
SE	Normal	0.011	0.39	3.98×10^{-6}	3.98×10^{-6}	0.14	2.4×10^{4}	40%		
12421024	SX1734	0.017	0.61	6.31×10^{-5}	3.26×10^{-7}	0.06–0.34	6.7×10^{4}	7.83×10^{-2}	220	LYR
SE	Normal	0.017	0.69	5.85×10^{-6}	5.85×10^{-6}	0.16	9.1×10^{2}	10%		
12B14150	SX1999	0.011	0.08	3.16×10^{-7}	1.00×10^{-9}	0.01–0.06	2.7×10^{8}	4.00	1000	TAU
SE	Normal	0.011	0.11	1.26×10^{-1}	1.59×10^{-2}	2.16–3.70	3.0×10^{1}	50%		
13811101	SX2133	0.015	0.39	2.00×10^{-4}	1.00×10^{-4}	0.40–0.50	1.1×10^{3}	2.74×10^{-1}	1500	SPO
SE	Na–poor	0.015	0.15	1.26×10^{-4}	1.00×10^{-4}	0.43	5.4×10^{2}	30%		
14814153	SX2414	0.003	0.06	1.26×10^{-6}	5.01×10^{-10}	0.01–0.09	4.8×10^{5}	4.48×10^{-3}	2040	SPO
SE	Normal	0.003	0.07	2.00×10^{-7}	1.59×10^{-7}	0.05	1.2×10^{4}	60%		
DRA01	SXDRA01	0.022	0.30	2.14×10^{-6}	2.04×10^{-6}	0.10–0.11	5.5×10^{4}	1.54×10^{-1}	440	DRA
SE	Normal	0.022	0.82	2.29×10^{-10}	2.29×10^{-10}	0.01	5.9×10^{7}	17%		
DRA03	SXDRA03	0.027	0.63	7.70×10^{-6}	7.70×10^{-6}	0.16–0.17	2.5×10^{4}	4.26×10^{-1}	99	DRA
SE	Normal	0.027	0.66	7.08×10^{-7}	7.08×10^{-7}	0.08	2.4×10^{5}	50%		
DRA05	SXDRA05	0.032	0.73	1.38×10^{-5}	1.00×10^{-7}	0.04–0.21	5.3×10^{5}	3.56×10^{-1}	370	DRA
SE	Normal	0.032	0.84	4.07×10^{-7}	3.89×10^{-7}	0.05–0.06	9.5×10^{4}	14%		
DRA06	SXDRA06	0.015	0.15	3.63×10^{-6}	2.24×10^{-8}	0.02–0.13	2.0×10^{7}	2.68	390	DRA
SE	Normal	0.015	1.02	2.46×10^{-10}	2.46×10^{-10}	0.01	1.5×10^{9}	16%		

7.3 The SX336 Geminid meteor and other Sun – approaching meteoroids

The meteoroid with the highest negative difference of half mass heights of Na and Mg in Figures 7.2 and 7.3 is the Geminid meteoroid SX336. We will focus on this special case in more detail and we will try to answer why the release of the sodium was so delayed.

As all Geminids, this meteor was on a Sun–approaching orbit. The spectrum was classified as Normal. It is one of two meteoroids with a Sun–approaching orbit that were not classified as Na–poor or Na–free (the second one was Iron). Although the relatively large lower mass limit predicts later release of sodium, this meteor differs a lot from the dependence in Figures 7.2 and 7.3. As it can be seen in Figure 7.7, the shape of the magnesium and the iron lines are similar, with lower intensity for the iron line. They both show two maxima. The release of the magnesium was the quickest. The sodium increase was slower. The slope of the sodium line was almost same during the flight until the maximum at the very end of the meteor. It only gets little bit higher after the second stage of fragmentation starts. This might suggest the difference in the inner structure for the magnesium, iron and sodium. When we observe two stages of the fragmentation we usually assume that there is a part of the material that was unaffected by the erosion until some point of the flight. After that point the erosion starts the second part. Thanks to the shape of the lightcurve we are able to estimate the properties of this stronger part. The results from the fragmentation model for both stages of the erosion are shown in the Table 7.2. The number of grains in the first stage was two orders higher. There were only larger (millimetre sizes) grains released during the second stage. The ablation coefficient σ was of one order larger for the second stage, i. e. the ablation was faster in the second stage. This different ablation coefficient for different stages of erosion is somehow unusual. All other meteoroids with second stage of the erosion showed the same ablation coefficient for both stages of erosion. On the contrary, the erosion coefficient η was one order of magnitude larger for the first stage. In other words, the erosion in form of larger grains was slower in the second stage. In the first stage, about 1.5×10^3 grains were released and in the second stage, only 19 grains were released.

The Geminids are well know for the variations of the amount of sodium in their spectra. It was suggested by Čapek and Borovička [2009] that the sodium depletion is caused in the interplanetary space during close approaches to the Sun. The sodium depletion does not depend on meteoroid sizes for Geminids. The porosity and the grain sizes play a key role in the rate of this depletion. Meteoroids with smaller grains deplete the sodium faster during their passages around the Sun. Čapek and Borovička [2009] did not have the actual data for sizes of the grains for Gemind members. According to their work, they predicted sizes of grains for Geminids to be in the size range $\approx 100 - 400$ μm. Three of four modelled members of Geminids in our work have their grain sizes in the range $\approx 60 - 270$ μm. Only the SX336 meteoroid has grain sizes in the range of $\approx 200 - 2300$ μm. This meteoroid contained large grains both in the first and in the second stage of the erosion. Moreover, in the first stage there were smaller grains. But in the second stage of erosion there were only large grains (more than 1 mm in size). This might be the reason why was the spectrum classified as Normal.

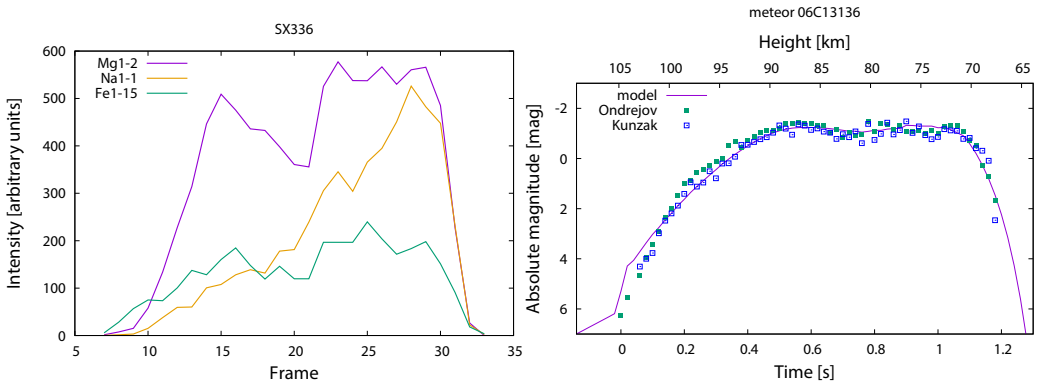

Figure 7.7: The 06C13136 (SX336) Geminid meteor. Monochromatic lightcurve on the left and the integral lightcurve on the right.

In the case of the spectrum SX336 the different parts probably contained different relative amount of sodium and magnesium. The part with smaller grains fragmented first. Thanks to a faster depletion of sodium on the orbit for smaller grains there was less sodium than it corresponds to the chondritic composition. The material in the second stage of erosion was different. Thanks to larger grains the depletion of the sodium was much slower or did not take place at all. When the stronger part of the meteoroid started to fragment, the relative intensity of the sodium line started to correspond to the chondritic composition. Thanks to the difference within the inner structure we can observe much later release of the sodium than it was typical for other meteoroids.

7.3.1 Sun – approaching meteoroids

We will try to put the results of the SX336 Geminid analysis in the context of other Sun–approaching meteoroids. Since the theoretical work of Čapek and Borovička [2009] suggested some prediction to sodium depletion and the connection to the grain sizes, we will try to compare our observed results with their theoretical work.

First we will discuss the members of the Geminid shower. According to the Table 7.4, the bulk density δ is relatively high for Sun – approaching meteoroids, thus the porosity is not high. The energy necessary to start the erosion E_s is usually of the order of 1×10^6 J . m^{-2}, but there are two cases with E_s of one order higher. As mentioned before, the work of Čapek and Borovička [2009] suggested the size range of grains for Geminids to be $\approx 100 - 400$ μm. Except for Draconids, they did not know grain sizes for other meteoroids or other members of meteor showers. According to their results, the smaller the grains and the smaller the perihelion q, the more likely will the meteoroids loose sodium. We included the values of perihelion distance and grain sizes in the Table 7.4. They are visualised in the Figure 7.8. It is clear, that among the Sun – approaching class most of the Na–free meteoroids contain small grains and have low perihelia. Na–poor meteoroids contain a little bit larger grains or their perihelia are larger for the given grain size. The meteoroid with the largest grains is the SX336 Geminid, classified as Normal. These trends are as expected although the division between Na–free and Na–poor according to grain sizes and perihelia is not strict. One

Table 7.2: Comparison of first stage of the erosion to the second stage of the erosion for the Geminid meteor SX336. Results from the fragmentation model.

(a) First stage erosion

HE_B	HE_E	σ	η	E_s	δ
km	km	s^2 . km^{-2}	s^2 . km^{-2}	J . m^{-2}	kg .m^{-3}
103.9	86.7	0.0035	0.52	1.2×10^6	2200
GUML	GLML	grain sizes	N	m	v_∞
g	g	mm		g	km . s^{-1}
2.00×10^{-5}	2.00×10^{-8}	0.23 – 2.16	1.38×10^3	5.0×10^{-1}	36.2

(b) Second stage erosion

HE_B	HE_E	σ	η	mass
km	km	s^2 . km^{-2}	s^2 . km^{-2}	%
86.7	80.2	0.019	0.030	30
GUML	GLML	grain sizes	N	E_s
g	g	mm		J . m^{-2}
3.89×10^{-5}	5.01×10^{-6}	1.46 – 2.32	19	6.6×10^7

Note. HE_B and HE_E stands for the beginning and end height of the erosion. σ is the ablation coefficient, η is the erosion coefficient. E_s is the energy necessary for the start of the erosion. δ is the bulk density. GUML and GLML is the grain mass upper and lower limit for grains. N is number of grains in the meteoroid. m is the initial mass and v_∞ is the initial velocity. The mass that is subject to the second stage of the erosion is in percent of the initial mass.

explanation can be (again according to Čapek and Borovička [2009]), that other parameters, like the age of the meteoroid or the semimajor axis, can also play a role. But their effect on the Na depletion is not as strong as the effect of the grain sizes and the perihelion distance. In general (compared to other meteoroids) the Sun–approaching orbital class contained relatively larger grains. Still these grains were small enough for the sodium depletion to take place. We can assume that if meteoroids with smaller grains (than it is typical for the Sun–approaching class) were on the Sun–approaching orbits, we would observe even more sodium depleted meteors.

Table 7.4: The parameters for the Sun – approaching members. The initial mass is m, q is the perihelion distance.

name	spectrum	m	q	δ	E_s	grain sizes	N	shower	spectrum
		g	AU	kg .m^{-3}	J . m^{-2}	mm			
06406048	SX001	2.6×10^{-5}	0.11	3300	9.4×10^{6}	0.136 – 0.147	2.4×10^{3}	SPO	Iron
06724023	SX045	7.0×10^{-5}	0.20	700	2.2×10^{6}	0.047 – 0.466	5.1×10^{4}	SPO	Na–poor
06A20126	SX151	7.2×10^{-6}	0.05	2590	7.5×10^{6}	0.102 – 0.174	1.8×10^{3}	SPO	Na–free
08728223	SX725	3.5×10^{-5}	0.07	1100	9.0×10^{6}	0.095 – 0.351	5.1×10^{3}	SPO	Na–free
08728280	SX731	3.2×10^{-5}	0.06	2000	7.1×10^{6}	0.034 – 0.294	6.8×10^{4}	SPO	Na–free
08729037	SX738	4.3×10^{-5}	0.08	1090	1.3×10^{7}	0.086 – 0.399	8.1×10^{3}	SPO	Na–free
09729165	SX1010	3.1×10^{-5}	0.08	2000	6.4×10^{6}	0.034 – 0.466	6.1×10^{4}	SPO	Na–free
09818120	SX1041	1.3×10^{-4}	0.09	1500	3.4×10^{6}	0.125 – 0.216	7.6×10^{3}	SPO	Na–poor
09820027	SX1087	3.6×10^{-5}	0.09	2300	4.2×10^{6}	0.040 – 0.370	4.8×10^{4}	SPO	Na–free
12814214	SX1920	7.7×10^{-5}	0.07	2800	1.4×10^{7}	0.159 – 0.185	8.3×10^{3}	SPO	Na–poor
10408088	SX1217	3.8×10^{-5}	0.10	1900	7.4×10^{6}	0.172 – 0.233	2.6×10^{3}	SPO	Na–free
11505072	SX1594	1.7×10^{-4}	0.13	1400	1.5×10^{6}	0.092 – 0.146	6.3×10^{4}	SPO	Na–poor
13811283	SX2155	6.0×10^{-5}	0.08	2430	2.6×10^{6}	0.105 – 0.105	3.1×10^{4}	SPO	Na–free
06C13104	SX333	3.1×10^{-4}	0.14	2000	2.3×10^{6}	0.218 – 0.296	1.0×10^{4}	GEM	Na–poor
06C13136	SX336	5.0×10^{-4}	0.14	2200	1.2×10^{6}	0.233 – 2.334	1.5×10^{3}	GEM	Normal
06C13137	SX337	6.7×10^{-5}	0.14	1100	1.8×10^{6}	0.063 – 0.200	3.4×10^{4}	GEM	Na–free
06C14215	SX398	4.5×10^{-5}	0.14	1850	1.7×10^{6}	0.170 – 0.170	5.5×10^{3}	GEM	Na–poor
13811101	SX2133	2.7×10^{-4}	0.10	1500	1.7×10^{6}	0.399 – 0.503	1.1×10^{3}	SPO	Na–poor

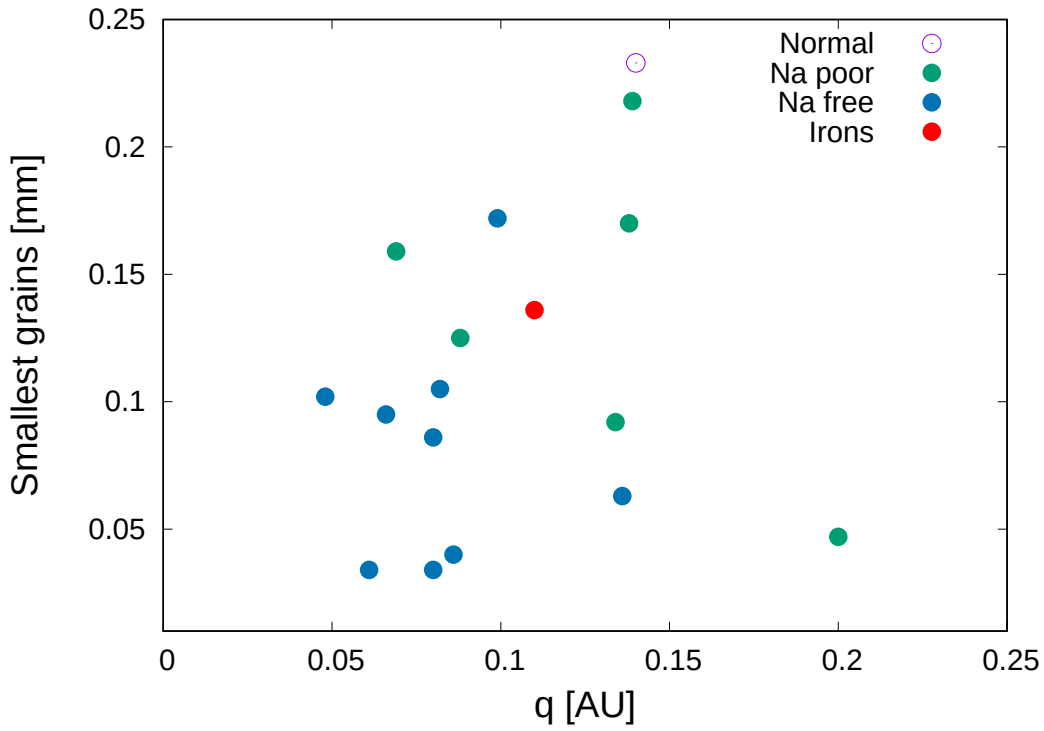

Figure 7.8: The perihelion and the smallest grain sizes for all Sun–approaching meteoroids. Every color represents different spectral class.

8. Summary

We reduced, measured and analysed total number of 152 observations of faint sporadic and shower meteors. All these meteors were observed from (at least) two stations using the video technique. They were observed both in white light and by using a spectral grating. Observations were run mainly from Czech Republic by the scientific staff from the Ondřejov observatory between the years 2004 – 2014. Results of expeditions to Tajikistan in 2009 and to northern Italy in 2011 were used too. Using the double station recordings, we obtained atmospheric trajectories and orbital parameters of observed meteoroids.

Reduced meteor spectra were classified according to spectral classification of faint meteor spectra suggested by Borovička et al. [2005]. This classification is based on the intensities of the low–temperature emission lines of Na, Mg, and Fe. In addition, we studied monochromatic lightcurves of these elements. To study atmospheric fragmentation of meteoroids we used the fragmentation model developed by Borovička et al. [2007]. Using the video technique, we easily obtained the time evolution of each meteoric spectral line. The total number of 94 meteors were modelled using the fragmentation model. This way we obtained complex information about a representative sample of millimetre sized meteoroids.

We confirmed that only part of millimetre sized meteoroids have typical chondritic compositions. Variety of Na depletion, Na enhancement and Fe depletion was observed. There are three populations of Na–free meteoroids: the meteoroids of the Iron spectral class, the Sun–approaching meteoroids with Na depleted by periodic close approaches to the Sun and the population of cometary origin with Na depleted by long exposure of cosmic rays. The Normal chondritic and the Iron spectral classes prevailed among the Asteroid–chondritic orbital class. For the Sun–approaching orbit the Na–poor and Na–free spectral class prevailed. Meteoroids with cometary orbits were usually members of the Normal spectral class.

Some of the measured parameters of atmospheric trajectories and orbits and also the spectral and the orbital parameters are included in the Table A.1 in the Appendix of the electronic version. Uncertainties are of order of last digits.

We also studied the morphology of meteors. The low resolution of the video did not allow us to study meteor wakes in detail. We were still able to obtain some results. We observed meteors with long or bright wakes, meteors with only faint wakes and meteors without any wakes. Meteors with elongated endings were also observed. Most of these meteors were Draconids. Generally, spectral classes with less sodium (Na–poor, Na–free, Iron) did not form long and bright wakes as much as other spectral classes. The formation of the wake also depended on the speed of the meteor. Meteors without a wake were in the whole range of speeds, but meteors with wakes (both short or long) were usually of lower speed up to ≈ 45 km . s^{-2}. We suspect that meteor wakes are formed by the fragmented grains from the meteoroid body. We therefore compared wake observations with the results from the fragmentation modelling. It can be expected that the bigger is the difference between the largest and the smallest grains in the meteoroid the longer a wake will be formed. The prolongation is caused by the difference in the drag for different grain sizes. However we did not observe such a dependency.

This fact strengthens the conclusion of Campbell-Brown et al. [2013] that the erosion model is not accurate in the simulation of wakes. Future work on the formation of wakes will be needed.

The results of the fragmentation model showed quite high range for some parameters among all meteoroids. The masses of grains ranged from smallest of a mass of $\approx 1 \times 10^{-10}$ g up to largest grains of mass of $\approx 3 \times 10^{-2}$ g. The corresponding sizes of grains were from 5 μm up to $\approx$ 2.5 mm. Individual meteoroids contained from 1×10^2 up to $\approx 1 \times 10^8$ grains. We compared sizes of grains derived from modelling with results of measurement of cometary particles collected by the ROSETTA spacecraft orbiting the 67/P Churyumov–Gerasimenko comet [Hornung et al., 2016]. We found good agreement in the distribution of sizes for grains collected from this Jupiter–family comet with results of our modelling of Jupiter–family meteoroids. The energy necessary for the start of the erosion E_s was highest for Iron class (up to $E_s \approx 4 \times 10^7$ J . s^{-2}). The meteoroid with the lowest value of E_s was a member of Fe–poor class with $E_s \approx 1 \times 10^5$ J . s^{-2}. Members of the Iron, Na–poor and Na–free class showed higher energy E_s for given start height of the erosion.

The erosion coefficient and the ablation coefficient showed increasing dispersion with increasing meteoroid mass. The connection of these coefficients with the energy necessary to ablate or fragment unit of mass suggests that larger meteoroids show wide range of inner composition in term of strength.

We compared our results with the work of Kikwaya et al. [2011]. We found similar densities for meteoroids on Halley type orbits. But high density for meteoroids on Jupiter–family orbits derived by Kikwaya et al. [2011] were in contrast with our results. Our results were more typical for cometary material. Among the Jupiter–family orbits there is Draconid shower with low density meteoroids. On the other hand, the Stardust mission found surprisingly high amount of μm sized CAI's when studying the material of Jupiter–family comet 81P/Wild. Thus high variety of density and porosity for millimetre sized cometary materials might be common.

A smaller part (38%) of all meteors was not modelled. Besides too short meteors and meteors with low precision, there were meteoroids with unsufficient deceleration for the fragmentation model to be used. We investigated if there was a possibility that meteoroids with low deceleration were single bodies. The position of the maximum brightness described by the F parameter, nevertheless, showed wide range of values not consistent with classical ablation of single bodies. Based on lightcurves, we did not find differences in properties for meteoroids that were modelled or that were not modelled.

The main goal of this work was the combination of results from the spectral and fragmentation analysis. We used time evolution of three spectral lines (monochromatic lightcurves). Lines of Na, Mg and Fe were used. Figures from A.1 to A.16 in the Appendix of the electronic version are showing all of the monochromatic lightcurves.

Figures from A.17 to A.35 in the Appendix of the electronic version are showing all of the modelled meteoroids. The most important physical parameters derived by the fragmentation model are included in the Table A.2 in the Appendix of the electronic version. Uncertainties are of order of last digits.

Shapes of monochromatic lightcurves varied for individual meteors. Differen-

tial ablation of sodium was observed. Not only we observed the early release of the sodium, but we also discovered meteors with later release od Na. To describe different release of each spectral element we used the height where each element was radiated. The difference in this height for sodium and magnesium depended on the sizes of grains of meteoroids. The early release of sodium was typical for meteoroids with small grains. Bodies with large grains released the sodium at the same time as the magnesium, in some cases even later than the magnesium.

There were also differences in the release of sodium and the sizes of grains for different sources of meteoroids. The Halley type showed rather early release of sodium and smaller grains. On the other hand, another meteoroids of cometary origin, the Jupiter–family members, had wide range of grain sizes. They did not contain the smallest grains, like Halley type meteoroids did. Thus the Halley type meteoroids showed early release of sodium more likely.

We also found meteoroids with two stages of erosion. We compared results of the fragmentation model with spectral analysis. Of total number of 152 meteors, only 10% showed two stages of the erosion. Only Normal and Na–poor classes were among the bodies with two stages of erosion. The orbits were of cometary and of Sun–approaching. The material in the second stage of the erosion was usually more coarse grained with larger grains. On the other hand, the material in the second stage for Draconids contained more smaller grains than in the first stage of the erosion.

Comparing the monochromatic lightcurves and lightcurves in white light we could see that the secondary brightening was very individual for each meteor. Sometimes there was a secondary brightening of just one monochromatic line. For other bodies the secondary brightening was caused by multiple monochromatic lines. We observed that if the erosion coefficient was smaller in the second stage, the secondary brightening was caused by the magnesium. The larger or the same erosion coefficient in the second stage was indicating the secondary brightening by the line of Na.

We found that millimetre sized meteoroids can be sometimes more complex than we would expect for such small bodies.

A special case was the Geminid meteor SX336. The differential ablation of the sodium was opposite than usually (late release of Na). This meteoroid fragmented in two stages. We proposed that different degree of sodium depletion in interplanetary space in the two parts was the reason of a later release of the sodium. In the interplanetary space, meteoroids with smaller grains are loosing sodium much faster than meteoroids with larger grains [Čapek and Borovička, 2009]. Smaller grains in the first stage caused higher relative intensity for magnesium. Larger grains and thus probably higher amount of the sodium in the second stage of fragmentation caused later maximum for the Na line.

We confirmed results of the work of [Čapek and Borovička, 2009]. We observed higher bulk density δ and lower porosity for Sun–approaching meteoroids. The grain sizes for the Geminid were similar as they predicted. We observed higher sodium depletion for meteoroids with low perihelia and small grains.

8.1 Na–free and Na–poor meteors

Throughout this work, there were two spectral classes that differ from the others. These are the Na–free and Na–poor groups. There is a real difference in the structure between sodium depleted class compared to other spectral classes. Now we will sum up these results for better. There are two sources for both Na–free and Na–poor meteoroids: the Sun–approaching meteoroids and the sodium depleted meteoroids on cometary orbits. But we did not observe much difference in physical properties for sodium depleted meteoroids, whether they were on the Sun–approaching orbits or on the cometary orbits. There were no two separated groups, that would correspond to the two sources of Na depleted meteoroids. So we will discuss the Na–free and Na–poor meteoroids of both sources together.

- **Stronger material**

  According to Figure 5.1 the Na–free and the Na–poor bodies tend to begin at lower heights for given velocity. The lower the beginning height is for given velocity the stronger the material is supposed to be. The sodium depleted material showed rather lower values of porosity. So the sodium depletion is making the meteoroid material stronger.

- **No wakes or only faint wakes**

  The study of meteor wakes and trails, i. e. the study of meteor morphology revealed that Na–free and Na–poor meteors did not produce wakes or their wakes were only faint. The Na–free meteors did not produce any meteor trails, but the Na–poor meteors produced trails in one third of cases.

- **Differences in the material properties**

  According to the Figure 6.11 the Na–poor and Na–free meteoroids tend to have lower mass. They need to obtain more energy to start the erosion. This is another proof of stronger material of sodium depleted meteoroids. According to Figure 6.14 the Na–free and Na–poor meteoroids contain smaller number of grains (compared with the Normal class). Both the erosion and the ablation coefficients tend to be lower for Na–poor and Na–free class (see Figure 6.12). The rate of the erosion and the ablation is slower for given grain sizes for sodium depleted meteoroids. According to limits of size for grains, the Na–poor and Na–free meteors usually do not contain very small grains. The sizes of grains are otherwise comparable to size of most of the Normal class (see Figures 6.11 and 6.12).

  All but two of the meteoroids with two stages of the erosion were classified as Normal. These two meteoroids were members of the Na–poor class.

- **Different release of sodium**

  Naturally, sodium could not be studied in the Na–free spectral class. However, the Na–poor meteoroids tend to release the sodium earlier for given grain size (compared to other spectral classes). This result can be seen in Figure 7.3. The study of the monochromatic lightcurves (Figure 7.4) suggests, that the early release of sodium is consequence of Na depletion in the interplanetary space. During the flight in the atmosphere, the sodium

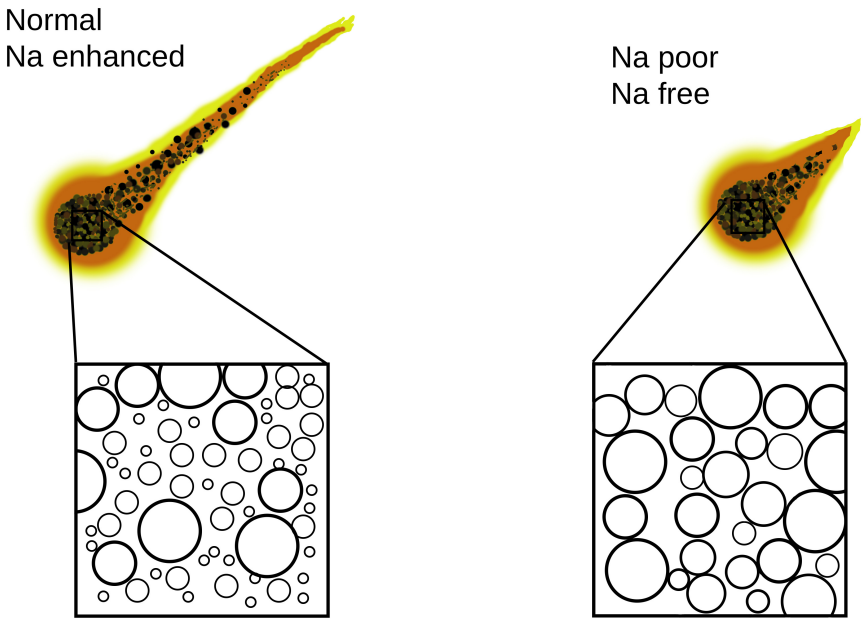

Figure 8.1: The schematic expression of difference of Na–poor and Na–free classes inner structure. Compared to Normal and Na–enhanced class.

is released with the same rate as the magnesium, but the smaller amount of sodium "runs out" at some point of the flight (earlier than magnesium). Thus we observe that for given grain size, the sodium is radiated out early for Na–poor class.

All these differences for Na–poor (and Na–free) meteoroids lead us to the conclusion that these classes might have different structure. Figure 8.1 shows schematic, but illustrative, idea of different structure for Na–poor and Na–free meteoroids: they do not contain grains larger than the other classes (in fact, some Normal meteoroids contained larger grains than any other Na–poor member). But unlike other classes, they usually do not contain very small grains. The smallest grains were probably depleted in the Solar system, during close approaches to Sun or by exposure to cosmic rays. The Na–poor and Na–free classes do not form long wakes. Probably because they contain less grains, but the fragmentation model was not able to prove this. They can form brighter trails, but the formation of trail is independent on the actual fragmentation.

8.2 Iron meteors on Halley type orbits

High inclinations and the value of the Tisserand parameter classified two Iron meteors among the Halley orbit members (for orbital parameters see Table 5.1). The question is: how the Iron meteoroids could get on the Halley type orbits?

Kikwaya et al. [2011] studied densities of millimetre sized meteoroids. One meteoroid with one of the highest density ($\sigma = 4495 \pm 600$ kg.m^{-3}) showed high inclination of 150° and the orbit was reminding Halley type comets. Although the

orbit was classified as Sun–approaching (possibly with a reduced a due to a high ejection velocity from the Sun–approaching parent comet when near perihelion). They concluded that it was probably an iron–rich inclusion from a Halley type comet, or it was a thermally processed meteoroid that has lost its volatiles and been sintered.

There are asteroids on Halley type orbits usually called Damocloids (named after 5335 Damocles). They are defined by Jewitt [2005] as point–source objects with Tisserand parameters relative to Jupiter $T_J \leq 2$. We compared the two Iron meteor orbits with the latest list of Damocloids according to Jewitt. Their orbits might seem similar, but the association according to Southworth–Hawkins D–criterion was low. Moreover, the Damocloids are believed to be dormant nuclei of Halley type comets. The behaviour of these object is asteroid like, but their composition is probably same as comets on Halley type orbits.

It is unlikely that these meteoroids come right from the asteroid belt using the gravity of Jupiter to their present orbit. Jupiter can greatly increase the eccentricity of meteoroids, but this process cannot increase the inclination over $\approx 40°$ (personal communication with David Nesvorný). Both Iron meteoroids showed inclination over 60°.

After personal communication with David Nesvorný he suggested one scenario. The material might originated in young Solar system when some planetesimals in the region between 5 and 30 AU were formed very quickly and this fast process allowed the differentiation. Some of these planetesimals might be transported to Oort cloud by then migrating Jupiter. According to model Grand Tack [Walsh et al., 2011] Jupiter migrated up to 1.5 AU close to the Sun and subsequently migrated outward. This migration was potentially responsible for transportation of some planetesimals into Oort cloud. But in this region there had to be collisions that allowed to escape the differentiated iron material as meteoroids. In our work we had 64 Halley type orbit meteoroids and only 2 were classified as irons. Thus the Grand Tack scenario is one of possible suggestions how this small number of meteoroids could acquire Halley type orbits.

Nevertheless, our view on the composition of cometary material changed after the Stardust mission. The Stardust mission discovery of CAI's and other high–temperature materials that are closely analogous to meteoritic components in the comet 81P/Wild 2 [Brownlee et al., 2012] was surprise. Brownlee et al. [2012] suggested that this inner Solar system material was probably transported behind the orbit of Neptune, where they accreted along with ice and organic components to form comet Wild 2. Their best data came from a restricted set of solid materials. The studied components that were sufficiently strong that they did not fragment during capture in aerogel were from 2 μm to a few 10 μm in diameter. Larger component were rare. Our Iron meteoroids were of millimetre size in diameter and although the comet Wild 2 is Jupiter–family type comet, we think that even the Halley type comets can contain up to few millimetre sized differentiated solid inclusion that can be source of some of iron meteoroids.

But the origin of Iron meteoroids on Halley type orbits might also be different. Future investigation is needed.

8.3 Fe–poor meteors

We classified 5 meteors as Fe–poor. They all had Halley type orbit with one exception, the SZ2466 showed transitional orbit between the Ecliptic and the Asteroidal–chondritic orbit. We did not observe beginning and end of this meteor, thus we have to take the orbit of this meteor with caution. But we think that it might be possible that a source of this meteor can be a short period comet. Fe–poor meteors showed no or only small wake, but bright trails prevailed. Only two Fe–poor meteors were modelled. Their material was fragile, with rather small grains. The meteoroid SZ2428 was one of the most porous materials in our work. We did not observe much difference for ablation of sodium and magnesium for Fe–poor meteoroids.

8.4 Na–rich and Na–enhanced meteors

We observed only two meteors classified as Na–rich, both with Jupiter–family orbit. They showed only small or no wake. We also classified 5 meteors as Na–enhanced. They had different orbits (Asteroidal–chondritic, Ecliptic, Jupiter–family, Halley). Na–enhanced and Na–rich were mostly slow with normal beginning heights for given speed. They were more massive than average meteoroids, with larger grains and the material was porous (but usually not extremely porous). The only one Na–enhanced meteoroid on Halley type orbit was different from other Na–enhanced meteoroids. It was fast with lower mass and smaller grains. It was also the most porous meteoroid among Na–enhanced/Na–rich meteoroids. We did not observe much difference for ablation of sodium and magnesium for Na–rich and Na–enhanced meteoroids. We think that meteoroids with high amount of sodium do not create a homogeneous group.

8.5 Normal meteors

Most meteoroids in our work were classified as Normal. Usually they showed normal chondritic composition often with somewhat fainter Fe lines. They had mixture of asteroidal and cometary orbits, but cometary orbits prevailed. Short wakes or no wakes prevailed for Normal meteors. As one would expect, they showed wide range of parameters derived from the modelling. Most of the Normal meteoroids had higher porosities (above ≈ 0.7). We observed wide range of differences for release of sodium and magnesium. Normal class makes the majority of sporadic meteoroids, but other classes are not negligible. Except for showers with low perihelia, most of the shower meteoroids were of Normal spectral class.

9. Conclusions and future work

The goal of this work was to improve our knowledge about millimetre sized meteoroids. The study was based on video observations of faint meteors. We combined the results of the fragmentation modelling with spectral observations. This was never done on a such large quantity of diverse meteoroids.

We found that size of the grains of meteoroids can affect the release of the sodium from the body during the flight in the atmosphere. Meteoroids with small grains tend to release the sodium earlier. We also find that the Na–poor class tends to release the sodium earlier for given grain size. We studied the morphology of meteors and we combined this analysis with the spectral and the fragmentation study. In the future, better fragmentation modes and narrow field observations of meteors can help us to find interesting results about meteor morphology. Time evolution of meteor features and the connection between these features and the fragmentation of the meteoroid is a matter of interest. We found evidence of Iron meteoroids on Halley type orbits. This can be proof of wild evolution of the early Solar System. We also compared sizes of modelled grains of observed meteoroids on Jupiter–family orbits with new results of the ROSETTA study of the 67/P Churyumov–Gerasimenko comet and we found good agreement for sizes of elementary grains that form the cometary material.

Even though the model we used was usually in agreement with other models and results of other works and even with studies of cometary material from spacecraft missions, it does not work well in some areas (e. g. simulation of meteor wakes). The more meteoroids we observed and studied, the more complex and heterogeneous we found the population of millimetre sized meteoroids. The fragmentation models of millimetre sized meteoroids have to deal wider variety of materials than we expected and thus the future models should be more complex to reflex this variety.

Bibliography

P. B. Babadzhanov and N. A. Konovalova. Some features of Geminid meteoroid disintegration in the Earth's atmosphere. *Astronomy and Astrophysics*, 428: 241–246, December 2004. doi: 10.1051/0004-6361:20041398.

M. Beech and D. Steel. On the Definition of the Term Meteoroid. *Quarterly Journal of the Royal Astronomical Society*, 36:281, September 1995.

J. Borovicka, R. Stork, and J. Bocek. First results from video spectroscopy of 1998 Leonid meteors. *Meteoritics and Planetary Science*, 34:987–994, November 1999. doi: 10.1111/j.1945-5100.1999.tb01418.x.

J. Borovicka, P. Spurný, P. Kalenda, and E. Tagliaferri. The Morávka meteorite fall: 1 Description of the events and determination of the fireball trajectory and orbit from video records. *Meteoritics and Planetary Science*, 38:975–987, July 2003. doi: 10.1111/j.1945-5100.2003.tb00293.x.

J. Borovička. Two components in meteor spectra. *Planetary and Space Science*, 42:145–150, February 1994. doi: 10.1016/0032-0633(94)90025-6.

J. Borovička. Meteor Trains - Terminology and Physical Interpretation. *Journal of the Royal Astronomical Society of Canada*, 100:194, October 2006.

J. Borovička. Spectroscopic Analysis of Geminid Meteors. In J. Rendtel and J. Vaubaillon, editors, *Proceedings of the International Meteor Conference, 26th IMC, Bareges, France, 2007*, pages 42–51, December 2010.

J. Borovička and J. Boček. Television Spectra of Meteors. *Earth Moon and Planets*, 71:237–244, December 1995. doi: 10.1007/BF00612965.

J. Borovička and P. Jenniskens. Time Resolved Spectroscopy of a Leonid Fireball Afterglow. *Earth Moon and Planets*, 82:399–428, 2000.

J. Borovička, P. Spurný, and P. Koten. Atmospheric deceleration and light curves of Draconid meteors and implication for the structure of cometary dust. *Astronomy and Astrophysics*, 473(282):661–671, 2007.

J. Borovička, P. Koten, P. Spurný, and R. Štork. Analysis of a Low Density Meteoroid with Enhanced Sodium. *Earth Moon and Planets*, 102:485–493, June 2008. doi: 10.1007/s11038-007-9194-y.

J. Borovička, P. Koten, P. Spurný, D. Čapek, L. Shrbený, and R. Štork. Material properties of transition objects 3200 Phaethon and 2003 EH_1. In J. A. Fernandez, D. Lazzaro, D. Prialnik, and R. Schulz, editors, *IAU Symposium*, volume 263 of *IAU Symposium*, pages 218–222, 2010. doi: 10.1017/S174392131000178X.

J. Borovička, P. Koten, L. Shrbený, R. Štork, and K. Hornoch. Spectral, Photometric, and Dynamic Analysis of Eight Draconid Meteors. *Earth Moon and Planets*, 113:15–31, October 2014. doi: 10.1007/s11038-014-9442-x.

J. Borovička, P. Spurný, and P. Brown. Small Near-Earth Asteroids as a Source of Meteorites. *ArXiv e-prints*, February 2015.

J. Borovička, L. Shrbený, P. Kalenda, N. Loskutov, P. Brown, P. Spurný, W. Cooke, R. Blaauw, D. E. Moser, and A. Kingery. A catalog of video records of the 2013 Chelyabinsk superbolide. *Astronomy and Astrophysics*, 585:A90, January 2016. doi: 10.1051/0004-6361/201526680.

J. Borovička, P. Spurný, V. I. Grigore, and J. Svoreň. The January 7, 2015, superbolide over Romania and structural diversity of meter-sized asteroids. *Planetary and Space Science*, 143:147–158, September 2017. doi: 10.1016/j.pss.2017.02.006.

J. Borovička. The comparison of two methods of determining meteor trajectories from photographs. *Bulletin of the Astronomical Institutes of Czechoslovakia*, 41:391 – 396, 1990.

J. Borovička, P. Koten, P. Spurný, J. Boček, and R. Štork. A survey of meteor spectra and orbits: evidence for three populations of Na-free meteoroids. *Icarus*, 174:15 – 30, 2005.

A. Bouvier and M. Wadhwa. The age of the Solar System redefined by the oldest Pb-Pb age of a meteoritic inclusion. *Nature Geoscience*, 3:637–641, September 2010. doi: 10.1038/ngeo941.

V. A. Bronshten. *Physics of meteoric phenomena*. Izdatel'stvo Nauka, 1983.

N. Brosch, L. S. Schijvarg, M. Podolak, and M. R. Rosenkrantz. Meteor observations from Israel. In B. Warmbein, editor, *Meteoroids 2001 Conference*, volume 495 of *ESA Special Publication*, pages 165–173, November 2001.

P. Brown, Z. Ceplecha, R. L. Hawkes, G. Wetherill, M. Beech, and K. Mossman. The orbit and atmospheric trajectory of the Peekskill meteorite from video records. *Nature*, 367:624–626, February 1994. doi: 10.1038/367624a0.

P. Brown, R. E. Spalding, D. O. ReVelle, E. Tagliaferri, and S. P. Worden. The flux of small near-Earth objects colliding with the Earth. *Nature*, 420:294–296, November 2002.

P. Brown, P. Wiegert, D. Clark, and E. Tagliaferri. Orbital and physical characteristics of meter-scale impactors from airburst observations. *Icarus*, 266: 96–111, March 2016. doi: 10.1016/j.icarus.2015.11.022.

D. Brownlee. The Stardust Mission: Analyzing Samples from the Edge of the Solar System. *Annual Review of Earth and Planetary Sciences*, 42:179–205, May 2014. doi: 10.1146/annurev-earth-050212-124203.

D. Brownlee, D. Joswiak, and G. Matrajt. Overview of the rocky component of Wild 2 comet samples: Insight into the early solar system, relationship with meteoritic materials and the differences between comets and asteroids. *Meteoritics and Planetary Science*, 47:453–470, April 2012. doi: 10.1111/j.1945-5100.2012.01339.x.

M. Campbell-Brown. A population of small refractory meteoroids in asteroidal orbits. *Planetary and Space Science*, 118:8–13, December 2015. doi: 10.1016/j.pss.2015.03.022.

M. D. Campbell-Brown and D. Koschny. Model of the ablation of faint meteors. *Astronomy and Astrophysics*, 418:751–758, May 2004. doi: 10.1051/0004-6361:20041001-1.

M. D. Campbell-Brown, J. Borovička, P. G. Brown, and E. Stokan. High-resolution modelling of meteoroid ablation. *Astronomy and Astrophysics*, 557: A41, September 2013. doi: 10.1051/0004-6361/201322005.

Z. Ceplecha. Experimental data on the final mass of the body landed on the Earth after penetrating the atmosphere at cosmical velocity. *Bulletin of the Astronomical Institutes of Czechoslovakia*, 11:9, 1960.

Z. Ceplecha. Geometric, dynamic, orbital and photometric data on meteoroids from photographic fireball networks. *Bulletin of the Astronomical Institutes of Czechoslovakia*, 38:222–234, July 1987.

Z. Ceplecha. Earth's influx of different populations of sporadic meteoroids from photographic and television data. *Bulletin of the Astronomical Institutes of Czechoslovakia*, 39:221–236, July 1988.

Z. Ceplecha, J. Borovička, W. G. Elford, D. O. Revelle, R. L. Hawkes, V. Porubčan, and M. Šimek. Meteor Phenomena and Bodies. *Space Science Reviews*, 84:327–471, September 1998. doi: 10.1023/A:1005069928850.

S. Drolshagen, J. Kretschmer, D. Koschny, G. Drolshagen, and B. Poppe. Mass accumulation of Earth from interplanetary dust, meteoroids, asteroids and comets. In J.-L. Rault and P. Roggemans, editors, *Proceedings of the International Meteor Conference Mistelbach, Austria, 27-30 August 2015*, pages 220–225, January 2015.

W. N. Edwards, P. G. Brown, P. Spurný, and D. O. Revelle. Listening to shower meteors with infrasound. *Acoustical Society of America Journal*, 117:2421–2421, April 2005.

A. J. Faloon, J. D. Thaler, and R. L. Hawkes. Searching for Light Curve Evidence of Meteoroid Structure and Fragmentation. *Earth Moon and Planets*, 95:289–295, December 2004. doi: 10.1007/s11038-005-9020-3.

M. Fries, J. Fries, M. Hankey, and R. Matson. Meteorite Falls Observed in U.S. Weather Radar Data in 2015 and 2016 (To Date). *LPI Contributions*, 1921: 6536, August 2016.

J. M. Greenberg and A. Li. All comets are born equal: infrared emission by dust as a key to comet nucleus composition. *Planetary and Space Science*, 47: 787–795, June 1999. doi: 10.1016/S0032-0633(98)00102-0.

G. A. Harvey. Nasa-Lrc Faint Meteor Spectra. *NASA Special Publication*, 319: 131, 1973.

R. L. Hawkes and J. Jones. Electro-optical meteor observation techniques and results. *Royal Astronomical Society, Quarterly Journal*, 27:569–589, December 1986.

R.L. Hawkes and J. Jones. A quantitative model for the ablation of dustball meteor. *MNRAS*, 133:411, 1975.

G. S. Hawkins and R. B. Southworth. The Statistics of Meteors in the Earth's Atmosphere. *Smithsonian Contributions to Astrophysics*, 2:349, 1958.

J. S. Hey, S. J. Parsons, and G. S. Stewart. Radar observations of the Giacobinids meteor shower, 1946. *Monthly Notices of the Royal Astronomical Society*, 107: 176, 1947. doi: 10.1093/mnras/107.2.176.

F. Hoerz, G. Cress, M. Zolensky, T. H. See, R. P. Bernhard, and J. L. Warren. Optical Analysis of Impact Features in Aerogel From the Orbital Debris Collection Experiment on the MIR Station. *NASA STI/Recon Technical Report N*, 99, August 1999.

K. Hornung, S. Merouane, M. Hilchenbach, Y. Langevin, E. M. Mellado, V. Della Corte, J. Kissel, C. Engrand, R. Schulz, J. Ryno, J. Silen, and COSIMA Team. A first assessment of the strength of cometary particles collected in-situ by the COSIMA instrument onboard ROSETTA. *Planetary and Space Science*, 133: 63–75, November 2016. doi: 10.1016/j.pss.2016.07.003.

L.G. Jacchia. The physical theory of meteors. VIII. fragmentation as cause of the faint meteor anomaly. *Astrophysical Journal*, 121:521, 1955.

D. Janches, L. P. Dyrud, S. L. Broadley, and J. M. C. Plane. First observation of micrometeoroid differential ablation in the atmosphere. *Geophysical Research Letters*, 36:L06101, March 2009. doi: 10.1029/2009GL037389.

P. Jenniskens. 2003 EH_1 Is the Quadrantid Shower Parent Comet. *The Astronomical Journal*, 127:3018–3022, May 2004. doi: 10.1086/383213.

P. Jenniskens, M. H. Shaddad, D. Numan, S. Elsir, A. M. Kudoda, M. E. Zolensky, L. Le, G. A. Robinson, J. M. Friedrich, D. Rumble, A. Steele, S. R. Chesley, A. Fitzsimmons, S. Duddy, H. H. Hsieh, G. Ramsay, P. G. Brown, W. N. Edwards, E. Tagliaferri, M. B. Boslough, R. E. Spalding, R. Dantowitz, M. Kozubal, P. Pravec, J. Borovicka, Z. Charvat, J. Vaubaillon, J. Kuiper, J. Albers, J. L. Bishop, R. L. Mancinelli, S. A. Sandford, S. N. Milam, M. Nuevo, and S. P. Worden. The impact and recovery of asteroid 2008 TC_3. *Nature*, 458:485–488, March 2009. doi: 10.1038/nature07920.

D. Jewitt. A First Look at the Damocloids. *The Astronomical Journal*, 129: 530–538, January 2005. doi: 10.1086/426328.

J.-B. Kikwaya, M. Campbell-Brown, P. G. Brown, R. L. Hawkes, and R. J. Weryk. Physical characteristics of very small meteoroids. *Astronomy and Astrophysics*, 497:851–867, April 2009. doi: 10.1051/0004-6361/200810839.

J.-B. Kikwaya, M. Campbell-Brown, and P. G. Brown. Bulk density of small meteoroids. *Astronomy and Astrophysics*, 530:A113, June 2011. doi: 10.1051/0004-6361/201116431.

J. Kissel, A. Glasmachers, E. Grün, H. Henkel, H. Höfner, G. Haerendel, H. von Hoerner, K. Hornung, E. K. Jessberger, F. R. Krueger, D. Möhlmann, J. M. Greenberg, Y. Langevin, J. Silén, D. Brownlee, B. C. Clark, M. S. Hanner, F. Hoerz, S. Sandford, Z. Sekanina, P. Tsou, N. G. Utterback, M. E. Zolensky, and C. Heiss. Cometary and Interstellar Dust Analyzer for comet Wild 2. *Journal of Geophysical Research (Planets)*, 108:8114, October 2003. doi: 10.1029/2003JE002091.

P. Koten and J. Borovička. Light curves of faint meteors. In B. Warmbein, editor, *Meteoroids 2001 Conference*, volume 495 of *ESA Special Publication*, pages 259–264, November 2001.

P. Koten, P. Spurný, J. Borovička, H. Betlem, S. Evans, and R. Štork. Atmospheric trajectories and light curves of the 2000 leonid meteors. In *Proceedings of the 2002 international science symposium on the Leonid meteor storms*, 2003a.

P. Koten, P. Spurný, J. Borovička, and R. Stork. Catalogue of video meteor orbits. Part 1. *Publications of the Astronomical Institute of the Czechoslovak Academy of Sciences*, 91:1–32, 2003b.

P. Koten, J. Borovička, P. Spurný, H. Betlem, and S. Evans. Atmospheric trajectories and light curves of shower meteors. *Astronomy and Astrophysics*, 428:683–690, December 2004. doi: 10.1051/0004-6361:20041485.

P. Koten, J. Borovička, and G. I. Kokhirova. Activity of the Leonid meteor shower on 2009 November 17. *Astronomy and Astrophysics*, 528:A94, April 2011a. doi: 10.1051/0004-6361/201016212.

P. Koten, K. Fliegel, S. Vítek, and P. Páta. Automatic Video System for Continues Monitoring of the Meteor Activity. *Earth Moon and Planets*, 108:69–76, May 2011b. doi: 10.1007/s11038-011-9380-9.

P. Koten, R. Štork, P. Páta, K. Fliegel, and S. Vítek. Simultaneous analogue and digital observations and comparison of results. In A. Roggemans and P. Roggemans, editors, *International Meteor Conference Egmond, the Netherlands, 2-5 June 2016*, pages 133–136, January 2016.

D. W. R. McKinley. *Meteor science and engineering.* 1961.

P. M. Millman. Meteor News. *Quarterly Journal of the Royal Astronomical Society*, 55:265, December 1961.

S. Molau. The meteor detection software MetRec. In *Proceedings of the International Meteor Conference, 17th IMC, Stara Lesna, Slovakia, 1998*, 1999.

C. E. Moore. A Multiplet Table of Astrophysical Interest. Revised Edition. Part I - Table of Multiplets. *Contributions from the Princeton University Observatory*, 20:1–110, 1945.

E. Murad and I. P. Williams. *Meteors in the Earth's Atmosphere*. September 2002.

E. J. Opik. *Physics of meteor flight in the atmosphere*. 1958.

P. Pecina and Z. Ceplecha. New aspects in single-body meteor physics. *Bulletin of the Astronomical Institutes of Czechoslovakia*, 34:102–121, March 1983.

J. M. Picone, A. E. Hedin, D. P. Drob, and A. C. Aikin. NRLMSISE-00 empirical model of the atmosphere: Statistical comparisons and scientific issues. *Journal of Geophysical Research (Space Physics)*, 107:1468, December 2002. doi: 10.1029/2002JA009430.

C. Pilger, L. Ceranna, J. O. Ross, A. Le Pichon, P. Mialle, and M. A. Garcés. CTBT infrasound network performance to detect the 2013 Russian fireball event. *Geophysical Research Letters*, 42:2523–2531, April 2015. doi: 10.1002/2015GL063482.

D. O. Revelle. On meteor-generated infrasound. *Journal of Geophysical Research*, 81:1217–1230, March 1976. doi: 10.1029/JA081i007p01217.

D. O. Revelle, P. G. Brown, and P. Spurný. Entry dynamics and acoustics/infrasonic/seismic analysis for the Neuschwanstein meteorite fall. *Meteoritics and Planetary Science*, 39:1605–1626, October 2004. doi: 10.1111/j.1945-5100.2004.tb00061.x.

L. A. Rogers, K. A. Hill, and R. L. Hawkes. Mass loss due to sputtering and thermal processes in meteoroid ablation. *Planetary and Space Science*, 53:1341–1354, November 2005. doi: 10.1016/j.pss.2005.07.002.

A. E. Rubin and J. N. Grossman. Meteorite and meteoroid: New comprehensive definitions. *Meteoritics and Planetary Science*, 45:114–122, January 2010. doi: 10.1111/j.1945-5100.2009.01009.x.

P. Spurný. Instrumentally documented meteorite falls: two recent cases and statistics from all falls. In S. R. Chesley, A. Morbidelli, R. Jedicke, and D. Farnocchia, editors, *Asteroids: New Observations, New Models*, volume 318 of *IAU Symposium*, pages 69–79, January 2016. doi: 10.1017/S1743921315009746.

P. Spurný and J. Borovička. The autonomous all-sky photographic camera for meteor observation. In B. Warmbein, editor, *Asteroids, Comets, and Meteors: ACM 2002*, volume 500 of *ESA Special Publication*, pages 257–259, November 2002.

P. Spurný and Z. Ceplecha. Is electric charge separation the main process for kinetic energy transformation into the meteor phenomenon? *Astronomy and Astrophysics*, 489:449–454, October 2008. doi: 10.1051/0004-6361:200810069.

P. Spurný, L. Shrbený, J. Borovička, P. Koten, V. Vojáček, and R. Štork. Bright Perseid fireball with exceptional beginning height of 170 km observed by different techniques. *Astronomy and Astrophysics*, 563:A64, March 2014. doi: 10.1051/0004-6361/201323261.

E. Stokan and M. D. Campbell-Brown. Transverse motion of fragmenting faint meteors observed with the Canadian Automated Meteor Observatory. *Icarus*, 232:1–12, April 2014. doi: 10.1016/j.icarus.2014.01.002.

E. Stokan and M. D. Campbell-Brown. A particle-based model for ablation and wake formation in faint meteors. *Monthly Notices of the Royal Astronomical Society*, 447:1580–1597, February 2015. doi: 10.1093/mnras/stu2552.

D. Čapek and J. Borovička. Quantitative model of the release of sodium from meteoroids in the vicinity of the Sun: Application to Geminids. *Icarus*, 202: 361–370, August 2009. doi: 10.1016/j.icarus.2009.02.034.

D. Čapek and J. Borovička. Ablation of small Fe meteoroids-First results. *Planetary and Space Science*, 143:159–163, September 2017. doi: 10.1016/j.pss.2017.03.004.

R. Štork, J. Borovička, J. Boček, and M. Šolc. TV spectra of shower meteors. In W. J. Baggaley and V. Porubcan, editors, *Meteroids 1998*, page 371, 1999.

V. Vojáček, J. Borovička, P. Koten, P. Spurný, and R. Štork. Catalogue of representative meteor spectra. *Astronomy and Astrophysics*, 580:A67, August 2015. doi: 10.1051/0004-6361/201425047.

T. Vondrak, J. M. C. Plane, S. Broadley, and D. Janches. A chemical model of meteoric ablation. *Atmospheric Chemistry & Physics*, 8:7015–7031, December 2008.

K. J. Walsh, A. Morbidelli, S. N. Raymond, D. P. O'Brien, and A. M. Mandell. A low mass for Mars from Jupiter's early gas-driven migration. *Nature*, 475: 206–209, July 2011. doi: 10.1038/nature10201.

R. J. Weryk, M. D. Campbell-Brown, P. A. Wiegert, P. G. Brown, Z. Krzeminski, and R. Musci. The Canadian Automated Meteor Observatory (CAMO): System overview. *Icarus*, 225:614–622, July 2013. doi: 10.1016/j.icarus.2013.04.025.

F. L. Whipple. Photographic meteor studies I. In *Publications of the American Astronomical Society*, volume 9 of *Publications of the American Astronomical Society*, page 136, 1939.

F. L. Whipple. A comet model. I. The acceleration of Comet Encke. *Astrophysical Journal*, 111:375–394, March 1950. doi: 10.1086/145272.

F. L. Whipple. A Comet Model. II. Physical Relations for Comets and Meteors. *Astrophysical Journal*, 113:464, May 1951. doi: 10.1086/145416.

F. L. Whipple. Photographic meteor orbits and their distribution in space. *Astronomical Journal*, 59:201, July 1954. doi: 10.1086/106998.

Appendix

Figure A.1: Monochromatic lightcurves of meteors. Intensities of sodium, magnesium and iron lines were derived from the fit of the spectrum.

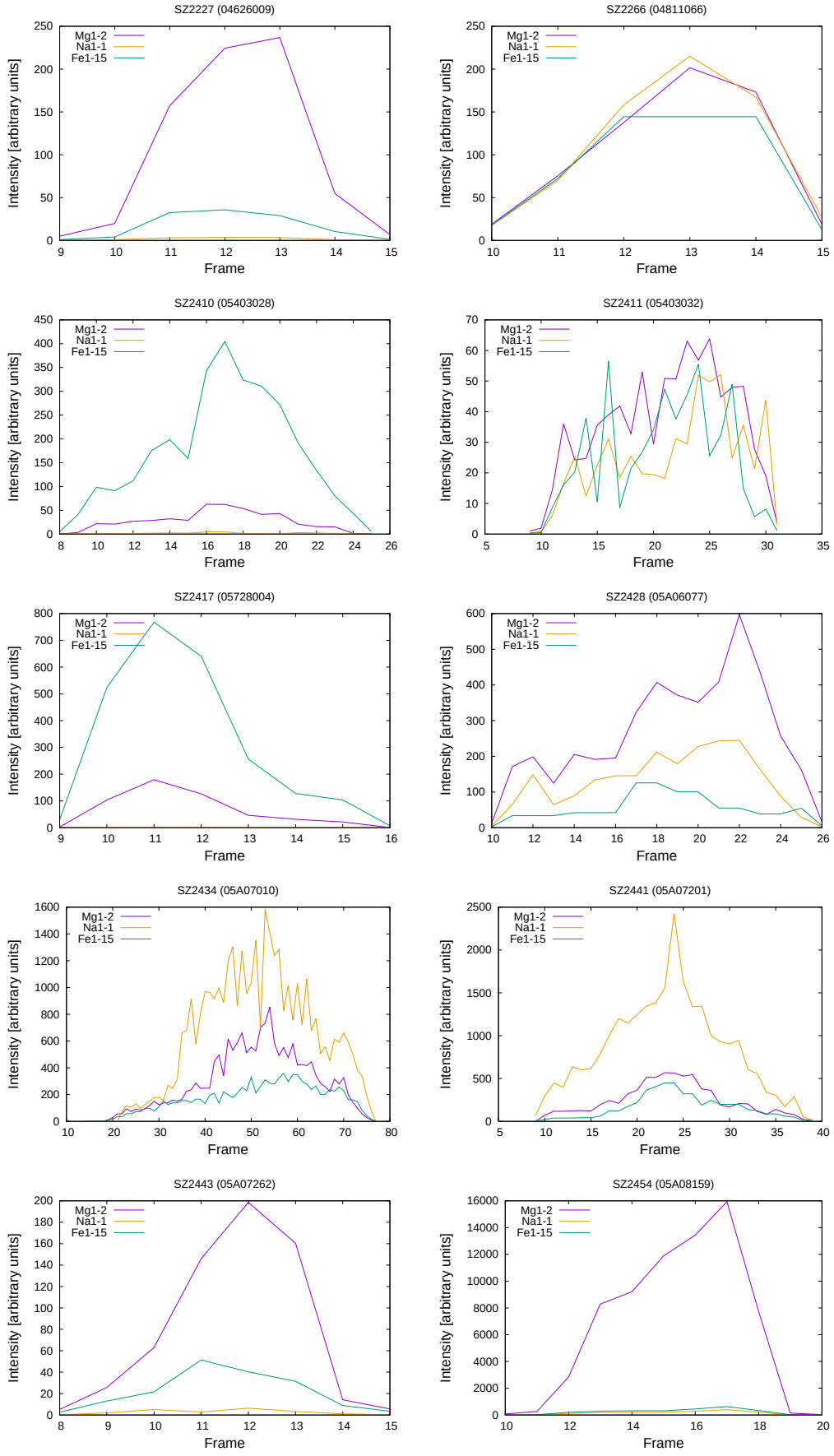

Figure A.2: Monochromatic lightcurves of meteors. Intensities of sodium, magnesium and iron lines were derived from the fit of the spectrum.

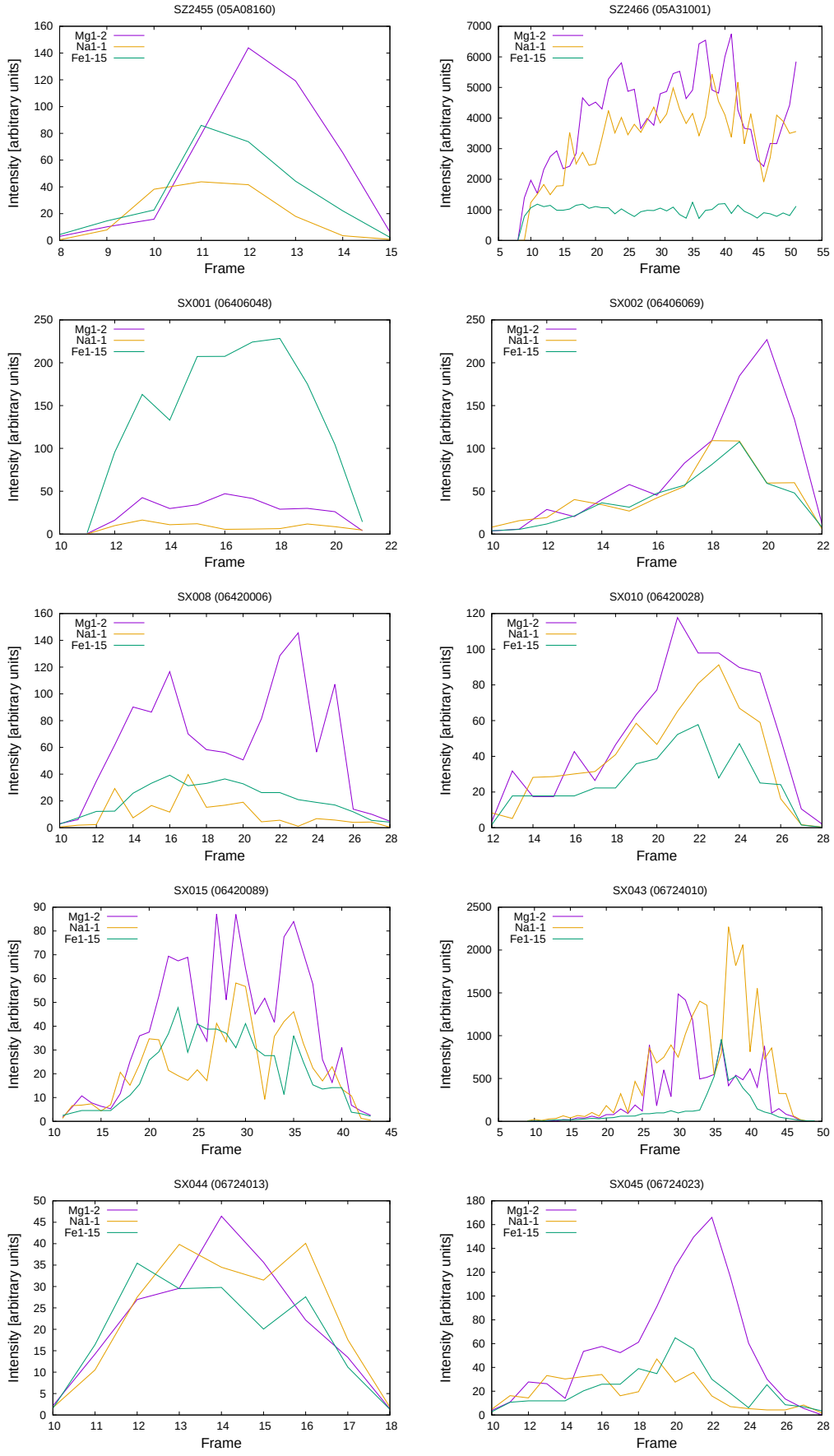

Figure A.3: Monochromatic lightcurves of meteors. Intensities of sodium, magnesium and iron lines were derived from the fit of the spectrum.

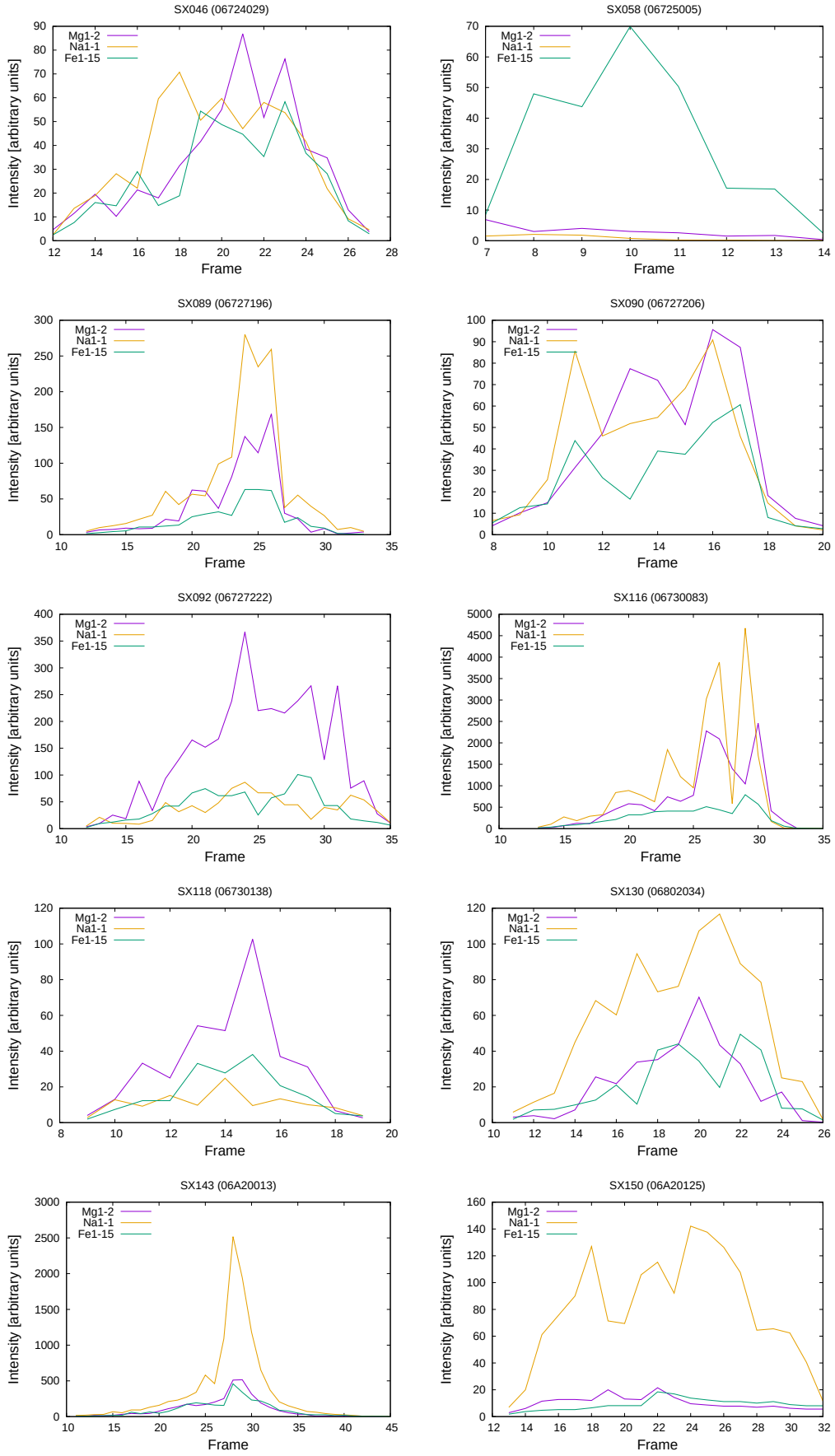

Figure A.4: Monochromatic lightcurves of meteors. Intensities of sodium, magnesium and iron lines were derived from the fit of the spectrum.

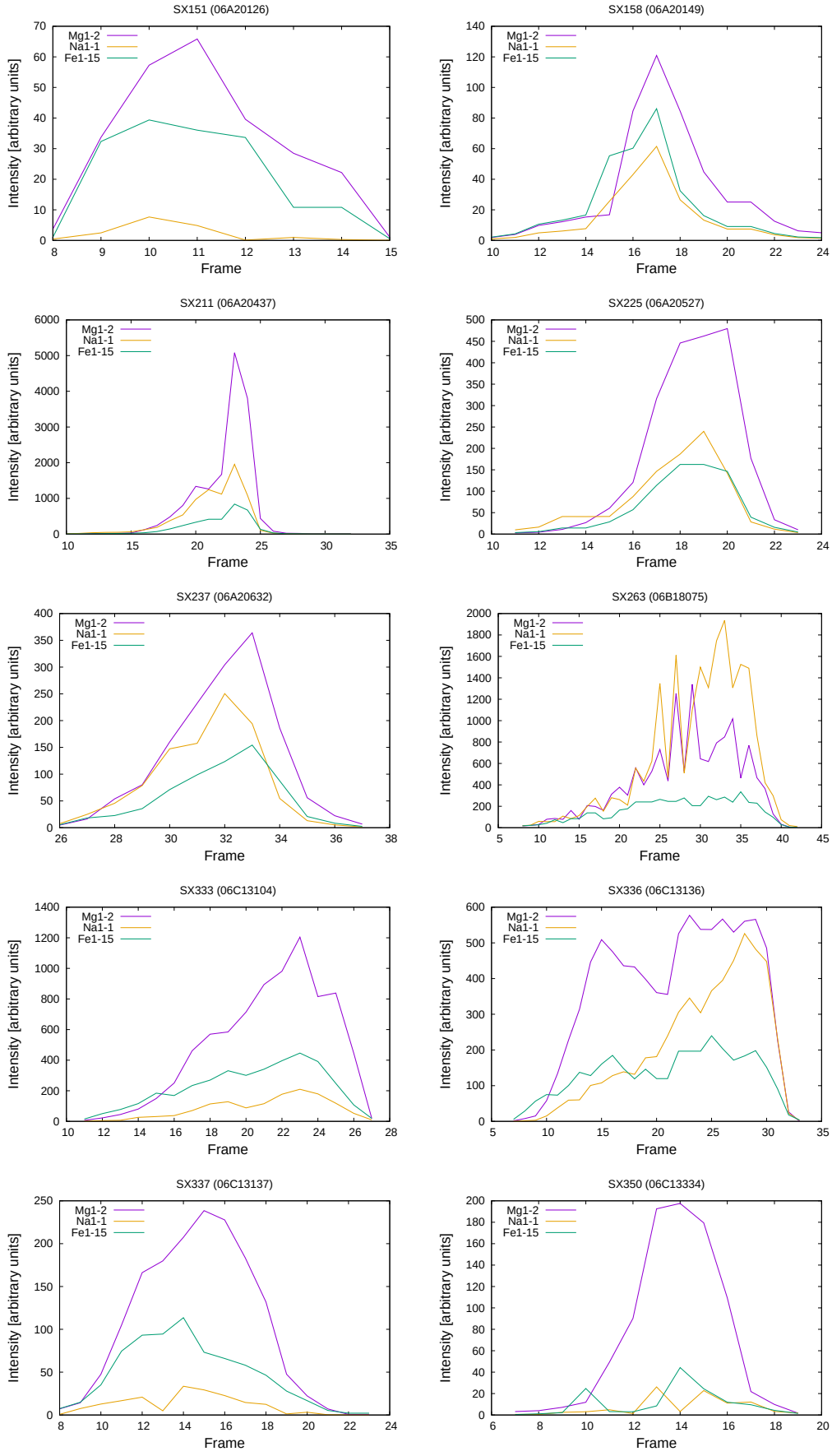

Figure A.5: Monochromatic lightcurves of meteors. Intensities of sodium, magnesium and iron lines were derived from the fit of the spectrum.

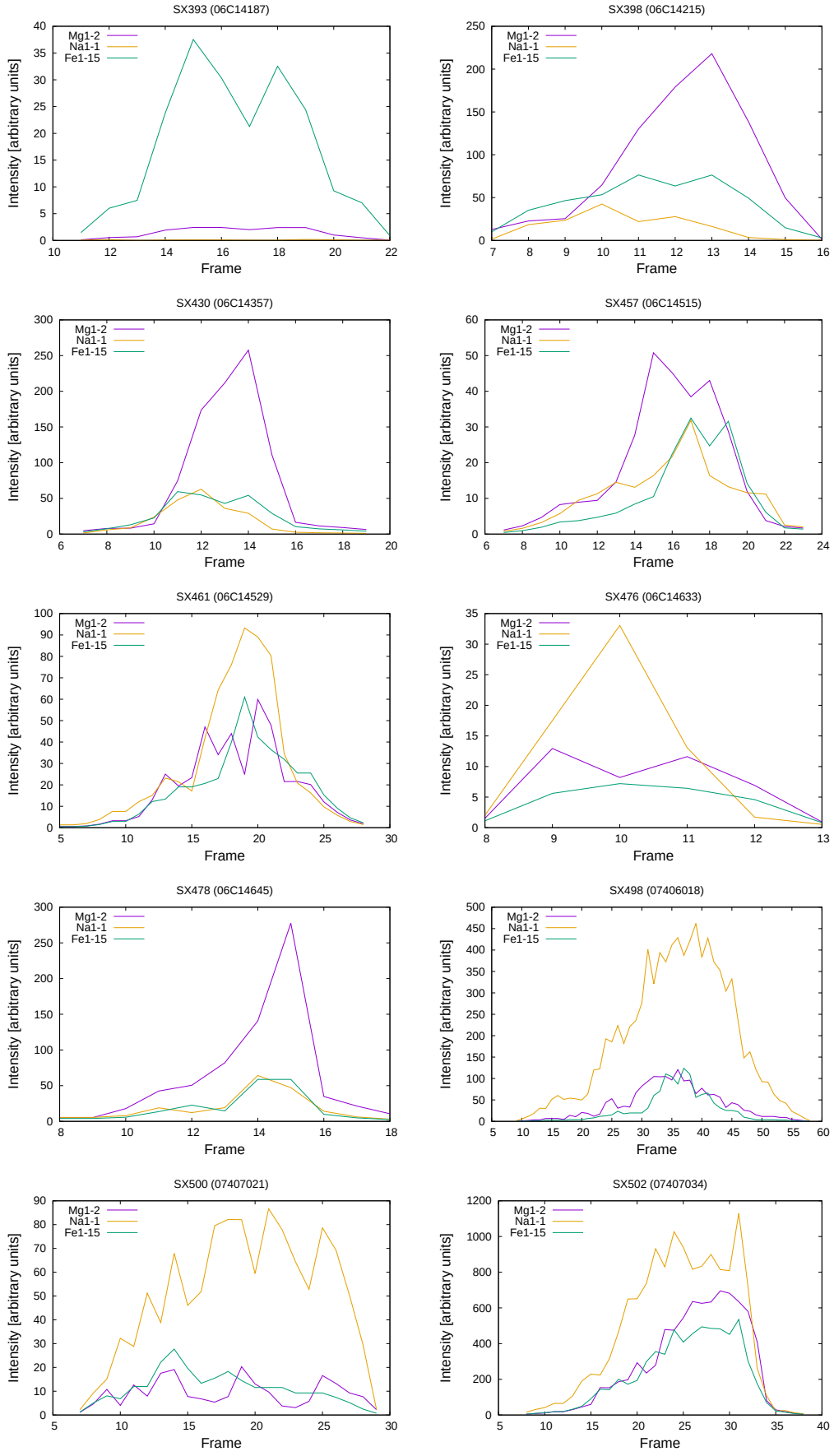

Figure A.6: Monochromatic lightcurves of meteors. Intensities of sodium, magnesium and iron lines were derived from the fit of the spectrum.

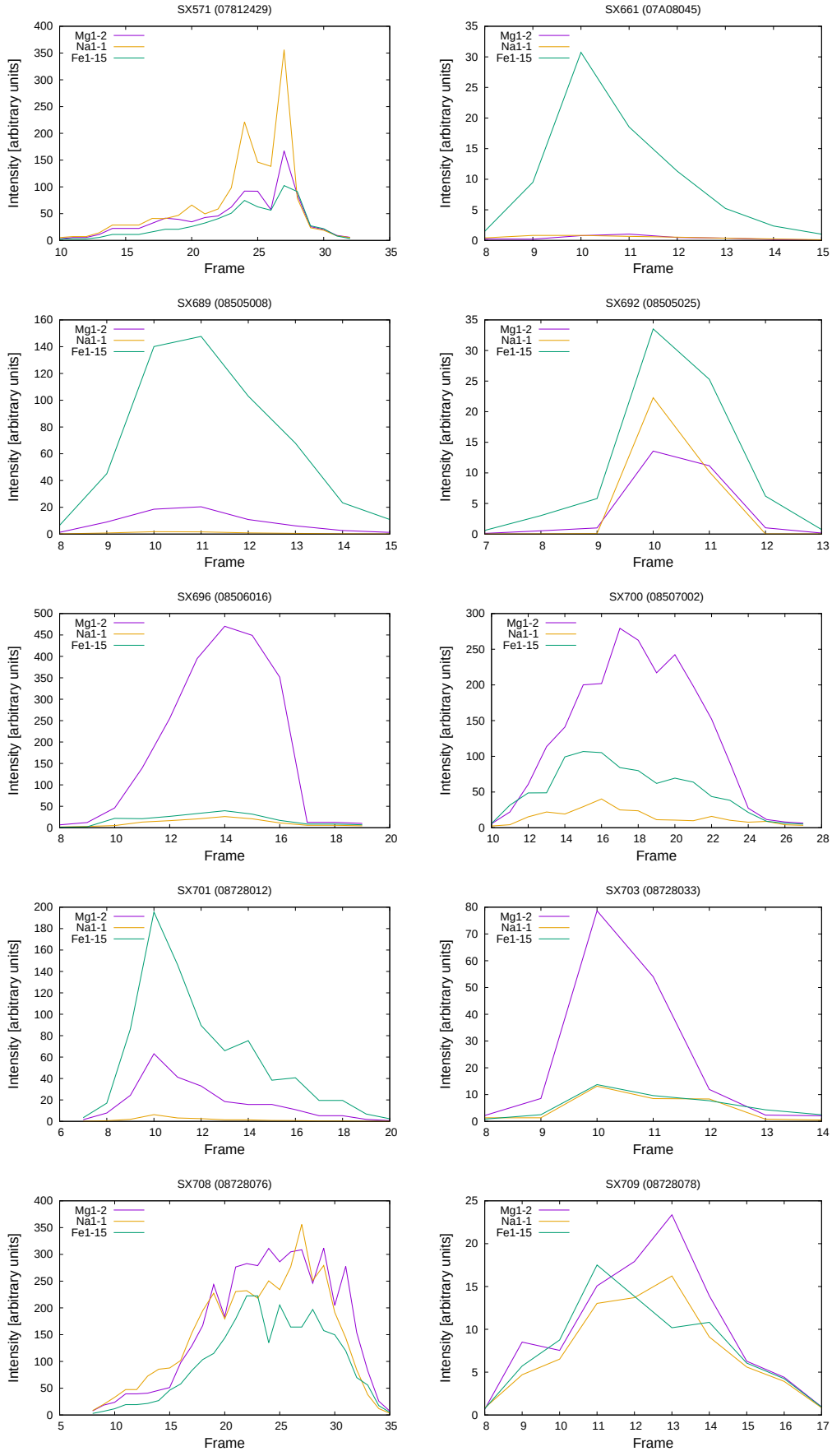

Figure A.7: Monochromatic lightcurves of meteors. Intensities of sodium, magnesium and iron lines were derived from the fit of the spectrum.

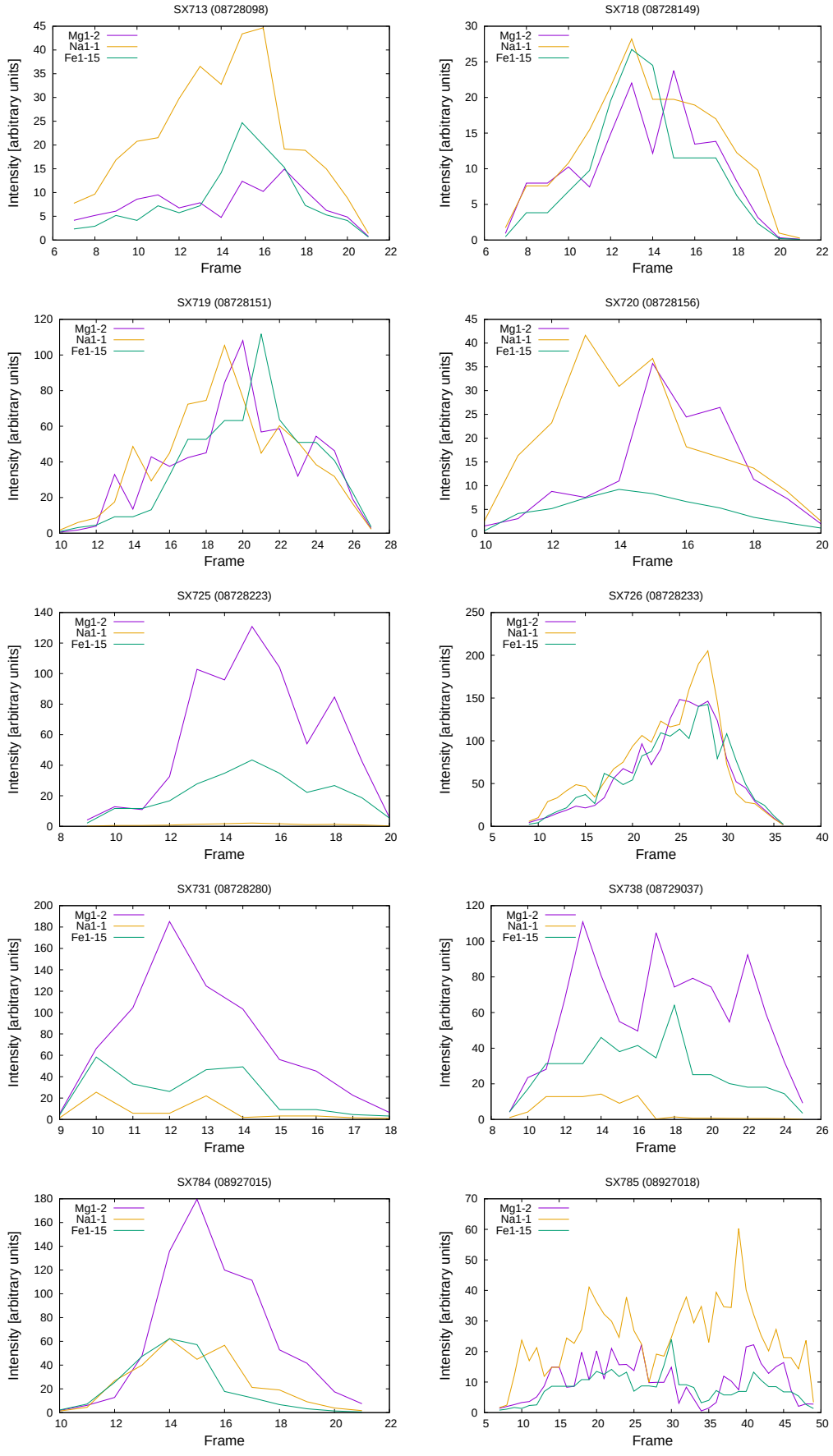

Figure A.8: Monochromatic lightcurves of meteors. Intensities of sodium, magnesium and iron lines were derived from the fit of the spectrum.

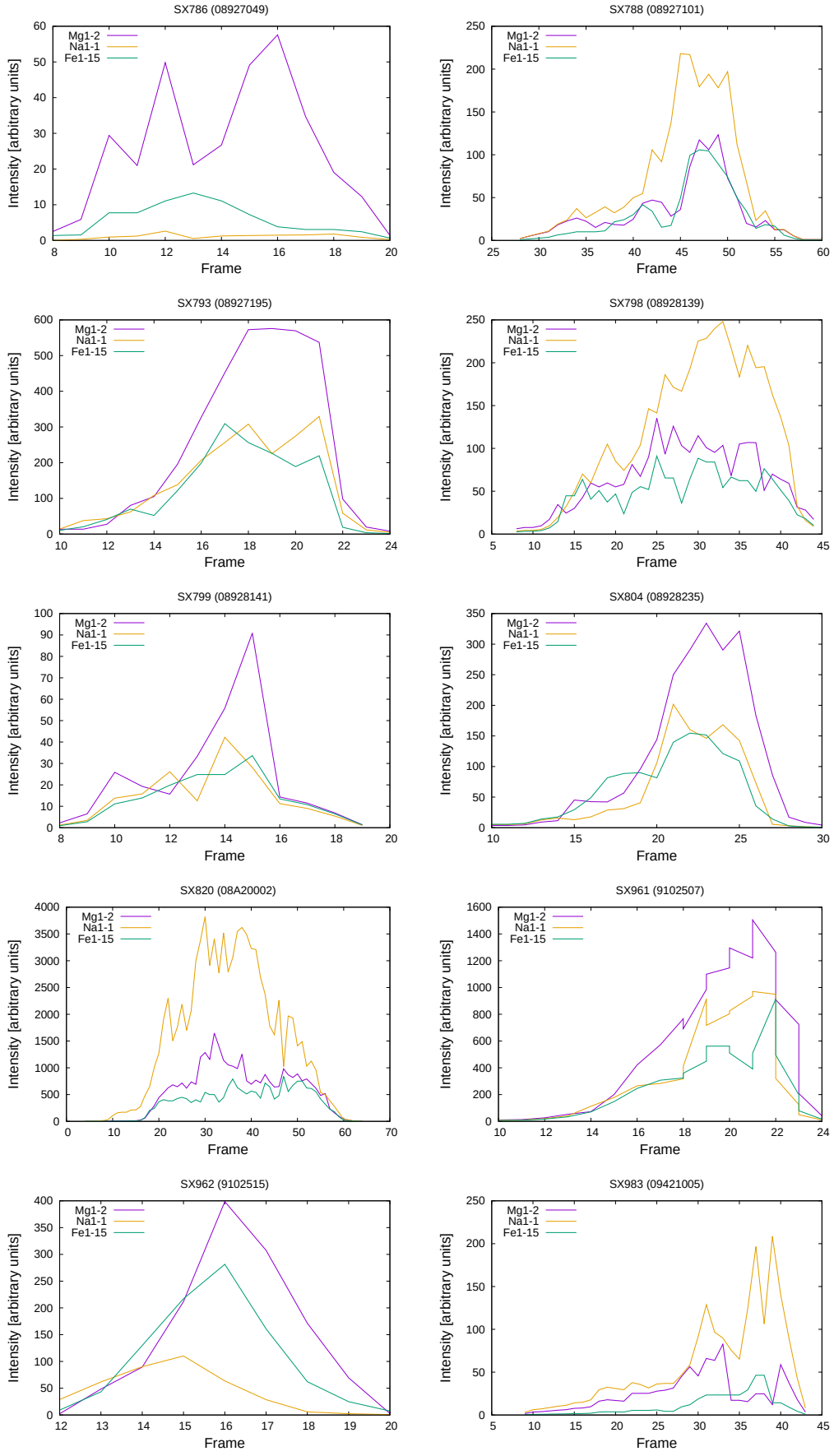

Figure A.9: Monochromatic lightcurves of meteors. Intensities of sodium, magnesium and iron lines were derived from the fit of the spectrum.

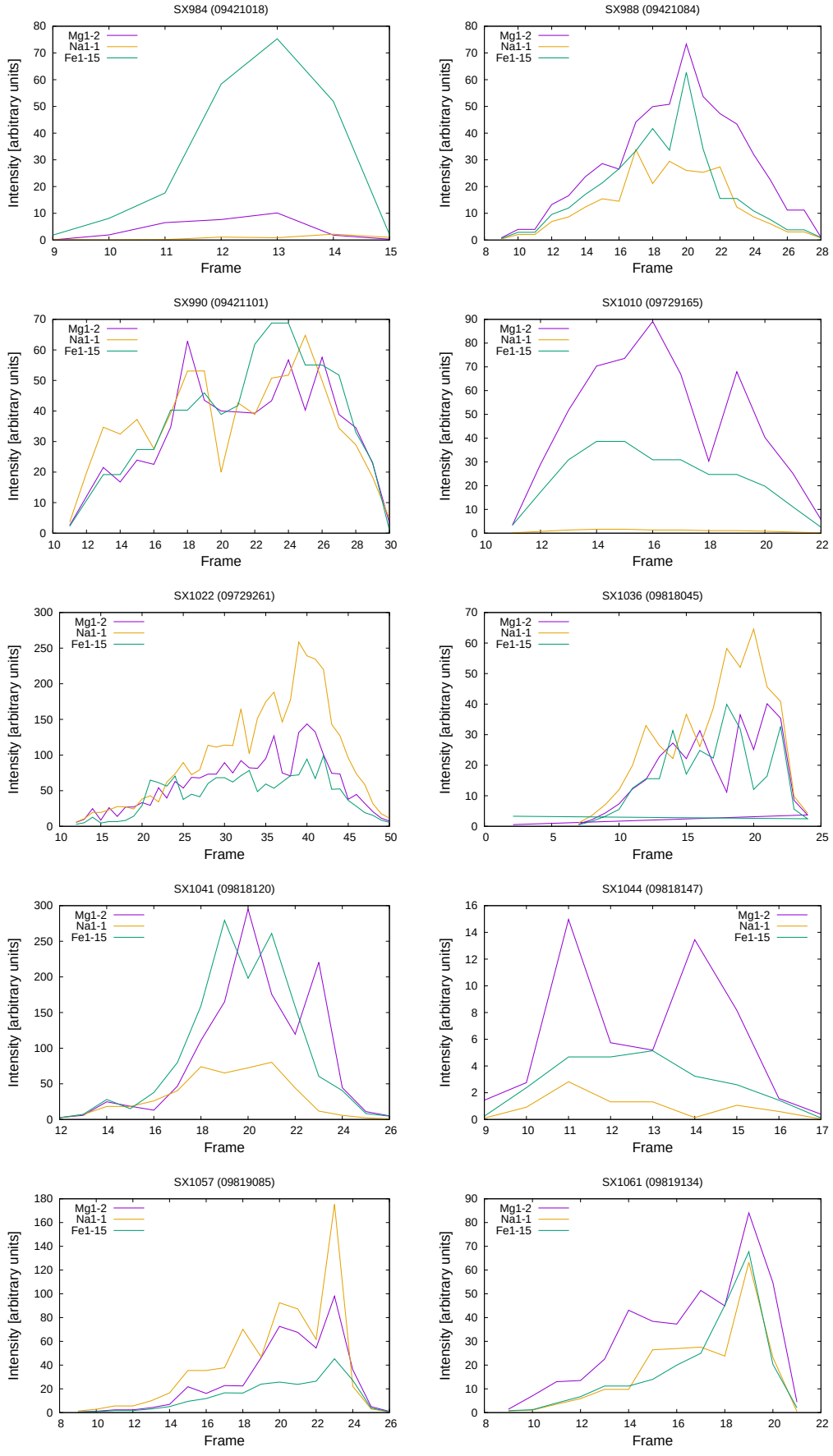

Figure A.10: Monochromatic lightcurves of meteors. Intensities of sodium, magnesium and iron lines were derived from the fit of the spectrum.

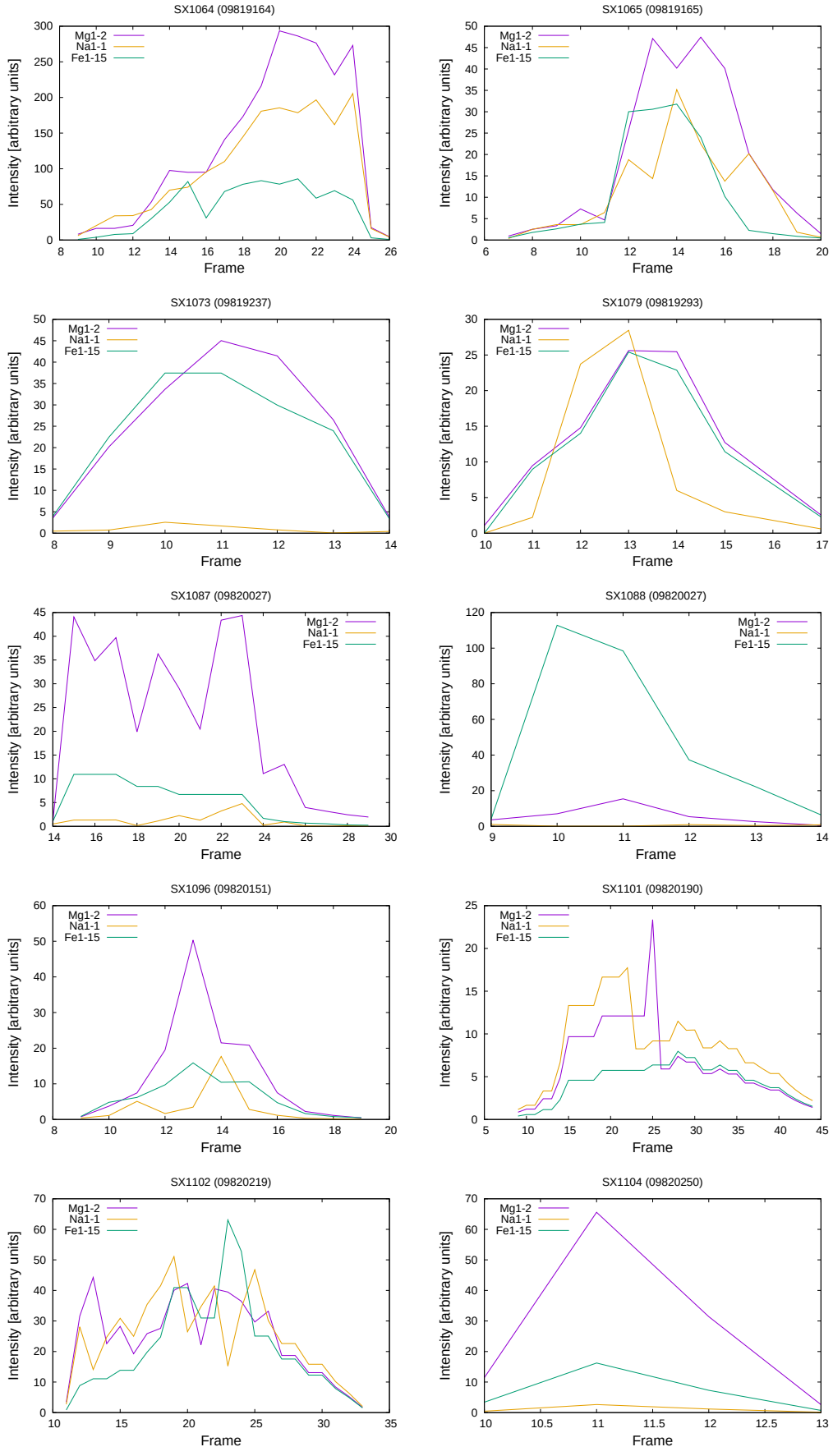

Figure A.11: Monochromatic lightcurves of meteors. Intensities of sodium, magnesium and iron lines were derived from the fit of the spectrum.

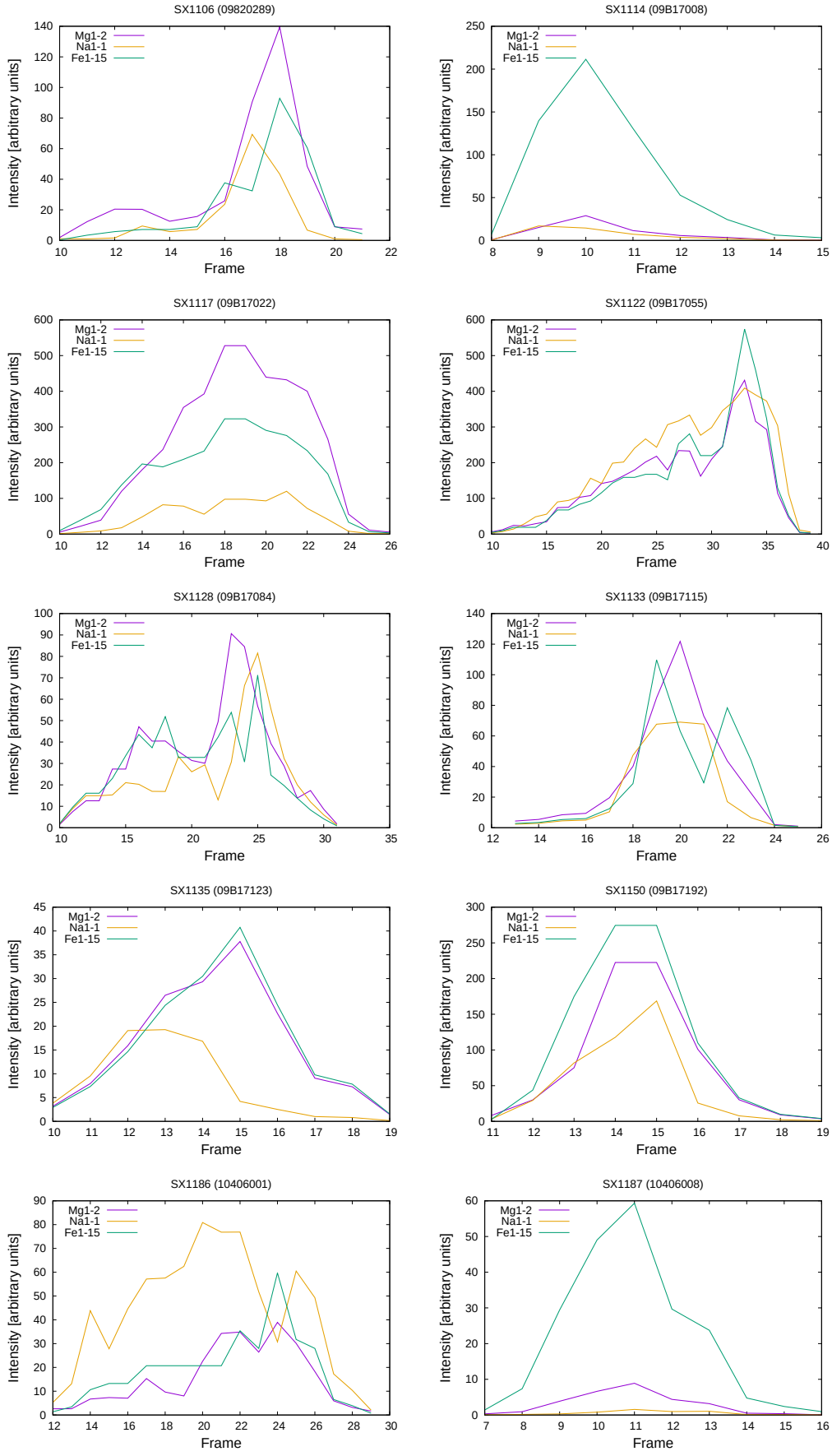

Figure A.12: Monochromatic lightcurves of meteors. Intensities of sodium, magnesium and iron lines were derived from the fit of the spectrum.

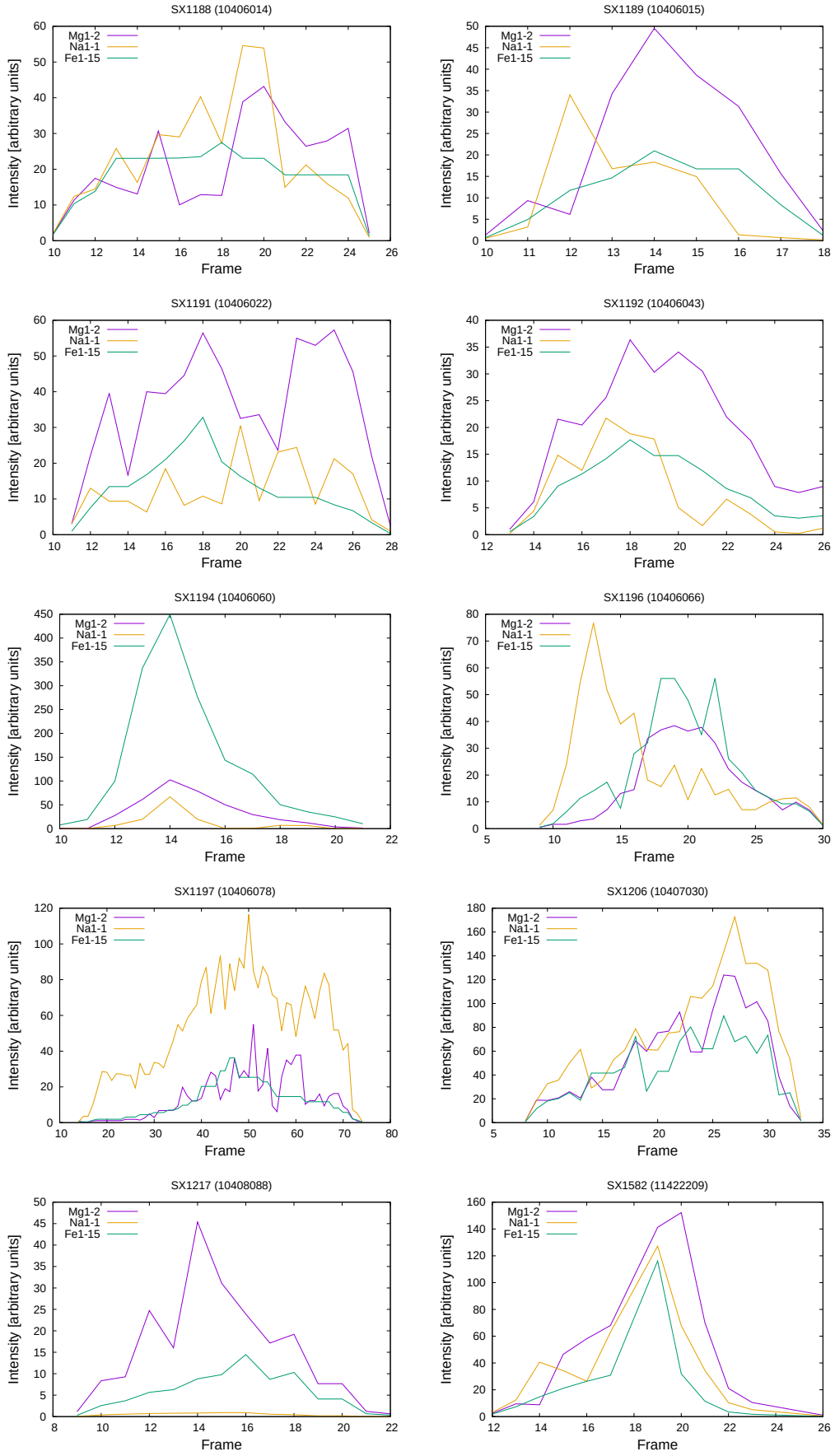

Figure A.13: Monochromatic lightcurves of meteors. Intensities of sodium, magnesium and iron lines were derived from the fit of the spectrum.

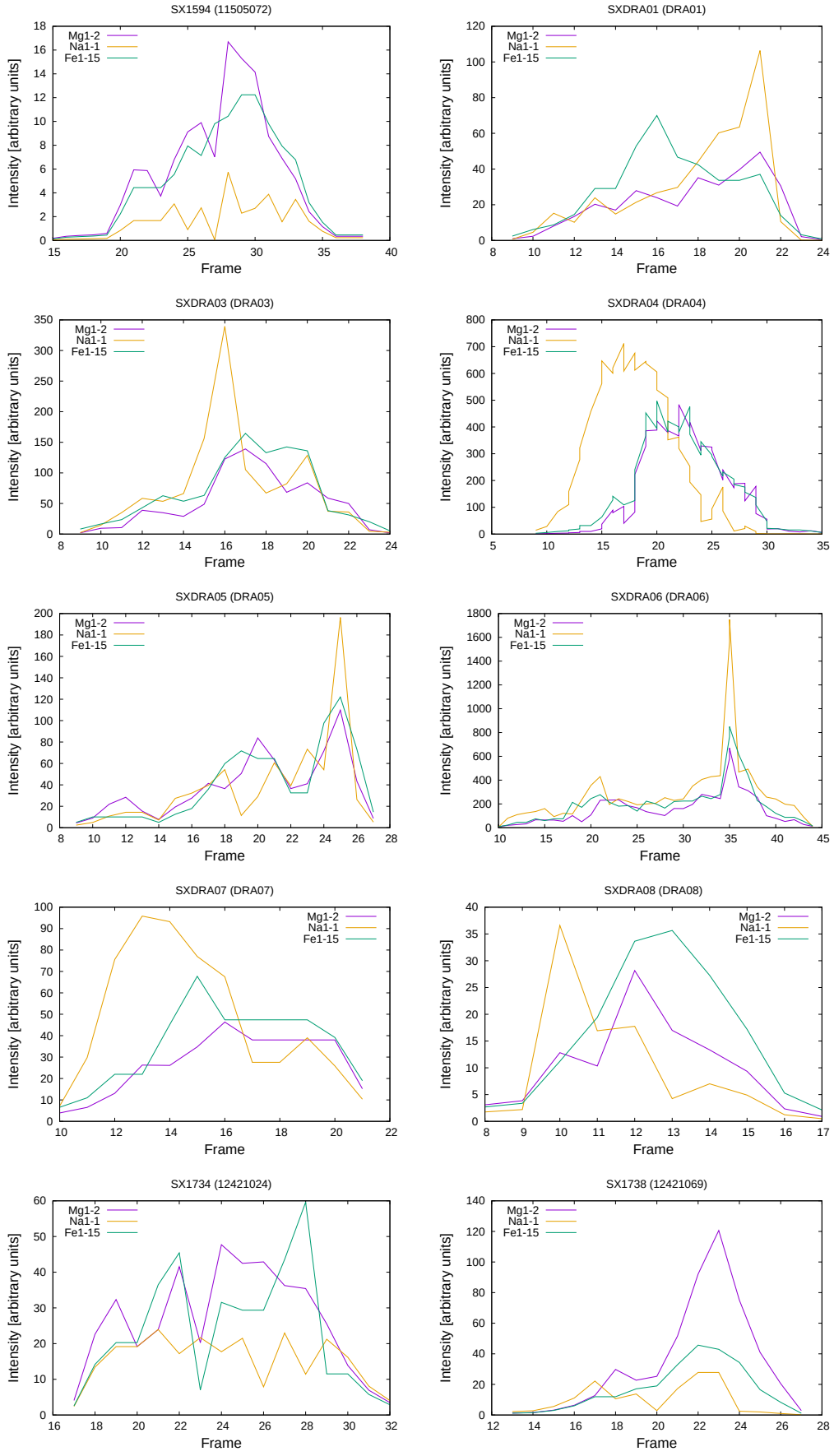

Figure A.14: Monochromatic lightcurves of meteors. Intensities of sodium, magnesium and iron lines were derived from the fit of the spectrum.

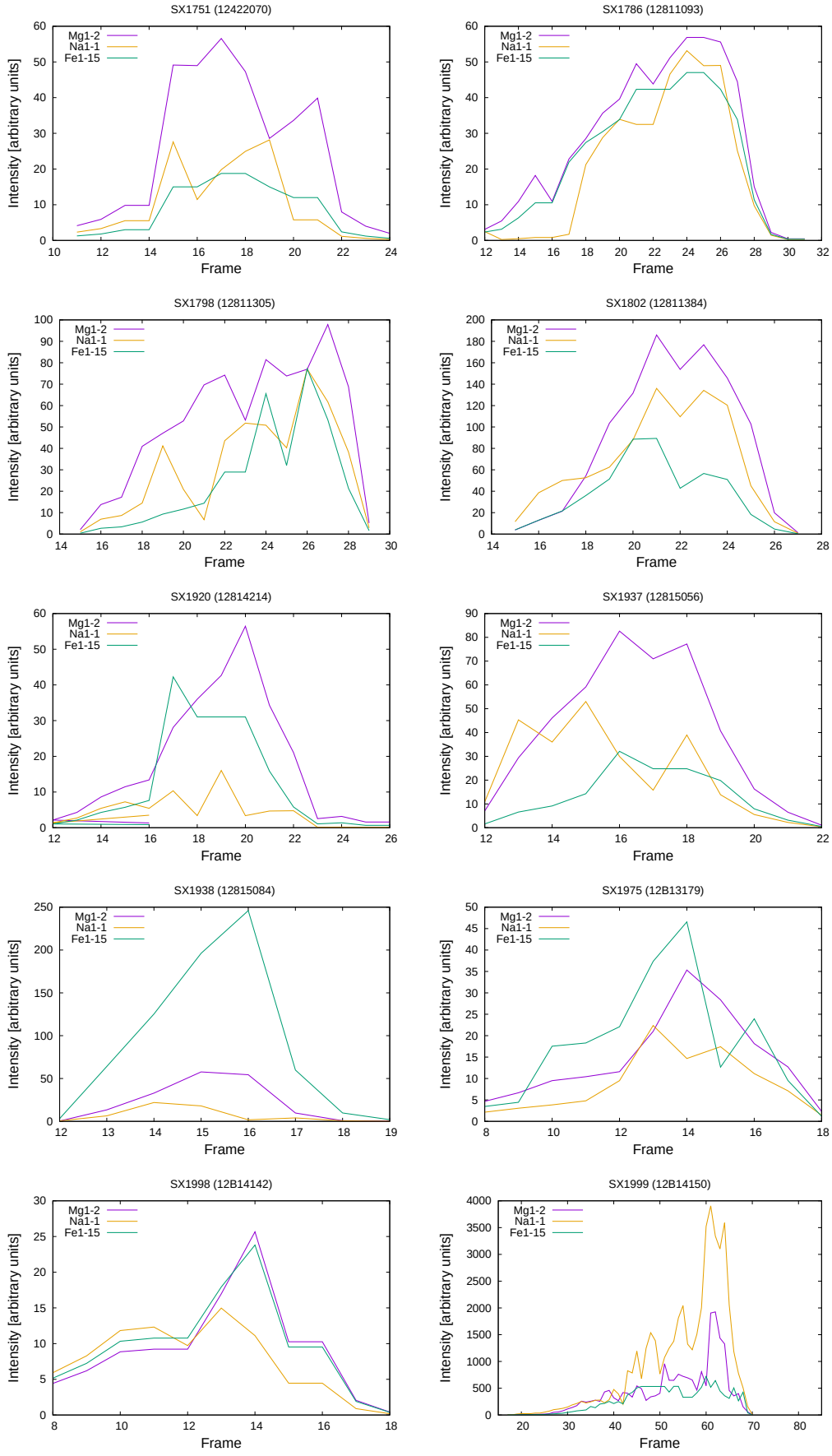

Figure A.15: Monochromatic lightcurves of meteors. Intensities of sodium, magnesium and iron lines were derived from the fit of the spectrum.

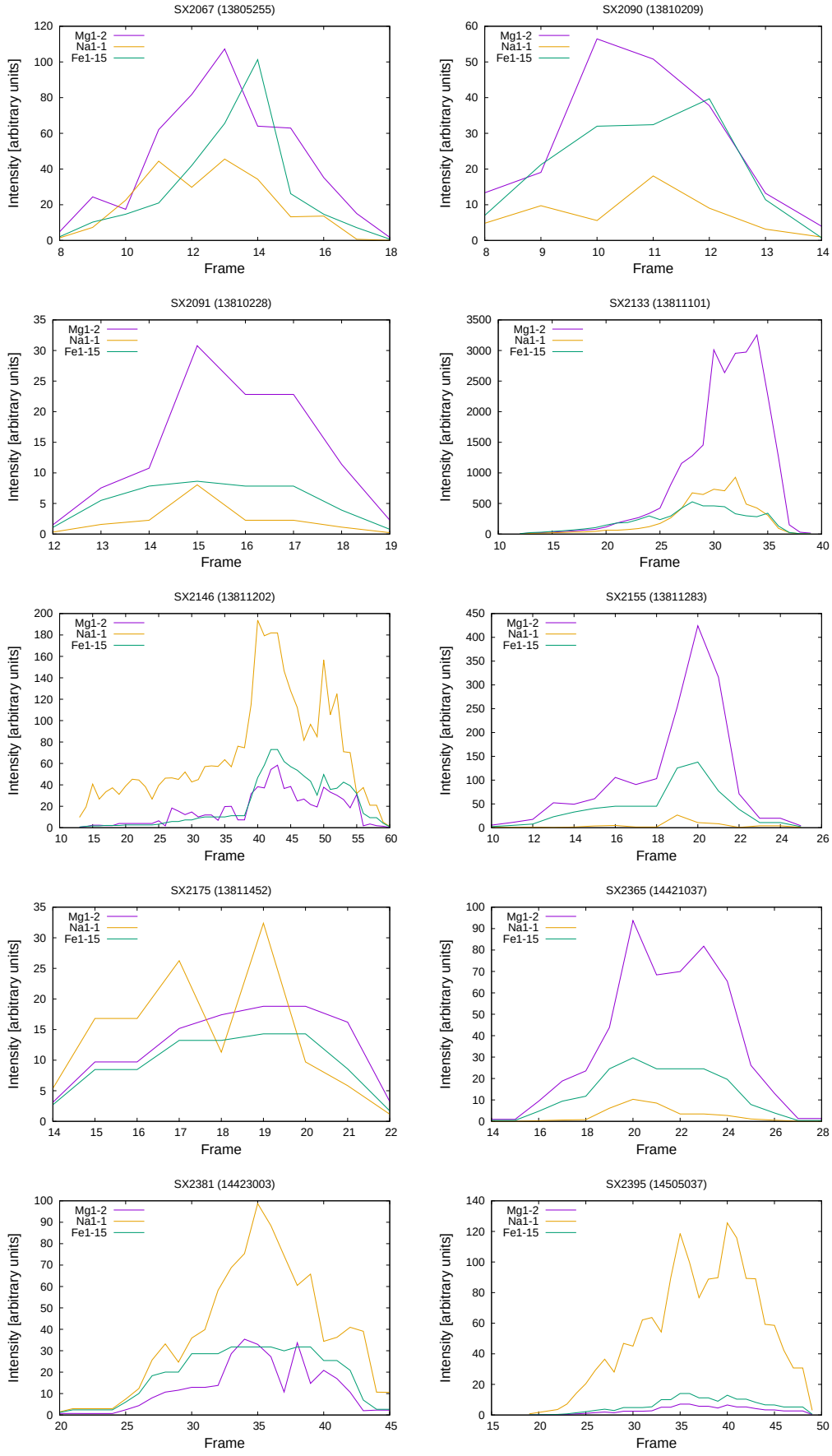

Figure A.16: Monochromatic lightcurves of meteors. Intensities of sodium, magnesium and iron lines were derived from the fit of the spectrum.

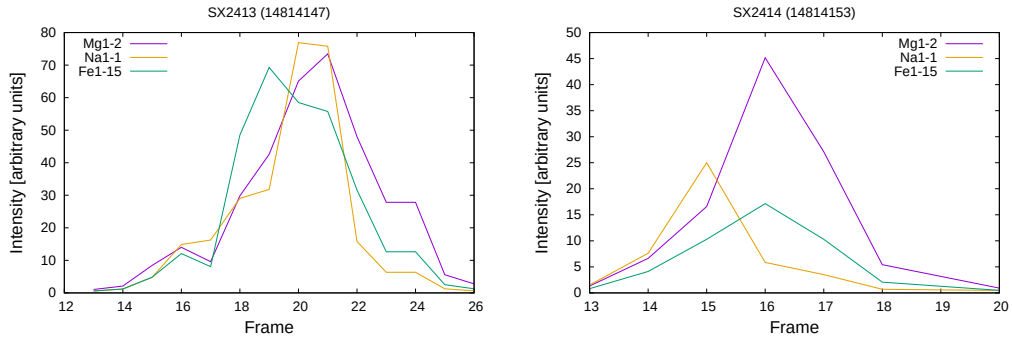

Figure A.17: Deceleration curves, lightcurves and the fit of the fragmentation model for modelled meteoroids.

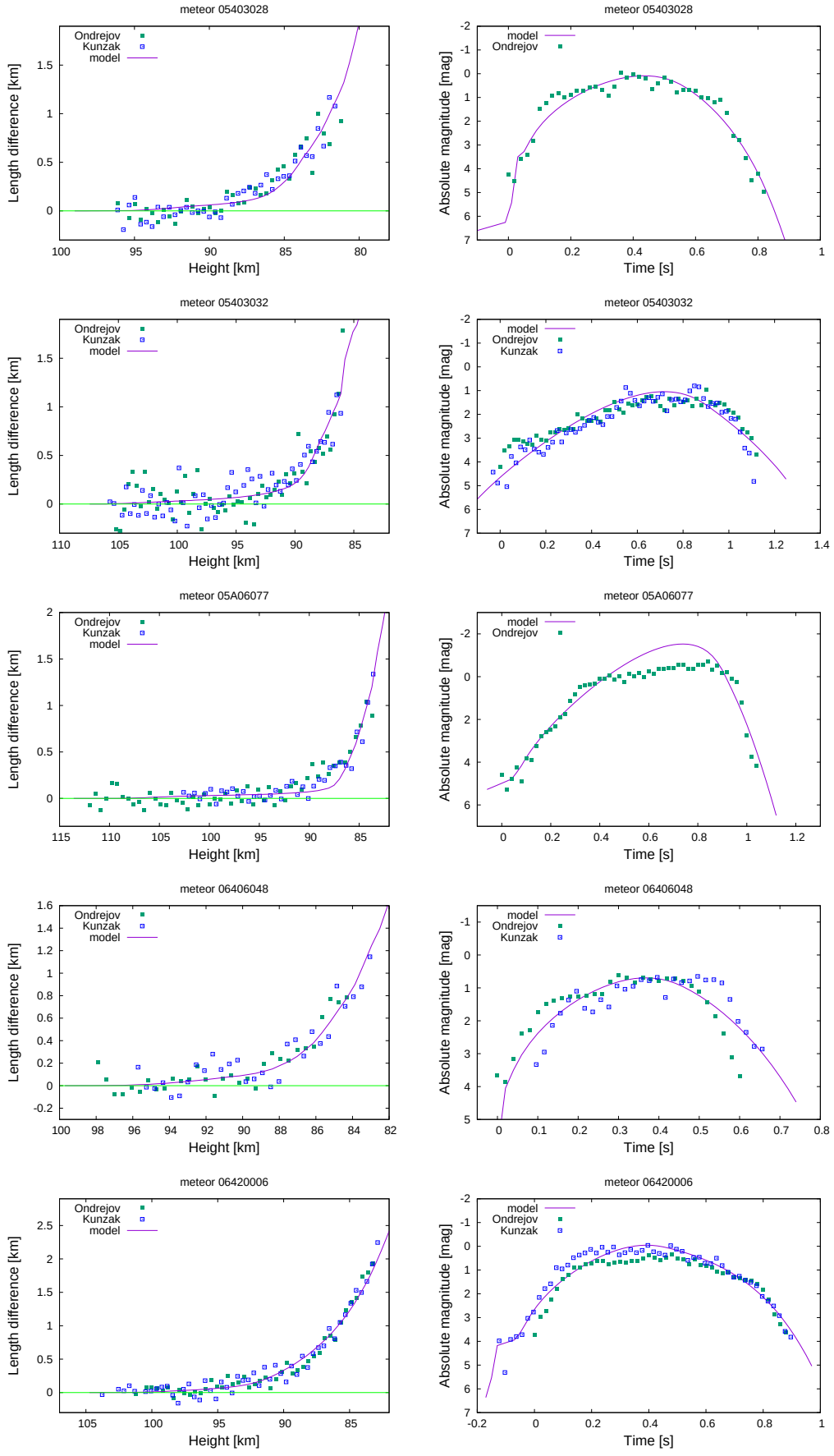

Figure A.18: Deceleration curves, lightcurves and the fit of the fragmentation model for modelled meteoroids.

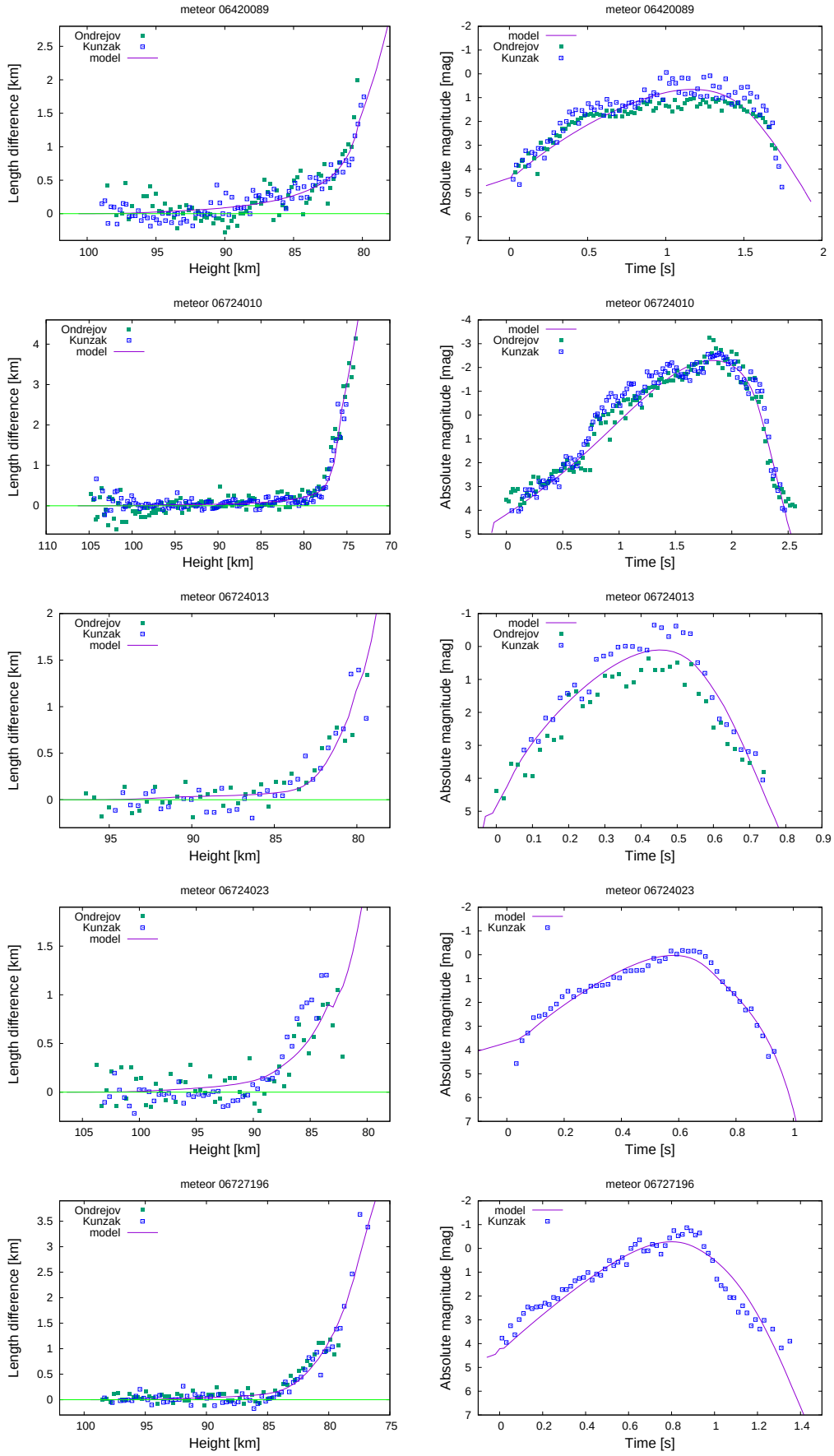

Figure A.19: Deceleration curves, lightcurves and the fit of the fragmentation model for modelled meteoroids.

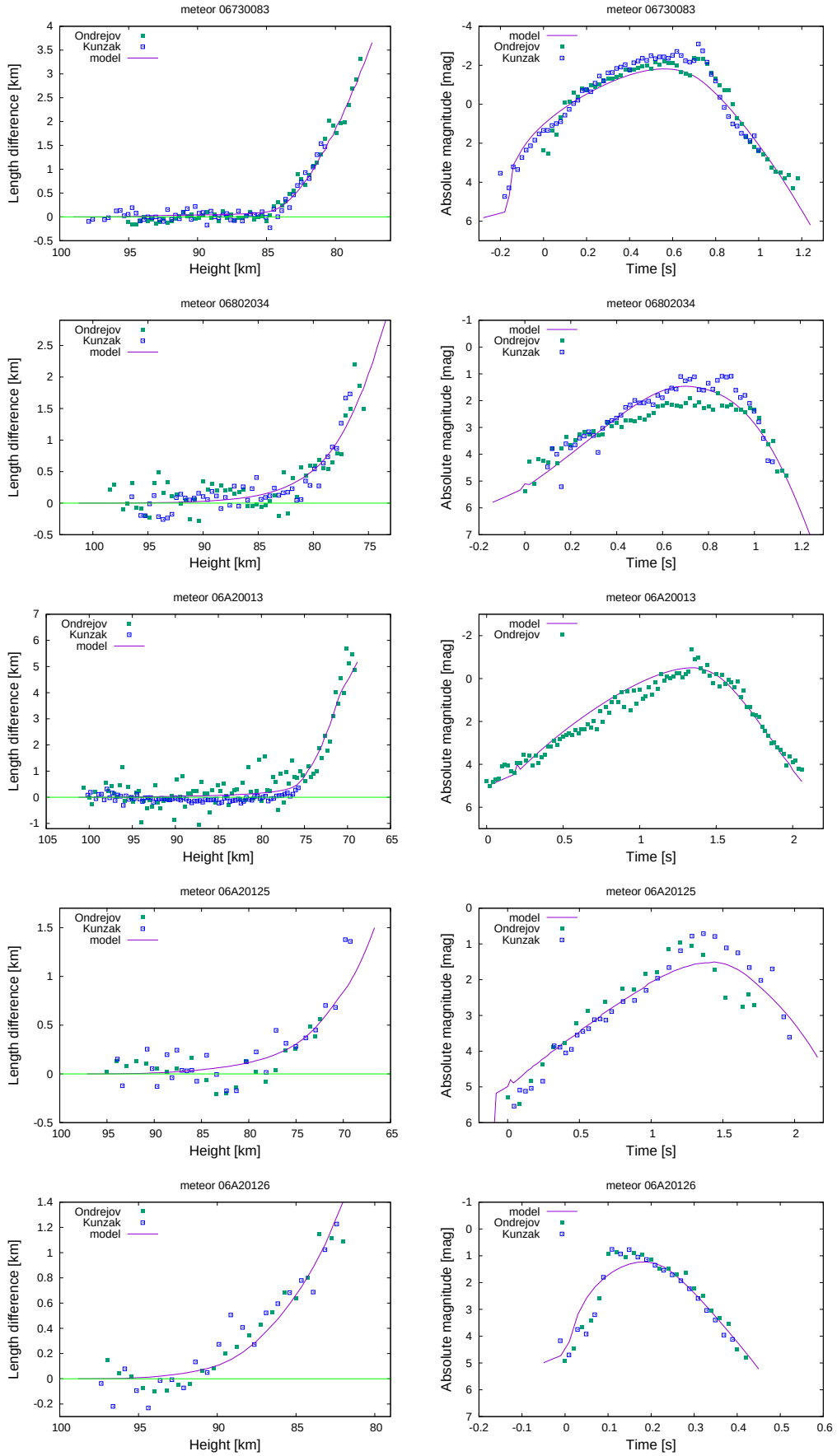

Figure A.20: Deceleration curves, lightcurves and the fit of the fragmentation model for modelled meteoroids.

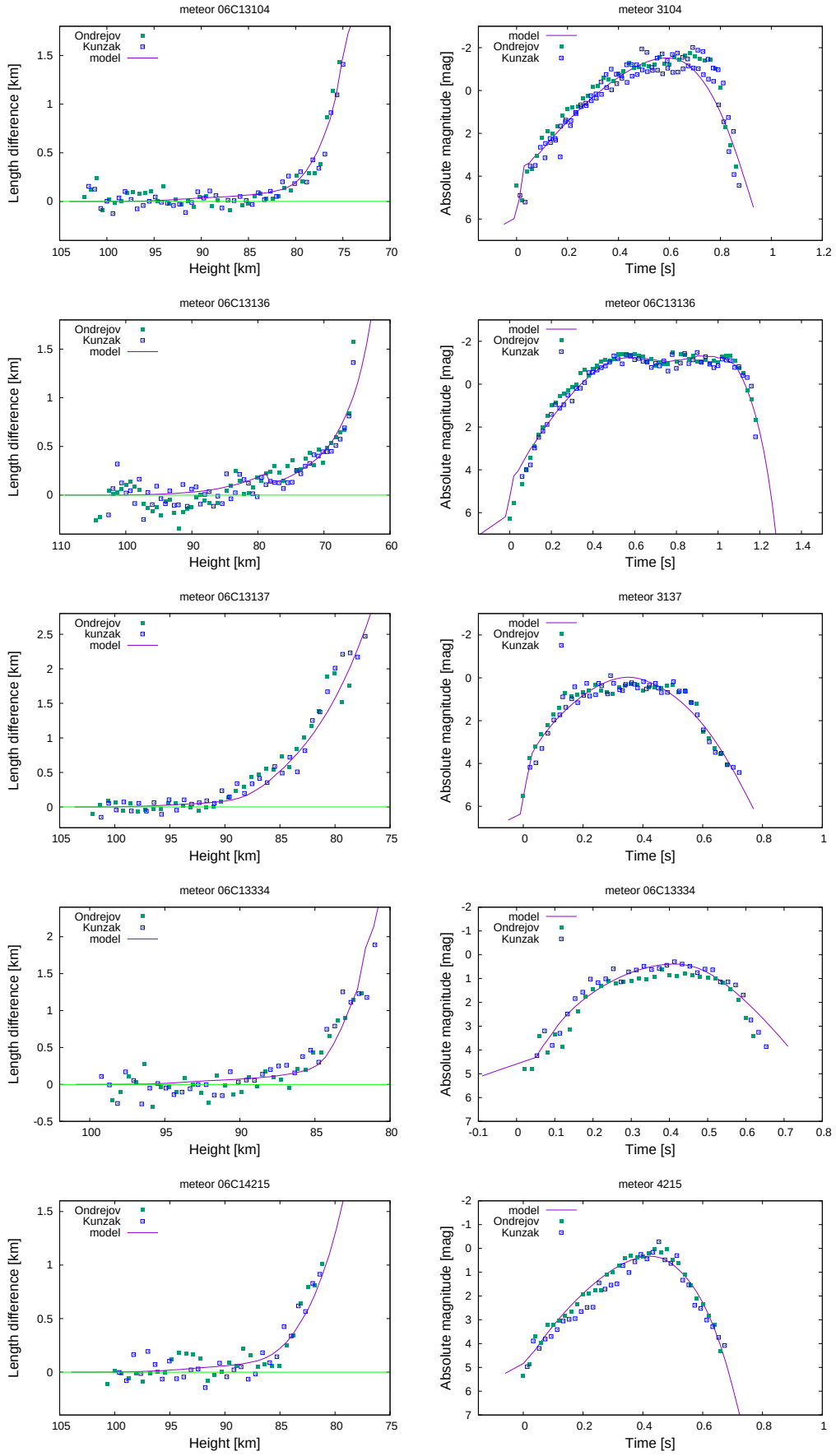

Figure A.21: Deceleration curves, lightcurves and the fit of the fragmentation model for modelled meteoroids.

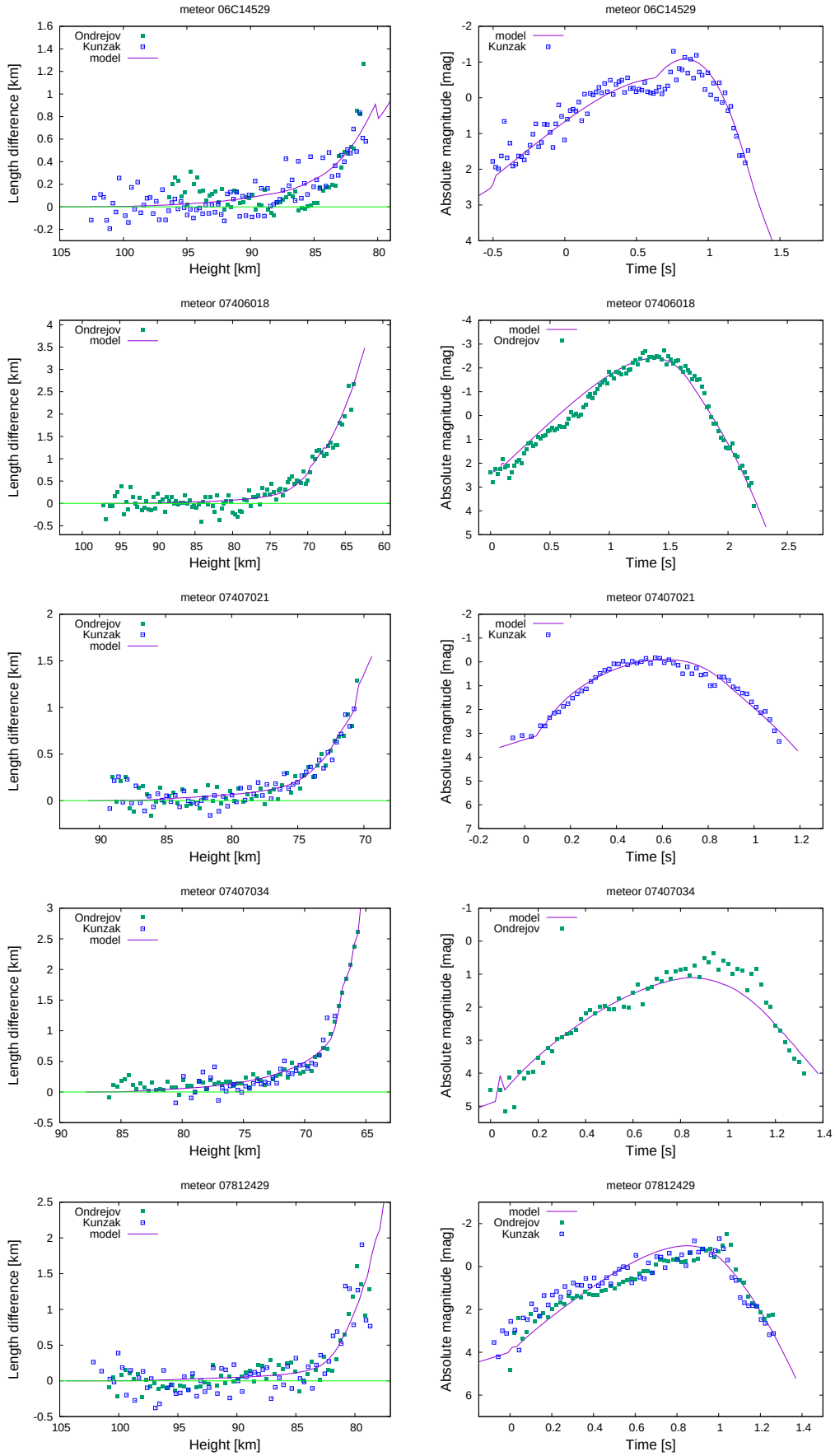

Figure A.22: Deceleration curves, lightcurves and the fit of the fragmentation model for modelled meteoroids.

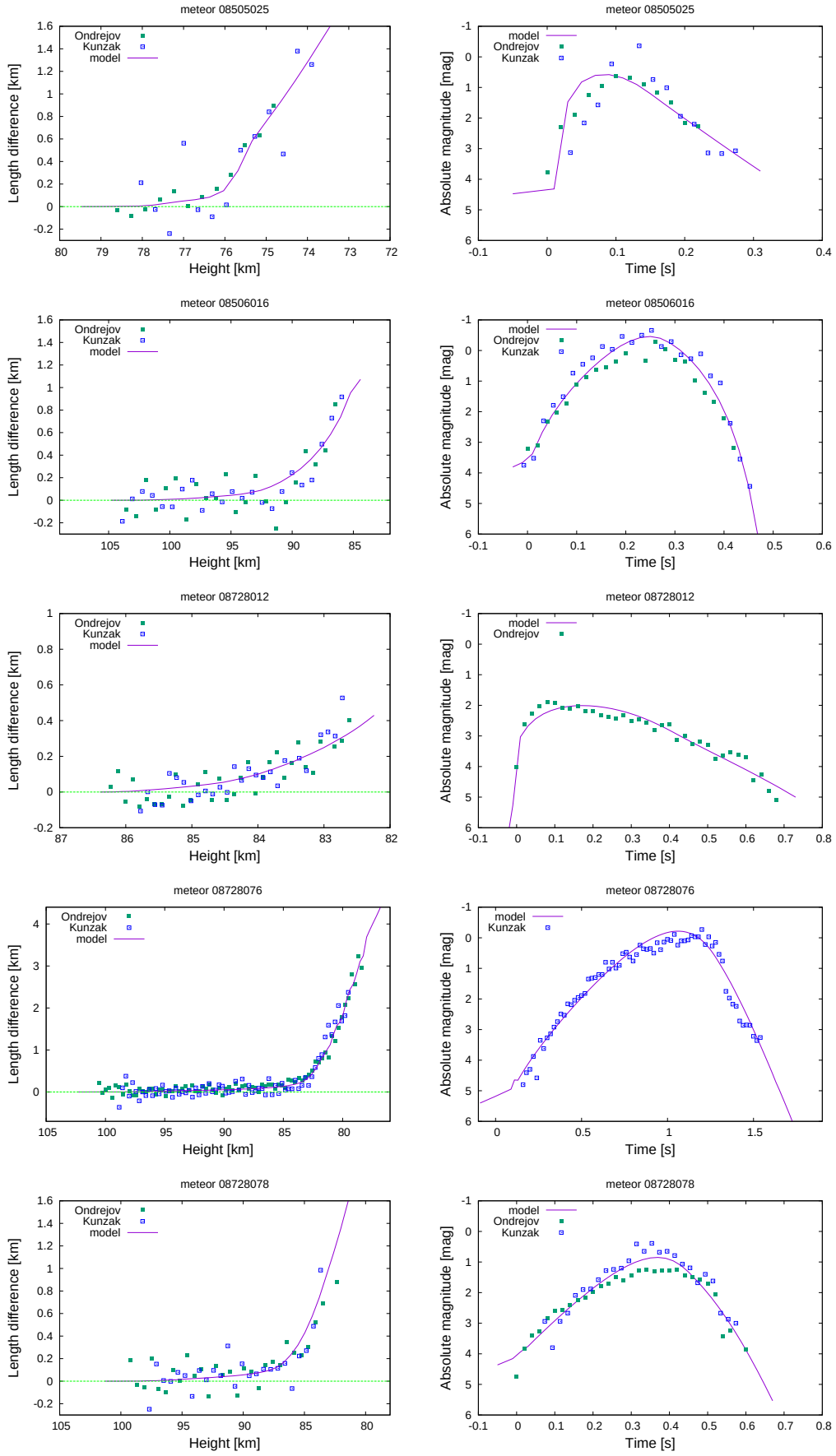

Figure A.23: Deceleration curves, lightcurves and the fit of the fragmentation model for modelled meteoroids.

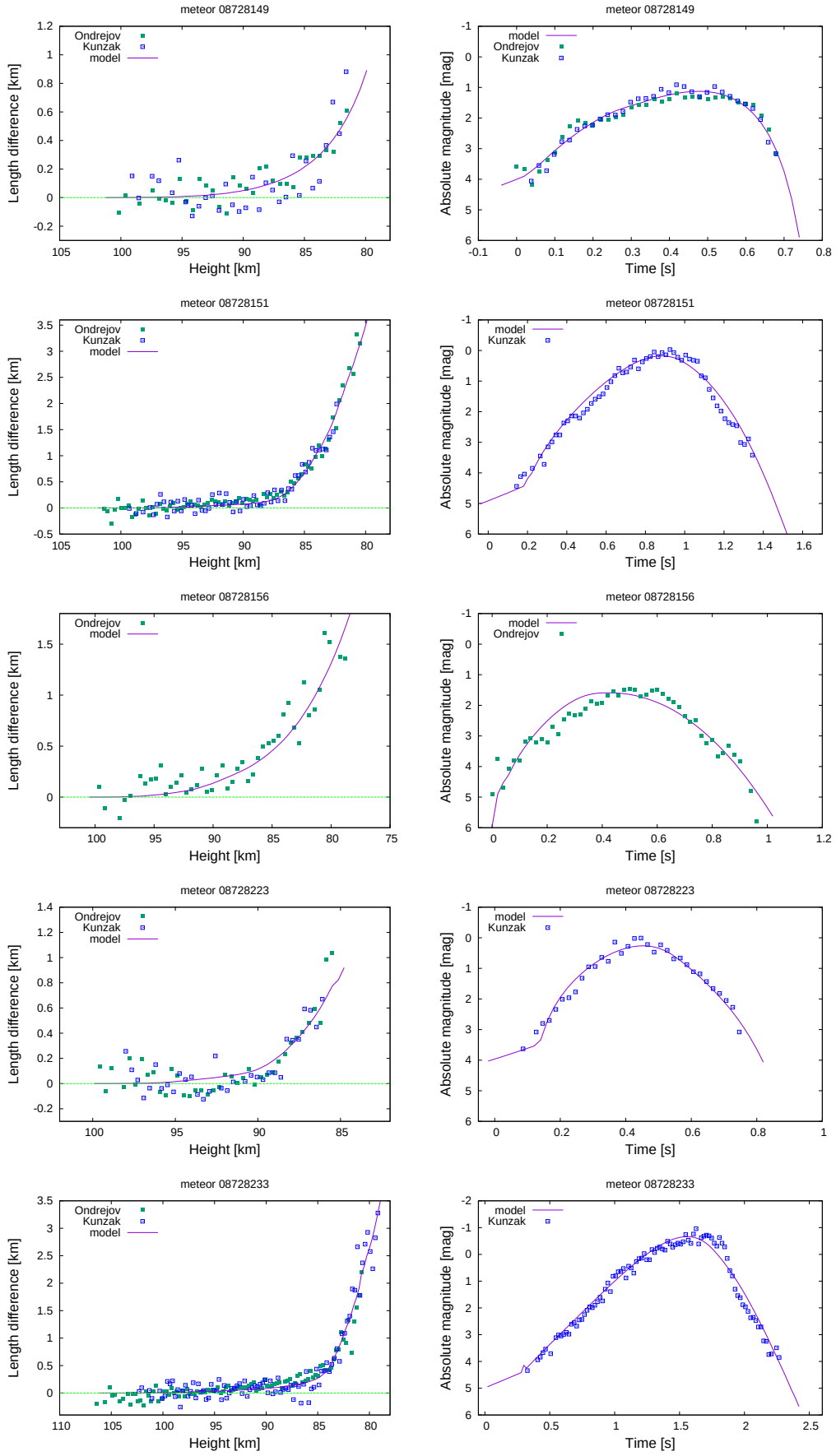

Figure A.24: Deceleration curves, lightcurves and the fit of the fragmentation model for modelled meteoroids.

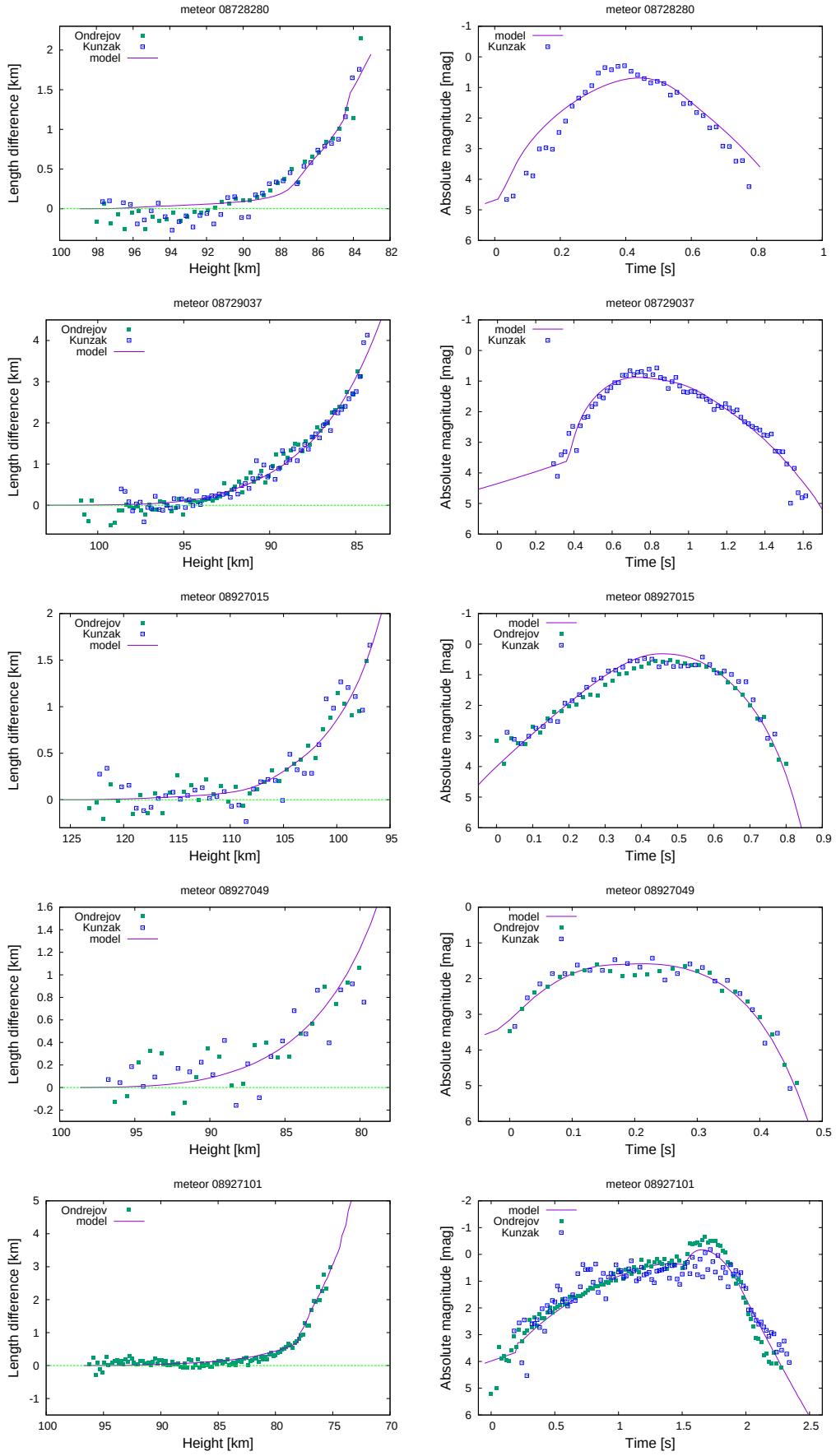

Figure A.25: Deceleration curves, lightcurves and the fit of the fragmentation model for modelled meteoroids.

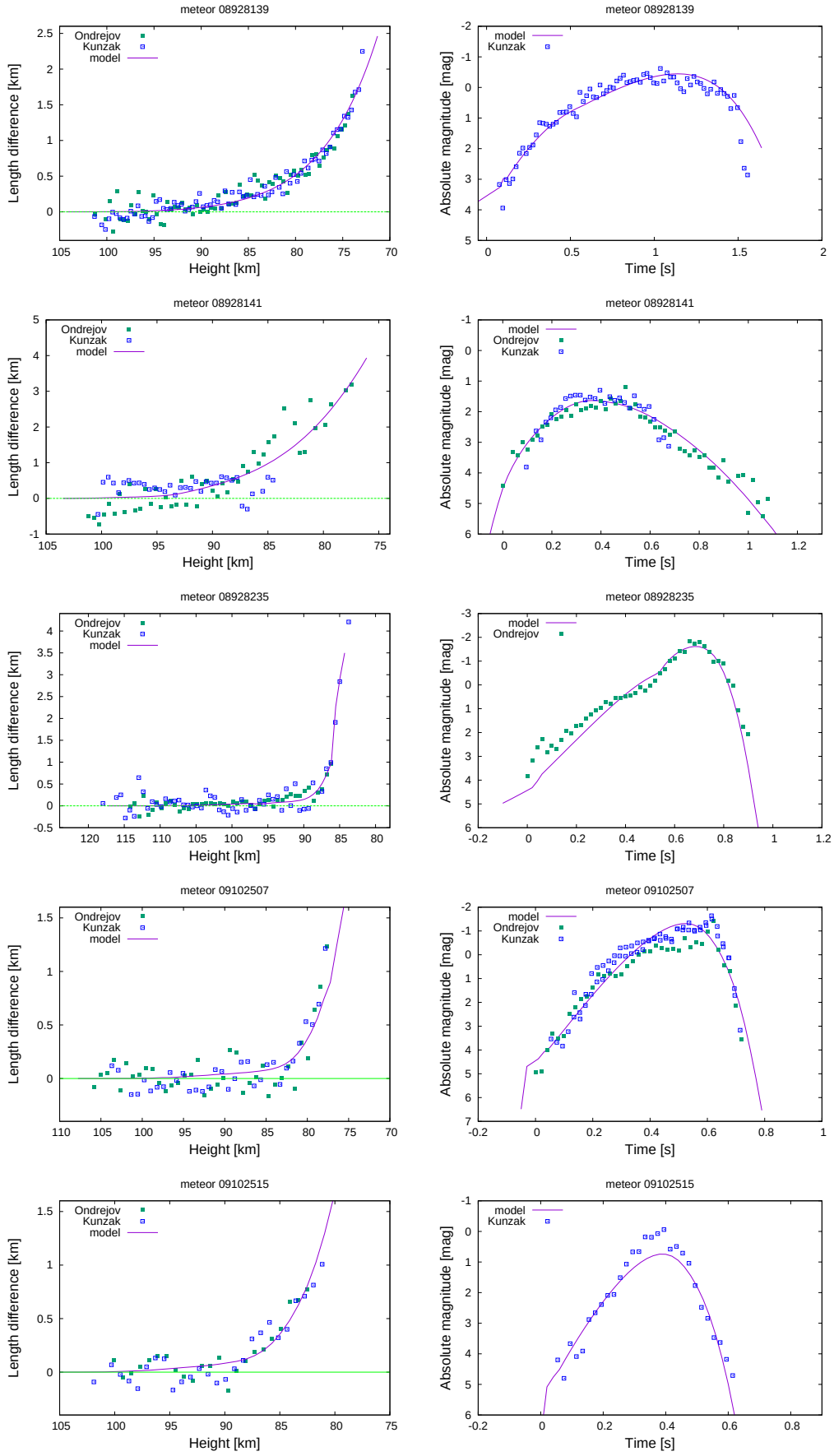

Figure A.26: Deceleration curves, lightcurves and the fit of the fragmentation model for modelled meteoroids.

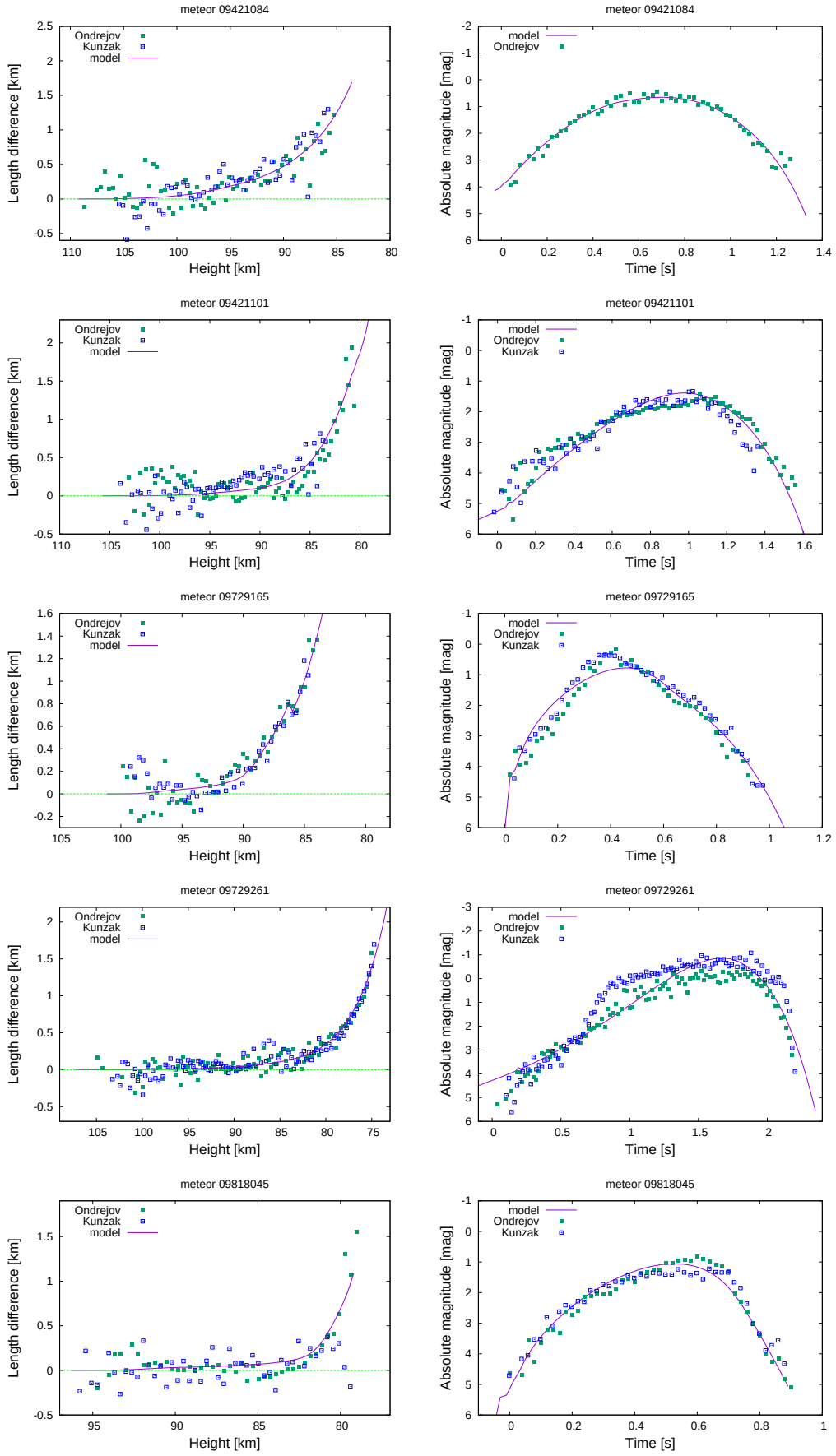

Figure A.27: Deceleration curves, lightcurves and the fit of the fragmentation model for modelled meteoroids.

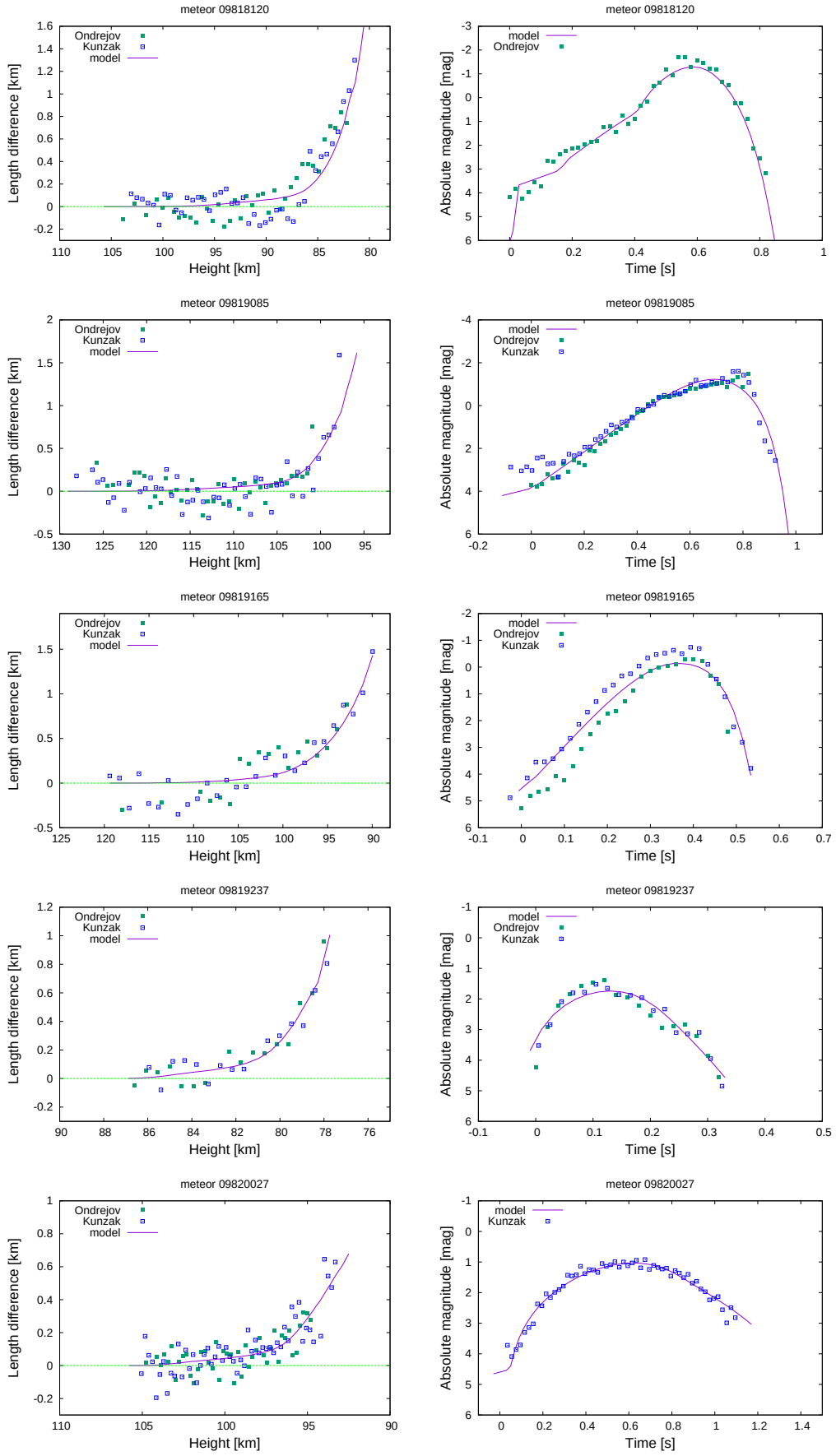

Figure A.28: Deceleration curves, lightcurves and the fit of the fragmentation model for modelled meteoroids.

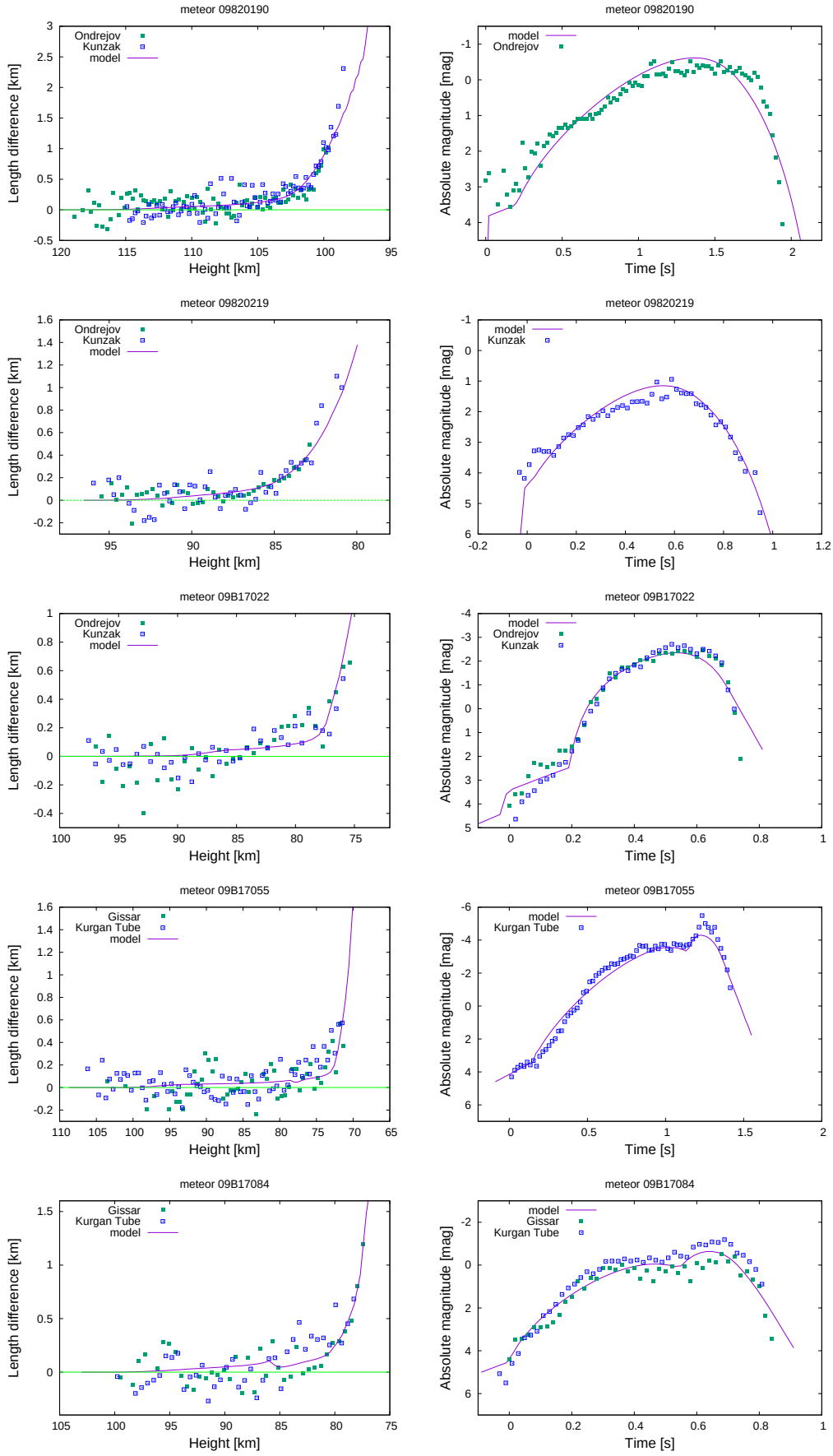

Figure A.29: Deceleration curves, lightcurves and the fit of the fragmentation model for modelled meteoroids.

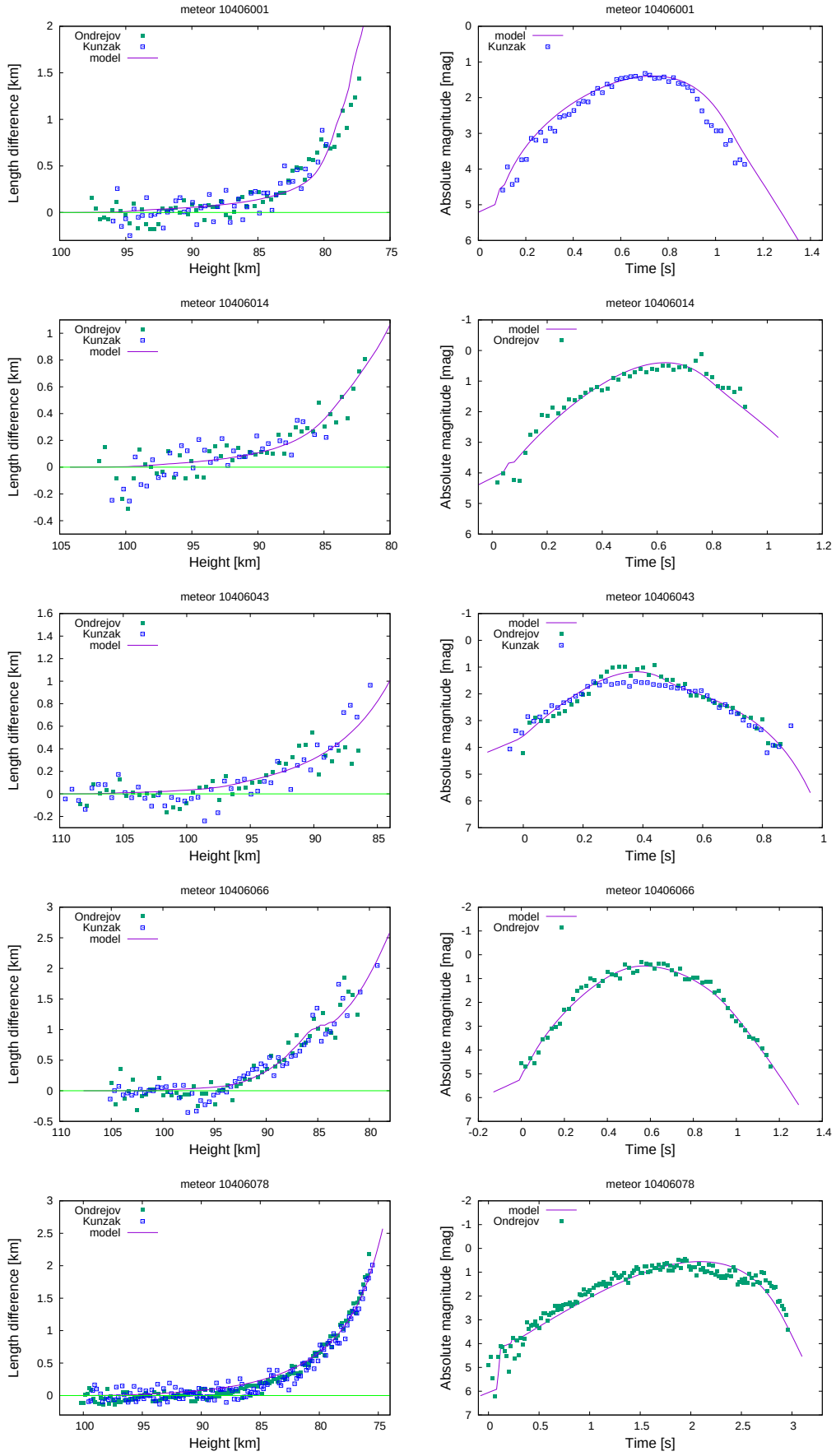

Figure A.30: Deceleration curves, lightcurves and the fit of the fragmentation model for modelled meteoroids.

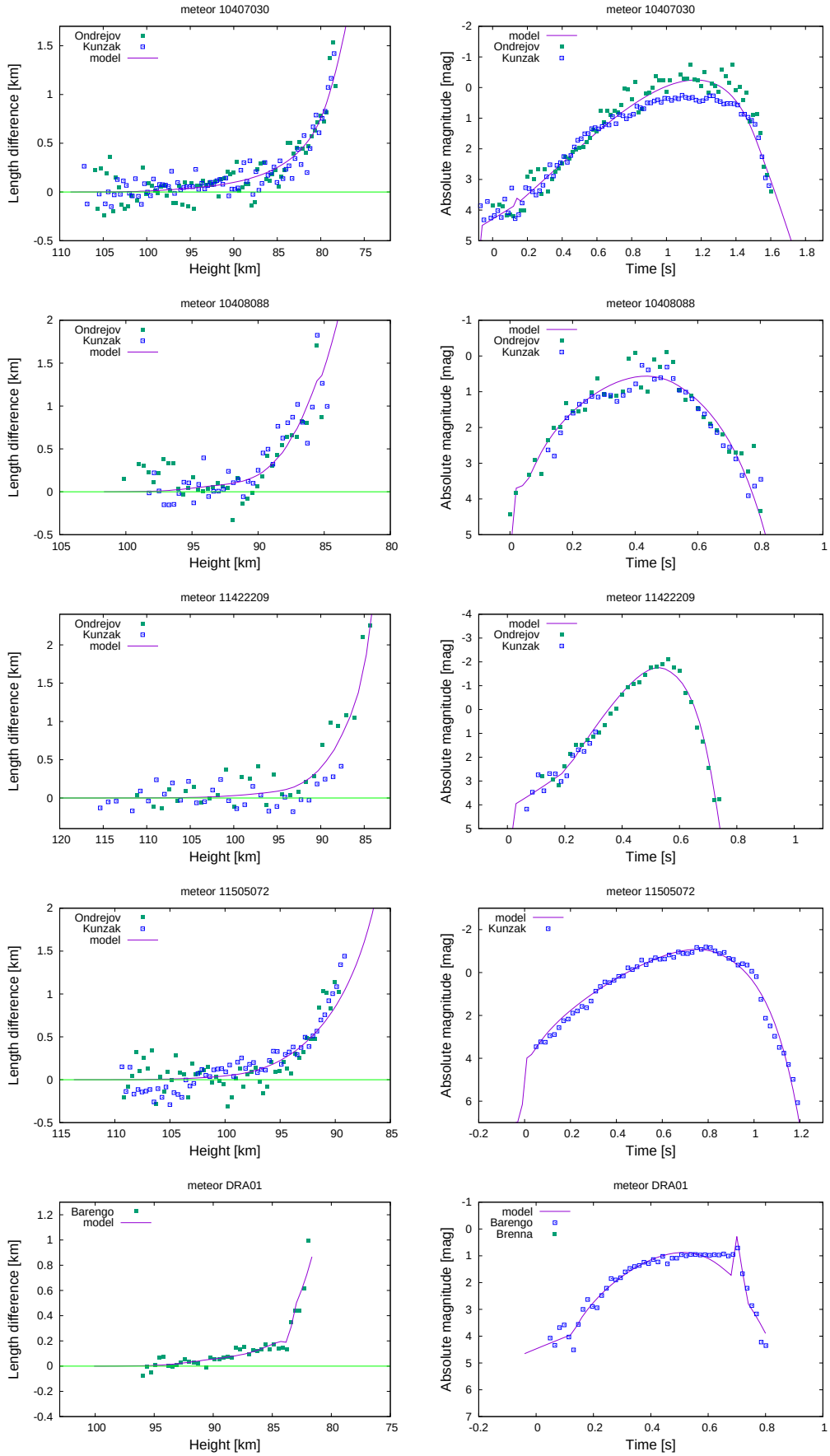

Figure A.31: Deceleration curves, lightcurves and the fit of the fragmentation model for modelled meteoroids.

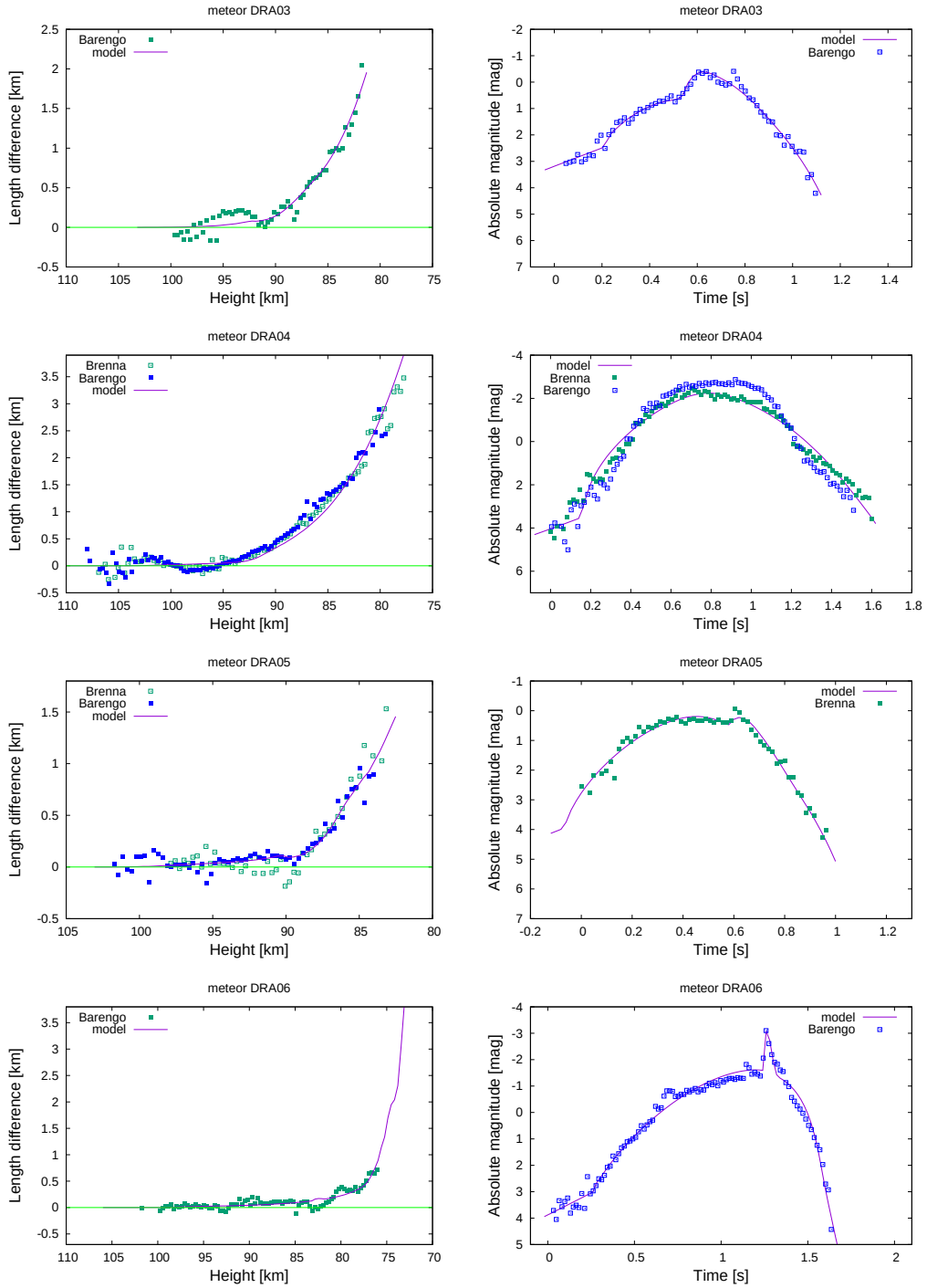

Figure A.32: Deceleration curves, lightcurves and the fit of the fragmentation model for modelled meteoroids.

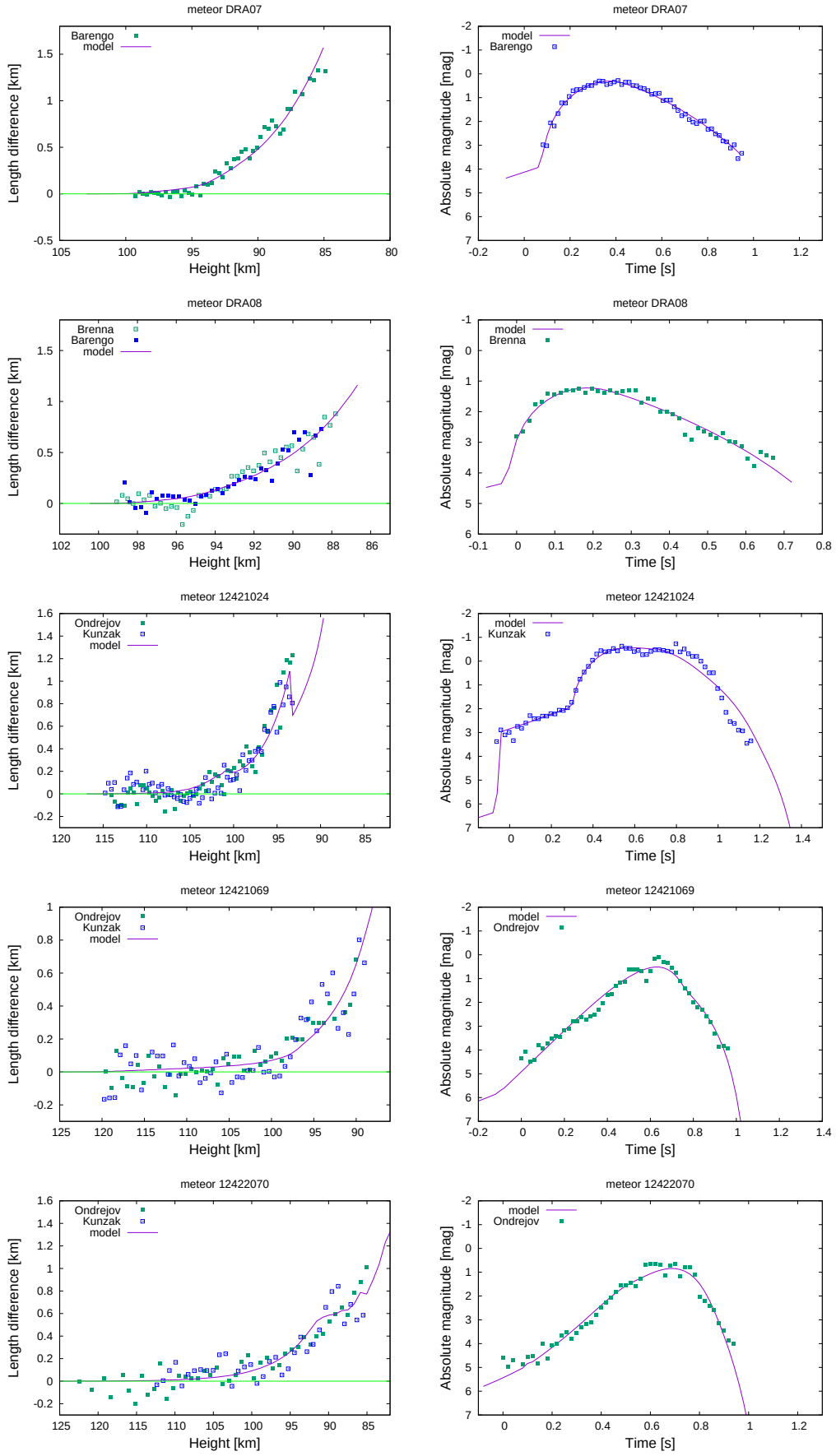

Figure A.33: Deceleration curves, lightcurves and the fit of the fragmentation model for modelled meteoroids.

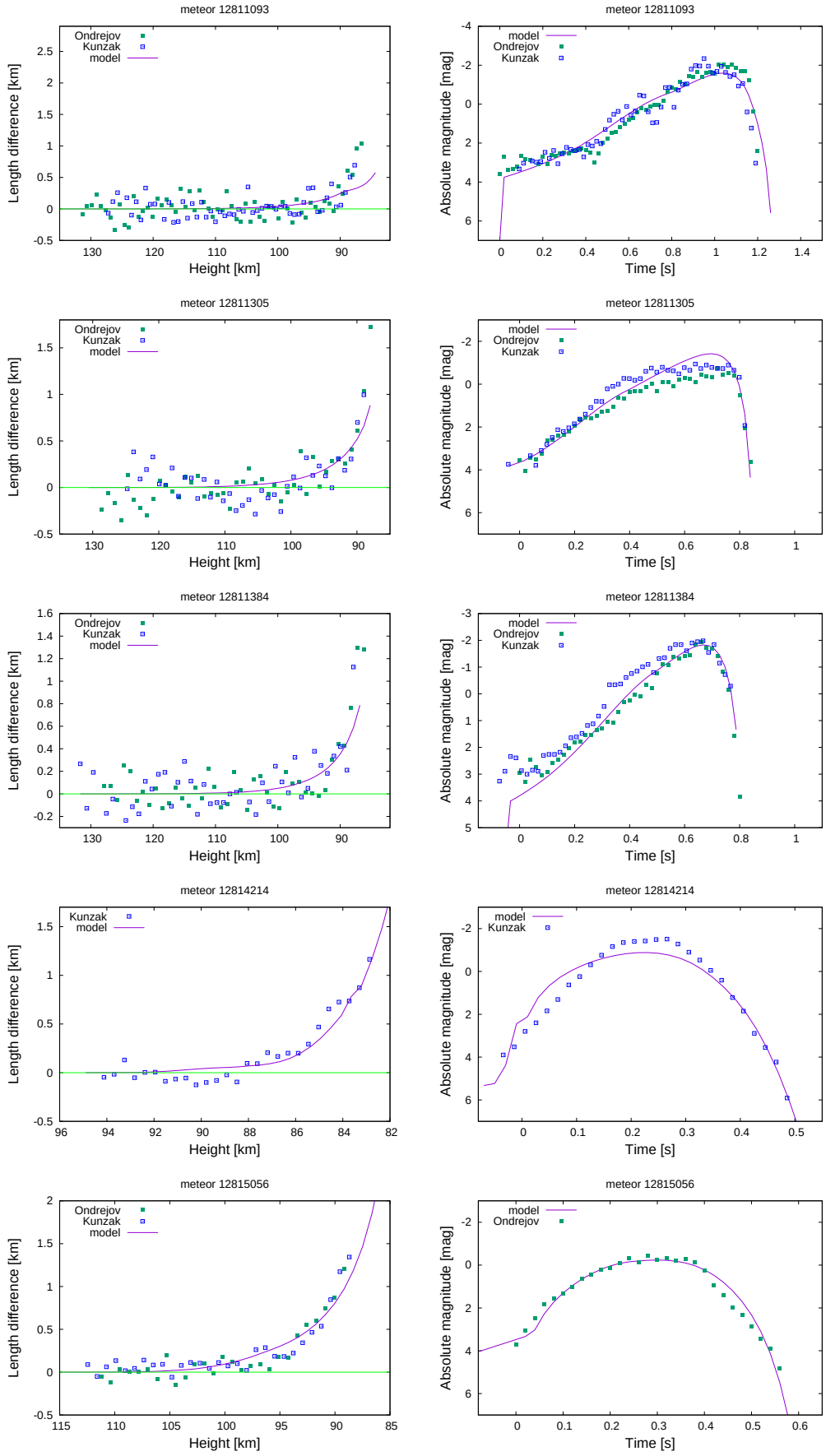

Figure A.34: Deceleration curves, lightcurves and the fit of the fragmentation model for modelled meteoroids.

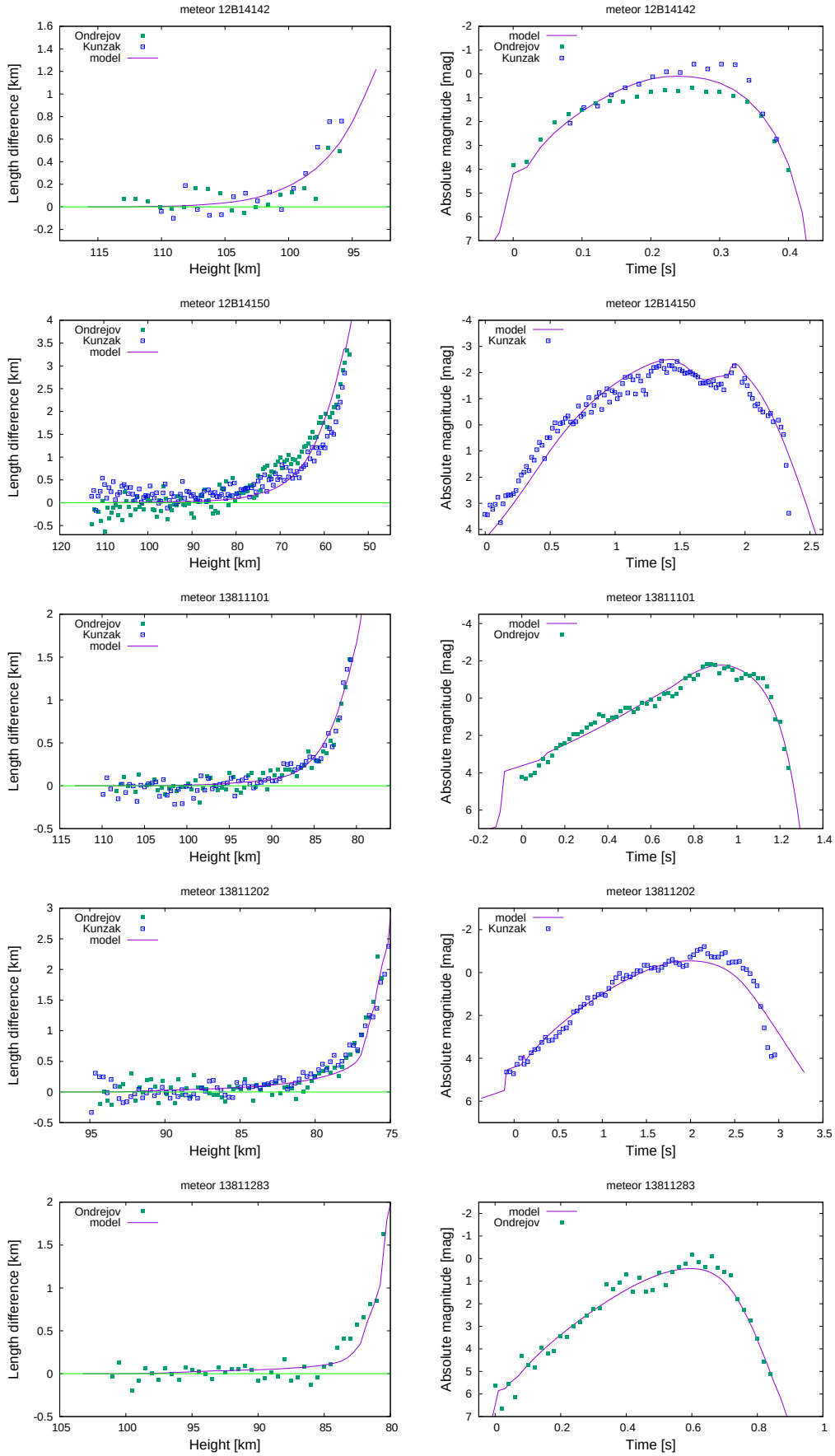

Figure A.35: Deceleration curves, lightcurves and the fit of the fragmentation model for modelled meteoroids.

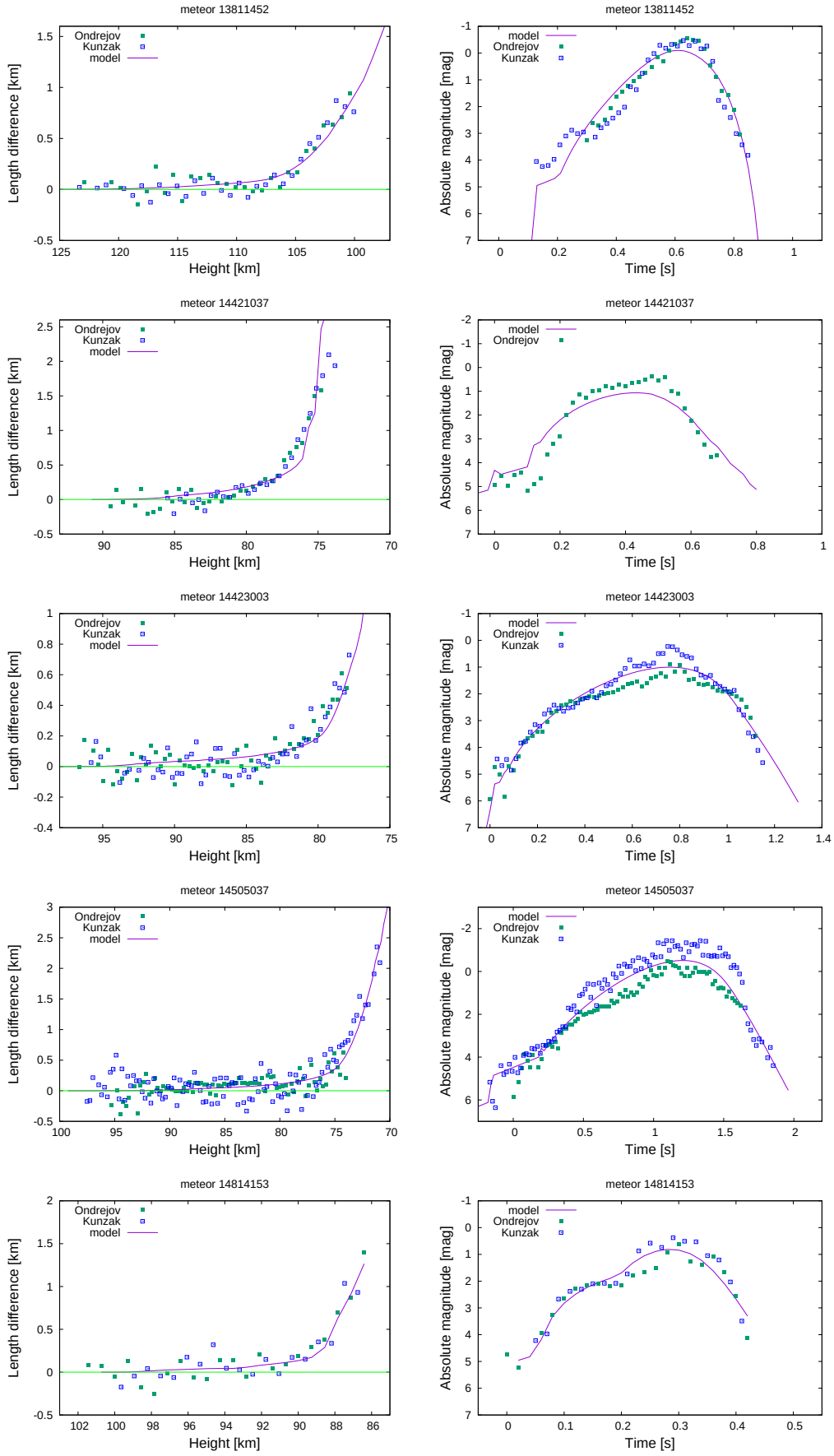

Table A.1: Meteors with the spectral and orbital classification. H_B is beginning height, v_∞ is the initial velocity of meteor, M_{max} is absolute magnitude in maximum, m_P is photometric mass, H_{Na-Mg} is the difference of heights where half of the sodium and magnesium was radiated out.

meteor	spectrum	shower	sp. class	orbit	H_B (km)	v_∞ (km.s^{-1})	M_{max} (mag)	m_P (g)	H$_{Na-Mg}$ (km)	$1/a$ (AU^{-1})	e	q (AU)	i (°)	ω (°)	T_j
04626009	SZ2227	SPO	Na–free	Halley	91.2	43	1.8	3.0×10^{-3}	0.2	0.3	0.7	1.015	74	185	2
04811066	SZ2266	SPO	Normal	J–F	94.9	26.8	1.0	3.0×10^{-2}	0.0	0.34	0.679	0.949	38.2	212.6	2.6
05403028	SZ2410	SPO	Iron	Halley	96.1	40.7	-0.8	9.4×10^{-2}	0.1	0.285	0.814	0.654	63.2	103.2	1.9
05403032	SZ2411	SPO	Normal	J–F	105.1	35.5	1.0	4.1×10^{-2}	-1.0	0.395	0.905	0.242	6	306.63	2.64
05728004	SZ2417	SPO	Iron	A–C	86.8	21.4	-0.7	1.4×10^{-1}	-0.1	0.48	0.67	0.69	3.2	258	3.4
05A06077	SZ2428	SPO	Fe–poor	Halley	102.6	40.45	-0.7	1.9×10^{-1}	0.6	0.191	0.809	0.998	65.74	175.7	1.48
05A07010	SZ2434	SPO	Normal	A–C	88.8	23.32	-1.5	3.6	0.2	0.893	0.638	0.405	3.61	301.74	5.356
05A07201	SZ2441	SPO	Normal	J–F	85.4	17.4	-0.9	2.4	0.1	0.344	0.684	0.92	12.28	216.4	2.85
05A07262	SZ2443	SPO	Na–free	Halley	97.1	67.1	-0.5	1.8×10^{-2}	0.6	0.25	0.76	0.948	145.6	332	0.4
05A08159	SZ2454	SPO	Na–free	Halley	94.4	41	-3.0	9.9×10^{-1}	-0.2	0.07	0.957	0.593	58.1	260.3	0.9
05A08160	SZ2455	SPO	Normal	Halley	99.3	67.1	1.2	2.8×10^{-3}	2.4	-0.06	1.03	0.445	171	95	-1.1
05A31001	SZ2466	SPO	Fe–poor	A–C	94.0	32.76	-3.1	9.2	-0.1	0.456	0.866	0.293	5.72	121.16	3.017
06406048	SX001	SPO	Iron	S–A	98.0	41.9	0.6	2.5×10^{-2}	0.8	0.4	0.957	0.11	28.9	325.1	2.4
06406069	SX002	SPO	Normal	Halley	109.7	42.2	-0.4	4.3×10^{-2}	1.3	0.01	0.99	0.999	66.3	174.5	0.6
06420006	SX008	SPO	Na–poor	Halley	103.8	41.9	0.0	6.6×10^{-2}	1.8	0.05	0.974	0.563	56.7	263.7	0.7
06420028	SX010	SPO	Normal	Halley	107.6	48.4	-2.3	2.3×10^{-1}	0.2	0.001	1	0.916	78.9	214.6	0
06420089	SX015	SPO	Normal	Ecl.	99.0	28.08	-0.1	2.6×10^{-1}	-0.2	0.377	0.812	0.498	4.88	97.21	2.79
06724010	SX043	SPO	Normal	Ecl.	104.9	24.11	-3.2	4.4	-1.4	0.337	0.779	0.656	6.13	259	2.69
06724013	SX044	SPO	Normal	J–F	96.5	23.3	0.4	1.2×10^{-1}	-0.2	0.29	0.72	0.953	28.9	211.6	2.5
06724023	SX045	SPO	Na–poor	S–A	103.0	37.57	-0.2	7.2×10^{-2}	3.1	0.512	0.898	0.2	35	314.2	3.1
06724029	SX046	SPO	Normal	Halley	101.1	31	-0.9	1.7×10^{-1}	1.7	0.37	0.66	0.916	47.3	221.2	2.7
06725005	SX058	SPO	Iron	A–C	83.9	20.1	0.9	7.2×10^{-2}	0.2	0.52	0.52	0.938	24.5	219	3.6
06727196	SX089	SPO	Normal	J–F	98.4	22.23	-0.9	5.4×10^{-1}	-0.1	0.283	0.733	0.943	26.3	213.73	2.48
06727206	SX090	SPO	Normal	Halley	121.7	64.4	-0.8	2.3×10^{-2}	1.4	0.02	0.989	0.495	147.1	271.8	-0.6
06727222	SX092	SPO	Na–poor	J–F	102.8	36.31	-2.1	8.5×10^{-1}	0.2	0.383	0.844	0.408	42.8	72.13	2.55
06730083	SX116	SPO	Normal	A–C	95.0	23.8	-2.4	2.3	0.1	0.436	0.73	0.619	7	265.72	3.17

Table A.1: continued.

meteor	spectrum	shower	sp. class	orbit	H_B (km)	v_∞ (km.s^{-1})	M_{max} (mag)	m_P (g)	H$_{Na-Mg}$ (km)	$1/a$ (AU^{-1})	e	q (AU)	i (°)	ω (°)	T_j
06730138	SX118	SPO	Na–poor	Halley	121.5	65.8	0.9	4.7×10^{-3}	0.9	0.2	0.82	0.882	142.6	135	0.2
06802034	SX130	SPO	Normal	J–F	96.6	21	1.1	1.3×10^{-1}	0.1	0.26	0.75	0.969	23.6	206.56	2.4
06A20013	SX143	SPO	Normal	Ecl.	106.6	17.6	-1.4	1.2	-0.3	0.396	0.657	0.865	6.84	227.95	3.1
06A20125	SX150	SPO	Na–rich	J–F	94.9	17.3	1.0	2.3×10^{-1}	-0.9	0.36	0.69	0.872	3.5	225.9	2.92
06A20126	SX151	SPO	Na–free	S–A	97.1	44.4	0.9	9.0×10^{-3}	0.8	0.32	0.985	0.048	19.9	336.6	1.9
06A20149	SX158	Ori	Normal	Halley	118.4	66.8	2.0	2.3×10^{-3}	0.7	0.16	0.908	0.576	163	83.5	-0
06A20437	SX211	Ori	Fe–poor	Halley	135.2	67.8	-2.4	4.1×10^{-2}	2.2	0.08	0.95	0.619	162.8	77.1	-0.5
06A20527	SX225	Ori	Normal	Halley	124.6	68.3	1.3	3.5×10^{-3}	1.4	0.02	0.99	0.61	163.9	77.2	-1
06A20632	SX237	Ori	Normal	Halley	125.6	66.2	1.0	4.3×10^{-3}	1.3	0.21	0.87	0.598	161.7	82	0.2
06B18075	SX263	Tau	Normal	Ecl.	104.8	28.15	-1.3	6.8×10^{-1}	-1.8	0.461	0.802	0.43	3.09	285.67	3.17
06C13104	SX333	Gem	Na–poor	S–A	102.4	36	-1.7	2.1×10^{-1}	0.0	0.773	0.894	0.137	23.1	325.4	4.43
06C13136	SX336	Gem	Normal	S–A	104.8	36.3	-1.5	4.9×10^{-1}	0.7	0.751	0.895	0.139	24.8	324.8	4.31
06C13137	SX337	Gem	Na–free	S–A	102.0	37.2	0.2	5.6×10^{-2}	-4.0	0.691	0.906	0.136	25.4	324.4	4
06C13334	SX350	SPO	Na–free	Halley	98.4	46.1	0.3	1.7×10^{-2}	-0.6	0.29	0.72	0.984	78.4	179.5	1.7
06C14187	SX393	SPO	Iron	A–C	78.2	12.7	0.2	2.0×10^{-1}	0.0	0.631	0.384	0.976	6.4	194.1	4.29
06C14215	SX398	Gem	Na–poor	S–A	102.1	36.9	0.0	3.7×10^{-2}	2.6	0.69	0.905	0.139	22.1	324	4
06C14357	SX430	SPO	Na–poor	Halley	123.6	64.9	0.5	5.0×10^{-3}	3.1	0.02	0.993	0.425	144.7	278.1	-0.6
06C14515	SX457	SPO	Normal	Halley	114.4	59.7	-1.0	3.0×10^{-2}	-0.2	0.04	0.991	0.222	129.7	123.8	-0.1
06C14529	SX461	SPO	Normal	J–F	102.4	25.66	-0.3	5.8×10^{-1}	-0.1	0.365	0.649	0.961	35.85	160.19	2.79
06C14633	SX476	SPO	Normal	Halley	106.9	70	0.2	2.0×10^{-3}	1.7	0.001	1	0.976	142.9	191	-1
06C14645	SX478	SPO	Na–poor	Halley	109.6	72.9	-0.6	5.2×10^{-3}	0.9	0.05	0.95	0.977	173	190.2	-1
07406018	SX498	SPO	Na–enh.	J–F	71.7	18.5	-2.7	4.3×10^{-1}	-0.8	0.303	0.734	0.878	2.88	224.7	2.66
07407021	SX500	SPO	Na–enh.	A–C	89.3	18.2	0.1	4.5×10^{-1}	-0.9	0.484	0.553	0.924	16.4	218.42	3.52
07407034	SX502	SPO	Normal	J–F	86.3	19.7	0.4	2.9×10^{-1}	1.3	0.36	0.641	0.998	23.8	172.7	2.9
07812429	SX571	SPO	Normal	J–F	100.7	24.7	-1.5	5.8×10^{-1}	-0.2	0.256	0.753	0.964	32.9	207.6	2.29
07A08045	SX661	SPO	Iron	J–F	88.5	31.06	1.2	2.5×10^{-2}	0.5	0.396	0.857	0.36	1.5	292.7	2.78
08505008	SX689	SPO	Iron	A–C	86.3	26.6	1.7	2.0×10^{-2}	0.1	0.54	0.48	0.966	41.3	150.2	3.6
08505025	SX692	SPO	Iron	A–C	78.6	16.1	0.6	1.1×10^{-1}	0.0	0.48	0.52	0.999	16	194	3.5
08506016	SX696	SPO	Na–free	Halley	103.7	57.4	-0.7	1.8×10^{-2}	0.5	0.07	0.97	0.524	108.4	269	0.1
08507002	SX700	SPO	Na–free	S–A	97.9	38.5	0.4	5.0×10^{-2}	0.7	0.374	0.941	0.159	2.4	137.7	2.43

Table A.1: continued.

meteor	spectrum	shower	sp. class	orbit	H_B (km)	v_∞ (km.s^{-1})	M_{max} (mag)	m_P (g)	H_{Na-Mg} (km)	$1/a$ (AU^{-1})	e	q (AU)	i (°)	ω (°)	T_j
08728012	SX701	SPO	Iron	A–C	86.2	19.3	0.3	1.5×10^{-1}	0.0	0.44	0.64	0.815	9.2	119.7	3.3
08728033	SX703	SPO	Na–poor	Halley	96.0	54	0.8	3.2×10^{-3}	-0.4	0.4	0.67	0.83	103.6	236	2
08728076	SX708	SPO	Normal	Ecl.	98.6	25.2	-0.3	3.6×10^{-1}	0.4	0.385	0.772	0.592	7.48	267.5	2.89
08728078	SX709	SPO	Normal	Halley	97.5	29.4	1.2	5.8×10^{-2}	0.1	0.03	0.97	0.982	40	201.2	1.1
08728098	SX713	SPO	Normal	J–F	93.6	17.41	0.8	3.2×10^{-1}	0.3	0.355	0.64	1.014	18.3	175.5	2.92
08728149	SX718	SPO	Normal	Halley	99.1	28.86	0.9	5.8×10^{-2}	0.0	0.038	0.963	0.981	39	201.4	1.1
08728151	SX719	SPO	Normal	J–F	101.2	24.95	-0.1	2.3×10^{-1}	0.4	0.388	0.768	0.598	7.65	266.9	2.91
08728156	SX720	SPO	Normal	A–C	99.8	24.3	1.5	6.8×10^{-2}	1.3	0.984	0.098	0.917	42.6	85	5.8
08728223	SX725	SPO	Na–free	S–A	99.6	43.5	0.7	2.4×10^{-2}	0.1	0.32	0.979	0.066	29.4	152.9	1.9
08728233	SX726	SPO	Normal	J–F	102.3	24.8	-1.0	7.4×10^{-1}	0.3	0.391	0.766	0.001	7.91	266.78	2.93
08728280	SX731	SPO	Na–free	S–A	97.7	42.3	0.3	2.7×10^{-2}	0.5	0.44	0.973	0.061	25.7	154.9	2.56
08729037	SX738	SPO	Na–free	S–A	98.7	42.5	0.6	3.8×10^{-2}	1.6	0.363	0.971	0.08	26.3	150.5	2.2
08927015	SX784	SPO	Normal	Halley	123.1	70.8	0.5	6.3×10^{-3}	1.0	0.02	0.98	0.891	161.78	39.1	-1
08927018	SX785	SPO	Normal	J–F	99.4	19.1	0.1	7.2×10^{-1}	-0.8	0.28	0.766	0.848	6.26	49.8	2.5
08927049	SX786	SPO	Na–free	Halley	96.7	38.9	1.6	1.1×10^{-2}	0.1	0.32	0.9	0.327	47	295.3	2.1
08927101	SX788	SPO	Normal	J–F	96.3	19.5	-0.7	1.1	0.2	0.29	0.73	0.949	20	209.1	2.6
08927195	SX793	SPO	Normal	Halley	118.4	60.77	-2.5	9.2×10^{-2}	0.9	0.005	0.997	0.749	113.99	119.6	-0.4
08928139	SX798	SPO	Normal	A–C	101.3	24.73	-0.6	7.0×10^{-1}	-1.8	0.417	0.76	0.577	6.43	269.04	3.04
08928141	SX799	SPO	Normal	J–F	100.0	27.3	1.4	5.6×10^{-2}	0.5	0.36	0.81	0.54	14.8	271.8	2.7
08928235	SX804	SPO	Normal	Halley	114.2	42.48	-1.8	1.6×10^{-1}	0.8	0.137	0.863	1.001	69.28	178	1.1
08A20002	SX820	SPO	Na–enh.	Ecl.	90.0	23.98	-0.7	1.1	0.5	0.39	0.758	0.621	2.71	82.63	2.943
09102507	SX961	Qua	Normal	Halley	103.8	41.7	-1.4	1.2×10^{-1}	0.3	0.32	0.69	0.983	69.3	176.6	2
09102515	SX962	Qua	Na–poor	Halley	103.1	42.5	0.7	2.2×10^{-2}	2.7	0.32	0.69	0.978	71	170.5	2
09421005	SX983	SPO	Normal	Ecl.	102.9	22.4	-0.1	6.4×10^{-1}	-1.9	0.375	0.726	0.731	7.18	249.4	2.93
09421018	SX984	SPO	Iron	A–C	83.7	18.1	2.1	3.2×10^{-2}	-0.9	0.42	0.6	0.972	18	204.1	3.2
09421084	SX988	SPO	Normal	J–F	105.7	31.1	-1.4	3.6×10^{-1}	0.6	0.31	0.868	0.43	10.1	283.4	2.37
09421101	SX990	SPO	Normal	J–F	103.3	21.9	1.4	1.4×10^{-1}	0.3	0.357	0.733	0.748	7.81	246.78	2.85
09729165	SX1010	SPO	Na–free	S–A	99.9	42.2	0.2	2.9×10^{-2}	0.2	0.39	0.969	0.08	28.2	150.8	2.3
09729261	SX1022	SPO	Normal	J–F	103.2	23.71	-1.1	1.3	-1.1	0.341	0.76	0.705	15.3	253.02	2.71
09818045	SX1036	SPO	Normal	J–F	94.5	19.37	0.8	1.7×10^{-1}	-0.5	0.309	0.714	0.925	17.1	217.59	2.66

Table A.1: continued.

meteor	spectrum	shower	sp. class	orbit	H_B (km)	v_∞ (km.s^{-1})	M_{max} (mag)	m_P (g)	H_{Na-Mg} (km)	$1/a$ (AU^{-1})	e	q (AU)	i (°)	ω (°)	T_j
09818120	SX1041	SPO	Na–poor	S–A	104.5	40.1	-1.7	1.4×10^{-1}	1.3	0.51	0.955	0.088	21.7	330.3	2.99
09818147	SX1044	SPO	Na–free	Halley	115.3	63.7	0.1	6.1×10^{-3}	1.7	0.28	0.73	0.96	133.8	208.6	0.7
09819085	SX1057	SPO	Na–enh.	Halley	125.8	69.41	-1.5	2.7×10^{-2}	0.5	0.018	0.982	0.989	147.8	162.6	-1
09819134	SX1061	SPO	Normal	Halley	114.1	57.33	-2.1	7.2×10^{-2}	-0.7	0.16	0.86	0.89	107	137	0
09819164	SX1064	SPO	Fe–poor	Halley	128.0	56.2	-2.8	2.0×10^{-1}	0.8	0.07	0.94	0.918	101.2	143.8	0.1
09819165	SX1065	SPO	Normal	Halley	119.8	66.1	-0.7	1.3×10^{-2}	0.1	0.04	0.97	0.751	141.2	241	-0.6
09819237	SX1073	SPO	Na–free	J–F	86.6	31.5	1.4	1.3×10^{-2}	0.8	0.25	0.8	0.794	43.5	239	2.1
09819293	SX1079	SPO	Normal	Halley	112.4	57.5	1.3	2.9×10^{-3}	1.4	0.11	0.9	0.916	106	143	0
09820027	SX1087	SPO	Na–free	S–A	105.0	41.89	0.9	3.3×10^{-2}	-0.8	0.308	0.974	0.086	2.2	148.77	1.96
09820028	SX1088	SPO	Iron	A–C	83.4	19.1	1.9	3.1×10^{-2}	-0.7	0.4	0.6	0.993	22.4	162	3.1
09820151	SX1096	SPO	Na–poor	Halley	116.0	60.4	0.2	5.2×10^{-3}	-0.7	0.37	0.823	0.479	139	279.6	1.3
09820190	SX1101	SPO	Atm.	Halley	119.3	64.94	-0.5	4.9×10^{-2}	0.3	0.049	0.954	0.946	129.17	29.9	-0.5
09820219	SX1102	SPO	Normal	J–F	96.1	22.8	0.9	1.0×10^{-1}	-0.1	0.349	0.647	1.011	31.4	181.81	2.8
09820250	SX1104	SPO	Na–free	Halley	98.3	65	-0.6	4.8×10^{-3}	0.0	0.4	0.6	1.01	143	175	1
09820289	SX1106	SPO	Normal	Halley	117.6	69.4	-0.9	1.4×10^{-2}	0.8	0.15	0.85	0.995	157.9	164.5	-0.3
09B17008	SX1114	SPO	Iron	A–C	84.9	23.8	0.8	1.0×10^{-1}	0.2	0.58	0.681	0.554	6.7	94.9	3.83
09B17022	SX1117	SPO	Na–poor	Ecl.	97.6	32	-2.5	9.4×10^{-1}	0.1	0.386	0.868	0.343	5.95	113.9	2.7
09B17055	SX1122	Tau	Normal	Ecl.	106.3	27.7	-5.5	1.3×10^{1}	-0.1	0.506	0.78	0.434	6.11	106.21	3.4
09B17084	SX1128	Tau	Normal	Ecl.	100.9	29.7	-0.5	1.9×10^{-1}	-1.3	0.42	0.832	0.398	5.28	288.37	2.94
09B17115	SX1133	Leo	Normal	Halley	117.7	72.6	-0.1	2.5×10^{-3}	0.3	0.02	0.98	0.98	163	169.6	-1
09B17123	SX1135	Leo	Normal	Halley	121.8	72	1.8	1.3×10^{-3}	2.8	0.05	0.95	0.985	160.3	172.6	-0.9
09B17192	SX1150	Leo	Normal	Halley	123.6	71.1	0.5	2.3×10^{-3}	0.6	0.15	0.86	0.985	161.5	173.3	-0.4
10406001	SX1186	SPO	Normal	A–C	97.7	19.13	0.1	3.3×10^{-1}	1.1	0.375	0.653	0.927	16.73	215.6	2.99
10406008	SX1187	SPO	Iron	A–C	81.9	14.5	2.6	5.5×10^{-2}	-0.3	0.5	0.52	0.959	1.7	28.5	3.64
10406014	SX1188	SPO	Normal	Halley	102.8	28.93	0.1	1.3×10^{-1}	1.2	0.07	0.948	0.744	26.06	241.8	1.31
10406015	SX1189	SPO	Na–poor	J–F	90.5	22.5	1.1	5.4×10^{-2}	1.1	0.36	0.71	0.793	16.8	240	2.87
10406022	SX1191	SPO	Na–poor	J–F	105.6	34.91	0.0	9.6×10^{-2}	-0.5	0.381	0.889	0.291	14.53	300.4	2.61
10406043	SX1192	SPO	Normal	Halley	108.2	34.1	0.9	3.7×10^{-2}	1.7	0.039	0.962	0.977	49.1	197.78	1
10406060	SX1194	SPO	Iron	J–F	92.1	32.6	0.5	4.4×10^{-2}	0.3	0.4	0.867	0.335	3.1	295.6	2.75
10406066	SX1196	SPO	Normal	A–C	105.1	21.3	0.3	2.9×10^{-1}	4.4	0.423	0.606	0.933	25.2	214.94	3.17

Table A.1: continued.

meteor	spectrum	shower	sp. class	orbit	H_B (km)	v_∞ (km.s^{-1})	M_{max} (mag)	m_P (g)	H_{Na-Mg} (km)	$1/a$ (AU^{-1})	e	q (AU)	i (°)	ω (°)	T_j
10406078	SX1197	SPO	Na–enh.	J–F	100.4	19.56	0.5	7.9×10^{-1}	-0.2	0.254	0.766	0.923	16.79	145.04	2.39
10407030	SX1206	SPO	Normal	Ecl.	107.4	24.47	0.3	3.7×10^{-1}	-0.5	0.373	0.758	0.65	7.12	259.3	2.87
10408088	SX1217	SPO	Na–free	S–A	100.2	40.6	-0.1	3.8×10^{-2}	0.2	0.48	0.952	0.099	21	327.9	2.9
11422209	SX1582	Lyr	Normal	Halley	115.2	48.5	-3.1	2.8×10^{-1}	1.2	0.05	0.96	0.92	80.4	214.2	0.4
11505072	SX1594	SPO	Na–poor	S–A	109.0	42.5	-1.2	1.6×10^{-1}	-0.3	0.11	0.985	0.134	13	318.4	1.03
DRA01	SXDRA01	Dra	Normal	J–F	99.3	22.7	0.7	6.5×10^{-2}	-0.5	0.34	0.67	0.997	30.5	173.5	2.7
DRA03	SXDRA03	Dra	Normal	J–F	102.1	21.75	-0.4	2.0×10^{-1}	0.8	0.397	0.604	0.996	29.4	172.9	3.03
DRA04	SXDRA04	Dra	Normal	J–F	107.5	22.04	-2.5	1.7	3.3	0.381	0.621	0.996	29.82	172.96	2.95
DRA05	SXDRA05	Dra	Normal	J–F	101.4	22.49	-0.1	1.6×10^{-1}	-1.2	0.36	0.65	0.996	30.5	173.3	2.8
DRA06	SXDRA06	Dra	Normal	J–F	105.5	23.3	-3.1	1.0	-0.7	0.304	0.697	0.996	31.5	173.23	2.55
DRA07	SXDRA07	Dra	Normal	J–F	101.3	21.8	0.3	1.3×10^{-1}	1.6	0.388	0.613	0.996	29.4	172.9	2.99
DRA08	SXDRA08	Dra	Normal	J–F	99.1	22.2	1.3	4.5×10^{-2}	0.9	0.37	0.63	0.996	30	172.9	2.9
12421024	SX1734	Lyr	Normal	Halley	113.9	48.51	0.3	3.5×10^{-2}	0.4	0.018	0.983	0.922	79.48	213.57	0.31
12421069	SX1738	Lyr	Na–poor	Halley	119.8	48.9	-0.7	4.4×10^{-2}	2.8	0.023	0.979	0.914	80.4	215.3	0.3
12422070	SX1751	Lyr	Normal	Halley	112.3	48.32	-0.7	4.2×10^{-2}	0.2	0.01	0.991	0.915	79.06	215	0.28
12811093	SX1786	Per	Normal	Halley	131.3	60.87	-2.0	8.2×10^{-2}	-0.5	0.013	0.988	0.954	113.62	151.9	-0.4
12811305	SX1798	Per	Normal	Halley	128.0	61.59	-0.7	2.3×10^{-2}	-0.5	-0.011	1.01 1	0.947	115.35	150.5	-0.6
12811384	SX1802	Per	Fe–poor	Halley	133.1	61.1	-2.0	6.7×10^{-2}	0.7	0.04	0.96	0.96	115.1	153.3	-0.3
12814214	SX1920	SPO	Na–poor	S–A	93.0	42.3	-1.5	3.5×10^{-2}	1.2	0.4	0.972	0.069	24.3	152.8	2.4
12815056	SX1937	SPO	Normal	Halley	111.2	60.4	-1.2	1.6×10^{-2}	1.7	0.03	0.98	0.922	113	215.1	-0.3
12815084	SX1938	SPO	Iron	Halley	92.2	43.4	-0.6	3.6×10^{-2}	1.2	0.28	0.87	0.486	68	277	1.7
12B13179	SX1975	SPO	Normal	Halley	106.5	58.9	0.3	3.5×10^{-3}	0.3	0.06	0.95	0.98	105.7	191.2	-0
12B14142	SX1998	SPO	Normal	Halley	110.0	62.4	0.6	9.7×10^{-3}	2.6	0.03	0.98	0.635	122.5	253.9	-0.4
12B14150	SX1999	Tau	Normal	Ecl.	112.3	29.03	-5.5	1.2×10^{1}	-2.7	0.425	0.821	0.422	5.28	105.8	2.97
13805255	SX2067	SPO	Normal	Halley	122.6	67.7	-0.7	9.6×10^{-3}	1.1	0.09	0.93	0.785	154.3	238	-0.5
13810209	SX2090	SPO	Na–poor	Halley	92.9	41.5	0.7	3.2×10^{-3}	0.0	0.39	0.83	0.436	64.5	285	2.3
13810228	SX2091	SPO	Na–poor	Halley	118.9	64	0.4	6.6×10^{-3}	1.2	0.04	0.96	0.82	129.3	232.4	-0.5
13811101	SX2133	SPO	Na–poor	S–A	108.3	41.59	-2.7	2.4×10^{-1}	1.3	0.315	0.968	0.101	20.3	326.15	2.01
13811202	SX2146	SPO	Normal	J–F	94.8	17	-0.2	1.8	0.4	0.27	0.751	0.924	2.05	217.3	2.52
13811283	SX2155	SPO	Na–free	S–A	101.8	37.2	-1.2	4.8×10^{-2}	0.2	0.765	0.937	0.082	16.2	334.1	4.31

Table A.1: continued.

meteor	spectrum	shower	sp. class	orbit	H_B (km)	v_∞ (km.s^{-1})	M_{max} (mag)	m_P (g)	H$_{Na-Mg}$ (km)	$1/a$ (AU^{-1})	e	q (AU)	i (°)	ω (°)	T_j
13811452	SX2175	SPO	Atm.	Halley	130.7	72.3	-0.5	9.0×10^{-3}	1.5	-0.1	1.1	1.011	159.8	5.3	-1.7
14421037	SX2365	SPO	Na–free	Halley	89.4	28.7	-1.1	7.6×10^{-2}	0.8	0.09	0.91	0.986	39.3	163.9	1.4
14423003	SX2381	SPO	Normal	A–C	96.6	20.16	0.2	1.7×10^{-1}	-0.3	0.502	0.505	0.987	26	199.13	3.57
14505037	SX2395	SPO	Na–rich	J–F	97.4	16.17	-0.5	3.3	-0.1	0.312	0.686	1.005	13	187.21	2.74
14814147	SX2413	SPO	Normal	Halley	125.9	67.3	-2.8	2.9×10^{-2}	0.9	-0.08	1.08	0.993	133.2	164	-1.3
14814153	SX2414	SPO	Normal	Halley	101.5	58.6	0.4	3.7×10^{-3}	1.5	0.11	0.987	0.121	159.9	141	0.2

Table A.2: Result of the fragmentation model: physical parameters of meteoroids. σ is the ablation coefficient, η is the erosion coefficient, δ is the bulk densitu (if marked, we observed the ablation before erosion), GUML is the grain upper mass limit and GLML is the grain lower mass limit, S is the grain mass distribution index, H_{er} is the height of the erosion start, n_0 is the number of grains in the first bin, N is the total number of grains, E_s is the energy necessary to start the erosion. If there are two lines for one meteor, the second line cintains parameters for second stage of the erosion (marked as SE). The total mass that was subject for the secon erosion is shown in the column for bulk density.

meteor	σ	η	δ	GUML	GLML	§	H_{er}	sizes	n_0	N	E_s
	s^2 . km^{-2}	s^2 . km^{-2}	kg . m^{-3}	g	g		km	mm			$MJ.m^{-2}$
05403028	0.013	0.23	5700	4.0×10^{-8}	3.2×10^{-9}	1.7	95.9	90–230	1.5×10^{2}	5.3×10^{3}	12.5
05403032	0.009	0.20	1300	2.5×10^{-8}	1.0×10^{-10}	2.0	107.4	40–250	8.2×10^{1}	1.0×10^{5}	1.2
05A06077	0.008	0.30	1700	2.5×10^{-9}	2.0×10^{-11}	1.9	110.3	20–120	5.5×10^{3}	2.3×10^{6}	0.8
06406048	0.009	0.25	5500	3.2×10^{-8}	1.0×10^{-9}	2.0	97.5	70–220	5.4×10^{1}	6.5×10^{3}	9.4
06420006	0.007	0.25	1210*	1.0×10^{-7}	4.0×10^{-10}	1.7	102.3	60–400	5.5×10^{1}	1.9×10^{4}	4.2
06420089	0.012	0.12	1400	1.2×10^{-7}	6.3×10^{-9}	1.9	98.6	160–430	1.6×10^{2}	9.7×10^{3}	4.2
06724010	0.011	0.21	1000	1.6×10^{-8}	1.3×10^{-8}	1.9	106.3	190–220	1.6×10^{5}	3.6×10^{5}	0.6
06724013	0.015	0.52	1100	9.8×10^{-10}	7.9×10^{-10}	2.0	96.2	90	2.5×10^{5}	2.5×10^{5}	1.3
06724023	0.019	0.14	700	1.6×10^{-7}	1.6×10^{-10}	2.0	102.5	50–470	1.2×10^{1}	5.1×10^{4}	2.2
06727196	0.023	0.45	690	3.2×10^{-8}	1.0×10^{-8}	1.7	98.5	190–270	4.2×10^{3}	3.0×10^{4}	1.0
06730083	0.019	0.86	1700	7.9×10^{-8}	2.5×10^{-9}	2.7	97.0	110–370	3.2×10^{2}	3.5×10^{5}	2.3
06802034	0.028	0.29	500	7.9×10^{-8}	6.3×10^{-8}	1.9	98.5	370	1.7×10^{3}	1.7×10^{3}	0.8
06A20013	0.009	0.29	400	7.9×10^{-9}	6.3×10^{-9}	2.0	98.4	170	3.1×10^{5}	3.1×10^{5}	0.9
06A20125	0.040	0.20	1700	2.5×10^{-5}	2.5×10^{-7}	1.8	94.8	500–2530	1.0	3.4×10^{2}	1.8
06A20126	0.007	0.22	2590	8.3×10^{-9}	2.0×10^{-9}	2.0	96.6	100–170	1.2×10^{2}	1.8×10^{3}	7.5
06C13104	0.011	0.19	2000	4.1×10^{-8}	2.0×10^{-8}	2.0	100.1	220–300	1.8×10^{3}	1.0×10^{4}	2.3
06C13136	0.004	0.52	2200	2.0×10^{-5}	2.0×10^{-8}	1.8	103.9	230–2330	1.0	1.5×10^{3}	1.2
SE	0.019	0.03	30%	3.9×10^{-2}	5.0×10^{-3}	1.9	80.2	1.46–2.32	1.0	1.9×10^{1}	66.1
06C13137	0.009	0.29	1100	1.3×10^{-8}	5.0×10^{-10}	1.8	101.6	60–200	4.7×10^{2}	3.4×10^{4}	1.8
06C13334	0.003	0.10	2600	1.3×10^{-8}	6.3×10^{-10}	2.0	96.6	70–200	1.7×10^{2}	1.2×10^{4}	9.6
06C14215	0.012	0.23	1850	7.8×10^{-9}	7.8×10^{-9}	2.0	101.3	170	5.5×10^{3}	5.5×10^{3}	1.7
06C14529	0.052	0.18	600	7.8×10^{-6}	6.3×10^{-9}	2.0	102.5	160–1700	1.0	1.9×10^{4}	1.3
SE	0.052	0.23	55%	2.5×10^{-4}	2.0×10^{-4}	2.0	88.7	0.47–0.54	7.6×10^{2}	1.7×10^{3}	16.4

Table A.2: continued.

meteor	σ	η	δ	GUML	GLML	§	H_{er}	sizes	n_0	N	E_s
	s^2 . km^{-2}	s^2 . km^{-2}	kg . m^{-3}	g	g		km	mm			$MJ.m^{-2}$
07406018	0.032	0.31	800	1.3×10^{-5}	1.0×10^{-7}	2.3	96.0	370–2000	1.7×10^{1}	3.7×10^{4}	1.5
07407021	0.030	0.40	1600*	1.6×10^{-6}	5.0×10^{-9}	2.0	87.9	140–1000	2.6×10^{1}	4.2×10^{4}	5.2
07407034	0.001	0.12	2090	1.6×10^{-7}	1.3×10^{-7}	1.9	85.9	430–470	1.7×10^{3}	3.8×10^{3}	10.0
07812429	0.017	0.30	590	2.5×10^{-8}	6.3×10^{-10}	2.0	100.6	70–250	2.1×10^{3}	3.1×10^{5}	1.1
08505025	0.003	0.80	3100	4.0×10^{-10}	1.6×10^{-10}	2.0	78.1	40–50	8.4×10^{4}	5.4×10^{5}	36.2
08506016	0.009	0.20	2500	3.2×10^{-8}	5.0×10^{-10}	1.9	103.2	70–270	3.2×10^{1}	5.9×10^{3}	4.5
08728012	0.080	1.31	5700	4.3×10^{-7}	1.0×10^{-10}	1.7	86.3	30–510	1.2×10^{1}	4.4×10^{4}	20.8
08728076	0.012	0.31	1100	4.0×10^{-8}	1.0×10^{-9}	2.3	99.5	90–290	4.3×10^{2}	1.5×10^{5}	1.5
08728078	0.030	0.21	500	2.0×10^{-9}	5.0×10^{-11}	2.0	99.5	30–110	1.5×10^{3}	2.2×10^{5}	1.2
08728149	0.035	0.74	500	1.6×10^{-7}	1.3×10^{-7}	2.1	99.0	400–470	1.6×10^{2}	3.7×10^{2}	1.4
08728151	0.018	0.50	790	2.0×10^{-8}	1.2×10^{-9}	1.8	98.5	90–230	1.5×10^{3}	7.2×10^{4}	1.8
08728156	0.014	0.58	200	2.0×10^{-8}	1.0×10^{-10}	2.0	98.8	40–230	1.9×10^{2}	1.5×10^{5}	1.0
08728223	0.016	0.10	1100	6.8×10^{-8}	1.7×10^{-9}	2.0	97.0	100–350	2.6×10^{1}	5.1×10^{3}	9.0
08728233	0.012	0.24	450	5.0×10^{-8}	1.1×10^{-9}	2.0	102.7	90–320	1.1×10^{3}	2.0×10^{5}	1.1
08728280	0.005	0.14	2000	4.0×10^{-8}	7.9×10^{-11}	2.0	97.8	30–290	2.7×10^{1}	6.8×10^{4}	7.1
08729037	0.006	0.29	1090	1.0×10^{-7}	1.0×10^{-9}	2.0	97.7	90–400	2.0×10^{1}	8.1×10^{3}	13.4
08927015	0.004	0.14	170	2.2×10^{-10}	3.0×10^{-12}	2.0	126.0	10–50	1.8×10^{3}	5.4×10^{5}	0.6
08927049	0.011	0.15	510	2.4×10^{-8}	1.6×10^{-8}	2.0	97.1	230–250	2.1×10^{2}	4.8×10^{2}	5.0
08927101	0.014	0.23	700	1.0×10^{-7}	7.9×10^{-9}	2.0	94.3	160–400	8.4×10^{2}	4.8×10^{4}	3.9
SE	0.014	0.27	30%	6.3×10^{-5}	4.0×10^{-7}	2.3	82.2	0.06–0.34	1.1×10^{2}	3.1×10^{5}	28.6
08928139	0.014	1.05	290	1.1×10^{-6}	1.1×10^{-6}	2.0	100.9	880	7.7×10^{2}	7.7×10^{2}	1.3
08928141	0.007	0.91	800	5.0×10^{-9}	3.2×10^{-11}	2.0	103.0	30–150	5.7×10^{2}	4.3×10^{5}	1.0
08928235	0.009	0.30	790	8.5×10^{-11}	5.0×10^{-11}	2.0	112.9	20–20	2.7×10^{5}	1.0×10^{6}	0.6
SE	0.009	0.17	56%	1.0×10^{-5}	8.0×10^{-6}	2.0	97.4	0.32	8.1×10^{3}	8.1×10^{3}	7.12
09102507	0.010	0.18	2600	3.2×10^{-8}	1.3×10^{-8}	1.8	104.6	200–270	1.0×10^{3}	5.6×10^{3}	1.2
09102515	0.009	0.12	1300	3.2×10^{-9}	2.5×10^{-9}	2.0	103.3	130	5.0×10^{3}	5.0×10^{3}	1.7
09421084	0.021	0.61	200	5.0×10^{-8}	7.9×10^{-10}	2.0	108.5	80–320	1.3×10^{2}	3.2×10^{4}	0.7
09421101	0.034	0.39	610	6.0×10^{-8}	1.0×10^{-8}	2.0	102.2	180–340	3.5×10^{2}	7.2×10^{3}	0.9
09729165	0.010	0.20	2000	1.6×10^{-7}	7.9×10^{-11}	2.0	99.1	30–470	5.0	6.1×10^{4}	6.4
09729261	0.031	0.14	720	2.0×10^{-6}	7.9×10^{-7}	2.0	102.3	800–1080	1.2×10^{2}	7.2×10^{2}	0.9

Table A.2: continued.

meteor	σ	η	δ	GUML	GLML	§	H_{er}	sizes	n_0	N	E_s
	s^2 . km^{-2}	s^2 . km^{-2}	kg . m^{-3}	g	g		km	mm			$MJ.m^{-2}$
09818045	0.019	0.50	2100	1.6×10^{-8}	1.3×10^{-9}	2.6	94.5	110–280	5.3×10^{2}	9.7×10^{4}	1.5
09818120	0.014	0.20	1500*	1.6×10^{-8}	1.3×10^{-8}	2.0	99.8	130–220	1.3×10^{3}	7.6×10^{3}	3.4
SE	0.014	0.26	70%	1.6×10^{-5}	6.3×10^{-6}	2.0	93.3	0.16–0.22	1.3×10^{3}	7.6×10^{3}	10.3
09819085	0.007	0.13	200	1.0×10^{-10}	5.0×10^{-11}	2.0	125.4	30–40	1.0×10^{5}	3.8×10^{5}	0.6
09819165	0.005	0.10	200	2.5×10^{-10}	6.3×10^{-11}	2.3	118.3	30–50	3.7×10^{3}	7.6×10^{4}	0.6
09819237	0.009	0.13	2100	2.0×10^{-8}	1.0×10^{-9}	2.0	86.9	90–230	5.7×10^{1}	4.3×10^{3}	15.1
09820027	0.019	0.51	2300	7.9×10^{-8}	1.0×10^{-10}	2.0	104.9	40–370	1.5×10^{1}	4.8×10^{4}	4.2
09820190	0.011	0.20	1100	3.2×10^{-9}	6.3×10^{-10}	2.0	117.0	70–130	2.4×10^{3}	3.7×10^{4}	2.5
09820219	0.034	0.43	1100	2.5×10^{-8}	1.3×10^{-8}	2.2	95.3	200–250	1.7×10^{3}	6.9×10^{3}	2.4
09B17022	0.003	0.35	2300	1.5×10^{-8}	1.5×10^{-8}	1.7	90.8	210	1.0×10^{5}	1.0×10^{5}	9.7
09B17055	0.007	0.64	2800*	3.0×10^{-9}	2.5×10^{-9}	1.8	102.3	80–230	2.4×10^{6}	2.4×10^{6}	1.0
SE	0.007	0.62	40%	2.0×10^{-5}	7.9×10^{-7}	2.0	78.1	0.08–0.23	1.7×10^{4}	1.5×10^{6}	52.7
09B17084	0.011	0.61	2100	2.0×10^{-8}	1.0×10^{-9}	2.0	100.3	90–230	6.1×10^{2}	4.4×10^{4}	1.7
SE	0.011	0.39	40%	4.0×10^{-6}	4.0×10^{-6}	2.0	85.4	0.14	2.4×10^{4}	2.4×10^{4}	19.8
10406001	0.013	0.22	400	1.3×10^{-8}	1.3×10^{-11}	2.1	96.2	20–200	5.1×10^{2}	3.5×10^{6}	1.5
10406014	0.010	0.10	300	1.6×10^{-7}	1.0×10^{-10}	2.1	101.2	40–470	1.7×10^{1}	2.6×10^{5}	1.6
10406043	0.062	0.33	300	4.0×10^{-8}	1.0×10^{-12}	1.9	108.9	10–290	2.8×10^{1}	1.8×10^{6}	0.6
10406066	0.018	1.20	200	5.0×10^{-9}	1.6×10^{-10}	2.8	104.8	40–150	9.0×10^{2}	1.3×10^{6}	0.3
10406078	0.020	0.09	500	2.0×10^{-7}	1.3×10^{-8}	2.4	98.3	200–500	2.5×10^{2}	3.1×10^{4}	2.1
10407030	0.015	0.07	200	1.6×10^{-8}	4.0×10^{-10}	1.9	103.6	60–220	2.2×10^{3}	3.2×10^{5}	0.8
10408088	0.013	0.20	1900	2.0×10^{-8}	7.9×10^{-9}	1.9	99.0	170–230	4.6×10^{2}	2.6×10^{3}	7.4
11422209	0.008	0.12	200*	7.8×10^{-10}	7.8×10^{-10}	2.0	108.8	80	1.2×10^{5}	1.2×10^{5}	1.1
11505072	0.015	0.52	1400	4.9×10^{-9}	1.3×10^{-9}	2.0	109.7	90–150	5.5×10^{3}	6.3×10^{4}	1.5
DRA01	0.022	0.30	440	2.1×10^{-9}	2.0×10^{-9}	2.0	96.1	100–110	5.5×10^{4}	5.5×10^{4}	1.9
SE	0.022	0.82	17%	2.3×10^{-10}	2.3×10^{-10}	2.0	84.0	0.01	5.9×10^{7}	5.9×10^{7}	15.7
DRA03	0.027	0.63	99*	7.7×10^{-9}	7.7×10^{-9}	2.0	98.3	160–170	2.5×10^{4}	2.5×10^{4}	1.5
SE	0.027	0.66	50%	7.1×10^{-7}	7.1×10^{-7}	2.0	92.3	0.08	2.4×10^{5}	2.4×10^{5}	4.2
DRA04	0.015	2.31	375	5.0×10^{-9}	3.9×10^{-11}	2.0	105.1	30–150	8.2×10^{4}	1.9×10^{7}	0.5
DRA05	0.032	0.73	370	1.4×10^{-8}	1.0×10^{-10}	2.0	102.0	40–210	2.4×10^{3}	5.3×10^{5}	0.9
SE	0.032	0.84	14%	4.1×10^{-7}	3.9×10^{-7}	2.0	90.3	0.05–0.06	9.5×10^{4}	9.5×10^{4}	6.3

Table A.2: continued.

meteor	σ	η	δ	GUML	GLML	§	H_{er}	sizes	n_0	N	E_s
	s^2 . km^{-2}	s^2 . km^{-2}	kg . m^{-3}	g	g		km	mm			$MJ.m^{-2}$
DRA06	0.015	0.15	390*	3.6×10^{-9}	2.2×10^{-11}	2.0	100.6	20–130	4.7×10^{4}	2.0×10^{7}	1.1
SE	0.015	1.02	16%	2.5×10^{-10}	2.5×10^{-10}	2.0	82.9	0.01	1.5×10^{9}	1.5×10^{9}	25.9
DRA07	0.014	0.96	161	1.6×10^{-9}	5.0×10^{-12}	2.0	100.2	20–100	1.9×10^{4}	7.6×10^{6}	1.2
DRA08	0.019	0.98	180	1.6×10^{-9}	8.0×10^{-12}	2.0	99.4	20–100	6.2×10^{3}	2.5×10^{6}	1.5
12421024	0.017	0.62	220*	6.3×10^{-8}	3.3×10^{-10}	2.5	108.6	60–340	9.0	6.7×10^{4}	2.7
SE	0.017	0.69	10%	5.9×10^{-6}	5.9×10^{-6}	2.2	101.8	0.16	9.1×10^{2}	9.1×10^{2}	8.1
12421069	0.015	0.14	400	1.6×10^{-8}	6.3×10^{-13}	2.0	123.3	10–220	2.5×10^{1}	2.6×10^{6}	0.3
12422070	0.010	0.16	100	1.3×10^{-5}	1.0×10^{-9}	2.9	119.2	80–320	1.0	7.4×10^{3}	0.3
12811093	0.020	0.30	250*	1.0×10^{-6}	1.0×10^{-7}	2.9	116.4	400–860	2.0	3.1×10^{2}	0.8
12811305	0.012	0.62	100	7.9×10^{-9}	5.0×10^{-9}	1.3	126.7	140–170	2.1×10^{3}	6.9×10^{3}	0.2
12811384	0.010	0.27	150	9.3×10^{-9}	9.3×10^{-9}	2.0	130.6	170–180	5.9×10^{3}	5.9×10^{3}	0.1
12814214	0.012	0.25	2800	1.0×10^{-8}	7.9×10^{-9}	2.0	93.2	160–190	3.7×10^{3}	8.3×10^{3}	14.3
12815056	0.006	0.27	300	2.0×10^{-9}	6.3×10^{-11}	2.2	109.5	30–110	3.7×10^{2}	7.2×10^{4}	1.7
12B14142	0.009	0.30	380*	2.0×10^{-10}	2.0×10^{-11}	1.4	113.0	20–50	6.3×10^{3}	9.9×10^{4}	1.1
12B14150	0.011	0.08	1000	3.2×10^{-10}	1.0×10^{-12}	2.0	114.9	10–60	2.2×10^{5}	2.7×10^{8}	0.2
SE	0.011	0.11	50%	1.3×10^{-1}	1.6×10^{-2}	2.0	66.9	2.16–3.70	1.0	3.0×10^{1}	337
13811101	0.015	0.39	1500	2.0×10^{-7}	1.0×10^{-7}	1.9	106.1	400–500	3.0×10^{2}	1.1×10^{3}	1.7
SE	0.015	0.15	30%	1.3×10^{-4}	1.0×10^{-4}	2.7	92.8	0.43	5.4×10^{2}	5.4×10^{2}	14.9
13811202	0.010	0.46	1400	2.0×10^{-7}	3.2×10^{-8}	2.0	93.6	270–500	4.4×10^{3}	9.0×10^{4}	2.9
13811283	0.007	0.15	2430	1.8×10^{-9}	1.8×10^{-9}	1.9	100.3	110	3.1×10^{4}	3.1×10^{4}	2.6
13811452	0.006	0.19	250	3.2×10^{-11}	4.0×10^{-12}	2.0	122.5	10–30	2.8×10^{4}	7.5×10^{5}	0.7
14421037	0.002	0.08	1400*	3.2×10^{-9}	2.5×10^{-9}	1.9	86.9	130	2.6×10^{4}	2.6×10^{4}	18.1
14423003	0.019	0.40	1600	3.2×10^{-8}	1.0×10^{-10}	1.9	95.6	40–270	4.9×10^{2}	3.7×10^{5}	1.8
14505037	0.015	0.39	800*	7.9×10^{-8}	7.9×10^{-9}	1.7	92.7	170–370	5.5×10^{3}	1.3×10^{5}	1.9
14814153	0.003	0.06	2040	1.3×10^{-9}	5.0×10^{-13}	2.0	99.3	6–90	3.8×10^{1}	4.8×10^{5}	9.1
SE	0.003	0.07	60%	2.0×10^{-7}	1.6×10^{-7}	2.0	94.3	0.05	1.2×10^{4}	1.2×10^{4}	21.2